The effect of infiltration by wave overtopping on the macro-stability of a dike

Master Thesis
Civil Engineering & Management

Wouter Kampman
September, 2021

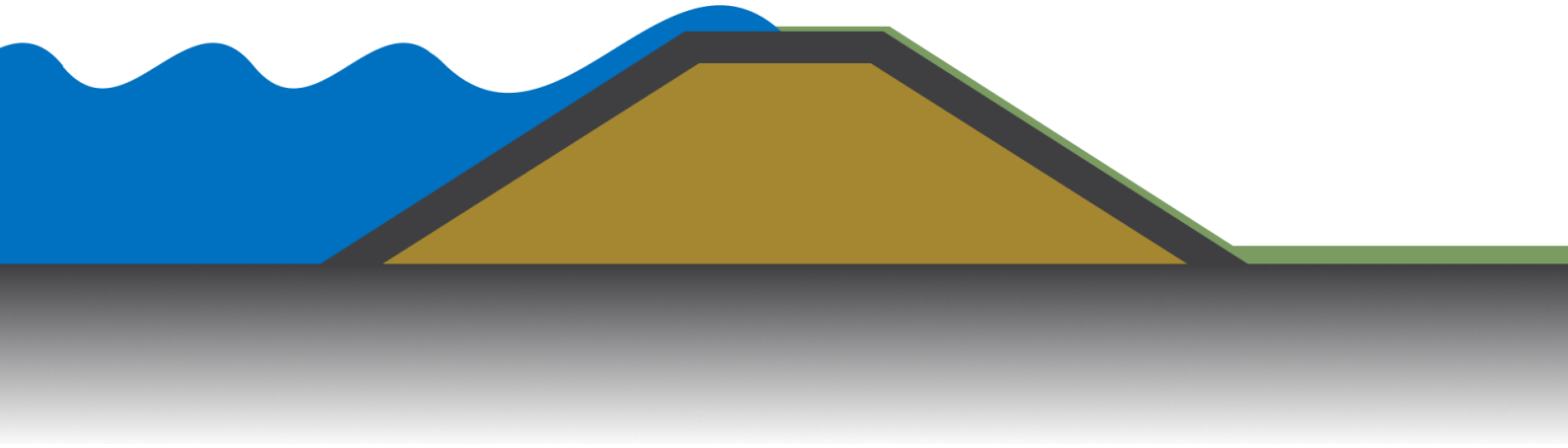

UNIVERSITY OF TWENTE.

SWECO

Author:
W.T. (Wouter) Kampman

Guided by:

ir. Kampen, M. (Maurits)	Adviseur Waterkeringen
dr. Warmink, J.J. (Jord)	UT supervisor
dr. Magnanimo, V. (Vanessa)	UT supervisor
dr. Cheng, H. (Hongyang)	UT supervisor

Foreword

This thesis report, titled: "*The effect of infiltration by wave overtopping on the macro-stability of a dike*", marks the end of my time as a Civil Engineering student at the University of Twente. I would like to take the opportunity to thank all my fellow students throughout my six years of studying, for making this an unforgettable time and for helping me learn everything I have learned since I moved to Enschede.

A word of thanks is also in its place for my supervisors, who have helped me during this research project. Jord Warmink, Vanessa Magnanimo and Hongyang Cheng, thank you for your feedback and for the discussions about my research! And thank you for helping me see the value of my work!

I also want to thank Maurits Kampen for his supervision from Sweco. I especially appreciate the confidence in me and the time taken for my questions and update stories. Also to the rest of team Waterkeringen at Sweco: thank you for including me in the team from day one.

I am looking forward to working with my new colleagues at Sweco from October onwards!

I hope you enjoy reading this thesis report.

Wouter Kampman
September, 2021

Summary

This research covers the effect of infiltration by wave overtopping on the macro-stability of a dike. It is known that water in the dike has an effect on the macro-stability of a dike. However, it is currently not known what the contribution of infiltration by wave overtopping is to the phreatic conditions of the dike and how these specific conditions affect the macro-stability. A better understanding of the effect of infiltration by wave overtopping may prevent the overdimensioning of dikes, saving both space and costs.

The research is conducted based on a case study. For this, dike cross-section DP202+74 of dike trajectory 48-1 is used. The case location provides the dike geometry and hydraulic boundary conditions for the research.

The research is split in two parts. The aim of the first part is to assess the effect of infiltration by wave overtopping on the phreatic conditions in the dike. The aim of the second part is to assess the effect of the phreatic conditions in the dike on the macro-stability of a dike. In the first part, important phreatic processes, related to infiltration by wave overtopping are identified, after which a sensitivity analysis is performed to determine the important parameters with respect to infiltration by wave overtopping. This is done using simulations in GeoStudio: Seep/W, which simulates flow of water through earth bodies. The sensitivity analysis is performed on different material properties (i.e. saturated volumetric water content (θ_s), saturated hydraulic conductivity (K_s) and fitting parameters α and n of the water retention and hydraulic conductivity equations by van Genuchten (1980)), the water flux as a boundary condition, the infiltration time ($T_{wet,\%}$), the thickness of a cover layer (D_{cl}) and on the saturated hydraulic conductivity of a cover layer ($K_{s,cl}$).

The second part of the research is performed using D-Stability, which is modeling software to determine the macro-stability of dikes. The phreatic conditions from GeoStudio: Seep/W, for four material types are transferred to D-Stability and the safety factor for macro-stability is determined for each material type.

The simulations in GeoStudio: Seep/W show that the phreatic response to infiltration by wave overtopping depends on the characteristics of the soil. A highly permeable soil allows the water to add to the phreatic line after infiltrating, while a barely permeable soil causes the water to remain in the surface layers of the dike. In both cases the unsaturated zone in the dike shrinks, but the effect on macro-stability is different, as explained below.

For the sensitivity analysis, the rate of decrease of the area of the unsaturated zone (unsaturated area) over time is used as a representative result to compare the effects of previously mentioned parameters. From this analysis, it is found that θ_s, K_s and α have a negative near linear, positive linear and negative exponential relation to the rate of decrease of the unsaturated area respectively. There is no clear relation between the fitting parameter n and the rate of decrease of the unsaturated area. The value of the flux boundary condition is of similar importance to the K_s of the soil, where the lowest of the two values is the limiting parameter. $T_{wet,\%}$ has a positive linear relation to the rate of decrease of the unsaturated area. Finally, a cover layer has a significant effect on the rate of decrease of the unsaturated area, drastically reducing the rate of infiltration: A one meter thick clay cover layer with a sandy core is found to be almost as effective as a complete clay dike with respect to the phreatic conditions in the dike.

The macro-stability analysis on four material types resulted in a pattern, found in the reduction of the safety factor over time as a result of infiltration by wave overtopping. The safety factor initially reduces quickly, but then slowly approaches the minimum. Due to the relatively low amount of simulations carried out for this assessment, it is not clear whether this pattern is valid for all possible material types. Also, the influence of other factors (e.g. geometry of the dike and strength parameters of the soil) are not considered.

Following from this research, a method is proposed to include infiltration by wave overtopping in the assessment of the macro-stability of a dike. Using the conclusions from the first part of the research, an estimation can be made on the time it takes for a dike to reach fully saturated conditions. A comparison between this duration and the normative duration of wave overtopping yields an indication on whether or not to take wave overtopping into account in the assessment of macro-stability. The macro-stability assessment should then be performed as usual, as there is currently insufficient evidence to assume a general quantitative rule with respect to phreatic conditions and macro-stability.

Contents

List of Figures

List of Tables

List of Symbols

A	Area of the unsaturated zone / Unsaturated area	$[m^2]$
$A\,(Darcy)$	Cross sectional area	$[m^2]$
c_{unsat}	Effective cohesion	$[kN/m^2]$
D	Coefficient of diffusion or dispersion	$[-]$
D_{cl}	Thickness of the cover layer	$[m]$
dA/dt	Rate of change in unsaturated area of time	$[m^2/h]$
E_n or E_{n+1}	Interslice force	$[kN]$
g	Gravitational acceleration	$[m/s^2]$
h	Suction	$[kN/m^2]$
h	Height with respect to NAP	$[m + NAP]$
H_{m0}	Significant wave height	$[m]$
h_k	Free crest height	$[m]$
K or K_w	Hydraulic conductivity	$[m/d]$
$K_{s,cl}$	Saturated hydraulic conductivity of the cover layer	$[m/d]$
K_s	Saturated hydraulic conductivity	$[m/d]$
m	Fitting parameter for Van Genuchten equations	$[-]$
M_v	Mass of water vapor	$[kg]$
m_w	Slope of the volumetric water content function	$[-]$
n	Fitting parameter for Van Genuchten equations	$[-]$
N_{waves}	Number of waves in a storm period	$[-]$
P_{ov}	Probability of a wave overtopping the dike	$[-]$
q	Mean overtopping discharge	$[m^3/s/m]$
$q\,(Darcy)$	Flux of water through soil	$[m^3/s/m^2]$
$Q\,(Darcy)$	Discharge of water through soil	$[m^3/s]$
s_0	Wave steepness	$[-]$
SF	Safety factor for macro-stability	$[-]$
Sr	Degree of saturation	$[-]$
T	Temperature	$[^o]$
T_{dry}	Time the inner slope is dry between two overtopping waves	$[s]$
T_m	Mean wave period	$[s]$
$T_{m-1.0}$	Spectral wave period	$[s]$
$T_{wet,\%}$	Infiltration time as a percentage of total time	$[-]$
T_{wet}	Inundation time. The time the inner slope remains wet after a wave overtops the dike	$[s]$
u or u_w	Pore water pressure	$[kN/m^2]$
u_a	Pore air pressure	$[kN/m^2]$
W	Weight of sliding mass (Bischop)	$[kg]$
$z_{2\%}$	Wave run up height that is exceeded by 2% of the incoming waves	$[m]$

α	Slope angle	$[-]$
α	Fitting parameter for Van Genuchten equations	$[-]$
α_w	Volumetric coefficient of thermal expansion at constant pressure	$[-]$
β	Soil structure compressibility	kPa
β_w	Isothermal compressibility of water	kPa
γ_β	Influence factor for the angle of inclination of incoming waves	$[-]$
γ_b	Influence factor for a berm	$[-]$
γ_f	Influence factor for the slope roughness	$[-]$
γ_v	Influence factor for a (vertical) wall on the slope	$[-]$
ϕ	Drained friction angle	$[-]$
ρ_w	Density of water	$[kg/m^3]$
σ	Total stress	$[kN/m^2]$
σ'	Effective stress	$[kN/m^2]$
σ''	Effective stress in case of unsaturated soil	$[kN/m^2]$
τ	Shear stress	$[kN/m^2]$
Θ or Θ_w	Volumetric water content	$[m^3/m^3]$
Θ_r	Residual volumetric water content	$[m^3/m^3]$
Θ_s	Saturated volumetric water content	$[m^3/m^3]$
ξ_0	Breaker parameter	$[-]$

Chapter 1

Introduction

Before 2017, flood protection of primary flood defences in the Netherlands was expressed in the exceedance frequency of a certain water level (Kok et al., 2016). A dike had to withstand a certain water level that was based on a specific return period. This return period was determined based on the value of the land behind the dike.

In January 2017, a new method was implemented. In this new method, water safety in the Netherlands is expressed as the probability of breaching. Rather than to withstand a certain water level, corresponding to a certain return period, the dike should have an overall probability, comprised of multiple failure mechanisms, of breaching that is lower than allowed for that specific dike trajectory. The probability of breaching that is allowed for a dike trajectory is determined based on risk. Risk is made up of probability- as well as consequences of dike failure (Kok et al., 2016). Dike trajectories that would cause a lot of casualties and economical damage in the case of failure, carry higher consequences and should therefore have a very low probability of failing.

In contrast with the former method, the new method for flood protection allows for wave overtopping to occur, as long as it does not cause the dike to fail. This means that the effect of infiltration by wave overtopping on the probability of breaching, has become an important aspect to consider. Infiltration by wave overtopping is assumed to have an effect on the saturation of water in the dike (TAW, 2004). Therefore, the probability of dike failure as a result of infiltration by wave overtopping must be considered in the safety assessment. However, the exact consequences of wave overtopping with respect to the saturation of water in the dike, and of saturation with respect to macro-stability, are currently unknown.

de Raadt et al. (2015) simulated the effect of wave overtopping on the phreatic surface on the Afsluitdijk in the Netherlands. Waves overtopping the Afsluitdijk will have no effect on the hinterland, because the hinterland (lake IJssel) can easily cope with the water supply from overtopping waves. Therefore, the Afsluitdijk is a perfect example of a dike with a high amount of allowable overtopping discharge. For the initial design of the planned reinforcement, a fully saturated dike was assumed. However, de Raadt et al. (2015) found that their simulation yielded a much lower phreatic surface and thus a much less conservative result than the initially chosen fully saturated dike. The results from the research resulted in high savings of costs, indicating the importance of understanding the effect of infiltration by wave overtopping on macro-stability.

As few is currently known about the effect of infiltration by wave overtopping on the macro-stability of a dike, instant fully saturated conditions are often assumed for any overtopping discharge larger than 1 $l/s/m$. This assumption reduces the stability of a dike significantly, which may lead to an overestimation of the probability of failure. Additionally, in the process of designing a dike, assuming fully saturated conditions may lead to an overdimensioned dike to account for the loss of stability. An overdimensioned dike needs more space and is more expensive than necessary. This research project aims to obtain a better understanding of the effect of infiltration by wave overtopping on the macro-stability of a dike.

The above mentioned research goal is split in two parts. First of which concerns the effect of infiltration by wave overtopping on the phreatic conditions in the dike. In this part, the research aims to qualitatively and quantitatively describe the processes that occur in the dike body in case of infiltration by wave overtopping. As a part of that aim, important parameters and their effect on the phreatic processes are identified by means of a sensitivity analysis.

The second part of the research goal concerns the effect of the phreatic conditions in the dike on macro-stability. The processes identified in the first part of the research are assessed by their effect on the macro-

stability of the dike.

The main question answered in this research project is as follows:

What is the effect of infiltration by wave overtopping on the macro-stability of a dike?

The accompanying sub-questions that will be answered for this research are:

Q1 What phreatic processes are related to water infiltration by wave overtopping and what is their quantitative response to infiltration by wave overtopping?

Q2 What parameters are important in the assessment of infiltration by wave overtopping and what is their quantitative effect on phreatic processes in the dike?

Q3 What is the qualitative and quantitative effect of phreatic conditions on the macro-stability of a dike?

Chapter 1 of this report describes the current state of the art and the theoretical framework of the study. Chapter 2 contains the method applied to perform the research. Chapter 3 describes the results from the research after which the discussion and conclusions are given.

Chapter 2

Theoretical framework and state of the art

This chapter describes the theoretical framework and the current state of the art considering infiltration by wave overtopping and its effect on macro-stability. Section 2.1 gives an introduction in the standard geometry of a dike in the Netherlands. Section 2.2 describes wave overtopping and the state of the art of both the theory behind wave overtopping and the practical implementation of wave overtopping in the assessment of macro-stability. Section 2.3 describes the relevant soil mechanics for this research project, including the flow of water through soils, the behaviour of saturated and unsaturated soils and the assessment of macro-stability using soil mechanics.

2.1 Dikes in the Netherlands

Dikes in the Netherlands can be divided into three main types: clay dikes, sandy dikes and dikes with a sandy core and a clay cover layer. A cross-section of the latter option is depicted in Figure 2.1. This figure also shows the names of different parts of the dike as used throughout this report. The sandy core is mainly for strength of the earthen structure while the cover layer is a more impermeable soil to stop water from flowing through the dike. Additionally, the cover layer protects the dike from erosion by wave overtopping. The phreatic line is the water level within the dike body and generally leads from the outside water level to the inner toe of the dike.

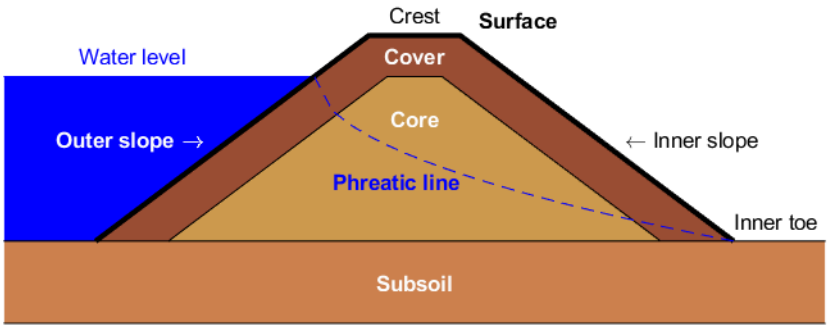

Figure 2.1: Schematic view of dike standard dike cross-section with normative high water level and phreatic line.

2.2 Wave overtopping and infiltration

Waves are generated on the water and, at some point, may reach the dike. This causes wave run-up. The height to which wave run-up occurs depends on wave conditions (e.g. wave height, wave period and angle of wave attack) and on conditions of the water-side slope of the dike (e.g. average slope, roughness and berms) (TAW, 2002). When the wave run-up is higher than the crest of the dike, the wave will overtop the dike. The water will flow over the crest and onto the land-side slope of the dike. This is called wave overtopping.

Wave overtopping has been an important failure mechanism for dikes, for as long as dikes exist. However, the main problem behind wave overtopping is usually considered not to be the infiltration, but rather the overflowing water eroding the land-side slope and flooding the hinterland (EurOtop, 2018; Warmink et al., 2018). Partially for that reason, wave overtopping is mainly described by the average overtopping discharge (TAW, 2002; Dutch Ministry of Infrastructure and the Environment, 2012; Spanjersberg, 2016; Visser and Jongejan, 2018). The average wave overtopping discharge does not, however, fully describe wave overtopping. For infiltration by wave overtopping specifically, the overtopping volume of an individual wave and the time this volume remains on the inner slope of a dike are more important than the average wave overtopping (Dutch Ministry of Infrastructure and the Environment, 2012). An average wave overtopping discharge of 1 $l/m/s$ can be achieved by low and short waves (e.g. one wave every second, overtopping one liter per meter per wave) or by high and long waves (e.g. one wave every 100 seconds, overtopping 100 liters per meter per wave). These two options have a vastly different effect on the infiltration on the inner slope of the dike. Soil has a limited infiltration capacity, which means that in case of large waves most water will discharge as runoff towards the hinterland, rather than infiltrate the dike body.

The overtopping volume of an individual wave is a function of the free crest height (i.e. the vertical distance between the dike crest and the still water level) and the wave height and length. Additionally, dike characteristics like the outer slope steepness and roughness and the presence of a berm may influence the overtopping volume of incoming waves (Chen et al., 2020). As it is near impossible to predict the exact characteristics of each incoming wave, the overtopping volume is expressed as a probability density function by TAW (2002). This allows for an estimation of the probability of overtopping for each individual wave. Together with the amount of waves attacking the dike and the time during which the inner slope remains wet, this yields a percentage of time during which infiltration can occur. This value is named the infiltration time and will be further elaborated on below.

As previously mentioned, wave overtopping is mainly described by the average wave overtopping discharge, but this does not fully describe wave overtopping. A method to schematise wave overtopping in such a way that it can be used to determine the infiltration is given by Dutch Ministry of Infrastructure and the Environment (2012) and Spanjersberg (2016). They state that in the case of a water level that corresponds to an average overtopping discharge of less than 0.1 l/s/m, infiltration by wave overtopping can be neglected. In any other case, they schematise wave overtopping as the time during which the land-side slope is wet from overtopping waves. In this schematisation they assume that the land-side slope of a dike remains wet for 30 seconds after the passing of an overtopping wave. This assumption is based on observations made during wave overtopping tests. Based on this assumption, they state that in the case that the time between overtopping waves is less than 30 seconds, the land-side slope remains wet at all times. When the time between overtopping waves is more than 30 seconds, the land-side slope remains wet for only a percentage of the time. The percentage of time, which they define as infiltration time, is computed using equations from TAW (2002) and depends only on the wave height and the average overtopping discharge. This schematisation also assumes that the overtopping volume is at all times larger than the infiltration capacity of the soil.

To describe wave run-up and overtopping, TAW (2002) provide a set of equations. Wave run-up and overtopping can be determined for a design case or for an assessment case. For a design case, the dike design is made such that the dike meets the set requirements. For the assessment case, the actual dike is tested against the set requirements. The calculation methods for the two cases are therefore inverted. A design calculation leads from probability of failure to dike geometry and characteristics, while an assessment calculation leads from dike geometry and characteristics to probability of failure. The assessment case is the main focus of this report.

As these equations are of empirical nature, they have been updated over time with the increase in knowledge

and data. The equations given below are the most recent versions. Run-up equations are generally based on the surf similarity parameter ξ_0, describing the behaviour of an incoming wave with respect to breaking. Waves break on the outer slope for values of ξ_0 lower than 2 to 2.5. The general equation for wave run-up, according to TAW (2002), is given by Equation 2.1

$$\frac{z_{2\%}}{H_{m0}} = 1.75\gamma_b\gamma_f\gamma_\beta\xi_0 \tag{2.1}$$

$$\xi_0 = \frac{\tan\alpha}{s_0}, \qquad s_0 = \frac{2\pi H_{m0}}{gT_{m-1.0}^2}$$

With a maximum for larger values of ξ_0 given by Equation 2.2

$$\frac{z_{2\%}}{H_{m0}} = \gamma_f\gamma_\beta\left(4.3 - \frac{1.6}{\sqrt{\xi_0}}\right) \tag{2.2}$$

In which $z_{2\%}$ is the height that is exceeded by 2% of incoming waves, H_{m0} is the significant wave height $[m]$, ξ_0 is the breaker parameter $[-]$, α is the slope angle of the outer slope $[-]$, s_0 is the wave steepness $[-]$, g is the gravitational acceleration $[m/s^2]$, $T_{m-1.0}$ is the spectral wave period at the toe of the dike and γ_b,γ_f and γ_β are influence factors for a berm, the slope roughness and the angle of inclination of incoming waves respectively. These equations hold for the domain $0.5 < \gamma_b\xi_0 < 8$ to 10.

As aforementioned, the infiltration time (i.e. the percentage of time during which the inner slope is wet) is determined by using the probability of overtopping for an individual wave, the inverted wave period (i.e. wave frequency) and the inundation time per wave. The probability of overtopping for an individual wave is determined using the equation below (TAW, 2002).

$$P_{ov} = \exp\left(-\left[\sqrt{-\ln 0.02}\frac{h_k}{z_{2\%}}\right]^2\right) \tag{2.3}$$

In which P_{ov} is the probability of a wave overtopping the dike $[-]$, h_k is the free crest height $[m]$ and $z_{2\%}$ is the wave run up height that is exceeded by 2% of the incoming waves $[m]$.

The probability of overtopping for an individual wave in combination with the wave frequency gives the frequency of overtopping waves, which can then be multiplied by the inundation time per wave to yield the final infiltration time.

$$T_{wet\%} = T_{wet}\frac{P_{ov}}{T_m}, \qquad with \qquad 0 \leq T_{wet\%} \geq 1 \tag{2.4}$$

In which $T_{wet\%}$ is the infiltration time as a percentage of total time $[\%]$, T_{wet} is the inundation time per wave $[s]$ and T_m is the mean wave period $[s]$. As the spectral wave period $T_{m-1,0}$ is a more commonly used wave characteristic, it is assumed that the mean wave period T_m is the sufficiently similar to the spectral wave period to perform this calculation.

The influence of the infiltration time on the phreatic condition in the dike will be further elaborated on in Section 3.3.

2.3 Soil mechanics and (ground)water flow

This section will give a basic description of the soil mechanics relevant for this research. This section also includes the behaviour of soils and flow through soils under saturated and unsaturated conditions and a description of the assessment of macro-stability.

2.3.1 Saturated and unsaturated soil strength

Soils are a granular material, causing them to act differently to solid materials like for example steel (Das, 2008). An important granular material characteristic is that the shear strength depends on the pressure that is applied to the sample. This happens because the particles in a soil sample will exert a force on each other, which increases with the pressure that is applied to the sample. This force between particles is called the effective stress and it causes the shear strength to increase. The effective stress is not only dependent on the pressure applied to the sample, but also on the pore water pressure in the soil. Water between soil particles will push soil particles away from each other, reducing their grip on each other and therefore reducing the shear strength of the sample. The effective stress can be described by Equation 2.5 (Das, 2008).

$$\sigma' = \sigma - u \tag{2.5}$$

In which σ' is the effective stress in the soil $[kN/m^2]$, σ is the total stress in the soil $[kN/m^2]$ and u is the pore-water pressure $[kN/m^2]$, which is often equal to the hydrostatic pressure.

The shear strength can then be described using Equation 2.6 (Das, 2008).

$$\tau = \sigma' \tan \phi \tag{2.6}$$

In which τ is the shear stress in a drained soil $[kN/m^2]$ and ϕ is the drained friction angle $[-]$.

2.3.2 Groundwater flow

Soils behave differently under saturated and unsaturated conditions. Below a phreatic line, the saturation of a soil is equal to unity, meaning that all the pores are filled with water (Tarantino and Di Donna, 2019). Above the phreatic line, the soil is not fully saturated, but there may still be water present in the soil. The zone where the soil is not fully saturated is named the unsaturated zone.

Flow through a homogeneously permeable medium can be described by Darcy's law (Darcy, 1856), which states that the flux (q) $[m^3/s/m^2]$ is given by the product of the pressure difference ($\frac{dh}{dx}$) $[m/m]$ and the saturated hydraulic conductivity (K_s) $[m/s]$, as shown in the equation below. Darcy's law is valid for saturated soils, as they are generally homogeneously permeable, assuming the soil structure is homogeneous and isotropic.

$$q = \frac{Q}{A} = -K_s \frac{dh}{dx} \tag{2.7}$$

Darcy's law assumes a homogeneously permeable medium, which is usually the case in saturated groundwater flow. The equation can be extended to be used for unsaturated soils (Shaw et al., 2017). In that case, the saturated hydraulic conductivity should be replaced by the hydraulic conductivity ($K_s \rightarrow K$), which depends on the level of saturation of the soil, as further elaborated on below.

In the case of infiltration, a fluid is flowing from a saturated region to an unsaturated region. Since the hydraulic conductivity depends on the level of saturation, this means that the soil is not homogeneously permeable. This causes a complex situation where the flux through the medium and the permeability of the medium are dependent on each other. This also applies to the drying process, where the level of saturation in the soil decreases over time.

2.3.3 Influence of the degree of saturation

The unsaturated zone is characterised by negative pore-water pressures (Tarantino and Di Donna, 2019). As previously explained, water between soil particles will push the particles apart, reducing their grip on each other. However, when the degree of saturation is below unity, there is more space for water than there is water, causing the water retained between the soil particles to apply a suction between particles, which in turn causes a form of cohesion in the soil. This suction causes an increase in effective normal stresses and therefore a stronger soil, as is apparent from Equation 2.5 with negative pore-water pressures. The negative pore water pressure is therefore also called suction.

Tarantino and Di Donna (2019) describe an extended version of Equations 2.5 and 2.6, in which the degree of saturation is included, given in Equations 2.8 and 2.9 respectively. Equation 2.8 shows that when the degree

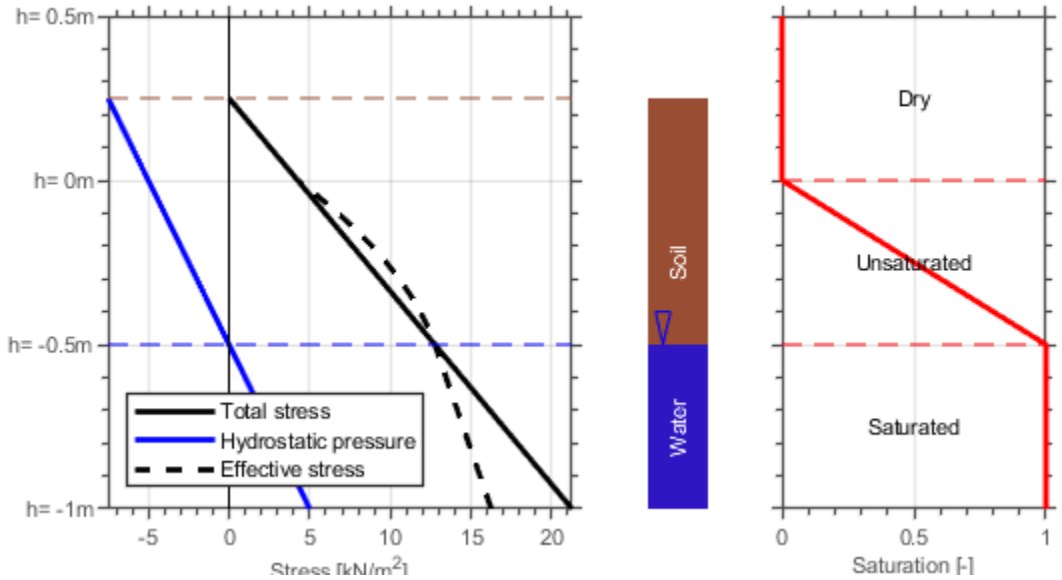

Figure 2.2: Visualisation of the effective stress (σ'') from Equation 2.8 as a result of the total stress (σ), the hydrostatic pore-water pressure (u) and the degree of saturation (S_r) in a soil sample with a water table at $h = -0.5m$.

of saturation is zero (i.e. when the soil is dry), the effective stress is equal to the total stress and in the saturated zone (i.e. below the water table), the equation reduces to Equation 2.5. The same holds for Equation 2.9, which reduces to equation 2.6 for a degree of saturation equal to zero.

$$\sigma'' = \sigma - u_w S_r \tag{2.8}$$

$$\tau = (\sigma - u_w S_r)\ \tan\phi \tag{2.9}$$

In which u_w is the pore-water pressure $[kN/m^2]$ and S_r is the degree of saturation reaching from 0 to 1 $[-]$.

Equation 2.8 is visualised in Figure 2.2 for an example case of a soil sample starting at $h = 0.25m$, a water table at $h = -0.5m$ and a degree of saturation that decreases linearly with height between $h = -0.5m$ and $h = 0m$. This figure shows that the effective stress below the water table is identical to the effective stress as determined using standard saturated soil mechanics with Equation 2.5. However, the effective stress in the unsaturated zone (i.e. just above the water table) increases slightly with respect to the total stress.

Equation 2.9 can be conveniently rewritten as follows (Tarantino and Di Donna, 2019).

$$\tau = \sigma\ \tan\phi + \underbrace{(-uS_r\ \tan\phi)}_{c_{unsat}} \tag{2.10}$$

This shows that the added shear strength of a soil sample, due to the suction in the unsaturated zone, can be described by a form of effective cohesion (c_{unsat}). Using this information, an estimation of the shear strength of an unsaturated soil sample can be made for a given pore-water pressure and degree of saturation, by applying an effective cohesion to the soil. It must be noted that this method should be treated with care, as the cohesion is not an actual property of the soil. When the soil becomes either fully saturated or fully dry, the effective cohesion should be removed from the calculation to prevent an overestimation of the soils shear strength.

2.3.4 Water retention and hydraulic conductivity curves

As explained, the level of saturation is an important parameter to determine both the permeability, as well as the shear strength of the soil locally. The level of saturation is determined based on the suction that is present above the phreatic line.

The relation between the level of saturation and the suction in the soil is described using water retention curves. The water retention curve is a specific characteristic of a type of soil, based on a standard temperature and corresponding water viscosity. This standard temperature is usually $20°C$ (Chappell and Ternan, 1997). Similarly, the hydraulic conductivity of a soil can be described by the hydraulic conductivity curve, which relates the suction (i.e. negative pore water pressure) to the hydraulic conductivity of a soil (Shaw et al., 2017).

According to van Genuchten (1980), water retention curves and hydraulic conductivity can be described by a set of five independent variables (θ_r, θ_s, α, n and K_s) using the equations below.

$$K(h) = K_s \frac{\left(1 - (\alpha h)^{n-1}\left[1 + (\alpha h)^n\right]^{-m}\right)^2}{\left[1 + (\alpha h)^n\right]^{m/2}}, \qquad with \qquad m = 1 - \frac{1}{n} \qquad and \qquad h = -u_w \tag{2.11}$$

$$\theta(h) = \theta_r + \frac{(\theta_s - \theta_r)}{\left[1 + (\alpha h)^n\right]^m}, \qquad with \qquad m = 1 - \frac{1}{n} \qquad and \qquad h = -u_w \tag{2.12}$$

In which K is the hydraulic conductivity $[m/s]$ as a function of the suction h $[kPa]$, K_s is the saturated hydraulic conductivity $[m/s]$, α, n and m are fitting parameters $[-]$, θ is the volumetric water content $[m^3/m^3]$, θ_r is the residual water content $[m^3/m^3]$ and the θ_s is the saturated water content $[m^3/m^3]$.

The saturated hydraulic conductivity (K_s) is a measure of permeability of the soil in the fully saturated state. The saturated water content (θ_s) is the maximum water that a soil can hold (i.e. when the soil is saturated). The residual water content (θ_r) is the water content that remains in the soil after it is drained. The α and n are fitting parameters, meaning that they have no strict physical meaning.

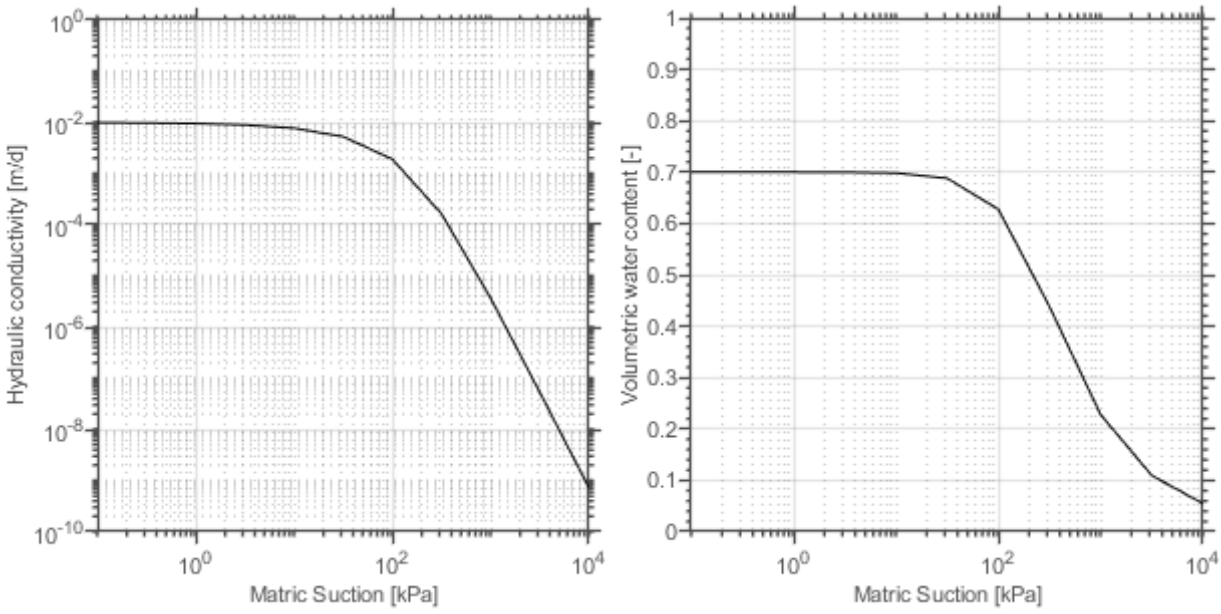

(a) (b)

Figure 2.3: Hydraulic conductivity (K) as a function of suction (h) according to equation 2.11 (a) and water retention (Θ) as a function of suction (h) according to equation 2.12 (b). Both figures correspond to an example case with parameter values $K_s = 0.01$, $\Theta_s = 0.7$, $\Theta_r = 0.01$, $\alpha = 0.005$ and $n = 1.7$.

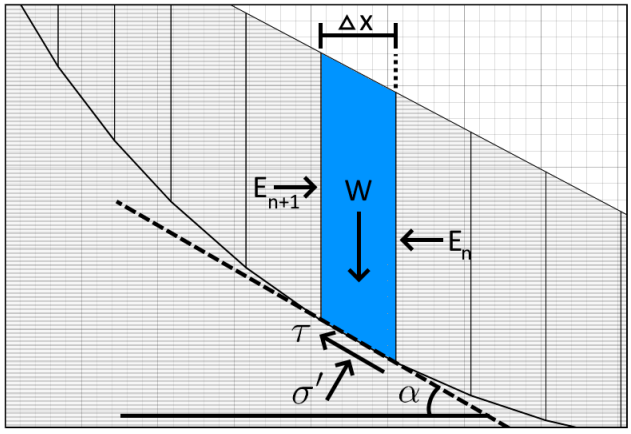

Figure 2.4: The forces on a slice in the method of Bishop, where W is the weight of the slice, E_n and E_{n+1} are the inter-slice forces, σ' is the effective normal stress, τ is the shear stress and α is the mean angle of the initial slice. Adapted from Bishop (1955).

2.3.5 Macro-stability

The above described soil mechanics is used to determine the macro-stability of a dike. Macro-instability on the landside slope is the sliding of the landside slope (Kok et al., 2016). This happens when the friction forces along a certain slip circle are insufficient to carry the weight of the landside slope of the dike.

A method to determine a safety factor with respect to macro stability is given by Bishop (1955). He states that macro-stability is governed by the ratio between the stabilising and the destabilising forces along a slip circle that can theoretically have any center location and any radius, as shown in Figure 2.4. The stabilising forces are the normal stress (σ') and shear stress (τ) along the slip circle. The destabilising force is the weight of the sliding mass (W). The normal and shear stresses along a slip circle are parameters that depend on the soil type and structure and on the pore-water pressure. As previously explained, the pore-water pressure decreases the effective normal and shear stress in the soil, according to Equations 2.5 and 2.6, and thus decreases the stabilising force along the slip circle. Additionally, a higher water content in the dike increases the weight of the sliding mass, increasing the destabilising force.

Another method that is often applied to determine the safety factor with respect to macro-stability is the Uplift-Van method (Van, 2001). This method is similar to the Bishop method and is further elaborated on in Section 2.5 on page 12.

In practice, in a macro-stability assessment, the phreatic line is usually determined using the guidelines in TAW (2004). If the situation is too complex to approximate with these guidelines, a geo-hydrological model is setup to determine the location of the phreatic line and corresponding pore water pressures, saturation levels and groundwater flows. Often, the soil above the phreatic line is assumed dry, as opposed to being unsaturated (Tarantino and Di Donna, 2019). As previously explained, this assumption leads to a weaker soil and thus a conservative result.

2.4 GeoStudio: Seep/W

GeoStudio is a modeling software package especially made for geo-engineering. The software contains different modules, including Seep/W, which is used for groundwater flow analyses in both steady state as well as transient conditions. GeoStudio: Seep/W solves the conservation of mass equation in the 2DV plane, as given below in Equation 2.13, for every grid cell for each timestep (Ltd GEOSLOPE International, 2020). This equation states that the rate of change in mass is governed by the rate of change in incoming mass, the rate of change in outgoing mass and a source or sink term.

$$\frac{\mathrm{d}M_{st}}{\mathrm{d}t} = \frac{\mathrm{d}m_{in}}{\mathrm{d}t} - \frac{\mathrm{d}m_{out}}{\mathrm{d}t} + \frac{\mathrm{d}M_S}{\mathrm{d}t} \tag{2.13}$$

In which M_{st} is the stored mass in the grid cell, m_{in} and m_{out} is the incoming and outgoing mass respectively and M_S represents a source or sink within the grid cell.

The software also solves a water flow equation. The complete version of this equation is given below in Equation 2.14.

$$\rho_w \left(\underbrace{\theta_w \beta_w \frac{\partial u_w}{\partial t}}_{\text{i}} + \underbrace{\beta \frac{\partial u_w}{\partial t}}_{\text{ii}} + \underbrace{m_w \frac{\partial}{\partial t}\left(u_a - u_w\right)}_{\text{iii}} \right) + \underbrace{\theta_w \rho_w \alpha_w \frac{\partial T}{\partial t}}_{\text{iv}} + \underbrace{\frac{\partial M_v}{\partial t}}_{\text{v}} = \underbrace{\frac{\partial}{\partial y}\left[\frac{K_w}{g}\left(\frac{\partial u_w}{\partial y} + \rho_w g \frac{\partial y}{\partial y}\right)\right]}_{\text{vi}} + \underbrace{D}_{\text{vii}} \tag{2.14}$$

In which ρ_w is the density of water, θ_w is the volumetric water content, β_w is the isothermal compressibility of water, u_w is the pore-water pressure, t is the time, β is the soil structure compressibility, m_w is the slope of the volumetric water content function, u_a is the pore air pressure, α_w is the volumetric coefficient of thermal expansion at constant pressure, T is the temperature, M_v is the mass of water vapor in the grid cell, K_w is the hydraulic conductivity of water, g is the gravitational acceleration and D is the coefficient of diffusion or dispersion.

The different terms in Equation 2.14 are described as follows.

- i is the change in storage caused by water compressibility.
- ii is the change in storage caused by soil structure compressibility.
- iii is the change in storage caused by changes in matric suction.
- iv is the thermal expansion of water.
- v is the water vapor mass transfer.
- vi is the water transfer equation according to Darcy's law.
- vii is the diffusion or dispersion term.

Equation 2.14 are simplified by ignoring water vapor transfer and thermal expansion. The equation is then divided by ρ_w, as the density of water is assumed spatially and temporally constant. This yields the following equation (Equation 2.15), which is solved by GeoStudio: Seep/W.

$$\left(\theta_w \beta_w + \beta\right) \frac{\partial u_w}{\partial t} + m_w \frac{\partial \left(u_a - u_w\right)}{\partial t} = \frac{\partial}{\partial y}\left[\left(\frac{K_w}{\rho_w g}\right)\frac{\partial u_w}{\partial y} + K_w \frac{\partial y}{\partial y}\right] \tag{2.15}$$

2.4.1 Boundary conditions in GeoStudio: Seep/W

GeoStudio: Seep/W allows for a number of boundary conditions to be applied (Ltd GEOSLOPE International, 2020). The software divides boundary conditions into 1^{st} type and 2^{nd} type boundary conditions. 1^{st} type boundary conditions are also known as Dirichlet type boundary conditions (Roos, 2019), which specify the value of an unknown at the boundary (e.g. $H(x = 0) = 0$, in which H is the pressure head). A 2^{nd} type boundary condition is also known as a Neumann boundary condition (Roos, 2019), which specifies the spatial derivative normal to the boundary of an unknown at the boundary (e.g. $\frac{\mathrm{d}H}{\mathrm{d}x}\ (x = 0) = 0$). The standard boundary condition is a no-flow condition, which means that flow out of or into the domain is not possible. Other options that are possible for this research will be discussed in this section.

Similar to the no-flow boundary condition, a given flow can be specified at the boundary. A special option for this boundary condition is the so called "*potential seepage face review*". This option ensures that the maximum

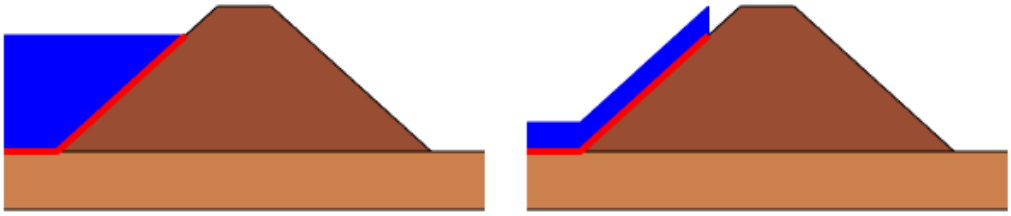

(a) (b)

Figure 2.5: Visualisation of the total head boundary condition (a) and the pressure head boundary condition (b) on a standard dike body. The red line indicates the boundary along which the condition applies and the head applied to the boundary is visualised by a height of water (blue surface).

pore-water pressure at the boundary does not exceed zero, which may occur when the applied water flow is higher than the infiltration capacity of the soil. This option is also used to simulate water discharging out of the domain. When the pore-water pressure would exceed zero, the potential seepage face review option sets the pore-water pressure to zero and determines the flow out of the boundary or limits the flow to the infiltration capacity.

Another boundary condition that can be applied is either the total head or the pressure head. These conditions apply a certain pressure at the boundary. In the case of a total head, the pressure at the boundary is determined based on a given water level. This boundary condition is therefore dependent on the vertical location of the grid cell and is used to specify the water level of a water body pressing on a dike. The pressure head condition applies a given pressure to the boundary, independent of vertical location of the grid. These two options are visualised in Figure 2.5.

A final relevant boundary condition is the Land-Climate interaction. This condition is used to simulate the effect of infiltration by precipitation and takes into account climate conditions like vegetation conditions and solar radiation to determine the flow through the boundary. This option also takes into account the infiltration capacity of the soil to determine the infiltrating portion, the evaporated portion and the runoff portion of the precipitation. This boundary condition is suitable for very detailed simulations on specific locations where a lot of information of local conditions is available.

2.5 D-Stability

D-Stability allows for the computation of a safety factor for a certain scenario based on three possible limit equilibrium models (van der Meij, 2019). Usually, all three limit equilibrium models are used in practice. The lowest resulting safety factor is then normative.

The first of these models is the simplified method of slices by Bishop (1955). The software uses brute force to find the worst case scenario with respect to slip circle location and size.

The second possible model is the Uplift-Van method, described by Van (2001). This method is similar to the simplified method of slices by Bishop, but while Bishop uses one single slip circle, Van uses an active and a passive slip circle, with a horizontal line in between to connect them. The safety factor is determined using the equilibrium of forces in the area between the two slip circles. The location of the slip circles in this model is determined using a so called Adaptive Particle Swarm Optimization (APSO). This algorithm uses a population of points with corresponding safety factors and improves the population for each generation. This method may yield local maxima, but it is computationally much less intensive than brute force.

The third and final model in D-Stability is the Spencer method, described by Spencer (1967). The slip plane in the Spencer method is not bound to be a circle, but can have any shape. For this reason, this method can be used to freely search the slip plane with the least resistance. The safety factor is again determined using the equilibrium of forces along the slip plane. The exact slip plane with the least resistance is found using a Genetic algorithm, which works similar to APSO, but is better suited for problems in which the objective function is of stochastic nature.

D-Stability computes the safety factor under the so-called dry-assumption. This means that the software assumes the soil above the phreatic line to be dry, rather than unsaturated. Section 2.3 describes how this assumption is a conservative approximation, as it neglects the suction in the soil above the phreatic line. This suction causes the effective stress within the soil to increase, leading to a stronger soil. The unsaturated zone can be implemented in D-Stability, by applying some effective cohesion to the soil above the phreatic line, which mimics the cohesion that is actually present in unsaturated soils due to suction forces.

Chapter 3

Method

The research is divided into two parts. The first part covers research questions **Q1** and **Q2** and concerns the effect of infiltration by wave overtopping on the phreatic processes in the dike. Flow patterns and phreatic processes that occur are investigated using ground water flow simulations. Additionally, the effect of different dike material properties, wave conditions, infiltration rates and cover layer characteristics are assessed on a 48 hour wave overtopping event. Again, the phreatic processes that occur are investigated and the rate of saturation of the dike body under these different scenarios is assessed.

This part is performed using the geo-hydrological model GeoStudio: Seep/W, previously described in Section 2.4. A number of simulations are performed in GeoStudio: Seep/W, with varying dike materials, wave conditions, infiltration rates and cover layer characteristics. From the results of these simulations the answer to research question **Q1** can be extracted. Also, the simulations serve as a sensitivity analysis on the named parameters, from which the answer to research question **Q2** is extracted.

The second part covers research question **Q3** and focuses on the effect of the identified phreatic processes on the macro-stability of a dike. Also, a relation is sought for between the rate of saturation of the dike body and the decrease of the macro-stability of a dike.

This part is performed using the macro-stability assessment software D-Stability, developed by Deltares, previously described in Section 3.5. In the second part, the results from GeoStudio: Seep/W simulations are translated to input into D-Stability, from which the change in macro-stability is determined.

Figure 3.1 shows an overview of the model setup for both the first as well as the second part of the research.

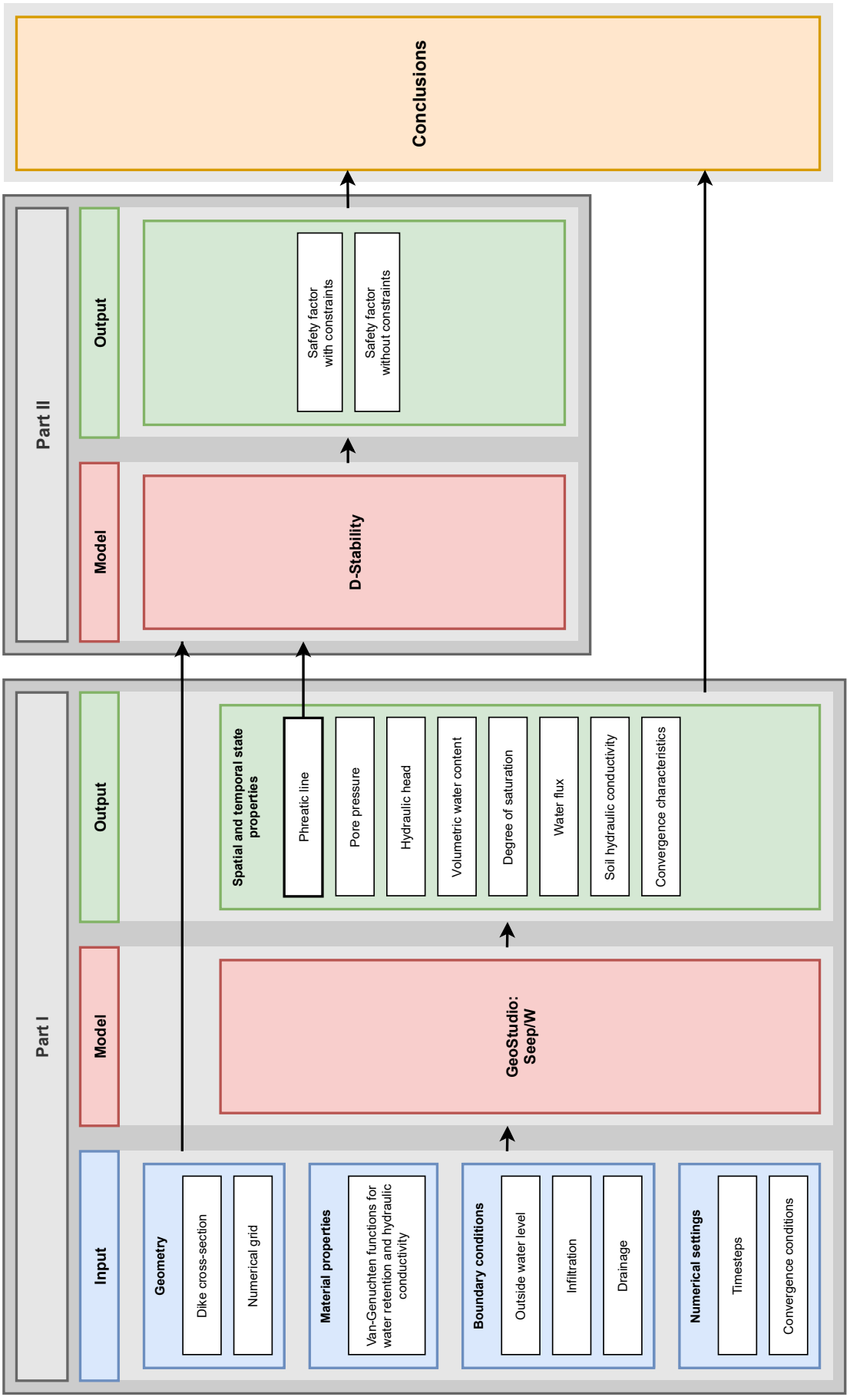

Figure 3.1: Flowchart of the research method with model input in blue, the model itself in red, the model output in green and the conclusions in Yellow.

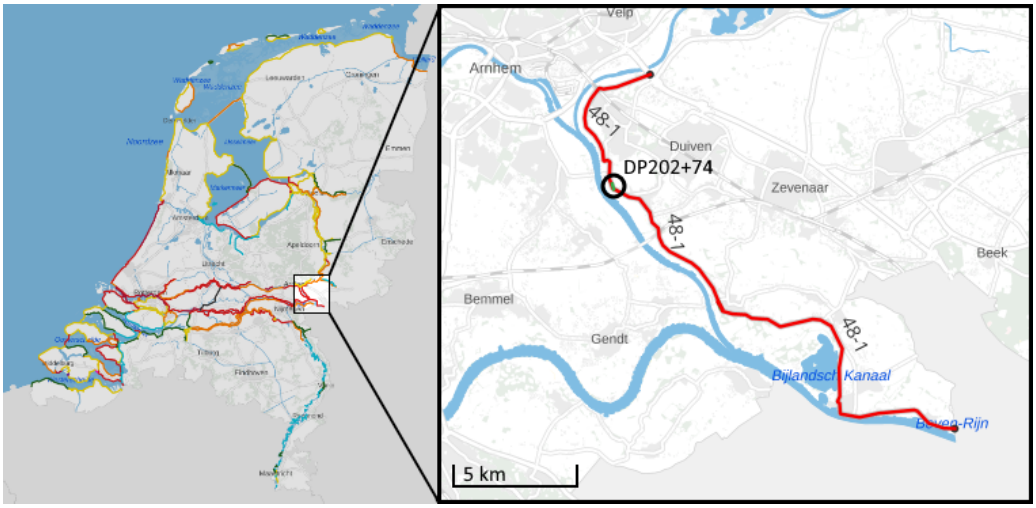

Figure 3.2: An overview of dike trajectory 48-1 with the location of cross section DP202+74. (Adapted from IHW (2017)

3.1 Case description

The case for this study is cross-section DP202+74 of dike trajectory 48-1, which is located along the Nederrijn from the border between Germany and the Netherlands onto the intersection with the A12 highway north of Westervoort, as shown in Figure 3.2. DP202+74 stands for 74 meters distance from dike pole 202. The reason for this particular case is the reinforcement project that is planned for this dike section, planned to start in 2021. The results from the research may be used in the design process for the planned dike reinforcement. The dike trajectory has a safety standard lower threshold of 1/10,000 per year and a corresponding alert value of 1/30,000 per year. In 2019, the trajectory was assessed unsafe in accordance with WBI2017. Later in 2021, the exploratory phase of the dike improvement project will start. The cross-section itself is described in Section 3.2.

3.2 GeoStudio: Seep/W model setup

As previously explained, GeoStudio: Seep/W will be used to answer research question **Q1** and **Q2**. For this, a number of simulations with varying scenarios will be performed. In each of these simulations, a 48 hour wave overtopping event is simulated, during which infiltration by wave overtopping occurs. Part I in Figure 3.1 shows a flowchart of the relevant input and output data for GeoStudio: Seep/W. This section will cover the general input of the model, which holds for all scenarios. Section 3.3 will elaborate on the specific model input for the different scenarios that will be used for the sensitivity analysis.

3.2.1 Geometry

As elaborated on in Section 3.1, the dike cross-section that will be used as a basis for all simulations in GeoStudio: Seep/W is dike cross-section DP202+74 of dike trajectory 48-1. The geometry of this dike cross-section is extracted from a stability assessment report of the dike trajectory (WRIJ, 2019). The domain is divided into a grid of rectangular and triangular grid cells of 1 $[m]$ in the subsoil. The resolution of the grid is increased locally at locations of interest. The core of the dike has grid cells of 0.5 $[m]$ and the top layer of roughly one meter has grid cells of 0.25 $[m]$. A visualisation of the numerical grid is given in Figure A.1 on page 65.

3.2.2 Material properties

A cross-section of the dike and the subsoil is given in Figure A.2 on page 66 in the Appendices. This figure shows that the subsoil, beneath the considered dike, consists of a very coarse sand layer from 7 $[m + NAP]$ downwards. On top of the sand, there is a clay layer of roughly four meters thick. The dike itself consists of an unknown mix of applied materials. The soils in the subsoil as well as the dike itself, each have their own characteristics. For example: the normal and shear strength, the water retention and the hydraulic conductivity. These characteristics describe the behaviour of the soil, as well as the behaviour of water present in the soil. The soil characteristics are obtained by classifying the soil to a certain soil type with corresponding standard soil characteristics.

For the assessment by HKV (2021), the soil in the dike is classified according to WTI-SOS material codes (Deltares, 2015), which is the standard soil classification for dike assessments in the Netherlands. The sand layer, clay layer and dike material are classified as materials P_Rg_zg, H_Rk_k and H_Aa_ht_k respectively, described in Table 3.1.

The WTI-SOS material classifications do not include information on the water retention and the hydraulic conductivity of soils. To obtain these soil characteristics for the given dike cross-section, a translation to a different classification is needed. Since 1987, the Staringreeks was developed and was updated three times (Wösten et al., 1987, 1994, 2001, 2018). The Staringsreeks contains water retention curves and hydraulic conductivity curves for 18 underground and 18 surface layer soils. Using this Staringsreeks and a description of the soils in the dike from the WTI-SOS classification, water retention and hydraulic conductivity curves are assigned to the clay and sand layer in the subsoil. Additional information is supplied by HKV (2021), who state that the saturated hydraulic conductivity of both the foreland and hinterland is 0.01 $[m/d]$. Based on the description in Table 3.1 and the information in HKV (2021), the clay layer is schematised as a B10 material and the sand layer as a O05 material. The water retention curves and the hydraulic conductivity curves for both soils are given in Figure 3.3. As previously described, the dike itself consists of an unknown mix

Material code	Description	Characteristics	Present in
H_Aa_ht_k	Applied material	Sand and clay, strongly varying materials.	Dike body.
H_Rk_k	Higher basin deposition	Clay with silt, possible isolated sand and peat layers of 0.1-0.3 m thick.	Cover layer of foreland and hinterland.
P_Rg_zg	Very coarse to extremely coarse river bed sand	Sand with highly varying grain sizes, often with patches of gravel.	Aquifer.

Table 3.1: WTI-SOS Material codes and corresponding description and characteristics (Deltares, 2015).

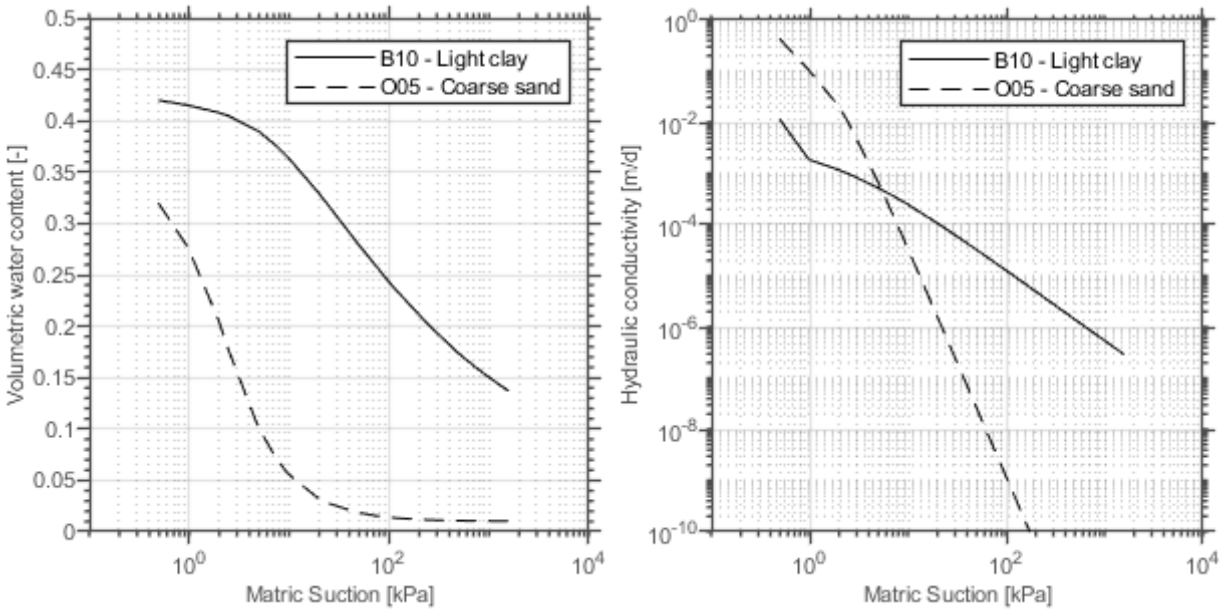

(a) (b)

Figure 3.3: Volumetric water content (a) and hydraulic conductivity (b) of the cover layer (B10) and of the soil in the aquifer (O05) versus matric suction (Wösten et al., 1987).

of applied materials (H_Aa_ht_k). Therefore, in the place of this soil, several types of materials are included in the sensitivity analysis, which is further described in Section 3.3.

3.2.3 (Hydraulic) Boundary conditions

The water level and wave conditions are examples of hydraulic boundary conditions that apply to the dike in case of a flood wave or storm period. These conditions are specific to each cross-section and depend on the scenario (e.g. climate change, river interventions and return periods) considered. Climate change, for example, will have its impact on the hydraulic boundary conditions, which is why it must be taken into account in the determination of the hydraulic boundary conditions. Additionally, hydraulic boundary conditions change for different exceedance probabilities. The hydraulic boundary conditions for all cross-sections in dike trajectory 48-1, corresponding to different exceedance probabilities, are determined and published in a database by HKV (2021). This database is accessed using Hydra-NL.

The peak water level for this cross-section is 15.23 $[m + N.A.P.]$. This value corresponds to an exceedance probability of 1/10.000 per year, which is the maximum allowable probability for this dike trajectory. Additionally, changes in the river system by the Room for the River project and by impoundment are taken into account, the climate scenario considered is 2080W+ and the river discharge is capped at $16,000$ $[m/s^3]$. The spectral wave period and the significant wave height are extracted from Hydra-NL and are 4.08 $[s]$ and 1.19 $[m]$ respectively for the case-study location.

Infiltration by wave overtopping

As described in Section 2.2, wave overtopping leads to infiltration on the inner slope of the dike. Each wave causes the inner slope to remain wet for a certain amount of time, during which infiltration can occur. At some point, the inner slope has dried and infiltration will no longer occur. This leads to a form of periodic infiltration.

This periodic infiltration, as it occurs in case of wave overtopping, is not a usual type of infiltration. To simulate this kind of infiltration, it is schematised based on the percentage of time during which the inner slope is wet (i.e. infiltration time [%]), as is shown in Figure 3.4. In the first subfigure (100%), the inner slope of the dike is always wet. This is illustrated with a constant straight line in Figure 3.4. For the other cases, the time during which the inner slope remains wet after a wave is assumed constant. According to literature (Dutch Ministry of Infrastructure and the Environment, 2012; Spanjersberg, 2016; van Bergeijk et al., 2020), this value

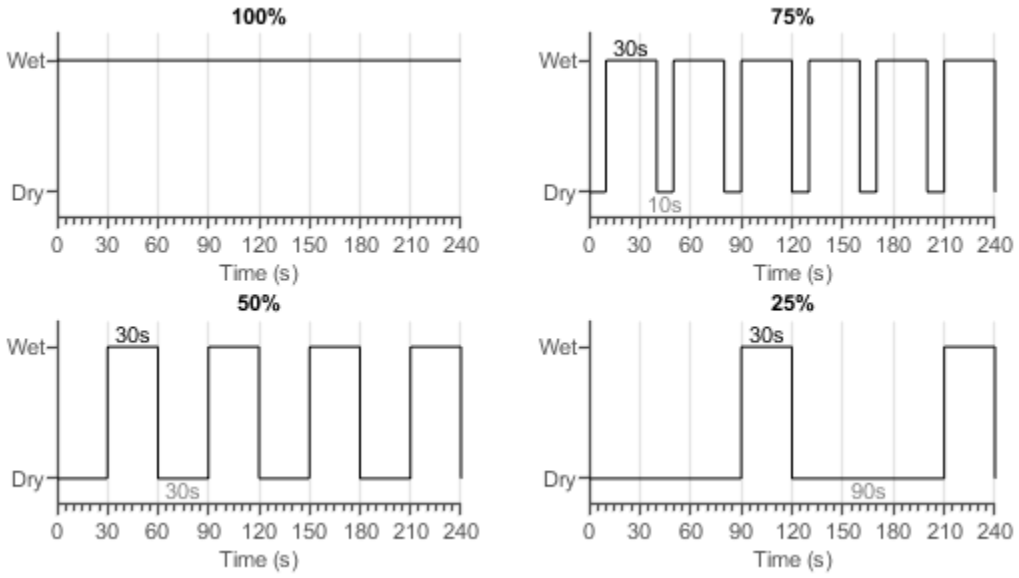

Figure 3.4: Schematisation of infiltration intervals 100%, 75%, 50% and 25%

ranges from 20 to 30 seconds. In the example in Figure 3.4, this value is 30 seconds. Depending on the specified infiltration time [%], the time during which the inner slope is dry increases. In the case of no wave overtopping, the infiltration time will be 0% and the time during which the inner slope is dry will be infinite.

Figure A.2 on page 66 shows the dike cross section and the boundary conditions applied.

3.2.4 Numerical settings

The model also requires the implementation of numerical settings. One important numerical setting is the time steps used throughout the simulations. Also, as GeoStudio: Seep/W uses an iterative procedure, which converges to a value of the flow of water through the soil, convergence criteria should be set.

The model simulates a duration of 48 hours of wave overtopping, divided into a number of timesteps. As infiltration occurs in intervals, the timestep cannot exceed T_{wet} or T_{dry}. Therefore, the timestep chosen for this model is 10 seconds. For model simulations with continuous infiltration ($T_{wet\%} = 100\%$), the timestep is not limited by T_{wet} or T_{dry}. However, to be able to correctly simulate the start of the run (transition from dry to (un)saturated soil), the timestep should be relatively small. GeoStudio allows for the option to increase the timestep exponentially throughout the simulation. This yields an initial timestep of 10 seconds and a final timestep of 305 seconds.

The convergence criteria specified in the model are altered from the default values of the model. In simulations with infiltration times lower than 100%, wetting and drying of the cover layer occurs constantly. This process of wetting and drying is a complex process, causing the software to need many iterations to satisfy the default convergence criteria. To reduce simulation time, the maximum amount of iterations used per timestep is reduced from 500 to 50.

3.3 Sensitivity Analysis

To identify the important parameters and their influence on the phreatic processes in the dike, a sensitivity analysis is performed. The general model setup is given in Section 3.2. This section describes the parameters that are varied in the sensitivity analysis and how these parameters are schematised in the model.

There are many different parameters that are relevant in the assessment of water infiltrating a dike. The parameters that will be taken into account for this sensitivity analysis are given below.

1. Residual volumetric water content of the dike core soil (Θ_r) in $[m^3/m^3]$.
2. Saturated volumetric water content of the dike core soil (Θ_s) in $[m^3/m^3]$.
3. Saturated hydraulic conductivity of the dike core soil (K_s) in $[m/d]$.
4. Fitting parameter α of the dike core soil $[-]$.
5. Fitting parameter n of the dike core soil $[-]$.
6. The water flux as the infiltration boundary condition in $[m^3/d/m^2]$.
7. The infiltration time ($T_{wet,\%}$) in $[\%]$
8. The thickness of a cover layer (D_{cl}) in $[m]$.
9. The saturated hydraulic conductivity of a cover layer ($K_{s,cl}$) in $[m/d]$.

The first five parameters listed above follow from the description of the water retention and hydraulic conductivity curves by van Genuchten (1980), as previously explained in Section 2.3.

The water flux is a strictly numerical parameter. As described in Section 2.4, one possibility for schematising infiltration in GeoStudio: Seep/W is a water flux boundary condition. This boundary condition simulates an amount of water $[m^3/d/m^2]$ infiltrating the domain. However, the possible rate of infiltration at a given location depends on the condition of the soil at that boundary (e.g. saturation and hydraulic conductivity). For that reason, the specified infiltration is not directly equal to the simulated infiltration. As it is currently unknown how fast water infiltrates the cover layer of a dike during wave overtopping or precipitation, the specified water flux should be calibrated using measurement data. Since there is currently no measurement data to calibrate with, the parameter will be included in the sensitivity analysis to determine the importance of the calibration.

The infiltration time is the percentage of time during which the inner slope of the dike is wet (i.e. inundated). This value depends on local conditions (e.g. crest height, outside water level, wave conditions, etc) and is therefore highly variable. To determine the sensitivity of the results to the infiltration time, this parameter is included in the sensitivity analysis.

Finally, as most dikes in the Netherlands have a cover layer, the properties of a cover layer are tested as well. The thickness and the saturated hydraulic conductivity are two main properties of a cover layer, which is why they are both included in this analysis.

Additionally, three separate sets of simulations will be performed to investigate additional matters. First of all, a set of standard material types, set up by Wösten et al. (1987) is simulated to validate that the found patterns are valid in any parameter value combination. This is further elaborated on in Section 3.3.5. Secondly, the effect of a hole in the cover layer will be assessed. Such a hole may be the result of severe erosion due to wave overtopping. This simulation is described in Section 3.3.6. The third and final additional simulation will be to determine the effect of a transient flood wave. For all other simulations, a steady state of the peak of the flood wave is considered as the initial condition, which may be a conservative method. This simulation will determine the effect of this initial condition in comparison to a more realistic scenario.

Some of the above mentioned parameters may have a combined effect, meaning that the sensitivity of the result to one parameter, may depend on the value of a second parameter. Therefore, simulating all possible combinations of different values for each parameter is the preferred method for this sensitivity analysis. However, due to the computation time in relation to the lead time of this research, this is not feasible. Instead, some parameters are ranged in separate sets of simulations based on the assumption that they do not have a combined effect. For example, the influence of the water flux on the phreatic conditions is assumed independent of the value of the infiltration time. Therefore, it is not necessary to simulate the complete range of values for the water flux, for each value of the infiltration time. Instead, the two parameters are ranged separately. The

saturated hydraulic conductivity of the dike core soil is added as a reference to be able to compare the results from each set of simulations.

This yields the following sets of simulations, in which the listed parameters are ranged.

Set 1: (256 simulations, see Table B.1)

- Saturated volumetric water content of the dike core soil (Θ_s) in $[m^3/m^3]$.
- Saturated hydraulic conductivity of the dike core soil (K_s) in $[m/d]$.
- Fitting parameter α of the dike core soil $[-]$.
- Fitting parameter n of the dike core soil $[-]$.

Set 2: (16 simulations, see Table B.2)

- Saturated hydraulic conductivity of the dike core soil (K_s) in $[m/d]$.
- The applied water flux as the infiltration boundary condition in $[m^3/d/m^2]$.

Set 3: (16 simulations, see Table B.3)

- Saturated hydraulic conductivity of the dike core soil (K_s) in $[m/d]$.
- The applied infiltration time ($T_{wet,\%}$) in $[\%]$

Set 4: (20 simulations, see Table B.4)

- The thickness of a cover layer (D_{cl}) in $[m]$.
- The saturated hydraulic conductivity of a cover layer ($K_{s,cl}$) in $[m/d]$.

The next step is to define the values to consider for each parameter. More parameter values to consider means a more detailed result, but also an increase in the amount of simulations to perform and thus also computation time. Therefore, as a compromise, four or five values are chosen for each parameter. The process of choosing parameter values for each set is explained below. The resulting parameter values considered per set of simulations is given in Table 3.2.

3.3.1 Set 1: Material hydraulic conductivity and water retention parameters

As explained in Section 2.3, van Genuchten (1980) described the water retention curves and hydraulic conductivity of a soil based on five independent variables (θ_r, θ_s, α, n and K_s). The ranges for these parameters are determined based on classifications by Wösten et al. (1987). They fitted the water retention and hydraulic conductivity curves of 999 Dutch soil samples to a slightly different form of Equations 2.11 and 2.12. While their equations are slightly different, the residual water content, the saturated water content and the saturated hydraulic conductivity are independent on the equation used. The values for α and n in the dataset by Wösten et al. (1987) will be slightly different to the values obtained when fitting according to Equation 2.11, but the dataset can still give an estimation of possible values. Relevant histograms of the dataset by Wösten et al. (1987) are given in Figure B.1 on page 68. Considered parameter ranges are based on these histograms.

As nearly 80% of all soil samples has a residual water content (θ_r) of 0.01, this variable is fixed on 0.01 and therefore excluded from the sensitivity analysis, reducing the amount of simulations needed. The saturated water content (θ_s) will range from 0.3 to 0.9, covering 95% of instances in the dataset by Wösten et al. (1987). The saturated hydraulic conductivity (K_s) will range from 0.005 to 0.0035, covering 87% of all instances. Fitting parameter α will range from 0.001 to 1, covering 75% of instances and fitting parameter n will range from 1.1 to 1.7, covering 67% of all instances. All values considered for these parameters are given in Table 3.2.

In this set of simulations, default values for the water flux and infiltration time are chosen at 1 $[m^3/d/m^2]$ and 100% respectively. 1 $[m^3/d/m^2]$ water flux is a relatively high value, which allows for a good distinction between the effect of other parameters. 100% infiltration time is chosen to reduce simulation time. In a simulation with 100% infiltration time, wetting and drying does not occur as often as for simulations with lower infiltration times. Since the wetting and drying process causes convergence issues due to the complexity of the process, simulation times are reduced quite substantially by only using 100% infiltration time.

This yields a total of 256 simulations in simulation set 1. All possible combinations, which are essentially material types, are listed in Table B.1 on page 69. As seen in this table, each combination is given a specific code (e.g. A-1-1). As the combinations represent individual material properties, some 'material types' may have both clay-like as well as sand-like properties. For this reason, the material codes cannot be translated to actual materials.

Set	Parameter	Unit	Values				
1	Saturated water content (θ_s)	$[m^3/m^3]$	0.3	0.5	0.7	0.9	
	Saturated hydraulic conductivity (K_s)	$[m/d]$	0.001	0.01	0.1	1	
	α	$[-]$	0.005	0.015	0.025	0.035	
	n	$[-]$	1.1	1.3	1.5	1.7	
2	Saturated hydraulic conductivity (K_s)	$[m/d]$	0.001	0.01	0.1	1	
	Water flux	$[m^3/d/m^2]$	0.001	0.01	0.1	1	
3	Saturated hydraulic conductivity (K_s)	$[m/d]$	0.001	0.01	0.1	1	
	Infiltration time ($T_{wet,\%}$)	$[\%]$	25	50	75	100	
4	Cover layer saturated hydraulic conductivity ($K_{s,cl}$)	$[m/d]$	0.001	0.01	0.1	1	
	Cover layer thickness (D_{cl})	$[m]$	0.6	0.8	1.0	1.2	1.4

Table 3.2: Parameters with corresponding values considered in the sensitivity analysis.

3.3.2 Set 2: Water flux

In simulation set 2, the saturated hydraulic conductivity of the dike core soil will be ranged using the same values as in set 1 (i.e. 0.001, 0.01, 0.1 & 1). This parameter is ranged in this set of simulations, so that the influence of the water flux can be compared to the influence of K_s, and therefore indirectly to the material properties covered in set 1. The water flux applied as a boundary condition will be ranged using the same values as the saturated hydraulic conductivity.

Default values for Θ_r, Θ_s, α, n and the infiltration time are chosen at 0.01, 0.5, 0.025, 1.5 and 100% respectively. For Θ_r, Θ_s, α and n, these are average values of the previously described ranges. The infiltration time is set at 100% for the same reason as for set 1.

This yields a total of 16 simulations in simulation set 2. All possible combinations are listed in Table B.2 on page 71.

3.3.3 Set 3: Infiltration time

Again, the saturated hydraulic conductivity of the dike core will be ranged using the same values as in set 1. The infiltration time theoretically ranges from 0 to 100%. However, the results from a 0% simulation are equal to the initial condition (steady-state analysis) and don't need an individual set of simulations. Therefore, the simulations are executed with infiltration times ranging from 25 to 100%.

Similar to set 2, default values for Θ_r, Θ_s, α, n and the water flux are chosen at 0.01, 0.5, 0.025, 1.5 and 1 respectively. The reason for this is that they are all average values of the previously described ranges.

This yields a total of 16 simulations in simulation set 3. All possible combinations are listed in Table B.3 on page 72.

3.3.4 Set 4: Cover layer

Finally, the thickness and the saturated hydraulic conductivity of the cover layer are ranged in set 4. As most cover layers are roughly 1 $[m]$ thick, the cover layer thickness is ranged from 0.6 to 1.4 $[m]$. The saturated hydraulic conductivity of the cover layer is ranged using the same values as in sets 1, 2 and 3. The core material of the dike in this set of simulations is material B-1-4 (see Table B.1). This material is theoretically highly permeable and can therefore clearly show the effect of a cover layer.

Default values for Θ_r, Θ_s, α, n of the cover layer material are the same as for the dike core material in set 1, 2 and 3. The default flux and infiltration time in this set of simulations are 1 $[m^3/d/m^2]$ and 100% respectively for the same reasons as previously given.

This yields a total of 20 simulations in simulation set 4. All possible combinations are listed in Table B.4 on page 72.

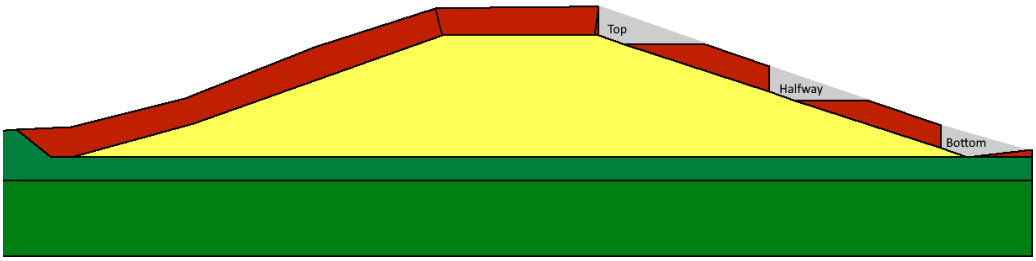

Figure 3.5: Schematisation of three possible holes in a cover layer of 1 m, at the top, halfway and at the bottom of the inner slope.

3.3.5 Set of standard materials

As described in Section 3.3.1, Wösten et al. (1987) set up a so called Staringreeks, given in Tables 3.3 and 3.4. This set contains 18 above-ground and 18 under-ground soil types, each with corresponding parameter values for Θ_r, Θ_s, K_s, α and n. The distinction between above- and underground soil types lies in the compactness due to the depth of the origin of the soil. Barely compacted soil can be compared to above-ground soils and highly compacted soil can be compared to under-ground soils. The soil types by Wösten et al. (1987) supply new combinations of parameter values with which to validate the results from simulation set 1. The results of the validation are given in Section 4.2.1.

3.3.6 Effect of a hole in the cover layer

Erosion of the inner slope could lead to a hole in the cover layer of a dike. Such a hole will locally affect the infiltration capacity of the surface of the dike. Whether a hole in the cover layer has a significant effect on the phreatic conditions in the dike will be investigated using a separate set of simulations.

For these simulations, a cover layer of 1 m thickness will be considered. The materials used for the cover layer are the same as in simulation set 4. van Bergeijk et al. (2020) state that erosion of the inner slope occurs predominantly at geometrical transitions on the dike and halfway of the inner slope, as pressures are maximal at these locations. Examples of geometrical transitions are the transition from crest to inner slope and the change of slope at the inner toe of the dike. Based on this, three locations for the hole in the cover layer will be considered; at the top, halfway and at the bottom of the inner slope. For the holes, a surface length of 1 m of the core material will be exposed, with a vertical and horizontal cut in the cover layer, as shown in Figure 3.5.

Material code	Description	Θ_r	Θ_s	K_s	α	n
Sand		$[m^3/m^3]$	$[m^3/m^3]$	$[m/d]$	$[-]$	$[-]$
B01	Lower peat, very fine to fairly fine sand	0.02	0.428	0.312	0.022	1.734
B02	Fairly peaty, very fine to fairly fine sand	0.02	0.434	0.832	0.022	1.349
B03	Very peaty, very fine to fairly fine sand	0.02	0.443	0.191	0.015	1.505
B04	Heavily peaty, very fine to fairly fine sand	0.02	0.462	0.349	0.015	1.397
B05	Coarse sand	0.01	0.381	0.637	0.043	1.808
B06	Clayey loam	0.01	0.385	1.041	0.021	1.242
Sabulous clay						
B07	Very light sabulous clay	0.00	0.401	0.146	0.018	1.248
B08	Fairly light sabulous clay	0.01	0.433	0.030	0.010	1.278
B09	Heavy sabulous clay	0	0.430	0.017	0.007	1.267
Clay						
B10	Light clay	0.01	0.448	0.038	0.013	1.135
B11	Fairly heavy clay	0.01	0.591	0.063	0.022	1.107
B12	Very heavy clay	0.01	0.530	0.022	0.017	1.091
Loam						
B13	Sandy loam	0.01	0.416	0.298	0.008	1.437
B14	Silty loam	0.01	0.417	0.009	0.005	1.302
"Moerig"						
B15	Peaty sand	0.01	0.528	0.875	0.024	1.282
B16	Sandy peat and peat	0.01	0.786	0.124	0.021	1.279
B17	Peaty clay	0	0.719	0.045	0.019	1.137
B18	Clayey peat	0	0.765	0.131	0.020	1.151

Table 3.3: Classifications of above surface (Bovengronds) soil types with corresponding descriptions as classified by Wösten et al. (1987).

Material code	Description	Θ_r	Θ_s	K_s	α	n
Sand		$[m^3/m^3]$	$[m^3/m^3]$	$[m/d]$	$[-]$	$[-]$
O01	Lower peat, very fine to fairly fine sand	0.01	0.366	0.223	0.016	2.163
O02	Fairly peaty, very fine to fairly fine sand	0.02	0.387	0.228	0.016	1.524
O03	Very peaty, very fine to fairly fine sand	0.01	0.340	0.124	0.017	1.703
O04	Heavily peaty, very fine to fairly fine sand	0.01	0.364	0.258	0.014	1.488
O05	Coarse sand	0.01	0.337	0.174	0.030	2.888
O06	Clayey loam	0.01	0.333	0.328	0.016	1.289
O07	"Beekleem"	0.01	0.513	0.376	0.012	1.153
Sabulous clay						
O08	Very light sabulous clay	0	0.454	0.086	0.011	1.346
O09	Fairly light sabulous clay	0	0.458	0.038	0.010	1.376
O10	Heavy sabulous clay	0.01	0.472	0.023	0.010	1.246
Clay						
O11	Light clay	0	0.444	0.021	0.014	1.126
O12	Fairly heavy clay	0.01	0.561	0.011	0.009	1.158
O13	Very heavy clay	0.01	0.573	0.097	0.028	1.080
Loam						
O14	Sandy loam	0.01	0.394	0.025	0.003	1.617
O15	Silty loam	0.01	0.410	0.028	0.008	1.287
Peat						
O16	Oligotrophic peat	0	0.889	0.015	0.010	1.364
O17	Mesotrophic and Eutrophic peat	0.01	0.849	0.034	0.012	1.272
O18	"Moerige tussenlaag"	0.01	0.580	0.360	0.013	1.316

Table 3.4: Classifications of below surface (Ondergronds) soil types with corresponding descriptions as classified by Wösten et al. (1987).

3.3.7 Effect of time dependent flood wave

As previously mentioned, the initial condition for each of the simulations is a steady state of the peak water level with corresponding phreatic line. This initial condition is a conservative assumption, as this water level is maintained for a relatively short period of time. Also, wave overtopping may already occur before the peak water level is reached. The difference in initial condition may have an influence on the phreatic processes in the dike. To determine whether or not this is the case a simulation of a complete flood wave with corresponding wave overtopping conditions is performed.

The flood wave propagation and the corresponding time dependent water level at the case location is determined using the 'Waterstandsverlopen Tool' by Helpdesk Water (Botterhuis et al., 2017). The flood wave has a duration of almost 24 days, during which the water level ranges between 11.23 $m+NAP$ and 15.23 $m+NAP$, as shown in Figure 3.6a. The wave characteristics corresponding to the flood wave are determined using Hydra-NL for a number of return periods. Each value of the water level is then assigned wave characteristics based on their shared return periods. The resulting wave height and period are given in Figure 3.6b and 3.6c respectively. From this information, the infiltration time is determined for each timestep using the equations given in Section 2.2, given in Figure 3.6d.

For this method, the assumption is made that water level and wave characteristics are correlated. However, on rivers waves are mostly generated by wind conditions, which are not correlated to the water level (Ministerie van Infrastructuur en Milieu, 2017). This assumption therefore leads to a conservative estimation of the wave conditions and especially of the duration of wave overtopping. According to Ministerie van Infrastructuur en Milieu (2021), the representative duration of wave overtopping for dikes along a river is roughly 5 hours. This value is based on the assessment of erosion of the crest and inner slope of the dike and may thus not be applicable for the assessment of infiltration by wave overtopping. Nevertheless, 5 hours is only a fraction of the 11 days resulting from the method described above and visualised in Figure 3.6d. As there is currently no better way to estimate the wave conditions during the passing of a flood wave, the method described above is chosen over the 5 hours estimated by Ministerie van Infrastructuur en Milieu (2021).

Furthermore, the material of the dike in this simulation is material K-2-2 (See Table B.1), as it is a relatively average material type, and the flux is set at 1 $[m^3/d/m^2]$.

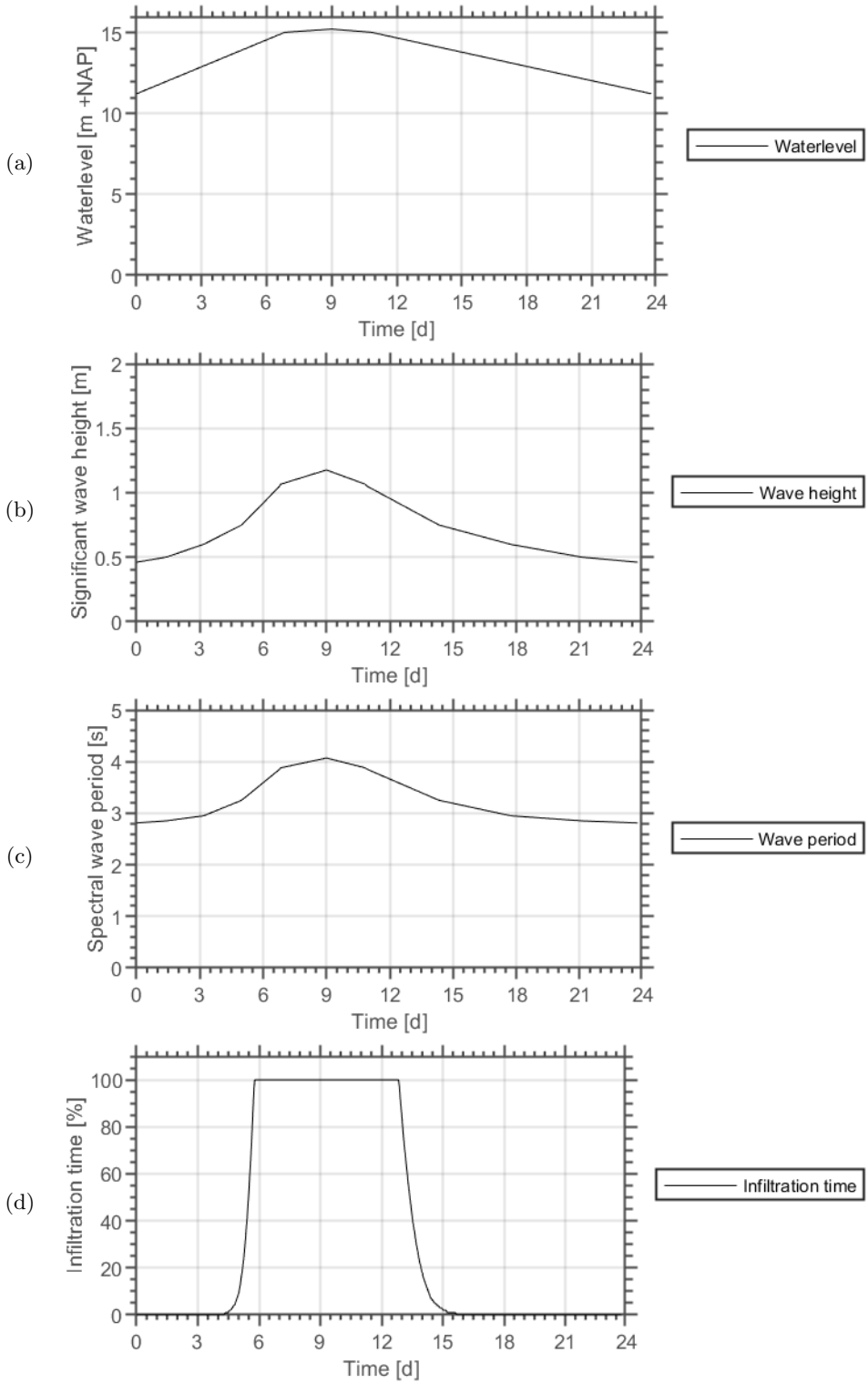

Figure 3.6: Hydraulic boundary conditions at DP202+74 as a result of a passing flood wave. Water level (a) extracted from 'Waterstandsverlopen Tool' by Helpdesk Water (Botterhuis et al., 2017), wave height (b) and wave period (c) determined using Hydra-NL for a number of timesteps (dots) and then linearly interpolated. Infiltration time (d) determined using equations given in Section 2.2.

3.4 Extracting results

As shown in the flowchart in Figure 3.1, the GeoStudio: Seep/W simulations result in a value for many water related parameters for each grid cell. Examples of these parameters are water content, degree of saturation, hydraulic head, water flux and water conductivity. These results are also transient, meaning that they change over time. This yields a set of spatially and temporally varying data. These data are summarised into one representative variable for each simulation, as described below.

As is explained in Section 2.3 and shown in Figure 3.7, the pore water pressures below the phreatic line are positive while the pressures above the phreatic line are negative. The area above the phreatic line is named the unsaturated zone, which' size is a good representation of the state of pore water pressures in the dike cross-section. The area of the unsaturated zone (unsaturated area) is therefore one single value that allows for the approximation of the pore water pressures and thus the height of the phreatic line in the dike.

The results are exported to be processed using code. The degree of saturation at each grid node within the dike core of each timestep of each scenario is used as representative data. As the grid cells are not all of equal size, this yields an inconsistent scatter of data, as shown in Figure 3.8a. To be able to make the data consistent, the spatial scatter is linearly interpolated to a 0.1 by 0.1 m constant grid, which is visualised in Figure 3.8b. Finally, all points with a degree of saturation that is lower than unity are classified as 'unsaturated' and all points with a degree of saturation that is unity are classified as 'saturated'. This yields Figure 3.8c, from which the area of the unsaturated zone in m^2 can be determined. In the case of scenario A-2-1, t=0h, this is 34 m^2.

As the area of the unsaturated zone is determined for each timestep, this value can then be plotted against time, as shown in Figure 3.9. From this, the rate of change of the unsaturated area (which is the time derivative of the area of the unsaturated area over time) is determined, given in Figure 3.10. For some scenarios the unsaturated area reaches an equilibrium before the full simulation has ended. Therefore, a simple average of dA/dt is not sufficient to find a representative average rate of change of the unsaturated area. To achieve this, the rate of change is determined only over the time until an equilibrium is reached. The timestep at which an equilibrium is reach is defined as the timestep where the unsaturated area is equal to or smaller than the unsaturated area at the end of the simulation. The unsaturated area over time is then simplified using the average rate of change, yielding a linear line from the initial unsaturated area to a fully saturated dike body. The resulting line for each scenario is visually checked against the actual unsaturated area over time to ensure a representative value.

The average rate of change of the unsaturated area per scenario can then be plotted against the input parameters for that scenario using boxplots. In the boxplots the median, the 25^{th} and 75^{th} percentile and the

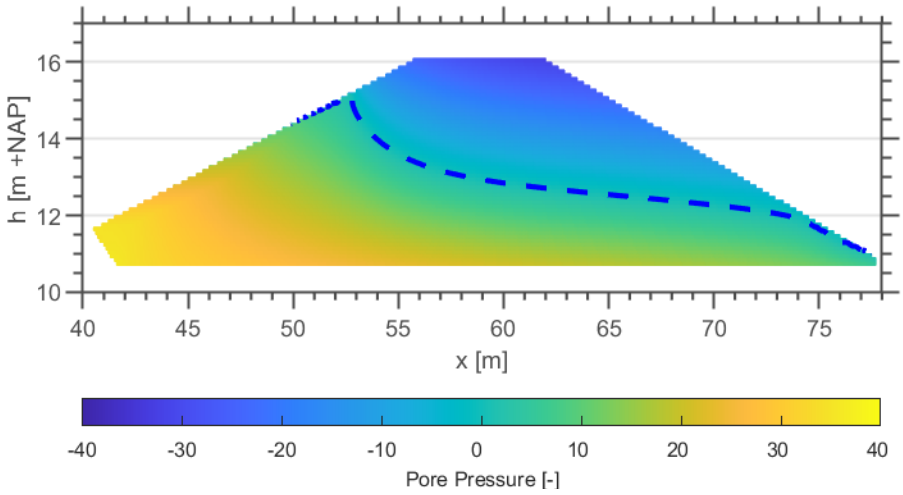

Figure 3.7: Pore water pressure in the dike cross section at t=0h in a dike with core material B-1-1.

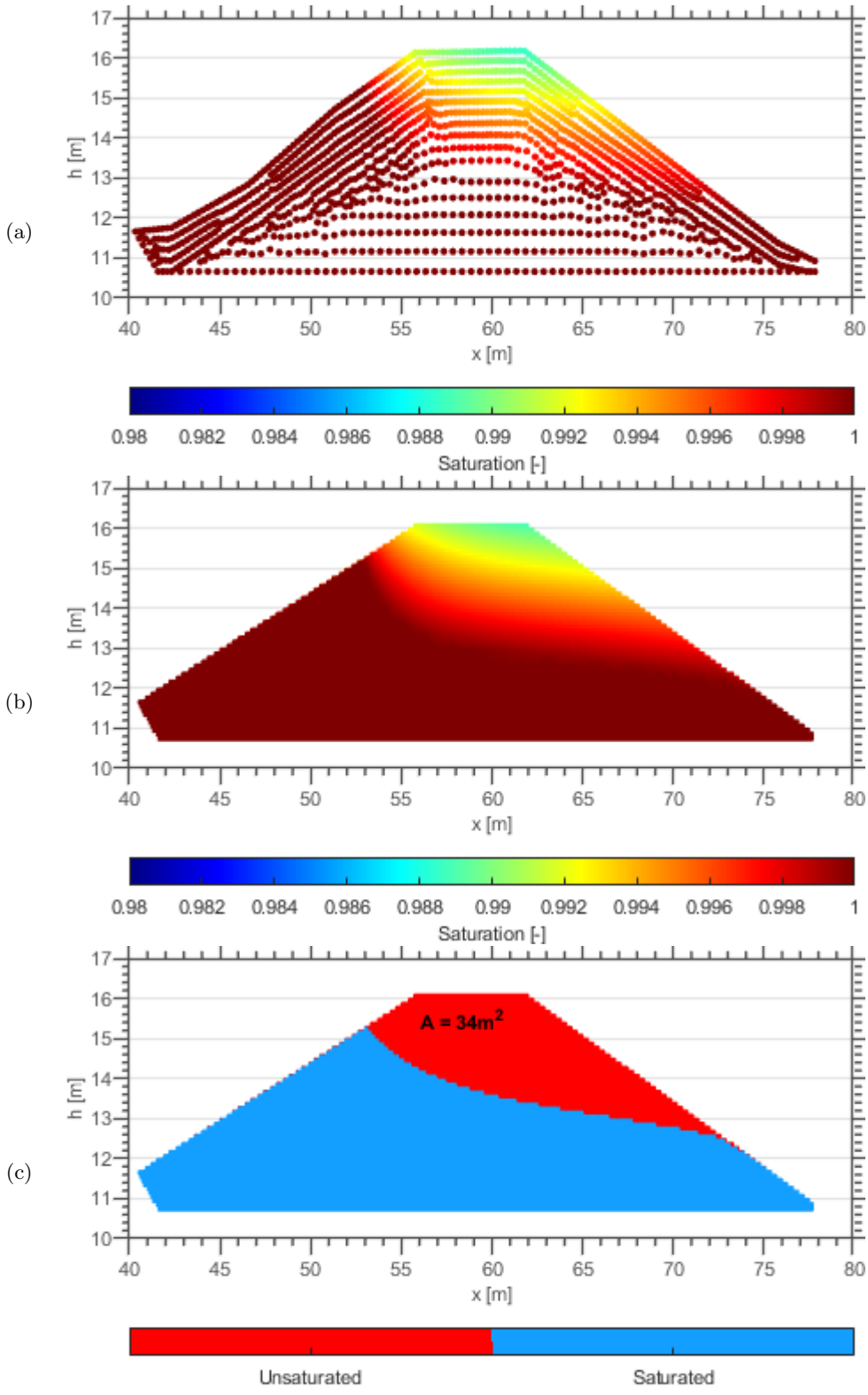

Figure 3.8: Visualisation of the data processing. Scenario with material A-1-2, t=0h taken as example. Raw data exported from GeoStudio (a), is interpolated to a 0.1 by 0.1 m grid (b) from which the area of the unsaturated zone is determined (c).

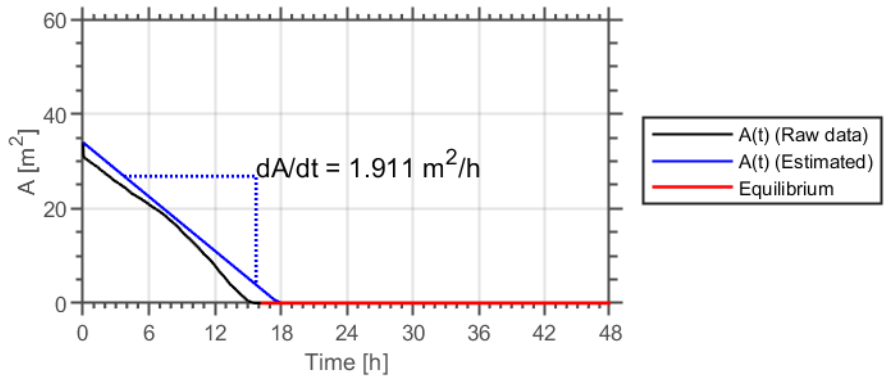

Figure 3.9: Actual and estimated unsaturated area over time of scenario A-1-2.

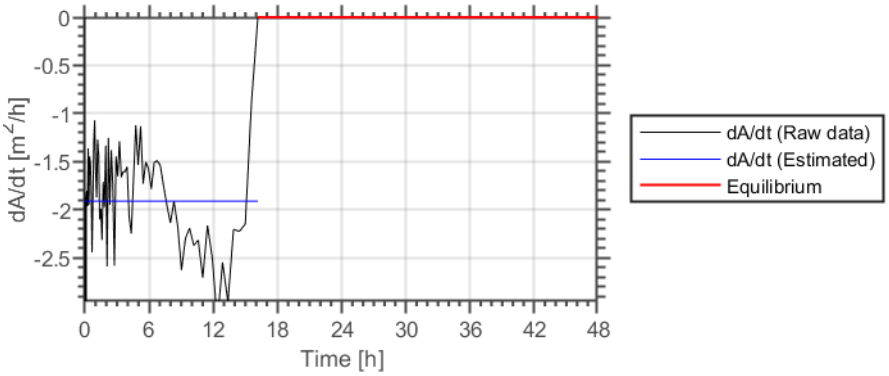

Figure 3.10: Actual and estimated rate of change in unsaturated area over time of scenario A-1-2.

full extent of all considered data are given. This allows for the visualisation of the influence of all different parameters on the average rate of change.

3.5 Macro-Stability

To connect the phreatic conditions to the macro-stability of a dike, a number of macro-stability assessments are performed in D-Stability. For these assessments, the phreatic conditions resulting from the GeoStudio: Seep/W simulations are used as input. Dikes with material types A-1-3, F-2-3. K-3-3 and P-4-3 (See Table B.1) are used for the macro-stability analyses. These material types are used as they show a wide range of possible soil parameters. This section describes how the assessments in D-Stability are set up and how the data from GeoStudio: Seep/W are translated to input in D-Stability.

The dike section considered for the macro-stability analysis is the same as for the GeoStudio model and thus the geometry and material properties are extracted from a stability assessment report of the dike trajectory (WRIJ, 2019). The geometry of the model with corresponding materials are shown in Figure C.1 one page 74. The material properties are given in Table 3.5. Additionally, a pre-overburden-pressure (POP) is applied on the two H_Rk_k regions on the outer side of the dike, and on the lower H_Rk_k region on the inner side of the dike. The method for the macro-stability analysis is partially based on results from the GeoStudio:Seep/W analyses. From these analyses, there are several things that theoretically have an influence on the macro-stability of a dike.

Infiltration by wave overtopping will increase the height of the phreatic line. This means that the pore water pressures in the dike body increase as well. According to soil mechanics theory (discussed in Chapter 2), this causes the effective stresses in the soil to decrease and therefore the shear strength of the soil decreases as well. A decrease in shear strength of the soil is a direct decrease in macro-stability of the dike.

Not only will the pore water pressures at the bottom of the cross section of the dike increase, there will also be higher pore water pressures at the surface layer of the dike. While this water has no effect on the pore water pressures in the rest of the dike, it does decrease the effective stress in the soil locally. This then reduces the shear strength of the soil and thus decreases the macro-stability of the dike.

Finally, the water that infiltrates the surface layer of the dike increases the weight of the dike itself. According to Bishop (1955), the safety factor for macro-stability of a dike is a ratio between the shear strength along the slip circle and the weight of the sliding mass. As water increases the weight of the sliding mass, the macro-stability will decrease.

D-Stability allows for the manual implementation of reference lines with corresponding head lines. A reference line indicates the location along which the water pressure applies, while a head line defines the value of the pressure applied along that line. Several reference lines and head lines can be implemented in the software and pore water pressures are then inter- and extrapolated to determine the pore water pressures throughout the dike body. To implement the three phenomenons described above, reference and head lines are used in a specific manner, based on the data from the GeoStudio: Seep/W.

From the simulations in GeoStudio: Seep/W, only the phreatic line is extracted. This phreatic line may be a regular line (i.e. from water level to dike toe), or a circular shape due to the infiltration by wave overtopping.

In case of a regular phreatic line, a reference line is applied on top of the impermeable layer below the dike. The head line corresponding to this reference line is the phreatic line. Additionally, an uplift pressure is applied on the bottom of the impermeable layer. The corresponding head line is then the uplift head line, decreasing the pore water pressure over distance. This situation is visualised in Figure 3.11.

In case of an unsaturated zone, the situation is similar, but the phreatic line has a different trajectory, a new head line is added and two reference lines are added. This situation is visualised in Figure 3.12. The new trajectory of the phreatic line will be explained from left to right. The line first follows the water level and then the surface of the dike until it reaches the x-coordinate where the unsaturated zone starts. It then drops to the lower edge of the unsaturated zone, which it follows towards the right side of the unsaturated zone. From there it jumps back to the surface of the dike, which it follows towards the inner toe of the dike, from where it follows its normal trajectory. A second head line is added along the water level and the surface of the dike to indicate the water pressures at the surface layer of the dike.

Two reference lines are then added. One which follows the exact line of the new phreatic line and one that follows a similar path, but follows the top of the unsaturated zone. The upper reference line is then coupled with the surface layer head line. Below the upper reference line (i.e. in the unsaturated zone), the pore water pressure is set to 0. The lower reference line, which follows the new phreatic line, is coupled to the phreatic line, allowing the pore water pressure above this reference line to be 0 and the pore water pressure below this

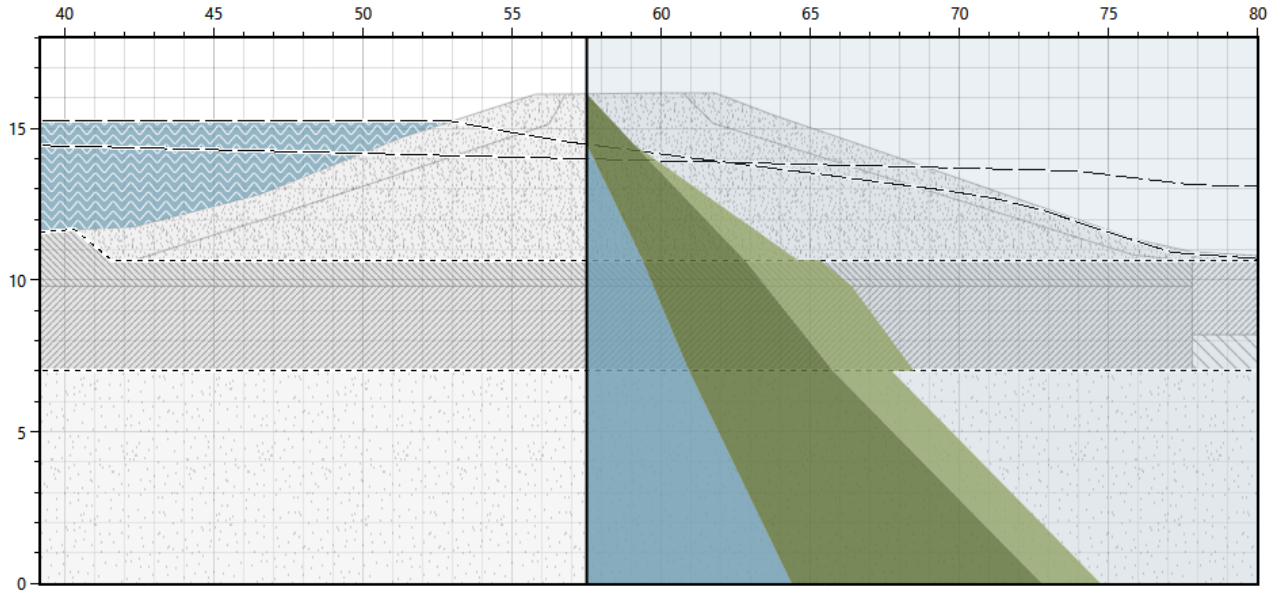

Figure 3.11: Schematisation of the phreatic line using D-Stability software. Phreatic line for t=0h for a dike with material A-1-3 (See Table B.1). The blue surface indicates the water pressures in the soil, the dark green surface indicates the effective pressure and the light green surface indicates the pre-overburden-pressure.

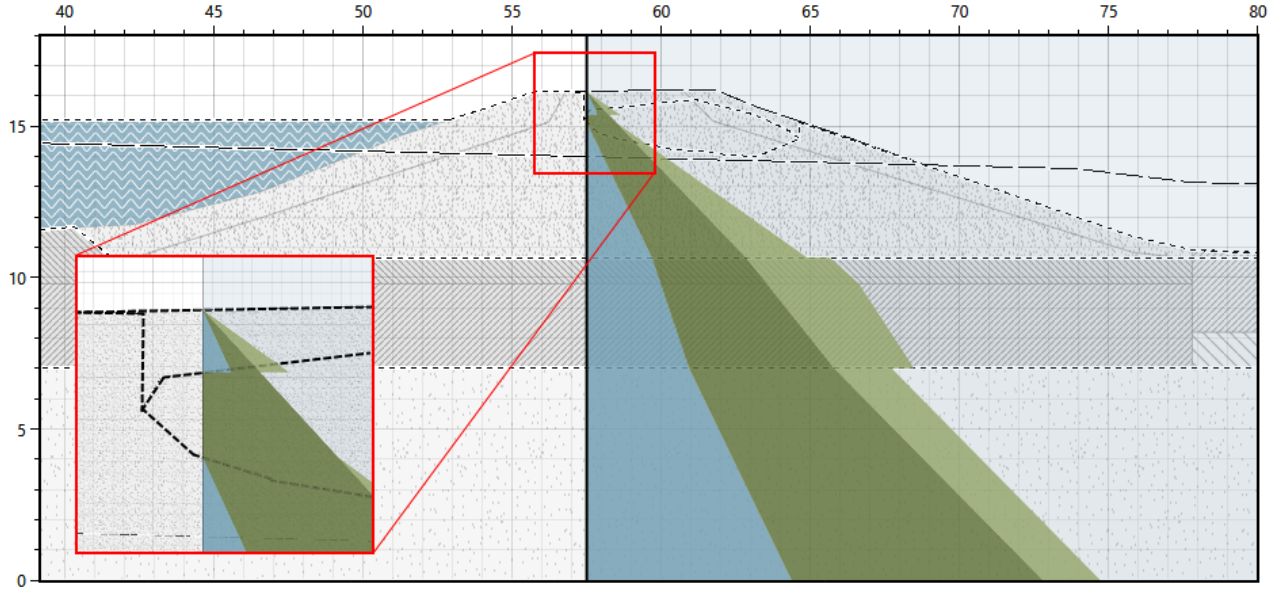

Figure 3.12: Schematisation of the unsaturated zone with a saturated cover layer using D-Stability software. Phreatic line for t=35min for a dike with material A-1-3 (See Table B.1). The blue surface indicates the water pressures in the soil, the dark green surface indicates the effective pressure and the light green surface indicates the pre-overburden-pressure.

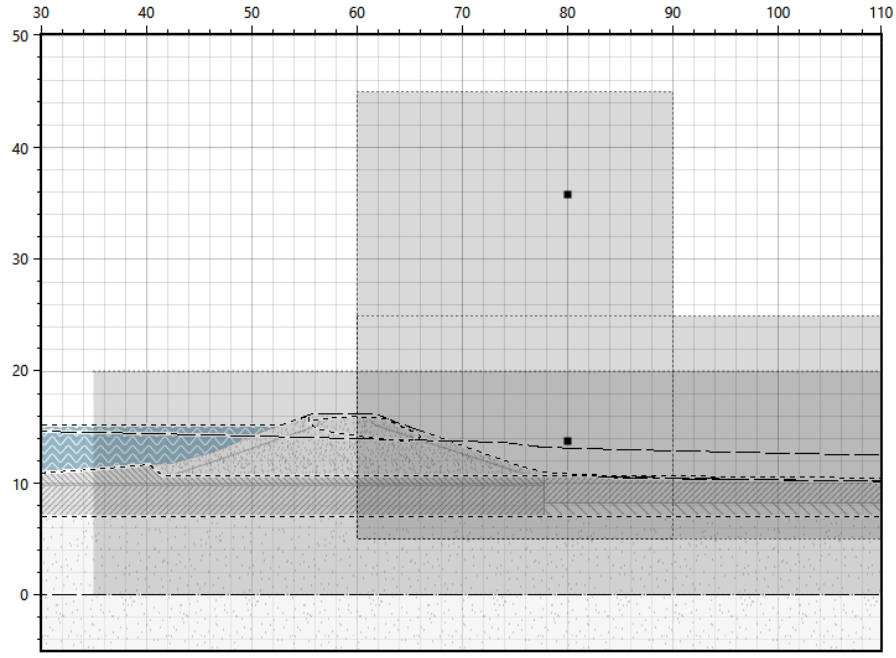

Figure 3.13: The search grid applied to the D-Stability assessments.

line be determined by the phreatic line. This yields the pressure profile as given in Figure 3.12. This method reasonably approximates the actual situation.

The ranges in height of the phreatic line and the sizes of the unsaturated zone are based on the results from the GeoStudio: Seep/W analyses and are implemented manually in D-Stability. To achieve consistent results, the analysis settings are fixed for all assessments. The analyses are conducted using the Uplift-Van method, as it is more versatile than the Bishop method. The search grid for the particle swarm method is visualised in Figure 3.13 and is set up as follows. The upper left corner of the search grid for the first circle is placed at $x = 60\ m$ and $z = 45\ m$ with a width of 30 m and a height of 40 m. The upper left corner of the search grid for the second circle is then placed at $x = 60\ m$ and $z = 25\ m$ with a width of 50 m and a height of 20 m. The tangent search grid (i.e. for the horizontal line to connect the two slip circles) ranges from $z = 0$ to $z = 20$. The search mode is set to thorough to achieve the best possible results. The analyses will be performed both with and without constraints for the slip circle. Without constraints, the slip circle is allowed to be infinitely small, which may lead to a slip circle that is irrelevant with respect to dike failure or that is not a measure of macro-stability. With constraints, the slip circle is guaranteed to represent macro-stability, but the safety factor may be highly dependent on the exact constraints. The constraints applied to the analyses are a minimum depth of the slip circle of 1 m and a minimum length of the slip circle of 10 m. Additionally, the slip circle must enter on the crest of the dike (i.e. between $x = 56$ and $x = 62\ m$).

The safety factor for both analysis methods are then plotted against the timestep corresponding to the applied phreatic conditions.

Parameter	**Unit**	**H_Aa_ht_k**	**H_Rk_k**	**P_Rg_zg**
Unit weight	$[kN/m^3]$	19.0	16.1	18.0
Submerged unit weight	$[kN/m^3]$	19.5	16.2	20.0
Cohesion	$[kN/m^2]$	0.0	0.0	0.0
Friction angle	$[^o]$	28.7	33.4	32.2
Dilatancy angle	$[^o]$	0.0	0.0	0.0

Table 3.5: WTI-SOS Material codes and corresponding parameter values (Deltares, 2015).

Chapter 4

Results

4.1 Phreatic processes

Figures 4.3, 4.4 and 4.5 each show three cross sections of a wave overtopping simulation, with corresponding levels of saturation and their phreatic lines. Figure 4.3 corresponds to a dike with material B-1-1 (see Table B.1), Figure 4.4 corresponds to a dike with material E-1-4 (see Table B.1) and Figure 4.5 corresponds to a dike with a cover layer of 80 *cm* thick and of material K-2-4 (see Table B.1). The top figure (a) of each Figure shows the initial condition of the dike body, the middle figure (b) shows the condition halfway through the overtopping simulation and the bottom figure (c) shows the condition either at the end of the simulation or the last timestep before the dike is fully saturated. The three figures correspond to the area of the unsaturated zone over time as given in Figures 4.6, 4.7 and 4.8 respectively.

The initial condition in these simulations represent a dike body without infiltration by wave overtopping. In that condition, the phreatic line leads from the outside water level towards the inner toe of the dike, as shown in Figures 4.3a and 4.4a. The permeability of different layers in the dike may affect the exact position of the line, as is visualised in Figure 4.5a. Figure 4.2 shows the flow patterns under initial conditions. In this steady state situation, phreatic water flows parallel to the phreatic line from the outer slope towards the inner toe of the dike. This flow is caused by the pressure difference as a result of the water level difference between the outside and the inside of the dike.

4.1.1 Infiltrating water

From Figures 4.3 and 4.4, it is found that water infiltrating into the cover layer can behave in two different ways. The first of which is that the infiltration will cause the cover layer to become saturated. In this situation the soil at the top of the dike is saturated, while the soil in the dike core is not. This is the case in Figure 4.3. The second option is that water flows directly through and around the unsaturated zone and adds to the

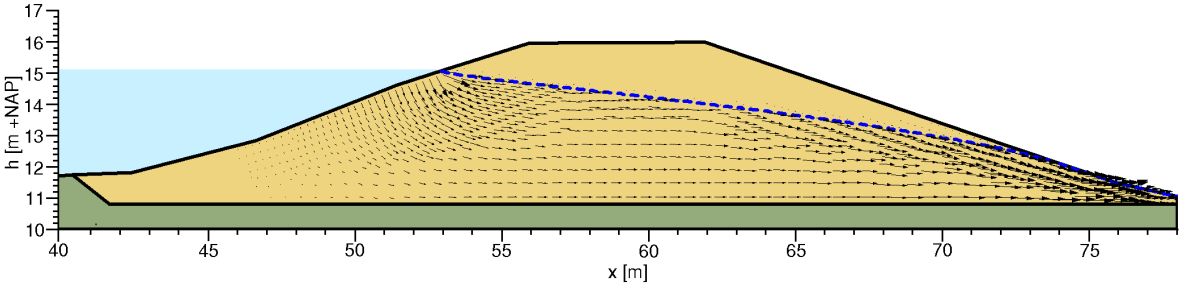

Figure 4.1: Visualisation of the flow patterns in the dike cross section under initial conditions. The core of the dike consists of material E-1-4 (see Table B.1). The blue dashed line visualises the phreatic line in the dike body.

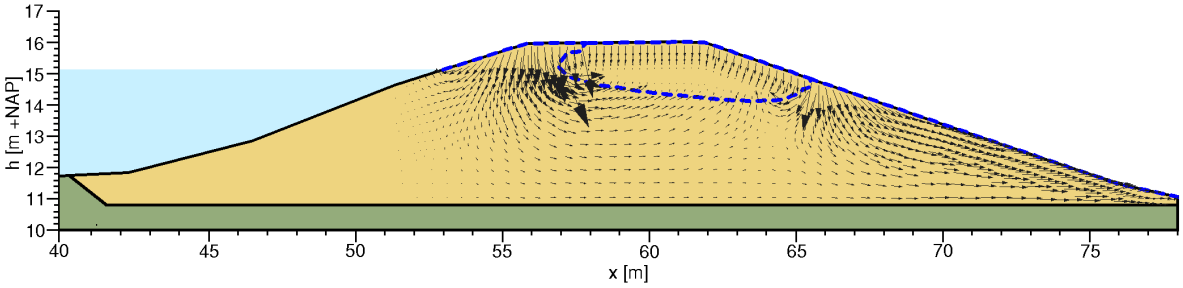

Figure 4.2: Visualisation of the flow patterns in the dike cross section at t=10min. The core of the dike consists of material E-1-4 (see Table B.1). The blue dashed line visualises the phreatic line in the dike body.

phreatic surface, heightening the phreatic line. This process is the case in Figure 4.4. While this may not have a different effect on the area of the unsaturated zone, it does affect the height of the phreatic line and therefore the pore water pressures in the dike body.

4.1.2 Flow patterns

During infiltration, the phreatic line will take on a circular shape in the center of the dike, as is shown in both Figures 4.3 and 4.4. The flow of phreatic water, visualised in Figure 4.2, is, in this case, not restricted to the direction of the phreatic line. Instead, the flow patterns in the dike are somewhat more complex.

As shown in Figure 4.2, infiltrating water enters the dike along the surface. The flow direction of water depends on where the water infiltrates and on where the unsaturated zone is located. Infiltrating water on the outside slope, to the left of the unsaturated zone, is transported back towards the outside water. Water infiltrating into the crest of the dike, to the left of the unsaturated zone, is transported downwards along the unsaturated zone, after which it flows towards the center of the dike body and eventually upwards into the unsaturated zone. From above the unsaturated zone, water is transported directly downwards into the unsaturated zone and, finally, water infiltrating on the inner slope of the dike is partially transport below and into the unsaturated zone and partially towards the inner dike toe where it discharges out of the dike body.

These flow patterns may slightly differ, depending on the rate of infiltration and the permeability of the soil. The general patterns, however, are similar for all simulations performed in this study.

4.1.3 Discharge and Runoff

Not all infiltrating water is transported towards the unsaturated zone. Part of it is discharged out of the inner toe of the dike. The discharge out of the dike body may have been present without infiltration by wave overtopping as well, but will increase due to infiltration.

The dike will eventually reach a fully saturated state where the unsaturated zone has disappeared. At that point, a large part of an overtopping wave will flow off the dike as runoff instead of infiltrate into the dike. Also, the discharge out of the dike at the inner toe will have reached an equilibrium with the water infiltrating the dike body by both infiltration as well as the outside water level.

4.1.4 Cover layer

Figure 4.5, shows that shows that the height of the phreatic line in the dike core is governed by the cover layer. The pore water pressures in the dike core are therefore lower than without a cover layer.

Additionally, from Figures 4.7 and 4.8, it is given that the average rate of decrease of the unsaturated area for this dike with a cover layer (Figure 4.8) is much lower than for the dike with core material E-1-4 (See table B.1) (Figure 4.7), despite the core materials having very similar characteristics.

4.1.5 Decrease of unsaturated area over time

Figures 4.6, 4.7 and 4.8 give the area of the unsaturated zone over time. Visible in Figures 4.6 and 4.8 is the initial reduction of the area of the unsaturated zone. This phenomenon is most likely caused by the numerical

interpretation of the data. The outermost grid nodes are almost instantly saturated. This drastically decreases the unsaturated zone. In reality, this process is most likely more gradual and the phenomenon of instant saturation along the cover layer is most likely not as profound. For this reason, this initial reduction is not taken into account in the estimation of the area of the unsaturated zone.

Also, some scenarios show a variable rate of decrease of the unsaturated zone, rather than the estimated constant rate of decrease. The most likely reason for this is the shape of the unsaturated zone, specifically the ratio between the circumference and the area of the unsaturated zone. A higher circumference means a larger area through which water can flow. Therefore, the ratio between the circumference and the area has an influence on the rate of decrease of the unsaturated zone. An oval shaped unsaturated zone will decrease in size faster than a perfectly circular unsaturated zone.

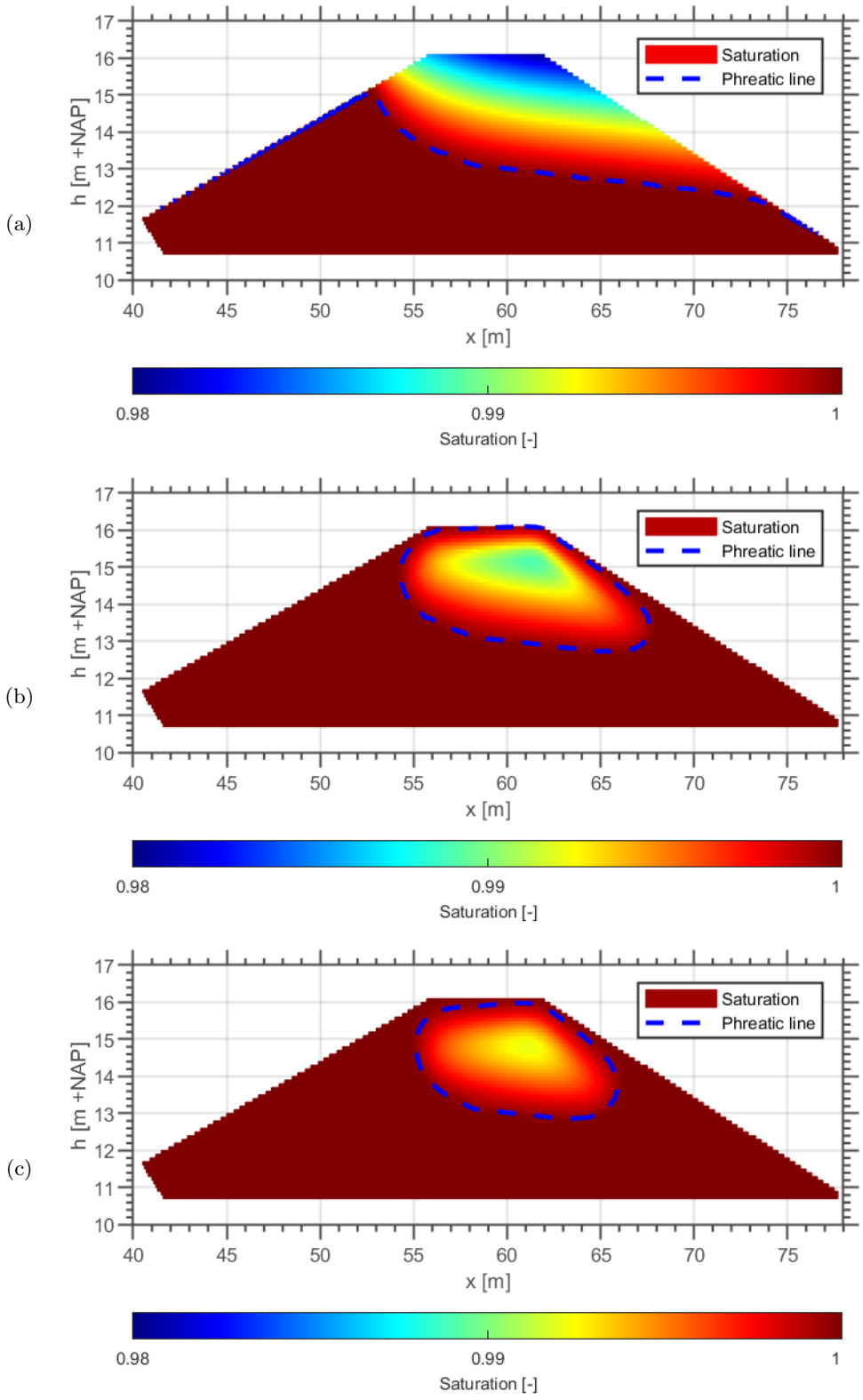

Figure 4.3: Visualisation of the levels of saturation in the dike cross section at t=0h (a), t=24h (b) and t=48h (c) corresponding to Figure 4.6. The core of the dike consists of material B-1-1 (see Table B.1). The blue dashed line visualises the phreatic line in the dike body.

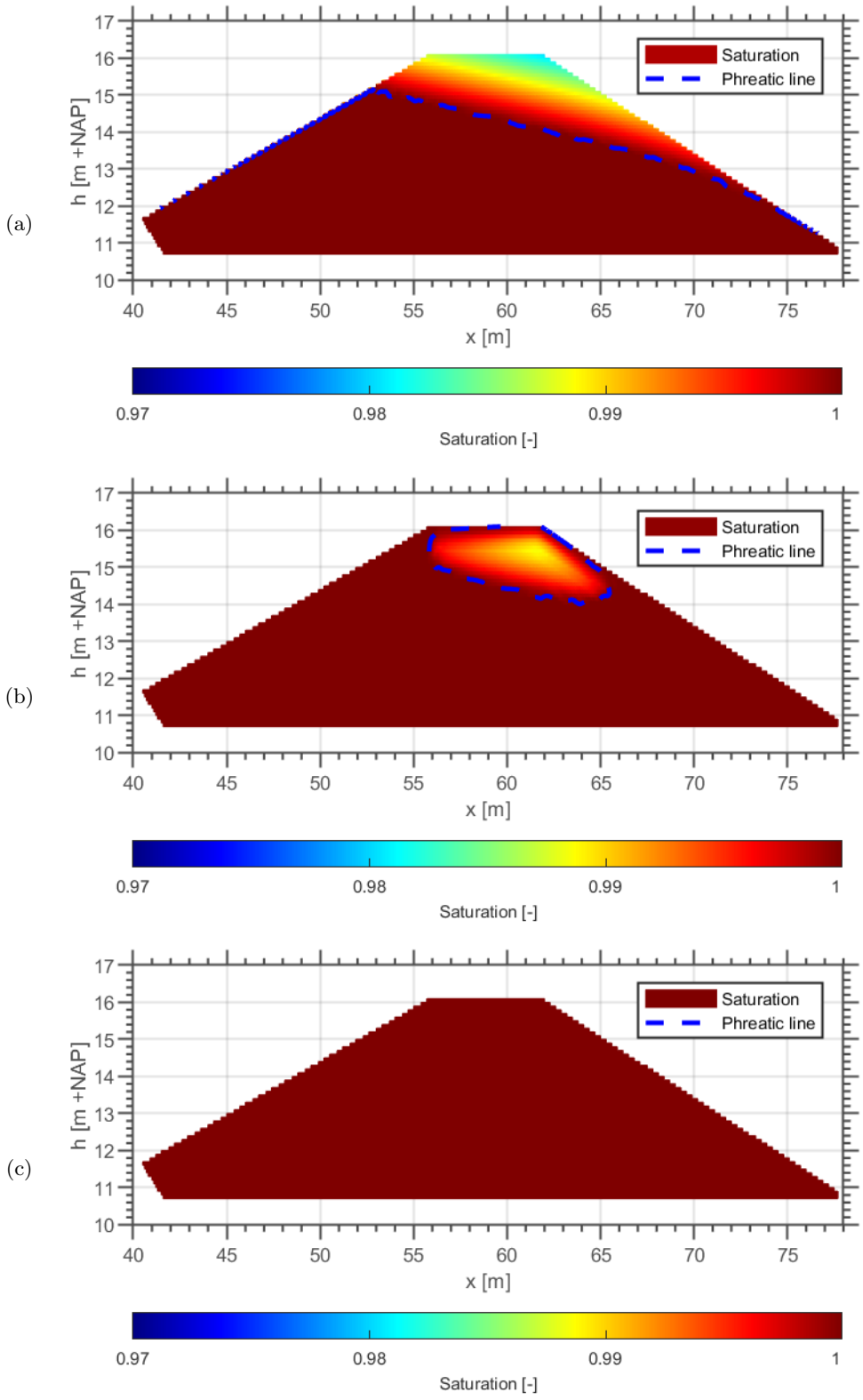

Figure 4.4: Visualisation of the levels of saturation in the dike cross section at t=0h (a), t=10min (b) and t=19min (c) corresponding to Figure 4.7. The core of the dike consists of material E-1-4 (see Table B.1). The blue dashed line visualises the phreatic line in the dike body.

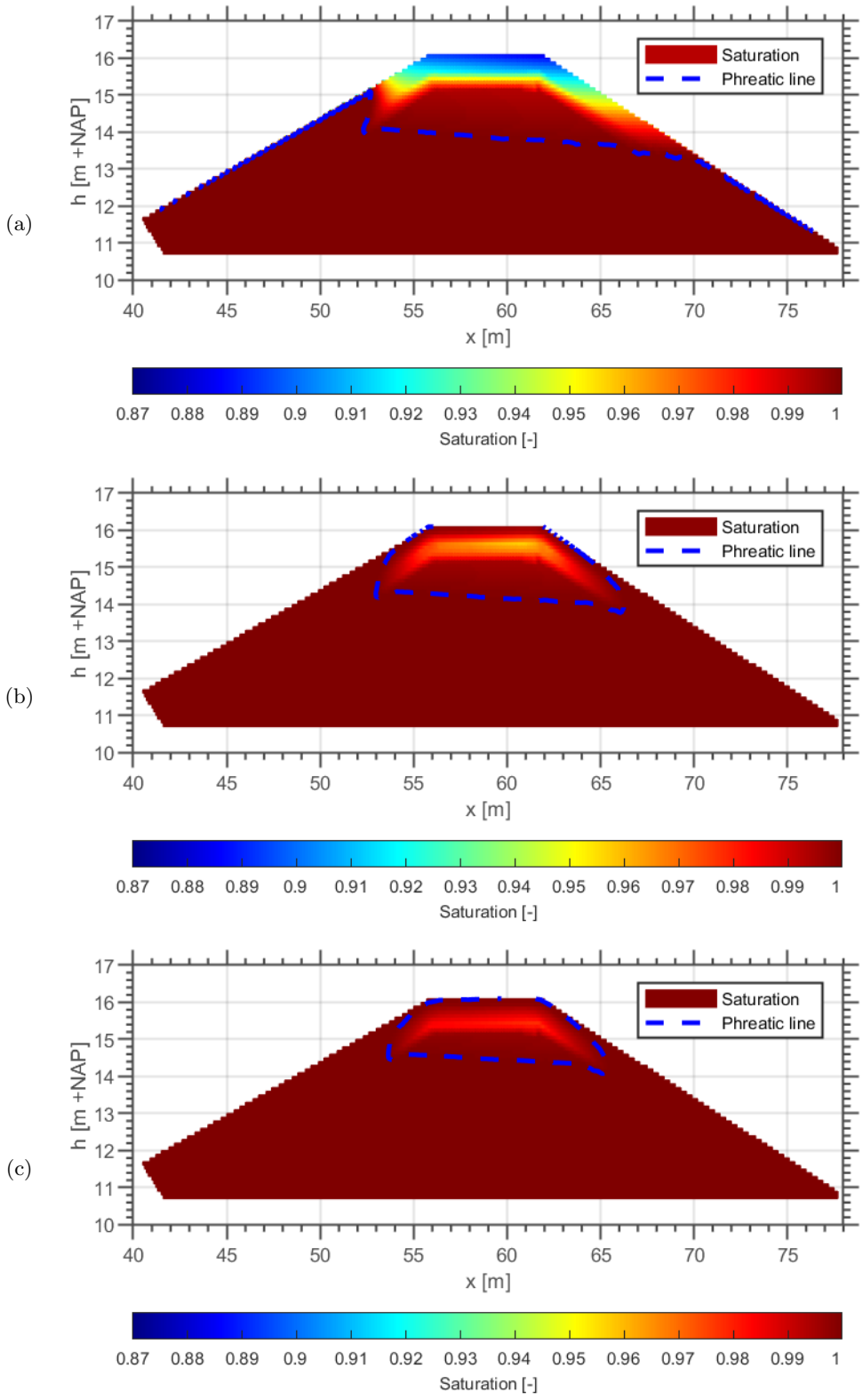

Figure 4.5: Visualisation of the levels of saturation in the dike cross section at t=0h (a), t=24h (b) and t=48h (c) corresponding to Figure 4.8. The cover layer has a thickness of 80cm, and consists of material K-2-4 (see Table B.1). The blue dashed line visualises the phreatic line in the dike body.

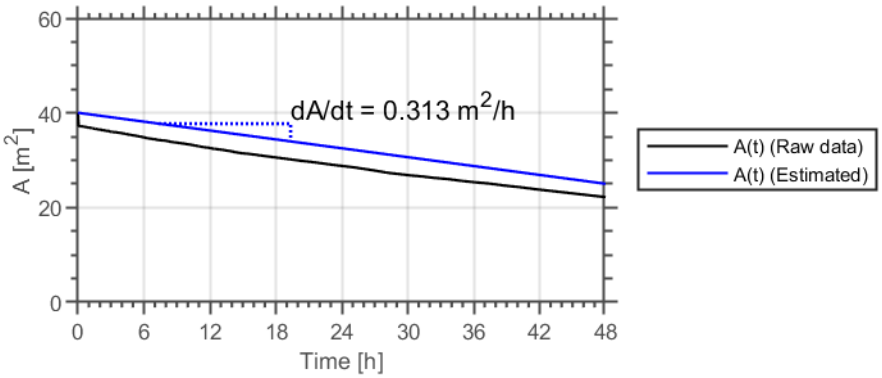

Figure 4.6: Actual and estimated unsaturated area over time of a dike with core material B-1-1. The dike is not yet fully saturated at the end of the simulation.

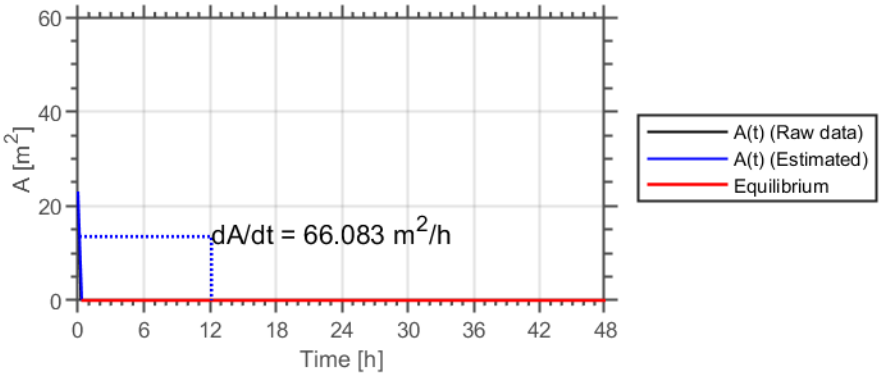

Figure 4.7: Actual and estimated unsaturated area over time of a dike with core material E-1-4. The dike is fully saturated after roughly 20 minutes, visualised by the red line at $A = 0m^2$.

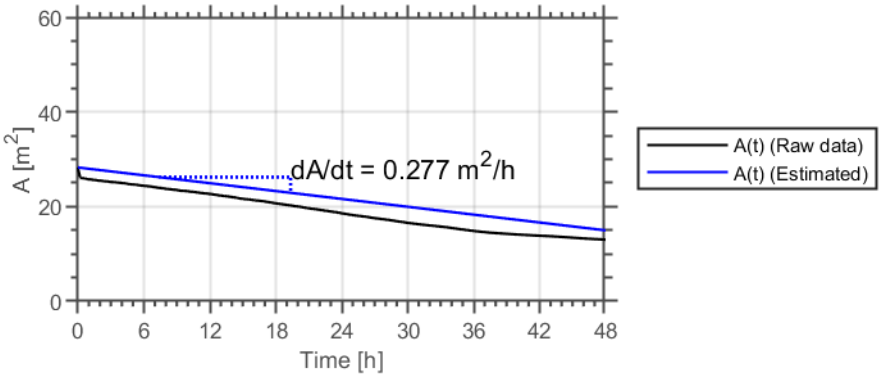

Figure 4.8: Actual and estimated unsaturated area over time of a dike with a cover layer. The dike is not yet fully saturated at the end of the simulation.

4.2 Important parameters

The second research question for this research project concerns the important parameters in the assessment of infiltration by wave overtopping. To answer this question, a sensitivity analysis is performed. The results of the sensitivity analysis are given in the form of boxplots. The boxplots describe the range of resulting rates of decrease of all scenarios, split into the different values for each parameter. The plots are given in Figures 4.9 to 4.13. Each figure describes a separate set of simulations. Figure 4.9 represents the set of simulations in which the saturated water retention (Θ_s), the saturated hydraulic conductivity (K_s) and fitting parameters α and n are varied. Figure 4.11 represents the set of simulations in which both the flux and the saturated hydraulic conductivity (K_s) are varied. Figure 4.12 represents the set of simulations in which both the flux and the infiltration time ($T_{wet,\%}$) are varied and finally, Figure 4.13 represents the set of simulations in which the thickness of the cover layer (D_{cl}) and the saturated hydraulic conductivity of the cover layer ($K_{s,cl}$) are varied. The unsaturated area over time for each simulation, including the estimated average rate of decrease of the unsaturated area, is given in Appendix F.

4.2.1 Material properties

The influence of Θ_s, K_s, α and n on the rate of decrease of the unsaturated area are given in Figure 4.9. These figures should be interpreted as follows, with the boxplot for $\Theta_s = 0.5$ as an example. For the left most subfigure of Figure 4.9, all scenarios are divided into four groups, depending on the value of Θ_s applied for that scenario. The dashed black line describes the full range of resulting values for the rate of decrease of the unsaturated zone, the blue box ranges from the 25^{th} to the 75^{th} percentile and finally the red line describes the median value. This means that for $\Theta_s = 0.5$, independent of the value of each of the other parameters considered in this set of simulations, the rate of decrease of the unsaturated zone does not exceed 0.055 m^2/s. Figure 4.9 also shows that a value for Θ_s of 0.9 yields a rate of decrease of the unsaturated zone that is less than 50% of the rate of decrease that would be obtained with a value for Θ_s of 0.3. The value of Θ_s thus has a large influence on the rate of decrease of the unsaturated zone.

Similarly, K_s has a large influence as well. Considering that the value for K_s in this figure increases exponentially, the value for K_s most likely has a linear relation with the rate of decrease of the unsaturated zone.

α also has a large influence on the rate of decrease of the unsaturated zone, according to Figure 4.9. Especially between a value for α of 0.005 and 0.015, there is a large difference in maximum rate of decrease. This difference reduces with higher values of α, suggesting an exponential relation.

Finally, there does not seem to be a clear correlation between the value of n and the rate of decrease of the unsaturated zone. The highest value of the rate of decrease for this set of simulations is obtained for a value for n of 1.3, with decreasing results for both decreasing as well as increasing values of n.

The saturated hydraulic conductivity has the largest influence on the average rate of decrease of the unsaturated area, closely followed by the fitting parameter α. These parameters are therefore the most important in the assessment of infiltration by wave overtopping. Nevertheless, the saturated water retention can still cause a factor two difference in average rate of decrease of the unsaturated area, meaning that this too is an important parameter to take into account. Fitting parameter n is the least important of the parameters considered in Figure 4.9.

Material classifications by Wösten et al. (1987)

Figure 4.10 shows the ranges as determined with simulation set 1 with the results of the simulations with the set of standard materials as classified by Wösten et al. (1987) (See Tables 3.3 and 3.4). This figure shows that these materials follow the same patterns as found in Figure 4.9. One clear example of this is material B13, with a rate of decrease of 0.021 m^2/s. This sandy loam type soil has parameter values that are close to the values that cause the maximum rate of decrease considered in simulation set 1, which causes the rate of decrease of material B13 to be high as well. This shows that the results from simulation set 1 can most likely be interpolated for any combination of the four independent parameter as defined by van Genuchten (1980) (i.e. Θ_s, K_s, α and n).

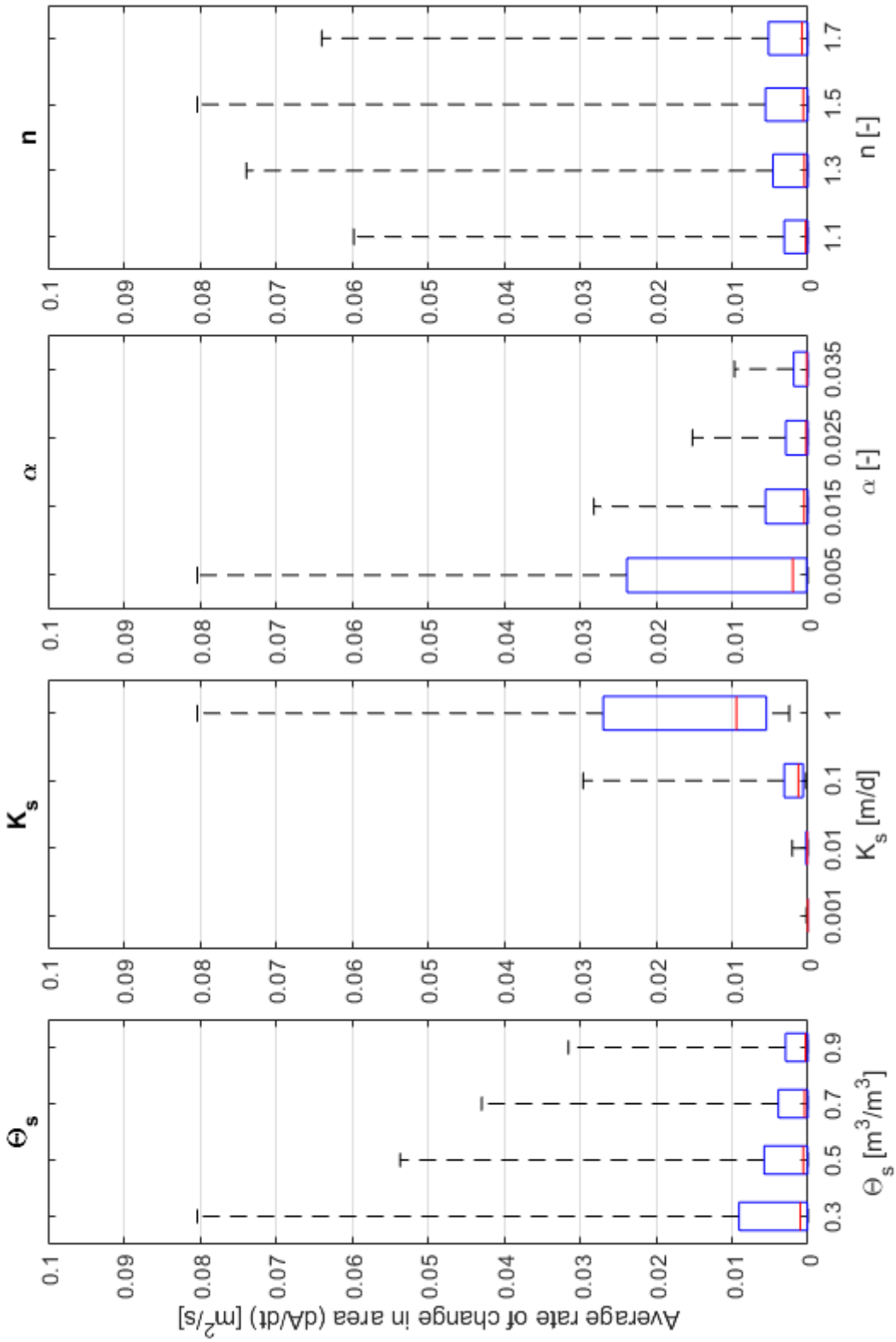

Figure 4.9: Influence of soil parameters on the rate of change in unsaturated area.

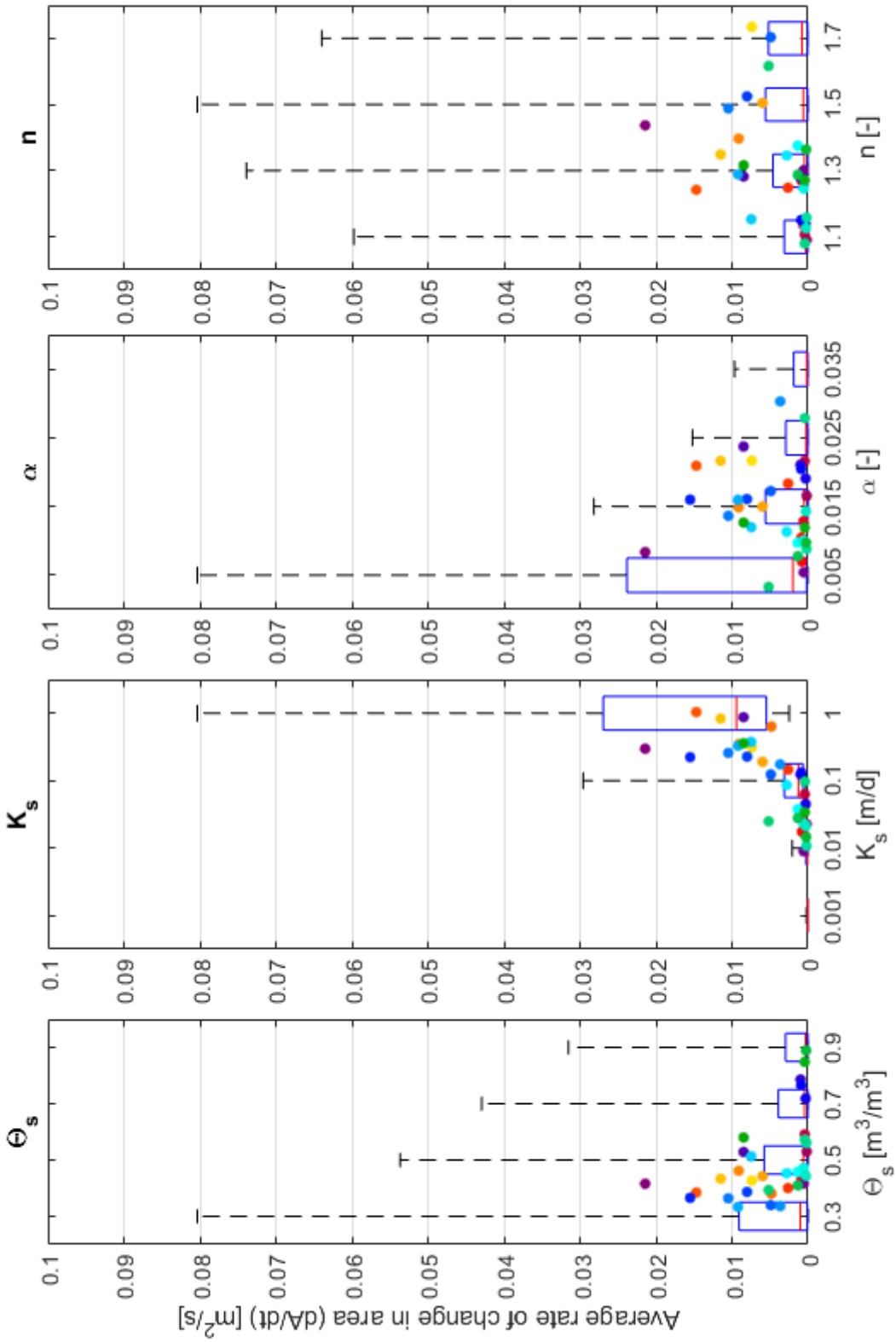

Figure 4.10: Result of materials from Staringreeks visualised in resulting ranges from the sensitivity analysis.

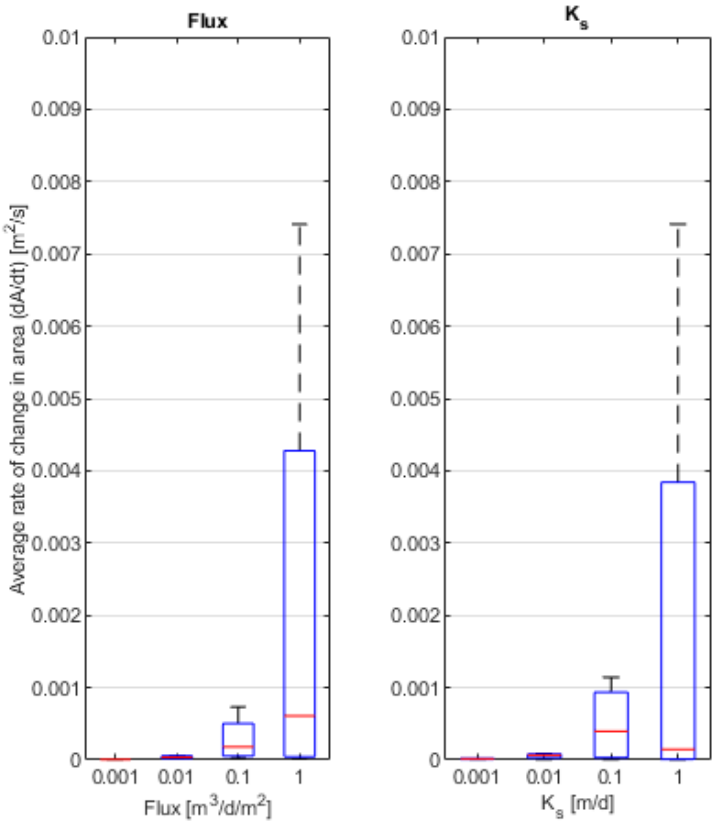

Figure 4.11: Influence of flux and K_s on the rate of change in unsaturated area.

4.2.2 Flux

The influence of flux compared to K_s is given in Figure 4.11. This figure shows that the flux has an influence on the rate of decrease of the unsaturated zone similar to K_s. Note that the value for Flux increases exponentially, similar to the value for K_s.

Figure 4.11 shows that either of the two parameters (Flux or K_s) limits the rate of infiltration. If the flux is high (i.e. when there is a lot of water to infiltrate and a high pressure difference), but K_s is low (i.e. the soil has a low permeability) then water will not be able to infiltrate and will instead runoff along the inner slope as surface water. Conversely, if K_s is high, but the flux is low, then there is less water available than can theoretically infiltrate. The rate of infiltration is then limited by the water availability.

This means that under the assumption that there is always enough water to infiltrate, the actual flux is equal to K_s. Also, as long as the flux value is set higher than the K_s value of the soil, then the infiltration will be limited by K_s independent of the exact value of the flux.

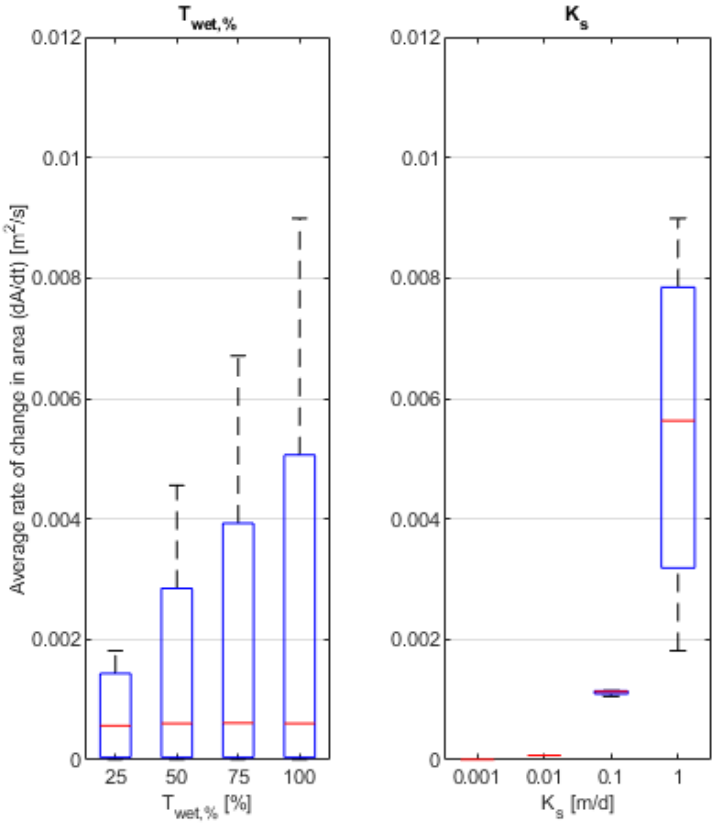

Figure 4.12: Influence of infiltration time and K_s on the rate of change in unsaturated area.

4.2.3 Infiltration time

The influence of infiltration time compared to K_s is given in Figure 4.12. This figure shows that the influence of the infiltration time is of linear nature. The rate of decrease of the unsaturated area increases for an increasing infiltration time. Also, Figure 4.12 shows a similar influence of the value for the saturated hydraulic conductivity as shown in Figures 4.9 and 4.11. This means that the infiltration time is an important factor in the assessment of infiltration by wave overtopping.

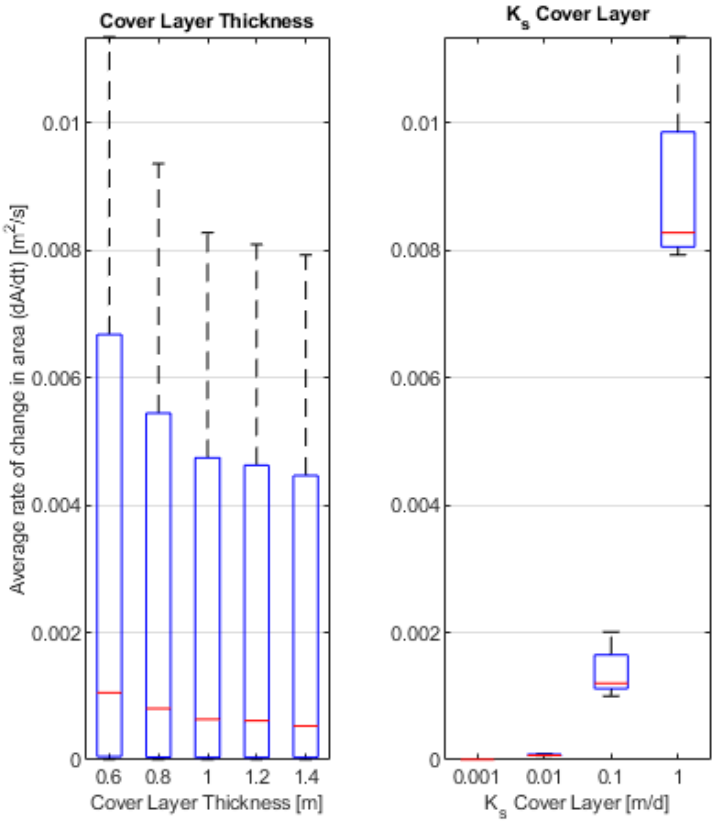

Figure 4.13: Influence of thickness and saturated hydraulic conductivity of the cover layer on the rate of change in unsaturated area.

4.2.4 Cover layer

Figure 4.13 shows the influence of the thickness and the saturated hydraulic conductivity (K_s) of a cover layer. The core material of the dike in this set of simulations is material B-1-4 (see Table B.1). Without a cover layer, the rate of decrease of a dike of material B-1-4 would be around 0.09 m^2/s. A cover layer of 0.6 $[m]$ already reduces that by almost 90% to 0.011 m^2/s. Figure 4.13 further shows that a thickness of the cover layer above 1 $[m]$ barely has any additional effect compared to a thickness of 1 $[m]$. The K_s of the cover layer has a clear relation with the resulting rate of decrease, similar to the effect of K_s of the core material given in Figure 4.9.

The difference in rate of decrease of the unsaturated area between a dike with a cover layer of material B-1-4 and a complete dike body of material B-1-4 is relatively small. From the previously simulated scenarios in simulation set 1, it was found that the rate of decrease for a complete dike body of material B-1-4 is 0.0075 m^2/s. From Figure 4.13, it can be seen that for a dike with a cover layer of material B-1-4, the rate of decrease ranges from 0.008 to 0.012 m^2/s, depending on the thickness of the cover layer. This shows that a cover layer of 1 m provides a similar protection against infiltration to a full dike body of the same material.

These results show that cover layer characteristics are important to include in the assessment of infiltration by wave overtopping. Especially the material properties of the cover layer are important to include, as they have a large influence on the rate of decrease of the unsaturated area. The thickness of the cover layer can be included as well, but is of lesser importance than the material properties.

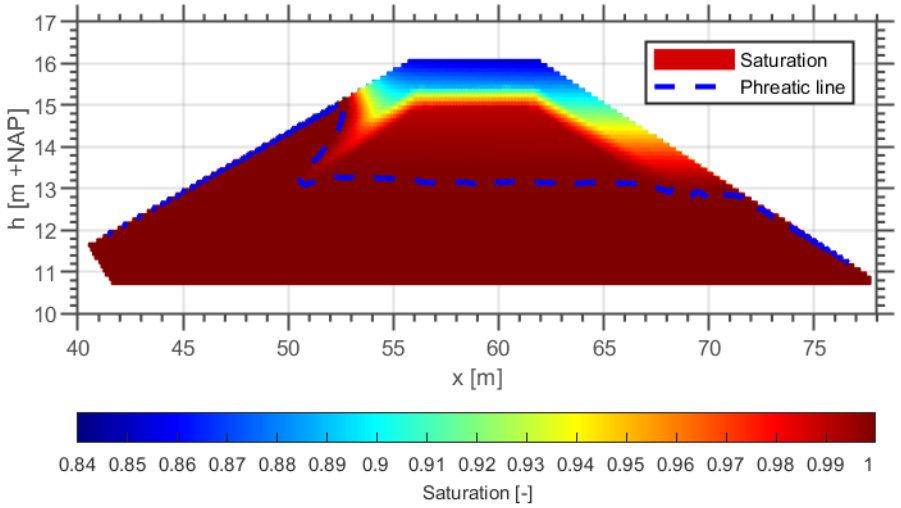

Figure 4.14: Phreatic conditions in the dike at t=0h for a dike with a cover layer of 1 m thickness and material K-2-4 (see Table B.1). The blue dashed line visualises the phreatic line in the dike body.

4.2.5 Hole in the cover layer

Figure 4.14 shows the initial condition of a dike with a cover layer of 1 m thickness and saturated hydraulic conductivity of 0.001 m/d. Figure 4.15 shows the initial conditions in the case of a hole in the cover layer at the top of the inner slope (Figure 4.15a), halfway the inner slope (Figure 4.15b) and at the bottom of the inner slope (Figure 4.15c). In the case of a hole at the top of the inner slope, there is initially barely any difference. In later timesteps, the simulation shows a fast decrease of the unsaturated area as the hole in the cover layer allows the phreatic line to rise up to the cover layer, filling up the dike body. A hole in the cover layer at the top of the inner slope therefore has a negative impact on the phreatic condition in the dike, especially on the height of the phreatic line. In the case of a hole further towards the bottom of the dike, the hole starts acting as a drain. The hole in the cover layer allows the water to drain from the dike body more easily, decreasing the height of the phreatic line. This process continues throughout the simulation. A hole in the cover layer below the phreatic line therefore has a positive impact on the height of the phreatic line. In reality however, the discharge through the hole in the cover layer will erode the dike body from the inside out. This process is called micro instability and will cause the dike to fail nonetheless.

If the possibility of a hole in the cover layer is considered, then the effect of the cover layer is cancelled. This connects the failure mechanism of erosion of the grass cover to that of macro stability. If the grass cover is eroded, then the probability of macro-instability increases as well.

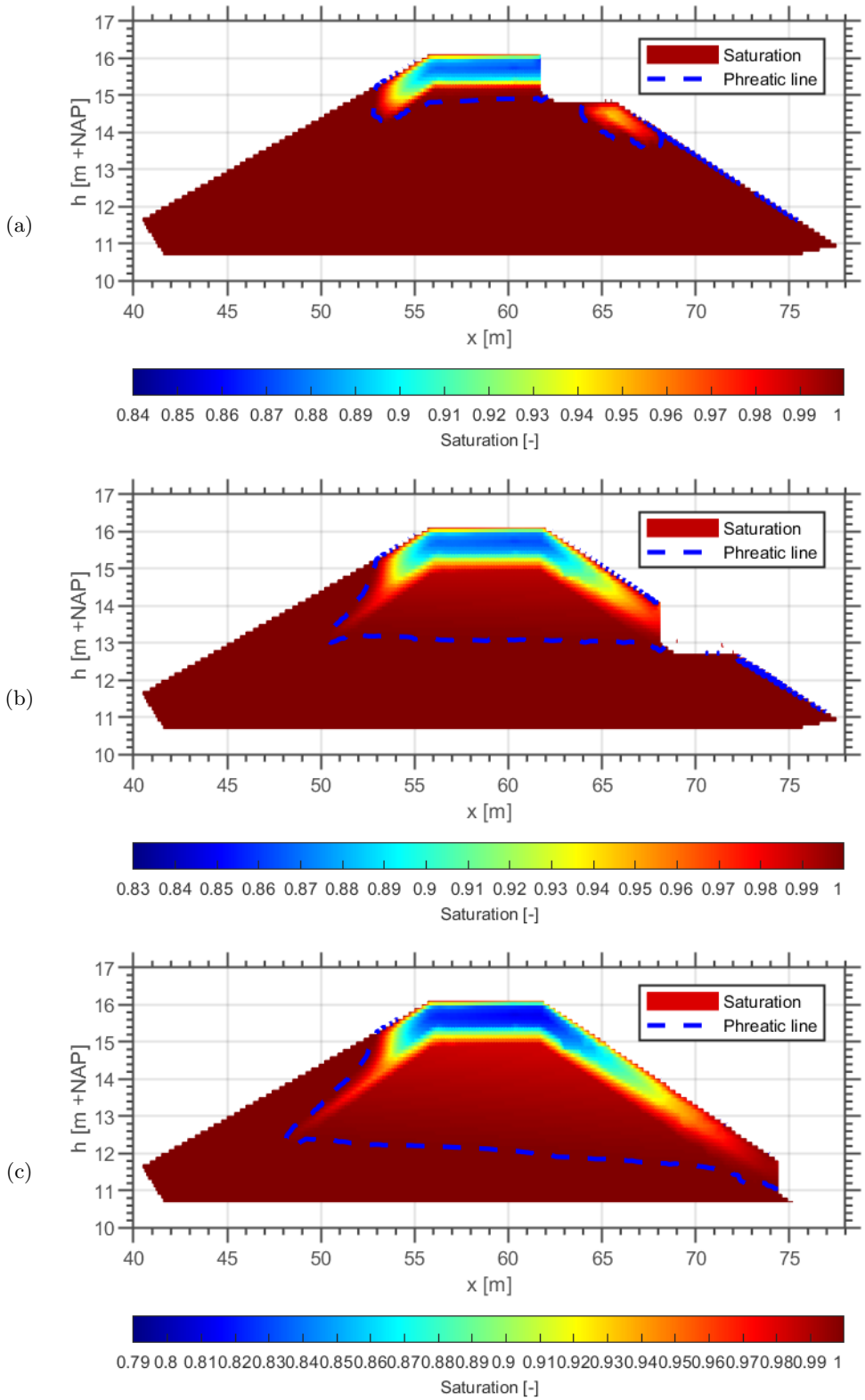

Figure 4.15: Visualisation of the effect of a hole in the cover layer at the top of the inner slope (a), halfway the inner slope (b) and at the bottom of the inner slope (c) on the levels of saturation in the dike cross section at t=24h. The cover layer has a thickness of 1 m and consists of material K-2-4 (see Table B.1). The blue dashed line visualises the phreatic line in the dike body.

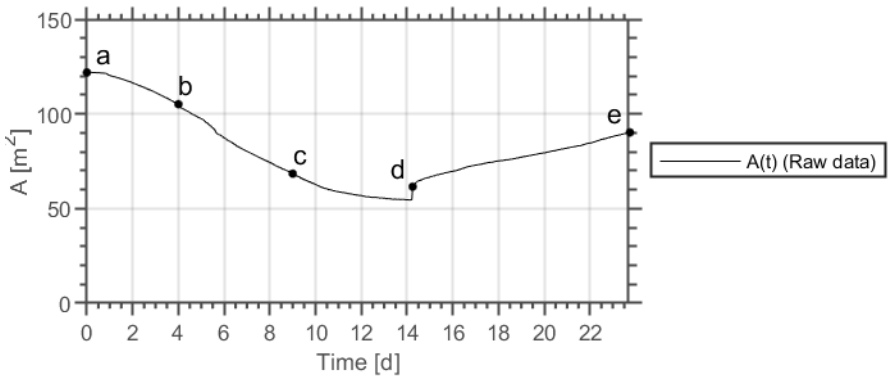

Figure 4.16: The unsaturated area over time when simulating a complete flood wave passing the dike.

4.2.6 A complete flood wave

Figure 4.16 shows the unsaturated area over time for the duration of a complete flood wave. Figure 4.17 shows the levels of saturation at five important moments in time.

From Figure 4.16, it can be seen that the decrease in unsaturated area is not linear, which is the case for simulations with a steady state initial condition. Instead, the unsaturated area over time follows a quarter sine shape. Note that, in this simulation, the decrease of the unsaturated area is not only a function of infiltration by wave overtopping, but also of the rise of the outside water level. At its lowest point, the area of the unsaturated zone is over $50m^2$, which is higher than at the initial condition of most other simulations performed for this research project. This may indicate that the steady state initial condition that is often used is a conservative assumption.

In Figure 4.17, it is shown that initially the full dike body is unsaturated (Figure 4.17a). The phreatic line then starts rising at the outer toe due to the rising water level. After four days, wave overtopping starts and as a result the phreatic line starts rising at the inner toe as well (Figure 4.17b). From this point, the phreatic line rises at both the outer and the inner toe, while it remains relatively low in the middle of the dike. At t=9d, the peak water level is reached, from which point the phreatic line at the outer toe starts to lower again as the outside water level drops (Figure 4.17c). Since infiltration by wave overtopping still occurs after the peak water level has passed, the phreatic line at the outer toe continues to rise. Eventually, the outside water level will drop to the point where wave overtopping no longer occurs and the phreatic line starts to lower at the outer toe as well (Figure 4.17d). From this point on, the phreatic line slowly returns to its initial condition. As a result of water retention and hydraulic conductivity, there is a lag in the system. This means that the dike has not yet returned to initial conditions at the moment the water level has returned to its normal level (Figure 4.17e).

This process shows that especially the inner toe is vulnerable to sliding off, as the phreatic line is the highest and therefore the pore water pressures are highest at that point. Conversely, the center of the dike is not as vulnerable to macro-stability, as the pore water pressures in the center are relatively low.

(a)

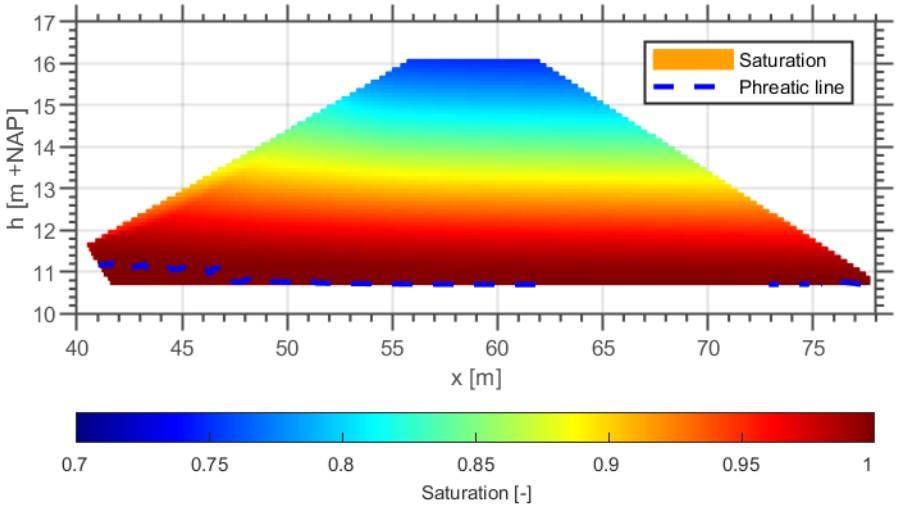
Saturation
Phreatic line
h [m +NAP]
x [m]
Saturation [-]

(b)

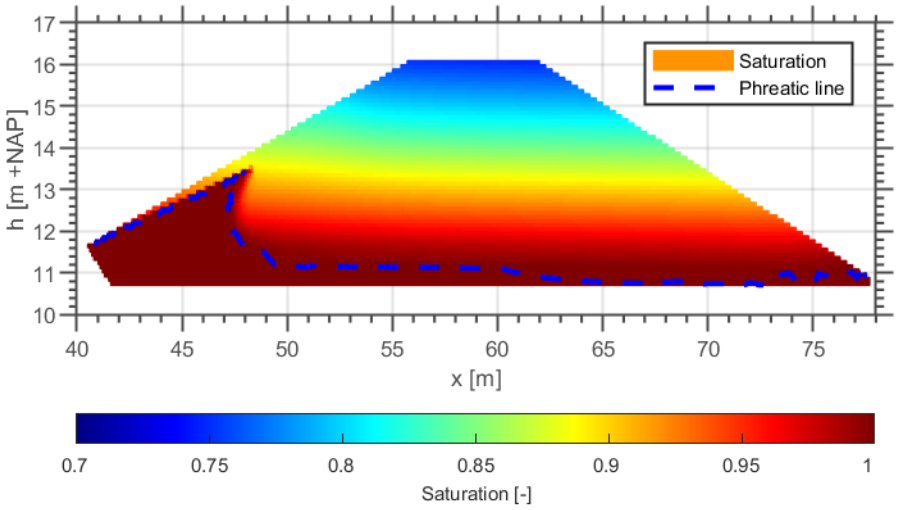
Saturation
Phreatic line
h [m +NAP]
x [m]
Saturation [-]

(c)

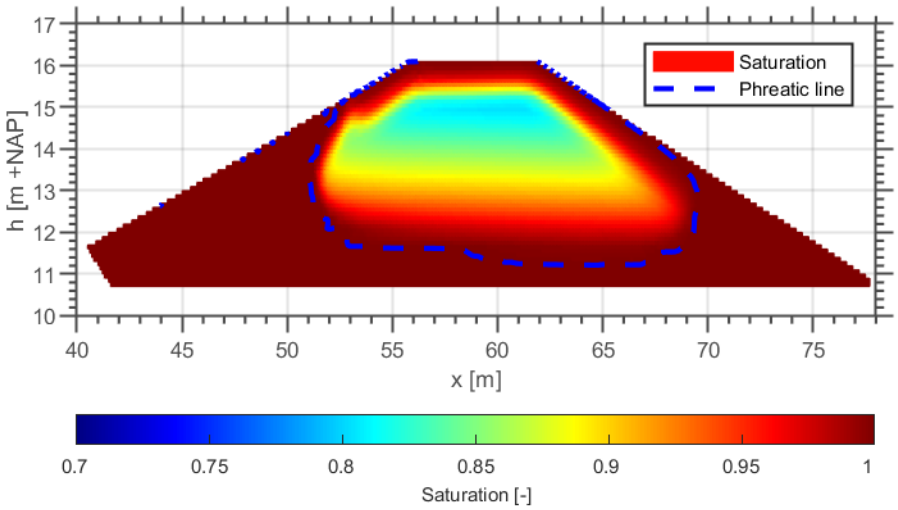
Saturation
Phreatic line
h [m +NAP]
x [m]
Saturation [-]

(d)

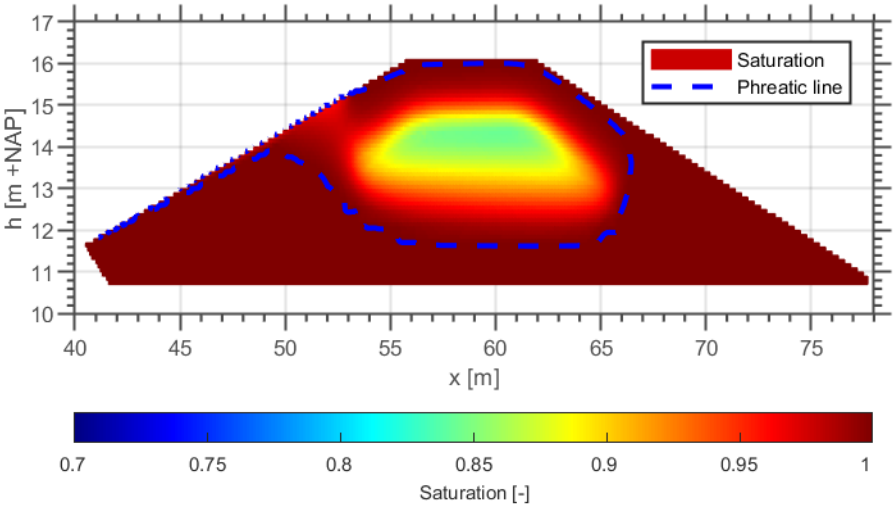

(e)

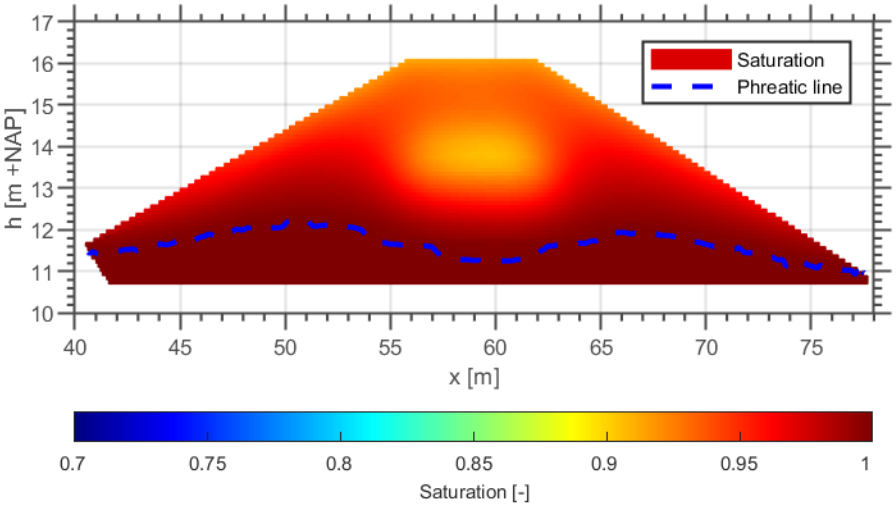

Figure 4.17: Visualisation of the levels of saturation in the dike cross section when simulating a complete flood wave passing the dike. t=0h (a), t=4d (b), t=9d (c), t=14d and 6h (d) and t=23d and 18h (e), corresponding to Figure 4.16. The dike core consists of material K-2-2 (see Table B.1). The blue dashed line visualises the phreatic line in the dike body.

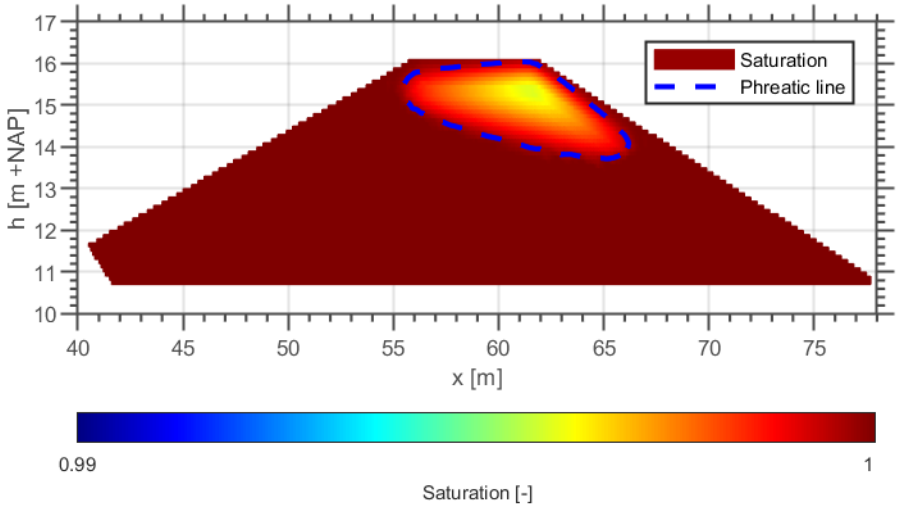

Figure 4.18: Visualisation of the levels of saturation in the dike cross section at t=24min for a dike with material A-1-3 (See Table B.1).

4.3 Macro-Stability

The third research question of this research project concerns the effect of phreatic conditions on the macro-stability of a dike.

Figure 4.18 shows the phreatic conditions for a dike of material A-1-3 (See Table B.1) at t=24min. The corresponding normative slip circle for these phreatic conditions, for an assessment with constraints on the slip circle, is given in Figure 4.19. The normative slip circle corresponding to the same phreatic conditions, but excluding constraints on the slip circle is given in Figure 4.20. From these figures, it is apparent that the slip circle in the assessment with constraints is much larger than the slip circle without using constraints and always enters in the crest of the dike. Therefore, the safety factor with constraints represents the safety factor for larger slip circles, that would likely lead to a dike breach. Without using constraints, the slip circle is allowed to be very shallow and will often avoid the unsaturated zone. Such slip circles do not necessarily reduce the stability of the dike and thus do not necessarily cause a dike breach. These smaller slip circles, found without using constraints, resemble erosion of the grass cover of the inner slope, rather than macro-stability.

Figure 4.21a shows the safety factor for macro-stability over time for dikes consisting of material types A-1-3, F-2-3, K-3-3 and P-4-3 (See table B.1) for assessments with- and without using constraints on the slip circle. Figure 4.21b shows the corresponding unsaturated area over time for the same material types.

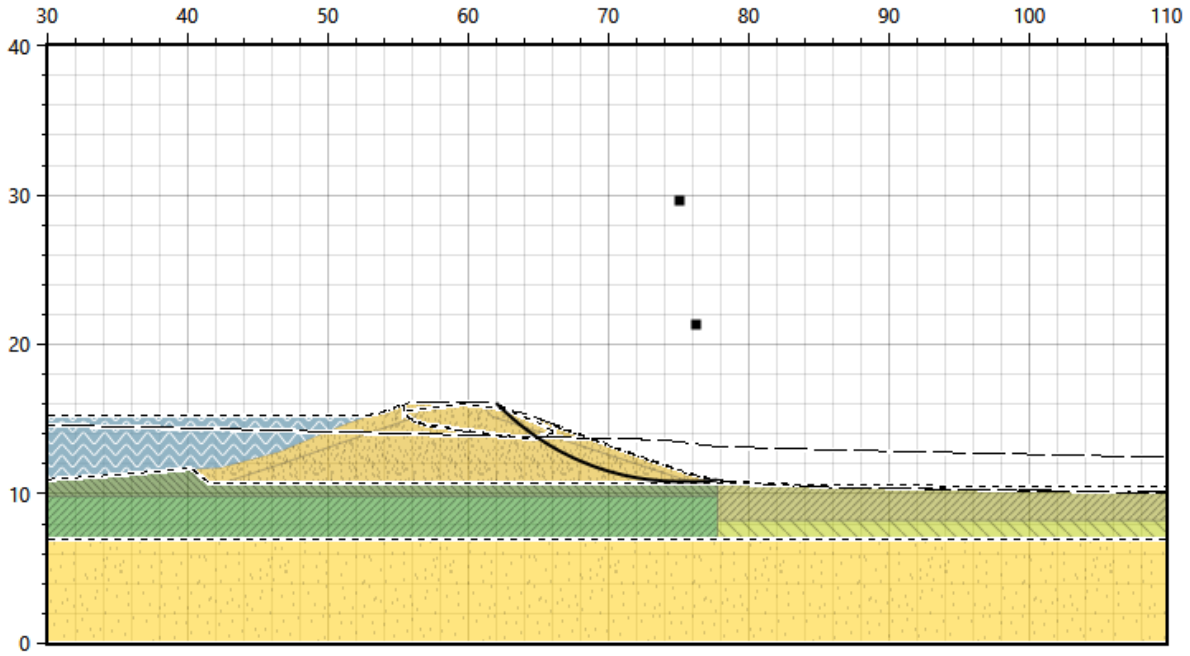

Figure 4.19: Normative slip circle, with center points for both circles in the Uplift-Van method, for a dike with material A-1-3 (See Table B.1) at t=24min using constraints on the slip circle. Phreatic conditions as given in Figure 4.18.

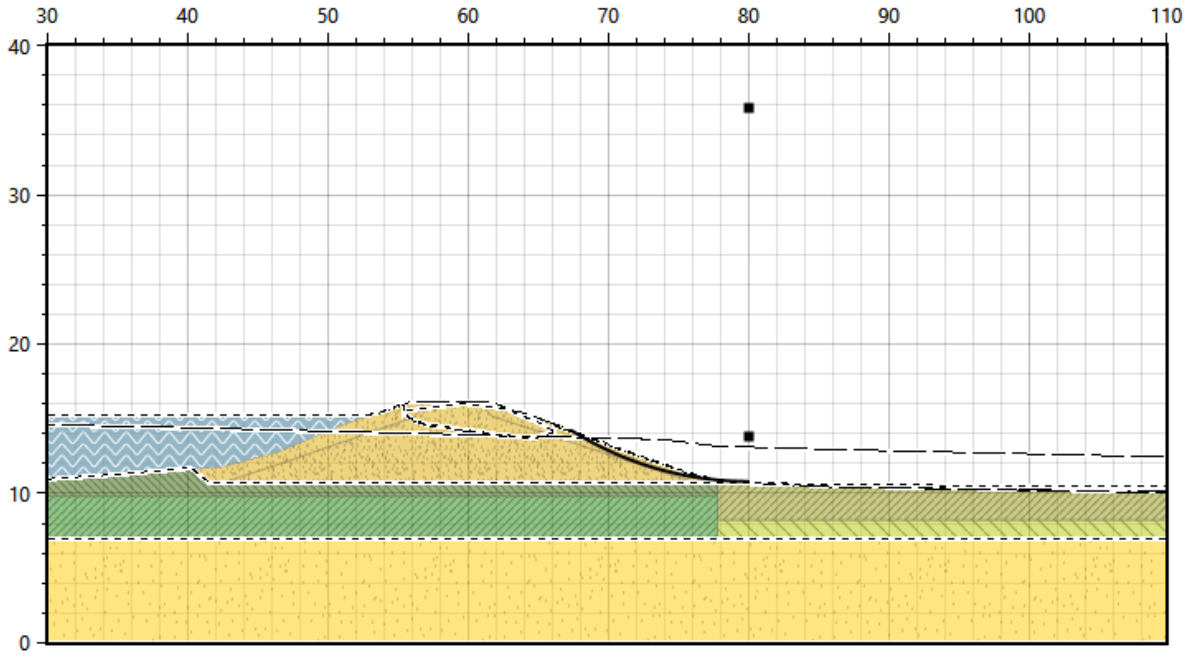

Figure 4.20: Normative slip circle, with center points for both circles in the Uplift-Van method, for a dike with material A-1-3 (See Table B.1) at t=24min without using constraints on the slip circle. Phreatic conditions as given in Figure 4.18.

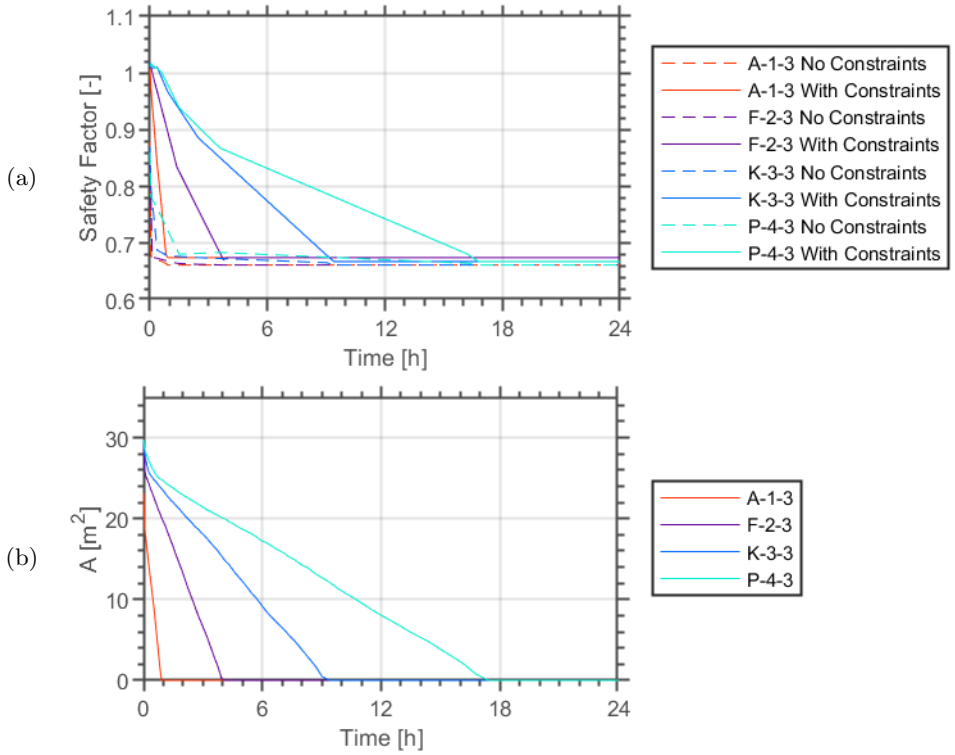

Figure 4.21: Safety factors over time for assessments with- and without using constraints (a) and unsaturated area over time for corresponding material types (b).

4.3.1 With constraints

Figure 4.21 shows that there is a reasonable resemblance between the decrease in unsaturated area and the safety factor for macro-stability when using constraints. As a result of infiltration by wave overtopping, the macro-stability initially decreases relatively quickly, after which the safety factor slowly reaches a minimum at the point where the dike is fully saturated. The same pattern is seen in all four scenarios. The above mentioned pattern likely originates from the shape of the unsaturated zone. While the unsaturated area decreases linearly, the shape and location of the unsaturated zone causes the macro-stability to behave in a more exponential way. For the case study dike cross-section, it seems that the safety factor for macro-stability can be estimated based on the unsaturated area.

4.3.2 Without constraints

Visible in Figure 4.21a is the near instant decrease in safety factor for assessments without using constraints. This happens because the inner slope at the toe of the dike is the first part of the dike to reach full saturation. This is also the location where the smaller slip circles will then occur, leading to a small slip circle with a low safety factor. As previously mentioned, these smaller slip circles may not immediately lead to macro-instability, but will reduce the overall safety of the dike.

Chapter 5

Discussion

Discretising infiltration

The phreatic processes as a result of wave overtopping infiltration were simulated using GeoStudio: Seep/W. This software is occasionally used by Sweco to simulate phreatic lines in both steady state, as well as transient analyses. Infiltration by wave overtopping is, however, not a standard option in the software. For that reason, a number of assumptions had to be made, which will be discussed here.

Firstly, no literature could be found on the rate of infiltration as a result of wave overtopping. The difference between infiltration by wave overtopping and infiltration by standing water is therefore unknown. The velocity and layer thickness may have an effect on the rate of infiltration, but it is currently unknown what this effect would be. Therefore, the rate of infiltration was assumed either 0 (dry inner slope) or at a constant value (wet inner slope). A decrease of rate of infiltration over time for each overtopping wave was not considered.

Secondly, the time during which the inner slope remains wet, is an estimation based on observations by Dutch Ministry of Infrastructure and the Environment (2012). This was assumed a constant value for each overtopping wave, independent of for example overtopping volume, inner slope steepness or layer thickness. It was found from preliminary simulations that the infiltration time per overtopping wave (T_{wet}) has a negligible influence as long as the infiltration time as a percentage of the total time ($T_{wet,\%}$) remains constant. For this reason, the infiltration time per overtopping wave (T_{wet}) is not included in the sets of simulations for the sensitivity analysis. As explained in Section 2.2, the infiltration time per overtopping wave does influence the infiltration time as a percentage of the total time ($T_{wet,\%}$), which means that it does have an indirect influence on the rate of decrease of the unsaturated zone. More field observations and measurements on the infiltration time per overtopping wave should be performed to test the assumption of a constant infiltration time per overtopping wave.

Thirdly, infiltration in intervals is not a usual type of infiltration in GeoStudio: Seep/W. This limited the options with respect to simulating infiltration. As mentioned above, infiltration was simulated as either 0 or constant. The ideal option for this would be to simulate a layer of water, that is equal to the layer thickness of the overtopping wave, on the inner slope of the dike. This can, however, not be done in the software in combination with 0 infiltration. Therefore, the water flux boundary condition was chosen, with which a water flux can be forced on the surface of the dike. As the rate of infiltration for overtopping waves is currently unknown, but according to this research has a large influence on the rate of decrease of the unsaturated zone, this value should be calibrated using measurement data. As an intermediate solution, the saturated hydraulic conductivity of the soil can be used as a value for the water flux boundary condition. This is based on the assumption that all water that the soil can absorb, will infiltrate the surface layer. This assumption was previously adopted by Dutch Ministry of Infrastructure and the Environment (2012) and Spanjersberg (2016) for their proposed method.

Finally, the soil in the simulations is assumed perfectly homogeneous. According to (TAW, 1996), soil structures (i.e. cracks and holes) are likely to occur in clay cover layers, increasing the permeability of the layer as a whole. This means that the actual effect of a cover layer is most likely less than stated in Chapter 4.

(Normative) duration of wave overtopping

The time during which wave overtopping occurs is unknown. Estimating this duration is difficult, especially in rivers. In rivers, wave conditions are not correlated to the water level (Ministerie van Infrastructuur en Milieu, 2017), but are a product of wind conditions. Estimating the representative duration of overtopping is a probabilistic matter in which the probability of a peak water level, the flood propagation and the wind conditions are important factors. A method to assess this probabilistic matter does currently not exist. As an estimation, Ministerie van Infrastructuur en Milieu (2021) propose a duration of 5 hours for river dikes. This estimation is made with cover-erosion of the outer slope in mind. They propose a representative duration of wave overtopping for sea-dikes of 3 hours. Comparing the 5 hours for river dikes to the results from simulation set 1, shows that roughly 36% of the simulations would reach fully saturated conditions during a representative storm. All simulations show a saturated cover layer of the inside slope after 5 hours.

Infiltration by precipitation

Infiltration by precipitation was not taken into account. TAW (2004) state that the influence of infiltration by extreme precipitation on the phreatic line, has a similar effect to wave overtopping. They state that in the past, a method was adopted in which measurements were taken after heavy rainfall events to find the relation between elevation of the phreatic line and the cumulative precipitation. From this relation, an estimation of the elevation of the phreatic line could be made based on the precipitation. This method was later abandoned, as the results scattered too much. Instead, a standard addition of $0.8m$ was made to the phreatic line as a consequence of a heavy rainfall event. To implement this method in the assessments done in this research, the initial unsaturated area should be determined with an $0.8m$ increase in height of the phreatic line. This will then reduce the time it takes for the dike to reach fully saturated conditions.

Sensitivity analysis

As previously mentioned in Section 3.3, the preferred method for the sensitivity analysis would be to include a wide range of possible values for each parameter and to simulate all possible combinations of parameter values. This will, however, result in an exponentially growing amount of simulations. Simulating this amount of simulations was not feasible within the time frame for this research project, as GeoStudio: Seep/W is not optimised for automating large amounts of simulations. Therefore, different sets of simulations were introduced. Some combined effects between parameters may have been missed by using this method. If automation of GeoStudio: Seep/W or other, similar, software is possible in the future, a simulation of all possible combinations could be done to ensure no combined effect was missed.

Wetting and drying

A process called wetting and drying constantly occurs throughout the simulations in GeoStudio: Seep/W. This is the process where the soils' degree of saturation changes. This is a complex process as the flow through the soil depends on the degree of saturation and the degree of saturation depends on the flow through the soil. This causes a complex numerical problem to solve, requiring many iterations to converge to an equilibrium state, where the degree of saturation corresponds to flow through the soil. The increase in run time is especially high for simulations with an infiltration time ($T_{wet,\%}$) lower than 100%. To counter the increase in run time due to the complexity of the wetting and drying process, the converge criteria of the simulation are changed. This slightly reduces the accuracy of the simulation, but also significantly reduces the run time. For practical reasons with respect to time and planning of the research, this compromise was accepted.

D-Stability

The macro-stability, resulting from the phreatic conditions from GeoStudio: Seep/W, was computed using D-Stability by Deltares. This software package is frequently used by Sweco to assess the macro-stability of dikes, which is the main reason it was used for this research. There are some drawbacks to D-Stability, discussed below.

One drawback of D-Stability is the dry-assumption, as elaborated on by Tarantino and Di Donna (2019). Unsaturated soil in the dike is assumed to be completely dry (i.e. $S_r = 0$). With this assumption, the level of effective cohesion caused by negative pore water pressures, elaborated on in Section 2.3, is not considered. The

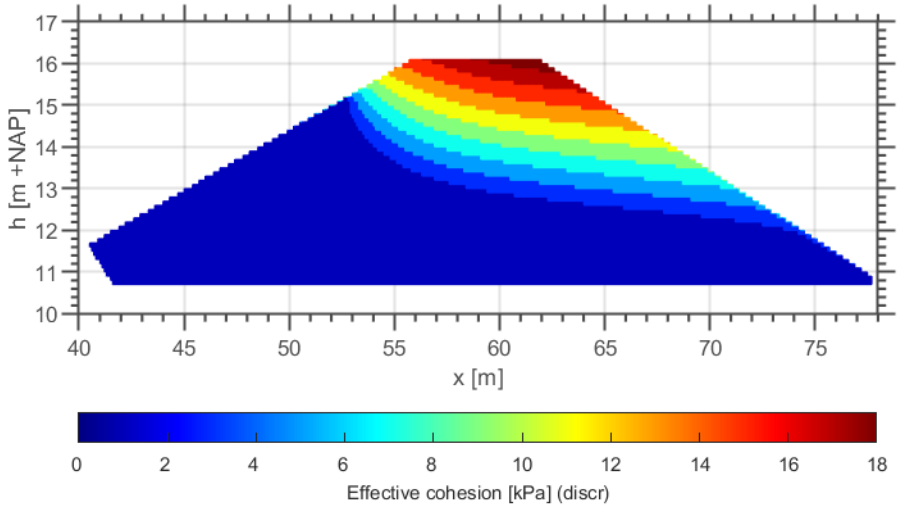

Figure 5.1: Level of effective cohesion, discretised into layers of C_{unsat} = 0, 2, 4, 6, 8, 10, 12, 14, 16 and 18 kPa for the initial condition with material B-4-1.

stabilising forces along the slip circle are therefore underestimated by D-Stability. The phenomenon is however not completely neglected. Safety-factors resulting from D-Stability are calibrated using measurement data from real dike failures. Through this calibration, the forces resulting from the unsaturated zone are indirectly included in the assessment of the safety-factor for macro-stability. Using the method suggested by Tarantino and Di Donna (2019) (i.e. applying an effective cohesion to layers of soil) the effect of the unsaturated zone can be taken into account in D-Stability. The layers with corresponding effective cohesion for the initial condition of material B-4-1, as computed using Equation 2.10 on page 7, are given in Figure 5.1. For the initial condition of material B-4-1, the increase in safety factor when using the method of effective cohesion, is nearly 9% (0.887 to 0.966). The considered condition has a relatively high level of effective cohesion as compared to all simulations done for this research. Also, the effect of the unsaturated zone decreases for higher phreatic lines and for a thicker saturated cover layer, as the unsaturated area decreases and therefore the levels of cohesion decrease as well. Nonetheless, the comparison shows that implementing the unsaturated zone in D-Stability is likely to yield a more accurate estimation of the probability of macro-instability. This method was not applied in the macro-stability assessments for this research.

A second drawback in D-Stability is the inability to manually specify pore water pressures. The way in which D-Stability allows for the implementation of the phreatic line is useful in a 'normal' situation (i.e. phreatic line according to rules of thumb). However, for simulating a saturated cover layer in combination with an unsaturated dike core, the D-Stability software is inconvenient. The method explained in Section 3.5, using several reference lines and head lines, is a reasonable approximation of reality, but is not a direct copy of the water pressures resulting from GeoStudio: Seep/W. Also, this method is inconvenient in practical use.

For these two reasons, it is recommended to repeat the macro-stability assessments using another software package which allows for the implementation of both the unsaturated zone and a saturated cover layer.

This research has focused specifically on the relation between infiltration by wave overtopping and macro-stability. However, as previously mentioned in Section 2.2, the main failure mechanism related to wave overtopping is erosion of the inner slope. This is in line with the results from the macro-stability assessments in D-Stability. These assessments show that the most likely slip plane is a shallow slip plane along the saturated cover layer of the dike. While the main processes of erosion by wave overtopping and macro-stability of the saturated cover layer are different, the small slip circles can be classified as erosion of the inner slope. It should therefore be noted that the increase in probability of failure by macro-stability is not the only increase in probability of failure by wave overtopping.

Limited number of scenarios

The number of scenarios considered for the macro-stability assessment is relatively limited. Due to the manual nature of D-Stability, the setup of these models is time consuming. The four scenarios considered are not sufficient to substantiate any general conclusions. The patterns that are found in the results may indeed be valid for all possible scenarios, but it is far more likely that this is not the case. Examples of factors that may be of influence, that are not considered in the macro-stability assessment are different strength parameters for the main soil or the cover layer soil, a different geometry, a berm or different loading conditions due to for example a road on the dike. As there are many parameters that may influence the macro-stability as a function of the phreatic condition in the dike, a general rule is most likely not applicable. Instead, it is recommended to perform the macro-stability analysis manually, based on estimated phreatic conditions.

Material properties

The translation from the WTI-SOS classification to the classification as used in the Staringsreeks causes uncertainty. Both classifications were introduced for a different purpose and with a different philosophy. The classification for WTI-SOS was made without permeability as a relevant parameter for the distinction between soils. It is therefore not necessarily possible to assign values for water retention and hydraulic conductivity to specific soils within the WTI-SOS classification. For this reason, it is recommended to measure water retention and hydraulic conductivity of the used soil before drawing conclusions.

Relation to literature

This research has shown the effect of infiltration by wave overtopping on the phreatic conditions in the dike. To the best of the authors knowledge, this research is the first attempt at numerically simulating infiltration by wave overtopping on a dike body.

Dutch Ministry of Infrastructure and the Environment (2012) and Spanjersberg (2016) previously set up a method to assess the effect of infiltration by wave overtopping on the height phreatic line. In their method, they assume that all water infiltrating the dike instantly adds to the height of the phreatic line. This research has shown that the increase in the phreatic line is not the most important process. As described in Chapter 4 on page 32, the surface layer of the dike becomes saturated and pore water pressures in the surface layer increase, while the core of the dike remains unsaturated with negative pore water pressures. As described in Section 3.5, a saturated cover layer reduces the stability of the cover layer and increases the probability of small slip circles and of erosion of the inner slope. The probability of macro-instability with larger slip circles also increases with a saturated cover layer, similar to an increase in height of the phreatic line. These results are backed up by Ministerie van Infrastructuur en Milieu (2021), which is a report on the schematisation of the erosion of grass revetments. This report shows similar shapes of the unsaturated zone and of the phreatic line, corresponding to a clay dike and a sand dike, as a result of infiltration by wave overtopping. For a sand dike with a clay cover layer, they give a slightly different shape. Ministerie van Infrastructuur en Milieu (2021) indicate that, for clay dikes, infiltration by wave overtopping causes a decrease in macro-stability and for sand dikes, smaller slip circles and micro-instability are a threat. Finally, they state that for sand dikes with a clay cover layer, the increase in pore water pressures beneath the cover layer may cause the cover layer to be pushed off of the dike body, resulting in micro-instability as the sand in the dike may be flushed out. The latter statement is not in line with the results from this research. In this research, it was found that the water pressures below the cover layer are not higher than those in the cover layer itself.

Proposed method

Following from this research, a method is proposed to include infiltration by wave overtopping in the assessment of the macro-stability of a dike. Using the conclusions from questions **Q1** and **Q2** of the research, an estimation can be made on the time it takes for any dike to reach fully saturated conditions. This can be done by determining the area of the unsaturated zone under initial, steady state, conditions and the estimated average rate of decrease of the unsaturated zone, corresponding to the specific soil type. A comparison between the duration until full saturation and the representative duration of wave overtopping yields an indication on whether or not to take wave overtopping into account in the assessment of macro-stability. Note that this method gives an indication only. Therefore, infiltration by wave overtopping should only be neglected in case the duration until full saturation is much larger than the representative duration of wave overtopping.

The macro-stability assessment should then be performed as usual, with either the standard initial condition or a fully saturated dike. There is currently insufficient evidence to assume a general quantitative rule with respect to phreatic conditions and macro-stability, which means that any intermediate scenario (e.g. half saturation) would yield arbitrary results.

Chapter 6

Conclusions and recommendations

6.1 Conclusions

What phreatic processes are related to water infiltration by wave overtopping and what is their quantitative response to infiltration by wave overtopping?

Simulations were executed in GeoStudio: Seep/W to identify important phreatic processes as a result of infiltration by wave overtopping. From these simulations, it was found that an unsaturated zone appears in the middle of the dike. The unsaturated zone is the part of the dike that is not yet saturated and therefore contains negative pore pressures. With continuing infiltration, the unsaturated zone decreases in size, increasing the overall degree of saturation and increasing the pore water pressures in the dike. This decrease of the unsaturated zone happens either from the top or from the bottom. For soils with relatively low permeability, the water remains in the surface layer of the dike and slowly makes its way downward, decreasing the unsaturated zone in size from the top. This means that the surface layer is saturated before the unsaturated zone has vanished. For soils with a high permeability, the water flows around the unsaturated zone, elevating the phreatic line. In this situation, the unsaturated zone decreases in size from the bottom. The difference between the two possibilities is the resulting effect on the macro-stability, which will be discussed further below. Eventually, an equilibrium situation will be reached, where the infiltrating water is in equilibrium with the water discharging from the toe of the dike. This situation is only reached when the dike body is fully saturated. The quantitative response of the phreatic processes is fully dependent on dike and soil characteristics. Therefore, this will be discussed below.

What parameters are important in the assessment of infiltration by wave overtopping and what is their quantitative effect on phreatic processes in the dike?

A sensitivity analysis was performed to identify the important parameters with respect to estimating the effect of infiltration by wave overtopping. This was done by taking the rate of decrease of the unsaturated area as a representative resulting parameter. From this analysis, it was found that Θ_s, K_s and α have a clear relation to the rate of decrease of the unsaturated area. Soils with a low saturated water content, a high saturated hydraulic conductivity and a low value for α are likely to reach fully saturated conditions the fastest. There is no clear relation between the fitting parameter n and the rate of decrease of the unsaturated area. Standard soil types are classified using these four parameters by Wösten et al. (1987). From these standard classifications, an estimation can be made on the time it takes for the dike to reach fully saturated conditions. Comparing this to the total duration of a storm will allow for an indication whether or not to take wave overtopping into account. The value of the flux boundary condition is of similar importance to the saturated hydraulic conductivity of the soil. The lowest of these two values is the limiting parameter. For example, if the soil is very permeable, but there is barely any water available to infiltrate, then the rate of infiltration will be low. If there is a lot of water available to infiltrate, but the soil is relatively impermeable, then most water will runoff on the surface and the rate of infiltration will be low as well. Under the assumption that there is enough water available for infiltration at all times, the value of the flux boundary condition is not important in the assessment of the rate of decrease of the unsaturated zone. The infiltration time as a percentage of the total time ($T_{wet,\%}$) has a positive linear

relation to the rate of decrease of the unsaturated area. A cover layer has a significant impact on the rate of decrease of the unsaturated area. The resulting rate of decrease for a cover layer of thickness between 0.6 and 1.4 m is similar to the rate of decrease for a complete dike of that material. The additional effect of the thickness of the cover layer decreases for a thickness higher than 1.0 m. The saturated hydraulic conductivity of the cover layer has a similar effect on the rate of decrease of the unsaturated area to the saturated hydraulic conductivity of the soil in case of a uniform cross-section.

Additionally, the effect of a hole in the cover layer and the effect of simulating a complete flood wave were assessed. A hole in the cover layer at the top of the inner slope causes the dike core to fill with water relatively quickly. This raises the height of the phreatic line significantly, increasing the probability of macro-instability. A hole halfway the inner slope has a limited influence on the phreatic conditions in the dike body. A hole at the bottom of the inner slope allows for the water to discharge out of the dike core, decreasing the height of the phreatic line. In theory, this increases the effective stresses in the dike core and therefore decreases the probability of macro-instability. In reality, however, the discharging water will carry soil with it as well. This process is called micro-instability and will eventually cause the dike to fail.

Simulating a full flood wave changes the initial condition of the simulation. A full flood wave was simulated for a dike consisting completely of material K-2-2 (See Table B.1). In previous simulations on the same dike type, the dike reached fully saturated conditions after roughly 6 days. When simulating a full flood wave of 24 days, during which wave overtopping took place for roughly 10 days, the dike never reached the fully saturated condition. This indicates that, theoretically, the previously performed simulations give conservative results, caused by the conservatively chosen initial condition. This is in line with observations by Van de Voort (2019), who showed the uncertainty of the location of the phreatic line over the duration of a flood wave. They obtained similar phreatic lines as a result of a flood wave.

What is the qualitative and quantitative effect of phreatic conditions on macro-stability?

The macro-stability as a result of phreatic conditions was assessed using D-Stability. Phreatic conditions following from a GeoStudio: Seep/W analysis of four scenarios were considered. The assessments were done both with and without using constraints on the size and location of the slip circle. From the assessments including constraints, a correlation was found in the decrease of macro-stability and the decrease of the unsaturated area. As a result of infiltration by wave overtopping, the macro-stability initially decreases relatively quickly, after which the safety factor slowly reaches a minimum at the point where the dike is fully saturated. This pattern was found in all four scenarios considered. The assessments without constraints showed a near instant decrease of the safety factor to its minimum. The reason for this is that small slip circles are formed at the toe of the dike, where the soil is already saturated. These small slip circles can be seen as a form of erosion of the grass cover rather than macro-stability and may not cause the dike to fail.

As there are many parameters in a macro-stability assessment that may be of influence on the safety factor, there is no way of knowing the exact reason for the found pattern with only four scenarios. Also, it is not likely that the found pattern can be assumed valid for all possible dike cross-sections. Instead, it is recommended to manually perform a macro-stability assessment based on estimated phreatic conditions.

6.2 Recommendations

A method is proposed to include infiltration by wave overtopping in the assessment of the macro-stability of a dike. This method provides an indication on whether or not to take infiltration by wave overtopping into account. As no general rule with respect to phreatic conditions and macro-stability is found, the macro-stability assessment should be performed as usual. Infiltration by wave overtopping may then be included by considering a fully saturated dike body.

Recommendations for further research

Important, but unknown, factors in the assessment of infiltration by wave overtopping are the infiltration time and the infiltration rate. In this research, a constant infiltration rate is assumed for a duration of 30 seconds. During these 30 seconds, the infiltration rate is equal to the hydraulic conductivity of the soil and thus independent of layer thickness or flow velocity. From the sensitivity analysis it was found that the hydraulic conductivity of the soil is therefore an important parameter. In reality, the infiltration rate is likely to decrease with decreasing water on the inner slope. More information on the actual infiltration rate over time as a result of an overtopping wave will provide a better assessment of infiltration by wave overtopping.

For future research, it is recommended to invest in the automation of simulations. This may increase the amount of simulations that can be done. An increase in the amount of simulations will allow for the inclusion of more parameters in the sensitivity analysis and a better assessment of the currently included parameters.

The unsaturated zone has its influence on the macro-stability. However, D-Stability does not take into account the effects of the unsaturated zone. For future research, it is beneficial to use a software package that does take the unsaturated zone into account. An example of such software is GeoStudio: Slope/W. This was not used in this research project for practical reasons with respect to licenses and the frequent use of D-Stability within Sweco.

Bibliography

Bishop, A. W. (1955). The use of the Slip Circle in the Stability Analysis of Slopes. *Géotechnique*, 5(1):7–17.

Botterhuis, T., Waterman, R., and Geerse, C. (2017). Gebruikershandleiding Waterstandsverloop: versie 3.0. *Software Manual*.

Chappell, N. A. and Ternan, J. L. (1997). Ring permeametry: design, operation and error analysis. *Earth Surface Processes and Landforms*, 22(13).

Chen, W., van Gent, M. R., Warmink, J. J., and Hulscher, S. J. (2020). The influence of a berm and roughness on the wave overtopping at dikes. *Coastal Engineering*, 156.

Darcy, H. (1856). Les fontaines publiques de la ville de Dijon. *Recherche*.

Das, B. M. (2008). *Advanced Soil Mechanics*, volume 11. Taylor & Francis, New York, third edition.

de Raadt, W. S., Jaspers Focks, D.-j., van Hoven, A., and Regeling, E. (2015). How to Determine the Phreatic Surface in a Dike During Storm Conditions with Wave Overtopping : A Method Applied to the Afsluitdijk. In *Geotechnical Safety and Risk V*.

Deltares (2015). Globale stochastische ondergrondschematisatie (WTI-SOS) voor de primaire waterkeringen. Technical report, Deltares.

Dutch Ministry of Infrastructure and the Environment (2012). Handreiking Toetsen Grasbekledingen op Dijken t.b.v. het opstellen van het beheersoordel (BO) in de verlengde derde toetsronde. Technical report.

EurOtop (2018). Manual on wave overtopping of sea defences and related structures. An overtopping manual largely based on European research, but for worldwide application. Technical report.

HKV (2021). Voorverkenning HWBP Project Spijk-Westervoort. Technical report, HKV Lijn in Water.

IHW (2017). Waterveiligheidsportaal. https://waterveiligheidsportaal.nl/#/nss/nss/norm.

Kok, M., Jongejan, R., Nieuwjaar, M., and Tanczos, I. (2016). *Fundamentals of Flood Protection*. Ministry of Infrastructure and the Environment and the Expertise Network for Flood Protection.

Ltd GEOSLOPE International (2020). *Heat and mass transfer modeling with GeoStudio 2020*. Calgary, Alberta, Canada, first edition.

Ministerie van Infrastructuur en Milieu (2017). Regeling veiligheid primaire waterkeringen 2017: Bijlage III Sterkte en veiligheid. Technical report.

Ministerie van Infrastructuur en Milieu (2021). Schematiseringshandleiding grasbekleding. WBI 2017. Technical report.

Roos, P. C. (2019). *Mathematical Physics of Water Systems*. Universtiy of Twente, Enschede, Netherlands, 11th edition.

Shaw, E. M., Beven, K. J., Chappell, N. A., and Lamb, R. (2017). *Hydrology in practice, fourth edition*.

Spanjersberg, D. (2016). Memo schematisering freatisch vlak bij golfoverslag. Technical report, Deltares.

Spencer, E. (1967). A Method of analysis of the Stability of Embankments Assuming Parallel Inter-Slice Forces. *Géotechnique*, 17(1):11–26.

Tarantino, A. and Di Donna, A. (2019). Mechanics of unsaturated soils: Simple approaches for routine engineering practice. *Rivista Italiana di Geotecnica*, (4):5–46.

TAW (1996). Technisch Rapport Klei Voor Dijken. Technical report.

TAW (2002). Technisch rapport golfoploop en golfoverslag bij dijken. Technical report.

TAW (2004). Technisch Rapport Waterspanningen bij dijken. Technical report.

Van, M. A. (2001). New Approach for Uplift Induced Slope Failure. *Géotechnique*, 5(1):7–17.

van Bergeijk, V. M., Warmink, J. J., and Hulscher, S. J. (2020). Modelling the wave overtopping flow over the crest and the landward slope of grass-covered flood defences. *Journal of Marine Science and Engineering*, 8(7):1–32.

Van de Voort, N. (2019). *How to determine the effects of flood waves on the temporal development of the phreatic line in earth-fill dike bodies.* PhD thesis, University of Twente.

van der Meij, R. (2019). D-Stability: User Manual. Technical report.

van Genuchten, M. T. (1980). A Closed-form Equation for Predicting the Hydraulic Conductivity of Unsaturated Soils.

Visser, M. D. and Jongejan, R. (2018). KPR factsheet Werkwijze macrostabiliteit i.c.m. golfoverslag OI2014v4. Technical Report 2, Kennisplatform Risicobenadering.

Warmink, J. J., van Bergeijk, V. M., Chen, W., and Hulscher, S. J. M. H. (2018). Modelling Wave Overtopping for Flood Defence Reliability. *e-Proc. ICCE 2018, Baltimore, USA*, (June):709745.

Wösten, J., Veerman, G., and Stolte, J. (1994). Waterretentie- en doorlatendheids- karakteristieken van boven en ondergronden in Nederland: de Staringreeks.

Wösten, J. H. M., Bannink, M. H., and Beuving, J. (1987). Waterretentie- en doorlatendheids- karakteristieken van boven en ondergronden in Nederland: de Staringreeks. Technical Report april 1986.

Wösten, J. H. M., Heinen, M., and Bakker, G. (2018). Waterretentie- en doorlatendheids- karakteristieken van boven en ondergronden in Nederland: de Staringreeks. Technical report, Wageningen Environmental Research, Wageningen.

Wösten, J. H. M., Veerman, G., de Groot, W., and Stolte, J. (2001). Waterretentie- en doorlatendheids-karakteristieken van boven en ondergronden in Nederland: de Staringreeks. Technical report.

WRIJ (2019). Eerste beoordeling primaire waterkering dijktraject 48-1. Hoofdrapport. Definitief. Technical report.

Appendices

Appendix A

Model setup in GeoStudio: Seep/W

Figure A.1 shows the numerical grid as used in the GeoStudio: Seep/W simulations. Figure A.2 shows the boundary conditions as applied for the GeoStudio: Seep/W simulations.

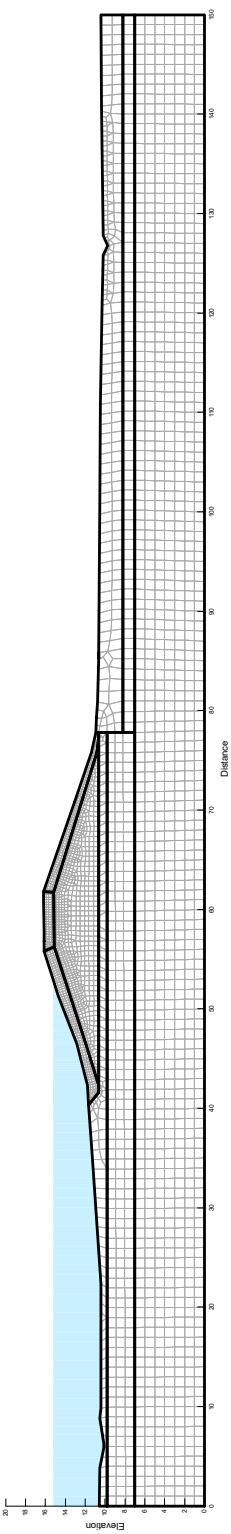

(a)

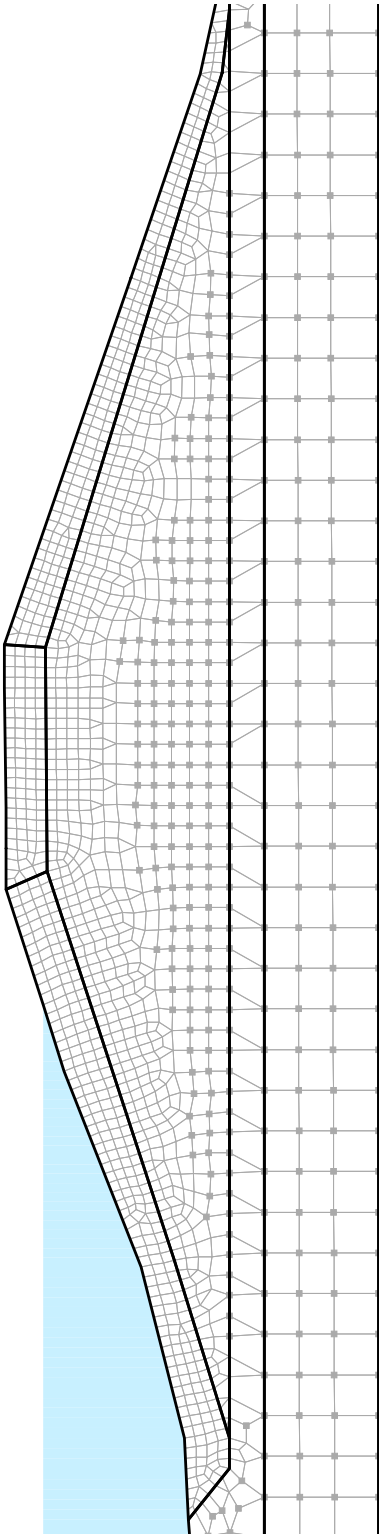

(b)

Figure A.1: Numerical grid of GeoStudio: Seep/W simulations (a), with higher resolution in areas of interest (b).

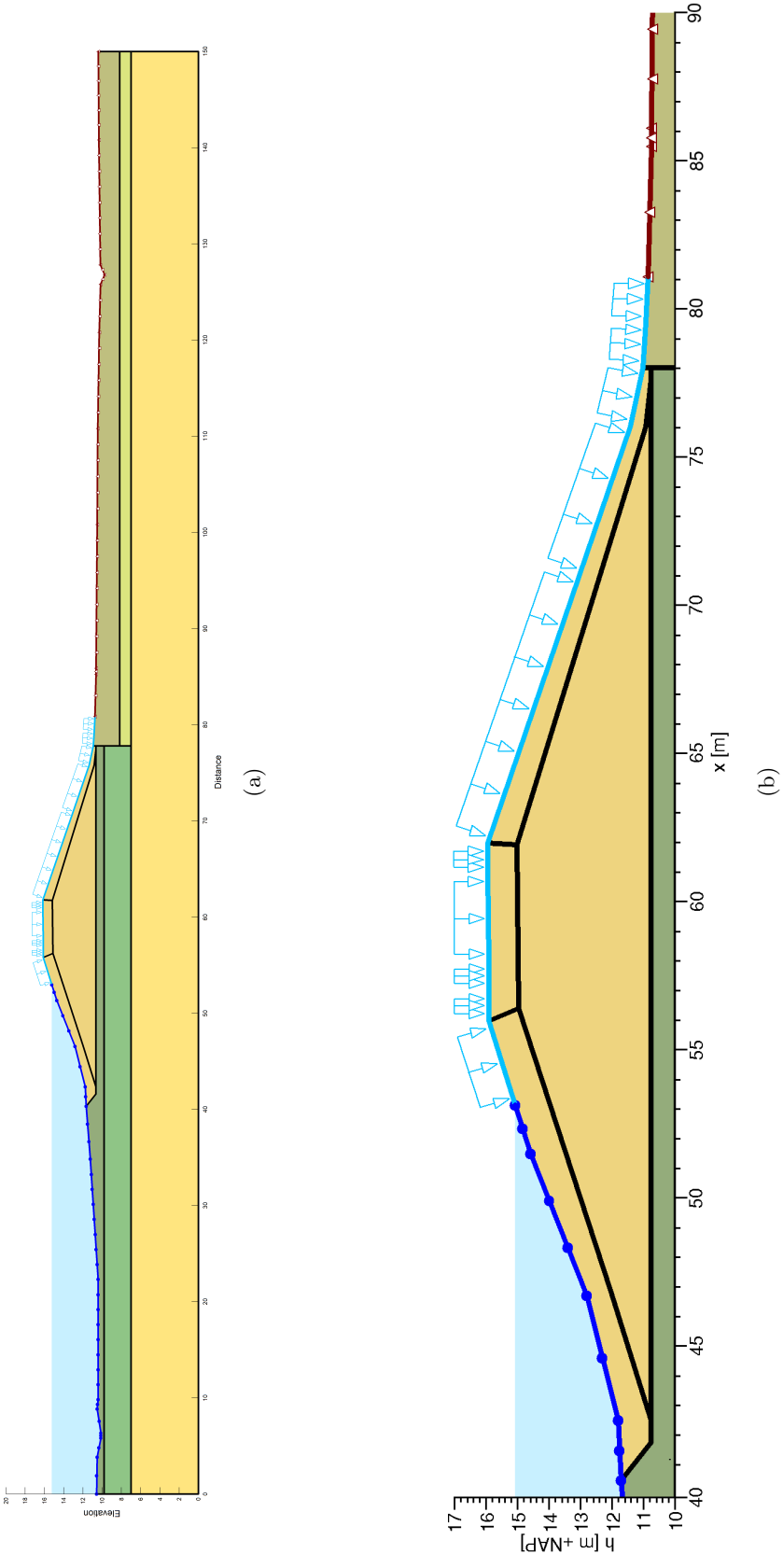

Figure A.2: Model setup for GeoStudio: Seep/W simulations (a), with zoom of areas of interest (b). The dark blue line represents the outside water level boundary condition, the light blue line represents the infiltration by wave overtopping and the red line represents a drainage boundary condition.

Appendix B

Possible scenarios for the sensitivity analysis

This appendix concerns the parameter values used for the sensitivity analysis. Figure B.1 shows histograms of occurrence of the parameter values of the residual water retention (θ_r), the saturated water retention (θ_s), the saturated hydraulic conductivity (K_s) and fitting parameters α and n in the dataset in (Wösten et al., 2018). Based on these histograms, part of the parameter values for the sensitivity analysis are determined. Tables B.1, B.2, B.3 and B.4 show all scenarios considered in the sensitivity analysis, divided into the different sets of simulations, as explained in Chapter 3. Method.

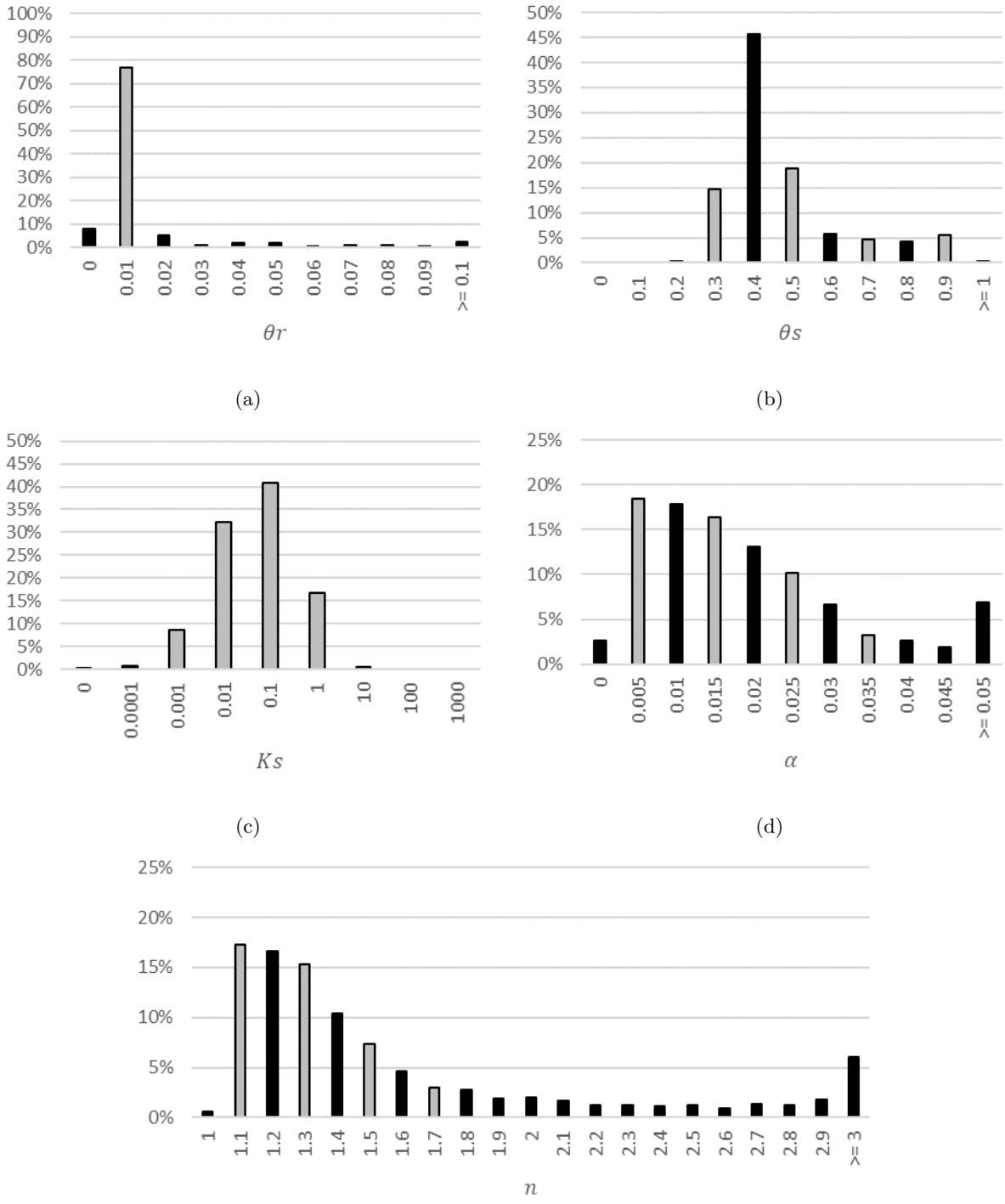

Figure B.1: Histograms of parameter values of θ_r, θ_s, K_s, α and n from the dataset in (Wösten et al., 2018). Grey bars indicate the considered values in the sensitivity analysis.

Scenario	θ_r	θ_s	K_s	α	n	Scenario	θ_r	θ_s	K_s	α	n
A-1-1	0.01	0.3	0.001	0.005	1.1	**A-1-4**	0.01	0.3	1	0.005	1.1
B-1-1	0.01	0.3	0.001	0.005	1.3	**B-1-4**	0.01	0.3	1	0.005	1.3
C-1-1	0.01	0.3	0.001	0.005	1.5	**C-1-4**	0.01	0.3	1	0.005	1.5
D-1-1	0.01	0.3	0.001	0.005	1.7	**D-1-4**	0.01	0.3	1	0.005	1.7
E-1-1	0.01	0.3	0.001	0.015	1.1	**E-1-4**	0.01	0.3	1	0.015	1.1
F-1-1	0.01	0.3	0.001	0.015	1.3	**F-1-4**	0.01	0.3	1	0.015	1.3
G-1-1	0.01	0.3	0.001	0.015	1.5	**G-1-4**	0.01	0.3	1	0.015	1.5
H-1-1	0.01	0.3	0.001	0.015	1.7	**H-1-4**	0.01	0.3	1	0.015	1.7
I-1-1	0.01	0.3	0.001	0.025	1.1	**I-1-4**	0.01	0.3	1	0.025	1.1
J-1-1	0.01	0.3	0.001	0.025	1.3	**J-1-4**	0.01	0.3	1	0.025	1.3
K-1-1	0.01	0.3	0.001	0.025	1.5	**K-1-4**	0.01	0.3	1	0.025	1.5
L-1-1	0.01	0.3	0.001	0.025	1.7	**L-1-4**	0.01	0.3	1	0.025	1.7
M-1-1	0.01	0.3	0.001	0.035	1.1	**M-1-4**	0.01	0.3	1	0.035	1.1
N-1-1	0.01	0.3	0.001	0.035	1.3	**N-1-4**	0.01	0.3	1	0.035	1.3
O-1-1	0.01	0.3	0.001	0.035	1.5	**O-1-4**	0.01	0.3	1	0.035	1.5
P-1-1	0.01	0.3	0.001	0.035	1.7	**P-1-4**	0.01	0.3	1	0.035	1.7
A-1-2	0.01	0.3	0.01	0.005	1.1	**A-2-1**	0.01	0.5	0.001	0.005	1.1
B-1-2	0.01	0.3	0.01	0.005	1.3	**B-2-1**	0.01	0.5	0.001	0.005	1.3
C-1-2	0.01	0.3	0.01	0.005	1.5	**C-2-1**	0.01	0.5	0.001	0.005	1.5
D-1-2	0.01	0.3	0.01	0.005	1.7	**D-2-1**	0.01	0.5	0.001	0.005	1.7
E-1-2	0.01	0.3	0.01	0.015	1.1	**E-2-1**	0.01	0.5	0.001	0.015	1.1
F-1-2	0.01	0.3	0.01	0.015	1.3	**F-2-1**	0.01	0.5	0.001	0.015	1.3
G-1-2	0.01	0.3	0.01	0.015	1.5	**G-2-1**	0.01	0.5	0.001	0.015	1.5
H-1-2	0.01	0.3	0.01	0.015	1.7	**H-2-1**	0.01	0.5	0.001	0.015	1.7
I-1-2	0.01	0.3	0.01	0.025	1.1	**I-2-1**	0.01	0.5	0.001	0.025	1.1
J-1-2	0.01	0.3	0.01	0.025	1.3	**J-2-1**	0.01	0.5	0.001	0.025	1.3
K-1-2	0.01	0.3	0.01	0.025	1.5	**K-2-1**	0.01	0.5	0.001	0.025	1.5
L-1-2	0.01	0.3	0.01	0.025	1.7	**L-2-1**	0.01	0.5	0.001	0.025	1.7
M-1-2	0.01	0.3	0.01	0.035	1.1	**M-2-1**	0.01	0.5	0.001	0.035	1.1
N-1-2	0.01	0.3	0.01	0.035	1.3	**N-2-1**	0.01	0.5	0.001	0.035	1.3
O-1-2	0.01	0.3	0.01	0.035	1.5	**O-2-1**	0.01	0.5	0.001	0.035	1.5
P-1-2	0.01	0.3	0.01	0.035	1.7	**P-2-1**	0.01	0.5	0.001	0.035	1.7
A-1-3	0.01	0.3	0.1	0.005	1.1	**A-2-2**	0.01	0.5	0.01	0.005	1.1
B-1-3	0.01	0.3	0.1	0.005	1.3	**B-2-2**	0.01	0.5	0.01	0.005	1.3
C-1-3	0.01	0.3	0.1	0.005	1.5	**C-2-2**	0.01	0.5	0.01	0.005	1.5
D-1-3	0.01	0.3	0.1	0.005	1.7	**D-2-2**	0.01	0.5	0.01	0.005	1.7
E-1-3	0.01	0.3	0.1	0.015	1.1	**E-2-2**	0.01	0.5	0.01	0.015	1.1
F-1-3	0.01	0.3	0.1	0.015	1.3	**F-2-2**	0.01	0.5	0.01	0.015	1.3
G-1-3	0.01	0.3	0.1	0.015	1.5	**G-2-2**	0.01	0.5	0.01	0.015	1.5
H-1-3	0.01	0.3	0.1	0.015	1.7	**H-2-2**	0.01	0.5	0.01	0.015	1.7
I-1-3	0.01	0.3	0.1	0.025	1.1	**I-2-2**	0.01	0.5	0.01	0.025	1.1
J-1-3	0.01	0.3	0.1	0.025	1.3	**J-2-2**	0.01	0.5	0.01	0.025	1.3
K-1-3	0.01	0.3	0.1	0.025	1.5	**K-2-2**	0.01	0.5	0.01	0.025	1.5
L-1-3	0.01	0.3	0.1	0.025	1.7	**L-2-2**	0.01	0.5	0.01	0.025	1.7
M-1-3	0.01	0.3	0.1	0.035	1.1	**M-2-2**	0.01	0.5	0.01	0.035	1.1
N-1-3	0.01	0.3	0.1	0.035	1.3	**N-2-2**	0.01	0.5	0.01	0.035	1.3
O-1-3	0.01	0.3	0.1	0.035	1.5	**O-2-2**	0.01	0.5	0.01	0.035	1.5
P-1-3	0.01	0.3	0.1	0.035	1.7	**P-2-2**	0.01	0.5	0.01	0.035	1.7

Table B.1: All simulated materials with corresponding material properties.

Scenario	θ_r	θ_s	K_s	α	n	Scenario	θ_r	θ_s	K_s	α	n
A-2-3	0.01	0.5	0.1	0.005	1.1	**A-3-2**	0.01	0.7	0.01	0.005	1.1
B-2-3	0.01	0.5	0.1	0.005	1.3	**B-3-2**	0.01	0.7	0.01	0.005	1.3
C-2-3	0.01	0.5	0.1	0.005	1.5	**C-3-2**	0.01	0.7	0.01	0.005	1.5
D-2-3	0.01	0.5	0.1	0.005	1.7	**D-3-2**	0.01	0.7	0.01	0.005	1.7
E-2-3	0.01	0.5	0.1	0.015	1.1	**E-3-2**	0.01	0.7	0.01	0.015	1.1
F-2-3	0.01	0.5	0.1	0.015	1.3	**F-3-2**	0.01	0.7	0.01	0.015	1.3
G-2-3	0.01	0.5	0.1	0.015	1.5	**G-3-2**	0.01	0.7	0.01	0.015	1.5
H-2-3	0.01	0.5	0.1	0.015	1.7	**H-3-2**	0.01	0.7	0.01	0.015	1.7
I-2-3	0.01	0.5	0.1	0.025	1.1	**I-3-2**	0.01	0.7	0.01	0.025	1.1
J-2-3	0.01	0.5	0.1	0.025	1.3	**J-3-2**	0.01	0.7	0.01	0.025	1.3
K-2-3	0.01	0.5	0.1	0.025	1.5	**K-3-2**	0.01	0.7	0.01	0.025	1.5
L-2-3	0.01	0.5	0.1	0.025	1.7	**L-3-2**	0.01	0.7	0.01	0.025	1.7
M-2-3	0.01	0.5	0.1	0.035	1.1	**M-3-2**	0.01	0.7	0.01	0.035	1.1
N-2-3	0.01	0.5	0.1	0.035	1.3	**N-3-2**	0.01	0.7	0.01	0.035	1.3
O-2-3	0.01	0.5	0.1	0.035	1.5	**O-3-2**	0.01	0.7	0.01	0.035	1.5
P-2-3	0.01	0.5	0.1	0.035	1.7	**P-3-2**	0.01	0.7	0.01	0.035	1.7
A-2-4	0.01	0.5	1	0.005	1.1	**A-3-3**	0.01	0.7	0.1	0.005	1.1
B-2-4	0.01	0.5	1	0.005	1.3	**B-3-3**	0.01	0.7	0.1	0.005	1.3
C-2-4	0.01	0.5	1	0.005	1.5	**C-3-3**	0.01	0.7	0.1	0.005	1.5
D-2-4	0.01	0.5	1	0.005	1.7	**D-3-3**	0.01	0.7	0.1	0.005	1.7
E-2-4	0.01	0.5	1	0.015	1.1	**E-3-3**	0.01	0.7	0.1	0.015	1.1
F-2-4	0.01	0.5	1	0.015	1.3	**F-3-3**	0.01	0.7	0.1	0.015	1.3
G-2-4	0.01	0.5	1	0.015	1.5	**G-3-3**	0.01	0.7	0.1	0.015	1.5
H-2-4	0.01	0.5	1	0.015	1.7	**H-3-3**	0.01	0.7	0.1	0.015	1.7
I-2-4	0.01	0.5	1	0.025	1.1	**I-3-3**	0.01	0.7	0.1	0.025	1.1
J-2-4	0.01	0.5	1	0.025	1.3	**J-3-3**	0.01	0.7	0.1	0.025	1.3
K-2-4	0.01	0.5	1	0.025	1.5	**K-3-3**	0.01	0.7	0.1	0.025	1.5
L-2-4	0.01	0.5	1	0.025	1.7	**L-3-3**	0.01	0.7	0.1	0.025	1.7
M-2-4	0.01	0.5	1	0.035	1.1	**M-3-3**	0.01	0.7	0.1	0.035	1.1
N-2-4	0.01	0.5	1	0.035	1.3	**N-3-3**	0.01	0.7	0.1	0.035	1.3
O-2-4	0.01	0.5	1	0.035	1.5	**O-3-3**	0.01	0.7	0.1	0.035	1.5
P-2-4	0.01	0.5	1	0.035	1.7	**P-3-3**	0.01	0.7	0.1	0.035	1.7
A-3-1	0.01	0.7	0.001	0.005	1.1	**A-3-4**	0.01	0.7	1	0.005	1.1
B-3-1	0.01	0.7	0.001	0.005	1.3	**B-3-4**	0.01	0.7	1	0.005	1.3
C-3-1	0.01	0.7	0.001	0.005	1.5	**C-3-4**	0.01	0.7	1	0.005	1.5
D-3-1	0.01	0.7	0.001	0.005	1.7	**D-3-4**	0.01	0.7	1	0.005	1.7
E-3-1	0.01	0.7	0.001	0.015	1.1	**E-3-4**	0.01	0.7	1	0.015	1.1
F-3-1	0.01	0.7	0.001	0.015	1.3	**F-3-4**	0.01	0.7	1	0.015	1.3
G-3-1	0.01	0.7	0.001	0.015	1.5	**G-3-4**	0.01	0.7	1	0.015	1.5
H-3-1	0.01	0.7	0.001	0.015	1.7	**H-3-4**	0.01	0.7	1	0.015	1.7
I-3-1	0.01	0.7	0.001	0.025	1.1	**I-3-4**	0.01	0.7	1	0.025	1.1
J-3-1	0.01	0.7	0.001	0.025	1.3	**J-3-4**	0.01	0.7	1	0.025	1.3
K-3-1	0.01	0.7	0.001	0.025	1.5	**K-3-4**	0.01	0.7	1	0.025	1.5
L-3-1	0.01	0.7	0.001	0.025	1.7	**L-3-4**	0.01	0.7	1	0.025	1.7
M-3-1	0.01	0.7	0.001	0.035	1.1	**M-3-4**	0.01	0.7	1	0.035	1.1
N-3-1	0.01	0.7	0.001	0.035	1.3	**N-3-4**	0.01	0.7	1	0.035	1.3
O-3-1	0.01	0.7	0.001	0.035	1.5	**O-3-4**	0.01	0.7	1	0.035	1.5
P-3-1	0.01	0.7	0.001	0.035	1.7	**P-3-4**	0.01	0.7	1	0.035	1.7

Table B.1: All simulated materials with corresponding material properties. (Continued)

Scenario	θ_r	θ_s	K_s	α	n	Scenario	θ_r	θ_s	K_s	α	n
A-4-1	0.01	0.9	0.001	0.005	1.1	**A-4-3**	0.01	0.9	0.1	0.005	1.1
B-4-1	0.01	0.9	0.001	0.005	1.3	**B-4-3**	0.01	0.9	0.1	0.005	1.3
C-4-1	0.01	0.9	0.001	0.005	1.5	**C-4-3**	0.01	0.9	0.1	0.005	1.5
D-4-1	0.01	0.9	0.001	0.005	1.7	**D-4-3**	0.01	0.9	0.1	0.005	1.7
E-4-1	0.01	0.9	0.001	0.015	1.1	**E-4-3**	0.01	0.9	0.1	0.015	1.1
F-4-1	0.01	0.9	0.001	0.015	1.3	**F-4-3**	0.01	0.9	0.1	0.015	1.3
G-4-1	0.01	0.9	0.001	0.015	1.5	**G-4-3**	0.01	0.9	0.1	0.015	1.5
H-4-1	0.01	0.9	0.001	0.015	1.7	**H-4-3**	0.01	0.9	0.1	0.015	1.7
I-4-1	0.01	0.9	0.001	0.025	1.1	**I-4-3**	0.01	0.9	0.1	0.025	1.1
J-4-1	0.01	0.9	0.001	0.025	1.3	**J-4-3**	0.01	0.9	0.1	0.025	1.3
K-4-1	0.01	0.9	0.001	0.025	1.5	**K-4-3**	0.01	0.9	0.1	0.025	1.5
L-4-1	0.01	0.9	0.001	0.025	1.7	**L-4-3**	0.01	0.9	0.1	0.025	1.7
M-4-1	0.01	0.9	0.001	0.035	1.1	**M-4-3**	0.01	0.9	0.1	0.035	1.1
N-4-1	0.01	0.9	0.001	0.035	1.3	**N-4-3**	0.01	0.9	0.1	0.035	1.3
O-4-1	0.01	0.9	0.001	0.035	1.5	**O-4-3**	0.01	0.9	0.1	0.035	1.5
P-4-1	0.01	0.9	0.001	0.035	1.7	**P-4-3**	0.01	0.9	0.1	0.035	1.7
A-4-2	0.01	0.9	0.01	0.005	1.1	**A-4-4**	0.01	0.9	1	0.005	1.1
B-4-2	0.01	0.9	0.01	0.005	1.3	**B-4-4**	0.01	0.9	1	0.005	1.3
C-4-2	0.01	0.9	0.01	0.005	1.5	**C-4-4**	0.01	0.9	1	0.005	1.5
D-4-2	0.01	0.9	0.01	0.005	1.7	**D-4-4**	0.01	0.9	1	0.005	1.7
E-4-2	0.01	0.9	0.01	0.015	1.1	**E-4-4**	0.01	0.9	1	0.015	1.1
F-4-2	0.01	0.9	0.01	0.015	1.3	**F-4-4**	0.01	0.9	1	0.015	1.3
G-4-2	0.01	0.9	0.01	0.015	1.5	**G-4-4**	0.01	0.9	1	0.015	1.5
H-4-2	0.01	0.9	0.01	0.015	1.7	**H-4-4**	0.01	0.9	1	0.015	1.7
I-4-2	0.01	0.9	0.01	0.025	1.1	**I-4-4**	0.01	0.9	1	0.025	1.1
J-4-2	0.01	0.9	0.01	0.025	1.3	**J-4-4**	0.01	0.9	1	0.025	1.3
K-4-2	0.01	0.9	0.01	0.025	1.5	**K-4-4**	0.01	0.9	1	0.025	1.5
L-4-2	0.01	0.9	0.01	0.025	1.7	**L-4-4**	0.01	0.9	1	0.025	1.7
M-4-2	0.01	0.9	0.01	0.035	1.1	**M-4-4**	0.01	0.9	1	0.035	1.1
N-4-2	0.01	0.9	0.01	0.035	1.3	**N-4-4**	0.01	0.9	1	0.035	1.3
O-4-2	0.01	0.9	0.01	0.035	1.5	**O-4-4**	0.01	0.9	1	0.035	1.5
P-4-2	0.01	0.9	0.01	0.035	1.7	**P-4-4**	0.01	0.9	1	0.035	1.7

Table B.1: All simulated materials with corresponding material properties. (Continued)

Scenario	K_s	Flux
1	0.001	0.001
2	0.001	0.01
3	0.001	0.1
4	0.001	1
5	0.01	0.001
6	0.01	0.01
7	0.01	0.1
8	0.01	1
9	0.1	0.001
10	0.1	0.01
11	0.1	0.1
12	0.1	1
13	1	0.001
14	1	0.01
15	1	0.1
16	1	1

Table B.2: Simulated scenarios in set 2 with corresponding parameter values.

Scenario	K_s	$T_{wet,\%}$
1	0.001	25
2	0.001	50
3	0.001	75
4	0.001	100
5	0.01	25
6	0.01	50
7	0.01	75
8	0.01	100
9	0.1	25
10	0.1	50
11	0.1	75
12	0.1	100
13	1	25
14	1	50
15	1	75
16	1	100

Table B.3: Simulated scenarios in set 3 with corresponding parameter values.

Scenario	D_{cl}	$K_{s,cl}$
1	0.6	0.001
2	0.6	0.01
3	0.6	0.1
4	0.6	1
5	0.8	0.001
6	0.8	0.01
7	0.8	0.1
8	0.8	1
9	1.0	0.001
10	1.0	0.01
11	1.0	0.1
12	1.0	1
13	1.2	0.001
14	1.2	0.01
15	1.2	0.1
16	1.2	1
17	1.4	0.001
18	1.4	0.01
19	1.4	0.1
20	1.4	1

Table B.4: Simulated scenarios in set 4 with corresponding parameter values.

Appendix C

D-Stability model setup

Figure C.1 shows the subsoil and soil classification as used in the GeoStudio: Seep/W simulations and the D-Stability assessments.

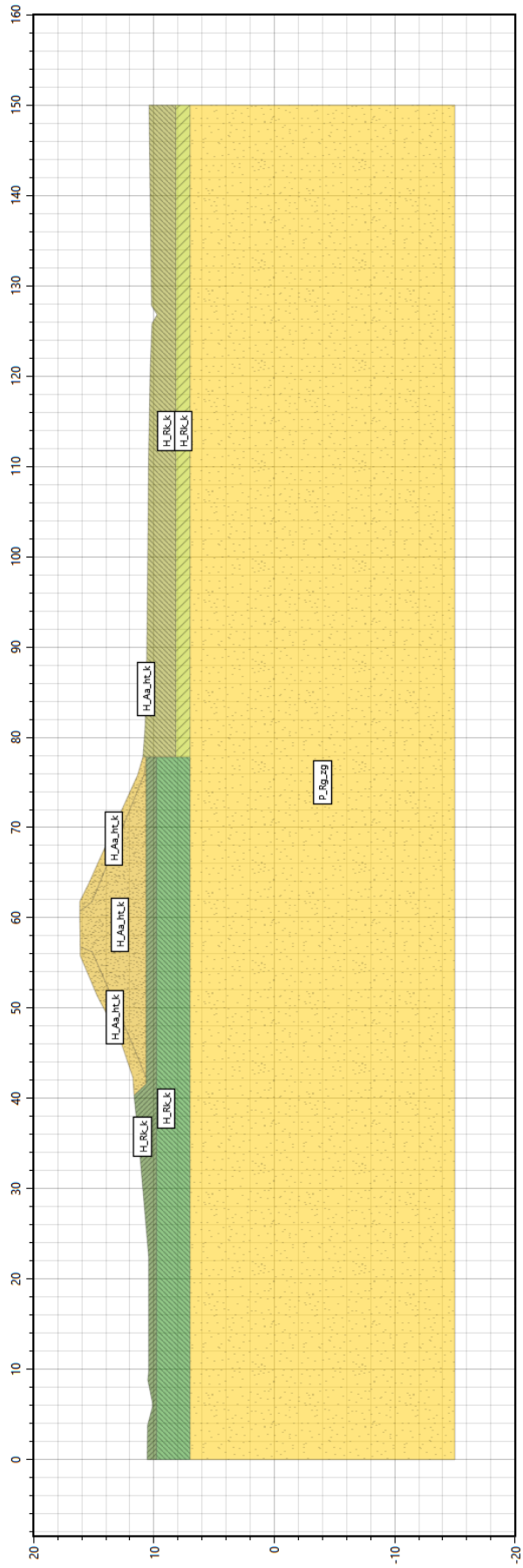

Figure C.1: Model geometry and materials of dike cross-section in D-Stability.

Appendix D

Practische Toepassing

This appendix gives a short summary of the research and describes the proposed method of implementation in Dutch for future use by the colleagues at Sweco.

In het onderzoek is onderzocht hoe infiltrerend water in de dijk zich gedraagt. Door het infiltrerende water ontstaat er een ovaalgevormde onverzadigde zone in de dijk. In deze zone zijn de waterspanningen negatief. Deze onverzadigde zone neemt af in formaat door infiltratie door golfoverslag. Bij hoog doorlatende grondsoorten zakt het water direct naar de freatische lijn, die daardoor stijgt. Bij minder doorlatende grondsoorten blijft het water hangen in de toplaag van de dijk, die daardoor verzadigd raakt. De onverzadigde zone krimpt in dit geval vanaf bovenaf.

Daarnaast is gekeken naar relevante parameters voor de snelheid waarmee de onverzadigde zone krimpt. Belangrijke grondparameters zijn de verzadigde hydraulische conductiviteit, de verzadigde water retentie en de waarde α, welke een fit-parameter is voor de formules voor hydraulische conductiviteit en water retentie, opgesteld door van Genuchten (1980). Deze drie waardes hebben een duidelijk verband met de snelheid waarmee de onverzadigde zone krimpt. Op basis van deze drie waardes kan dus een groffe inschatting gemaakt worden van deze snelheid.

Ten slotte is gekeken naar het effect van de freatische condities door golfoverslag op de macro-stabiliteit van de dijk. Op dit gebied zijn bijzonder veel parameters die invloed hebben op de macro-stabiliteit. Om die reden is er momenteel onvoldoende zekerheid om een algemene, kwantitatieve, regel op te stellen. De macro-stabiliteit zal dus voor elke dijkdoorsnede apart berekend moeten worden.

De conclusies van het onderzoek kunnen in de praktijk worden samengevat in het volgende stappenplan:

1. Vertalen van grondsoorten SOS naar grondsoorten Wösten et al. (1987).
   Hiermee zijn de van Genuchten (1980) grondparameters in te schatten. Voor deze standaard grondsoorten is een gemiddelde afname van de onverzadigde zone bepaald (gegeven in Tabellen 3.3 en 3.4). Als de dijk uit meerdere grondsoorten bestaat, is met name de deklaag van belang.

2. Bepalen/inschatten tijd tot volledige verzadiging dijkdoorsnede.
   Dit kan op basis van de gemiddelde afname van de onverzadigde zone en het initiele oppervlakte van de onverzadigde zone.

3. Bepalen/inschatten maatgevende duur golfoverslag.
   Voor verschillende soorten dijken worden hier verschillende waardes gebruikt. Voor het inschatten van de erosie van het binnentalud wordt een representatieve duur van golfoverslag van 5 uur aangehouden voor rivierdijken (Ministerie van Infrastructuur en Milieu, 2021). Voor zeedijken wordt 3 uur aangehouden.

4. Vergelijken van tijd tot volledige verzadiging dijkdoorsnede en maatgevende duur golfoverslag.
   Wanneer de tijd tot volledige verzadiging korter is dan de maatgevende duur van golfoverslag, moet rekening gehouden worden met een volledig verzadigde dijk.
   Wanneer de tijd tot volledige verzadiging (veel) langer is dan de maatgevende duur van golfoverslag kan de standaard phreatische lijn worden gebruikt. Een tussenvorm in de freatische condities wordt afgeraden, omdat er momenteel onvoldoende zekerheid is om een algemene kwantitatieve regel op te stellen, wat betekent dat een tussenvorm arbitraire resultaten zou opleveren. Anderzijds kan er een grondwatermodel worden opgezet zoals gebruikt voor dit onderzoek, om een betere inschatting te kunnen maken van de freatische condities.

Appendix E

Average rate of decrease of the unsaturated area for standard materials.

This appendix provides the average rate of decrease of the unsaturated area in m^2/s based on the simulations in GeoStudio: Seep/W. These tables are the same as Tables 3.3 and 3.4, but include the value for dA/dt.

Material code	Description	Θ_r	Θ_s	K_s	α	n	dA/dt
Sand		$[m^3/m^3]$	$[m^3/m^3]$	$[m/d]$	$[-]$	$[-]$	$[m^2/h]$
B01	Lower peat, very fine to fairly fine sand	0.02	0.428	0.312	0.022	1.734	26.61
B02	Fairly peaty, very fine to fairly fine sand	0.02	0.434	0.832	0.022	1.349	41.35
B03	Very peaty, very fine to fairly fine sand	0.02	0.443	0.191	0.015	1.505	21.51
B04	Heavily peaty, very fine to fairly fine sand	0.02	0.462	0.349	0.015	1.397	32.79
B05	Coarse sand	0.01	0.381	0.637	0.043	1.808	17.31
B06	Clayey loam	0.01	0.385	1.041	0.021	1.242	52.86
Sabulous clay							
B07	Very light sabulous clay	0.00	0.401	0.146	0.018	1.248	9.41
B08	Fairly light sabulous clay	0.01	0.433	0.030	0.010	1.278	3.14
B09	Heavy sabulous clay	0	0.430	0.017	0.007	1.267	2.81
Clay							
B10	Light clay	0.01	0.448	0.038	0.013	1.135	2.14
B11	Fairly heavy clay	0.01	0.591	0.063	0.022	1.107	1.53
B12	Very heavy clay	0.01	0.530	0.022	0.017	1.091	0.65
Loam							
B13	Sandy loam	0.01	0.416	0.298	0.008	1.437	77.09
B14	Silty loam	0.01	0.417	0.009	0.005	1.302	2.03
"Moerig"							
B15	Peaty sand	0.01	0.528	0.875	0.024	1.282	30.5
B16	Sandy peat and peat	0.01	0.786	0.124	0.021	1.279	3.49
B17	Peaty clay	0	0.719	0.045	0.019	1.137	1.11
B18	Clayey peat	0	0.765	0.131	0.020	1.151	3.22

Table E.1: Classifications of above surface (Bovengronds) soil types with corresponding descriptions as classified by Wösten et al. (1987) and rate of decrease of the unsaturated area.

Material code	Description	Θ_r	Θ_s	K_s	α	n	dA/dt
Sand		$[m^3/m^3]$	$[m^3/m^3]$	$[m/d]$	$[-]$	$[-]$	$[m^2/h]$
O01	Lower peat, very fine to fairly fine sand	0.01	0.366	0.223	0.016	2.163	55.8
O02	Fairly peaty, very fine to fairly fine sand	0.02	0.387	0.228	0.016	1.524	28.85
O03	Very peaty, very fine to fairly fine sand	0.01	0.340	0.124	0.017	1.703	17.6
O04	Heavily peaty, very fine to fairly fine sand	0.01	0.364	0.258	0.014	1.488	37.74
O05	Coarse sand	0.01	0.337	0.174	0.030	2.888	13.12
O06	Clayey loam	0.01	0.333	0.328	0.016	1.289	33.14
O07	"Beekleem"	0.01	0.513	0.376	0.012	1.153	26.87
Sabulous clay							
O08	Very light sabulous clay	0	0.454	0.086	0.011	1.346	10.06
O09	Fairly light sabulous clay	0	0.458	0.038	0.010	1.376	4.87
O10	Heavy sabulous clay	0.01	0.472	0.023	0.010	1.246	2.02
Clay							
O11	Light clay	0	0.444	0.021	0.014	1.126	0.95
O12	Fairly heavy clay	0.01	0.561	0.011	0.009	1.158	0.69
O13	Very heavy clay	0.01	0.573	0.097	0.028	1.080	1.5
Loam							
O14	Sandy loam	0.01	0.394	0.025	0.003	1.617	18.64
O15	Silty loam	0.01	0.410	0.028	0.008	1.287	4.8
Peat							
O16	Oligotrophic peat	0	0.889	0.015	0.010	1.364	0.87
O17	Mesotrophic and Eutrophic peat	0.01	0.849	0.034	0.012	1.272	1.52
O18	"Moerige tussenlaag"	0.01	0.580	0.360	0.013	1.316	30.48

Table E.2: Classifications of below surface (Ondergronds) soil types with corresponding descriptions as classified by Wösten et al. (1987) and rate of decrease of the unsaturated area.

Appendix F

Area of unsaturated zone over time for each simulation

This appendix includes a figure which shows the area of the unsaturated zone over time for each of the simulations performed for this study.

F.1 Simulation set 1

This section shows the area of the unsaturated zone over time for each of the simulations performed in set 1. The parameter values corresponding to each simulation are given in Table B.1.

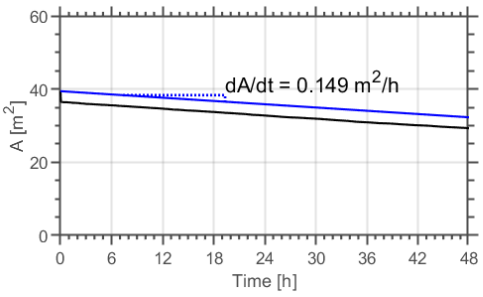

Figure F.1: A(t) of material A-1-1.

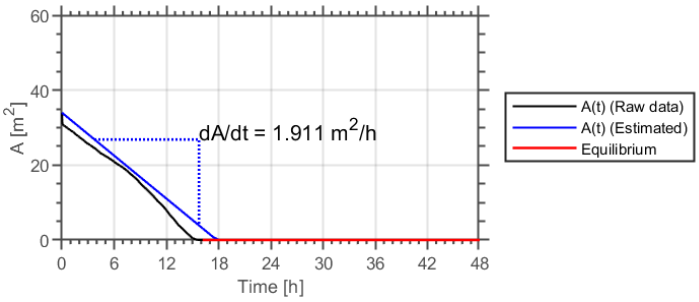

Figure F.2: A(t) of material A-1-2 (see Table B.1).

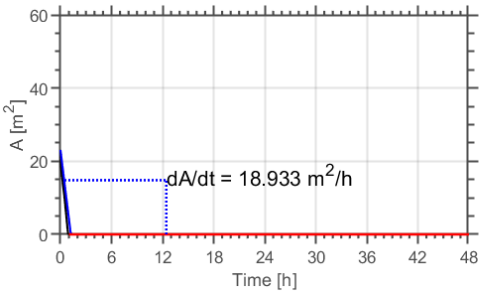

Figure F.3: A(t) of material A-1-3.

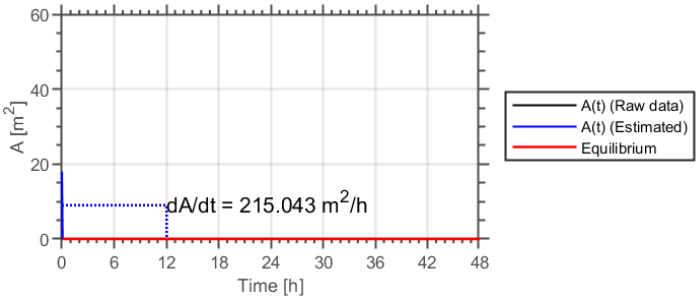

Figure F.4: A(t) of material A-1-4 (see Table B.1).

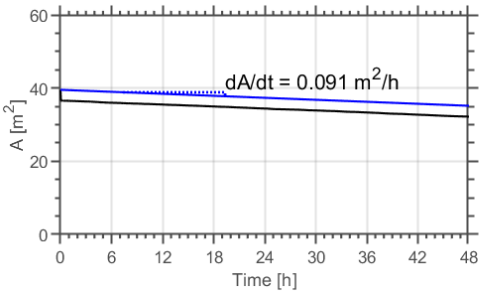

Figure F.5: A(t) of material A-2-1.

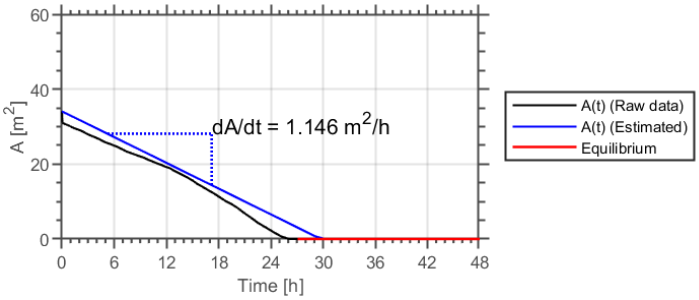

Figure F.6: A(t) of material A-2-2 (see Table B.1).

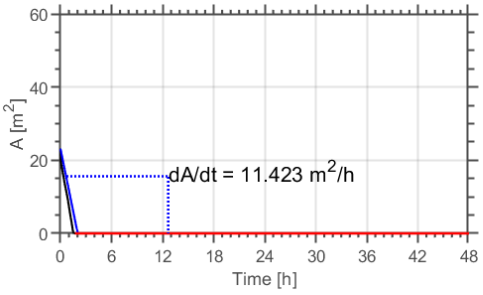

Figure F.7: A(t) of material A-2-3.

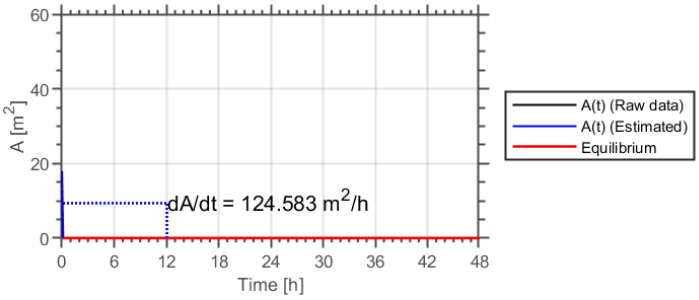

Figure F.8: A(t) of material A-2-4 (see Table B.1).

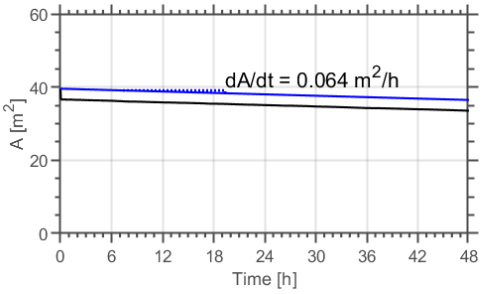

Figure F.9: A(t) of material A-3-1.

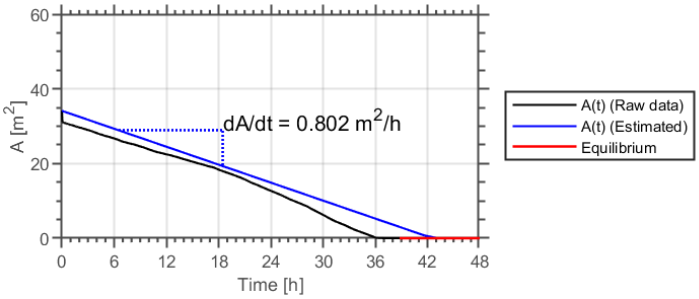

Figure F.10: A(t) of material A-3-2 (see Table B.1).

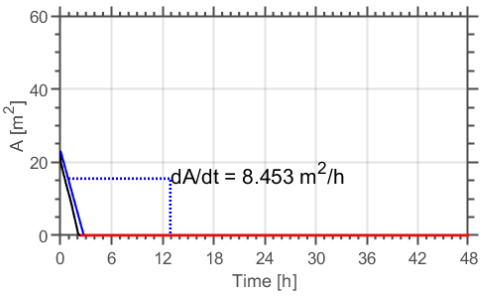

Figure F.11: A(t) of material A-3-3.

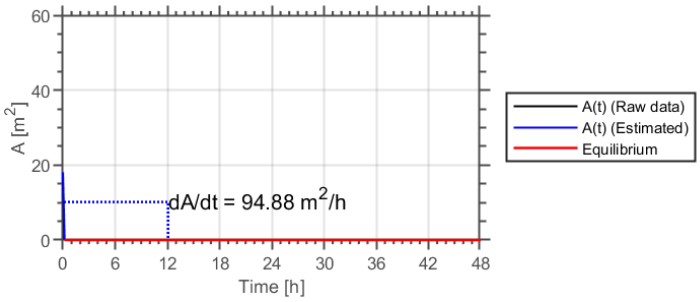

Figure F.12: A(t) of material A-3-4 (see Table B.1).

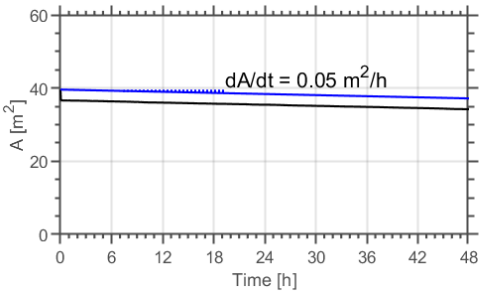

Figure F.13: A(t) of material A-4-1.

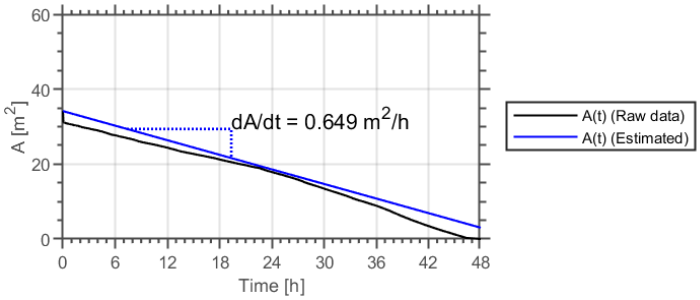

Figure F.14: A(t) of material A-4-2 (see Table B.1).

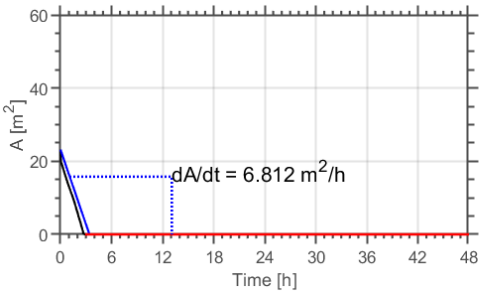

Figure F.15: A(t) of material A-4-3.

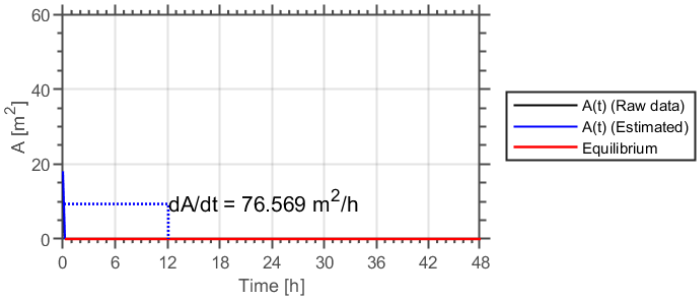

Figure F.16: A(t) of material A-4-4 (see Table B.1).

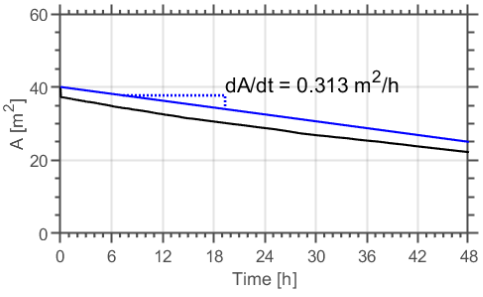

Figure F.17: A(t) of material B-1-1.

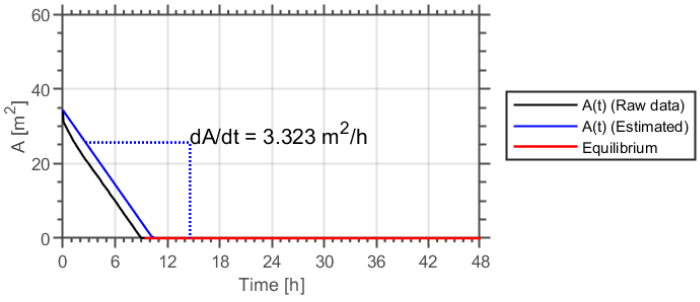

Figure F.18: A(t) of material B-1-2 (see Table B.1).

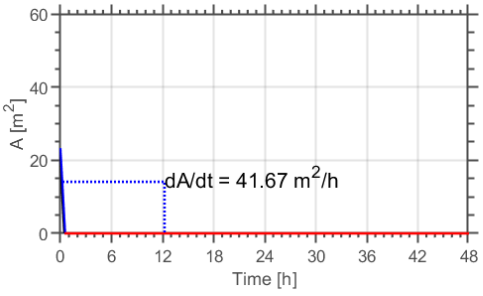

Figure F.19: A(t) of material B-1-3.

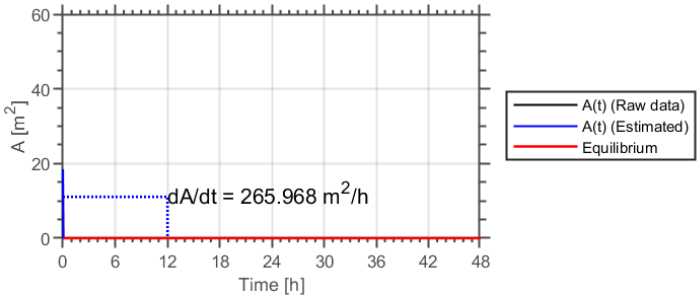

Figure F.20: A(t) of material B-1-4 (see Table B.1).

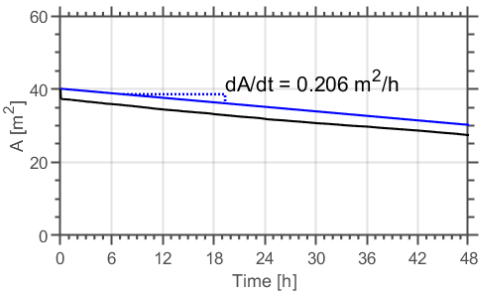

Figure F.21: A(t) of material B-2-1.

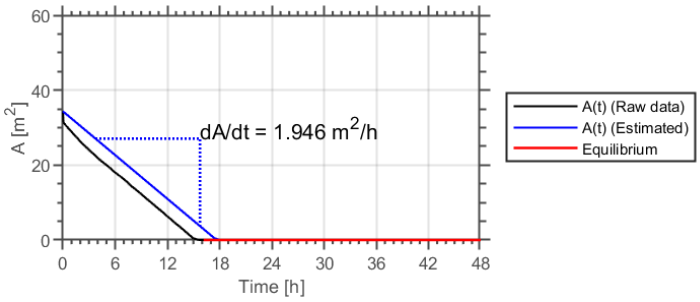

Figure F.22: A(t) of material B-2-2 (see Table B.1).

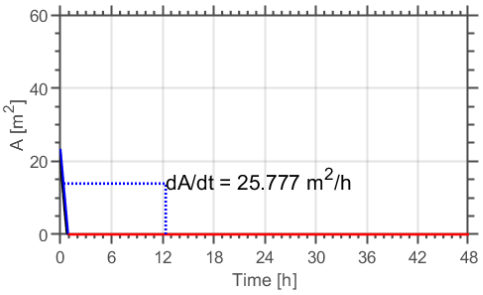

Figure F.23: A(t) of material B-2-3.

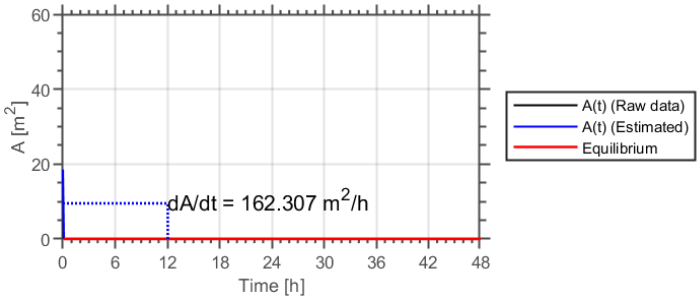

Figure F.24: A(t) of material B-2-4 (see Table B.1).

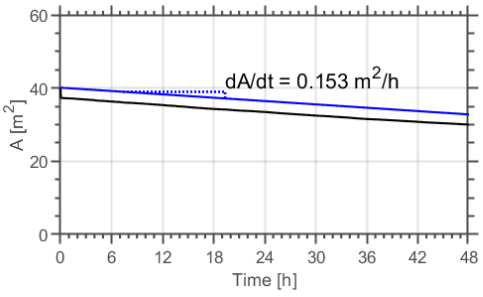

Figure F.25: A(t) of material B-3-1.

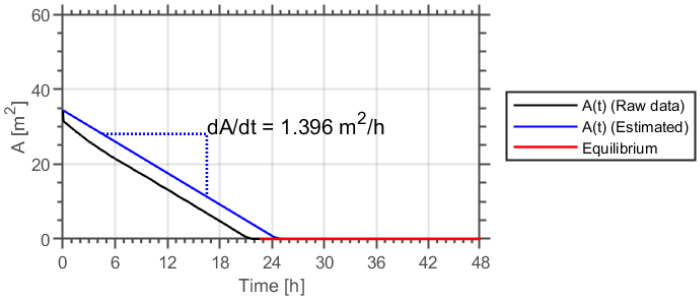

Figure F.26: A(t) of material B-3-2 (see Table B.1).

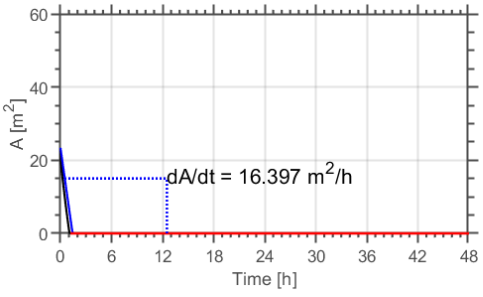

Figure F.27: A(t) of material B-3-3.

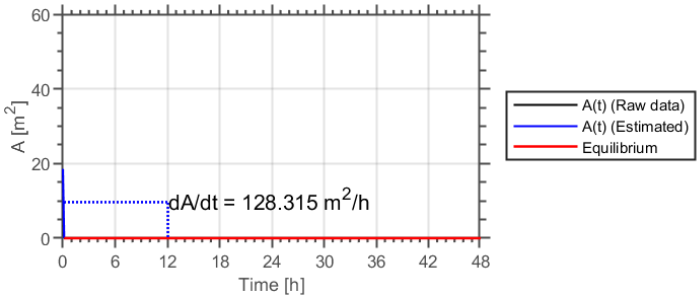

Figure F.28: A(t) of material B-3-4 (see Table B.1).

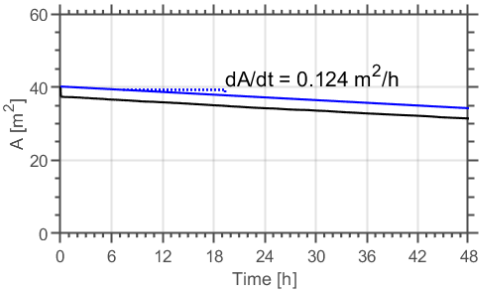

Figure F.29: A(t) of material B-4-1.

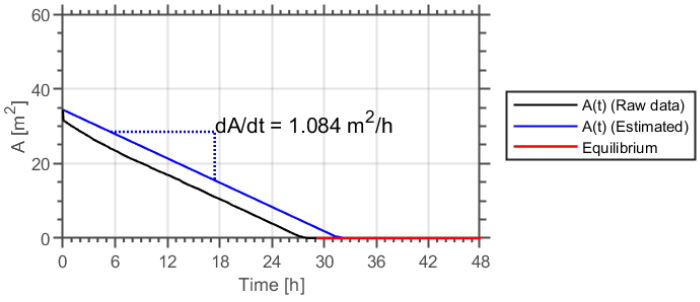

Figure F.30: A(t) of material B-4-2 (see Table B.1).

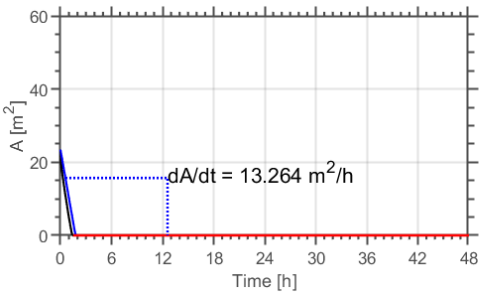

Figure F.31: A(t) of material B-4-3.

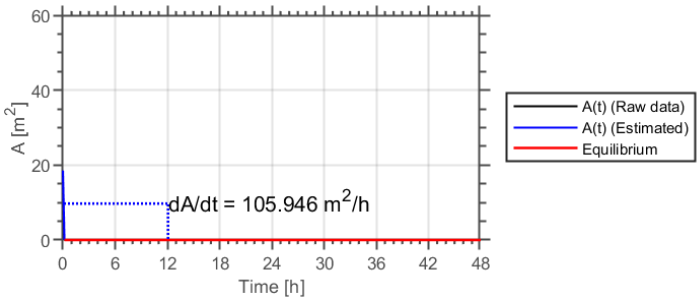

Figure F.32: A(t) of material B-4-4 (see Table B.1).

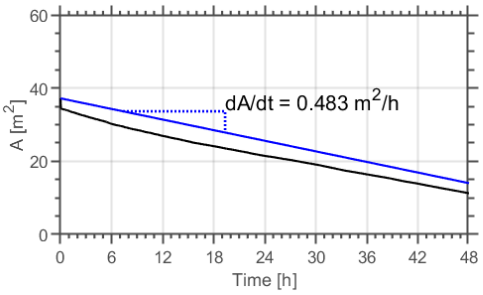

Figure F.33: A(t) of material C-1-1.

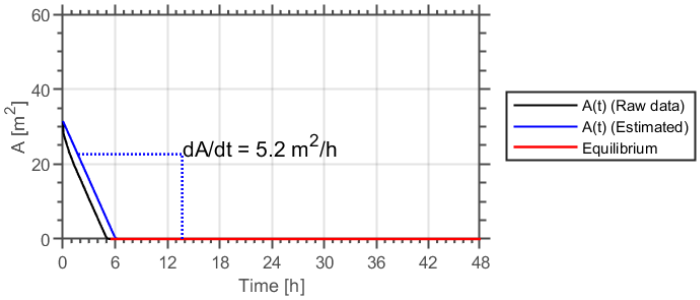

Figure F.34: A(t) of material C-1-2 (see Table B.1).

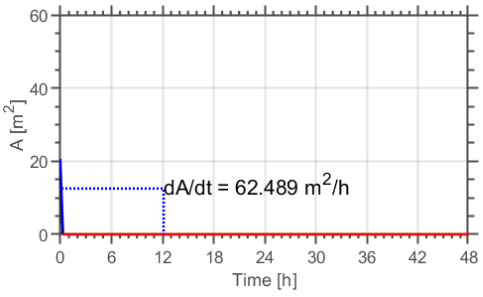

Figure F.35: A(t) of material C-1-3.

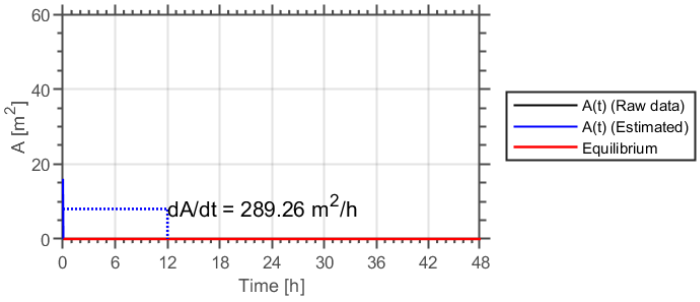

Figure F.36: A(t) of material C-1-4 (see Table B.1).

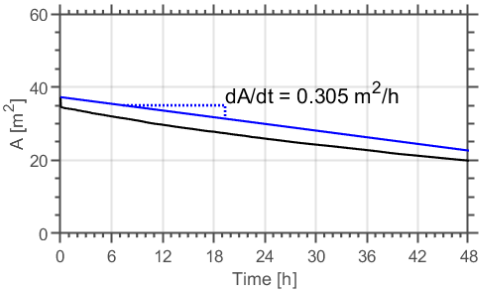

Figure F.37: A(t) of material C-2-1.

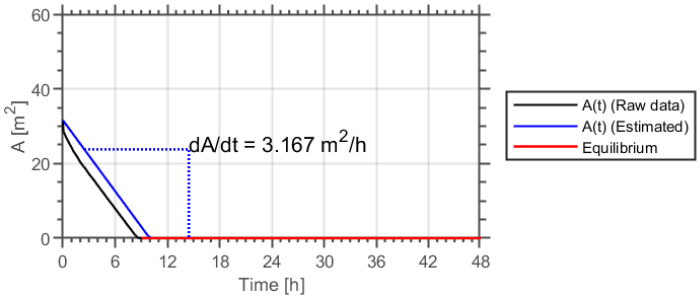

Figure F.38: A(t) of material C-2-2 (see Table B.1).

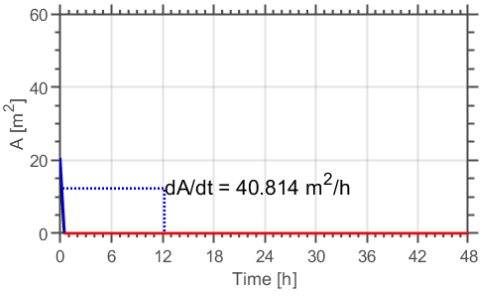

Figure F.39: A(t) of material C-2-3.

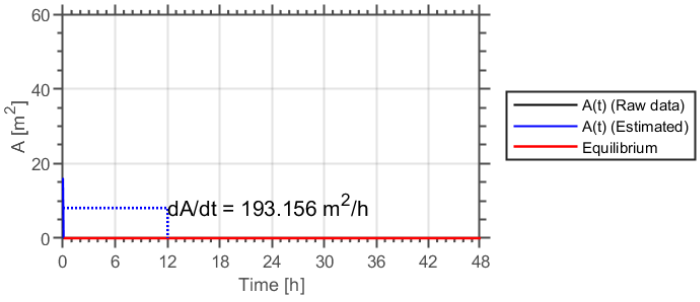

Figure F.40: A(t) of material C-2-4 (see Table B.1).

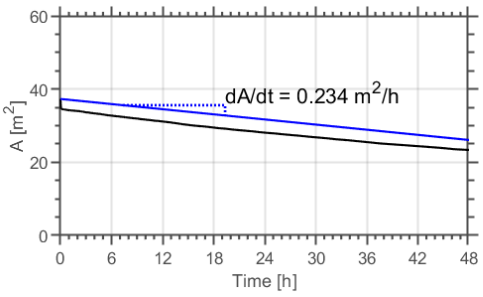

Figure F.41: A(t) of material C-3-1.

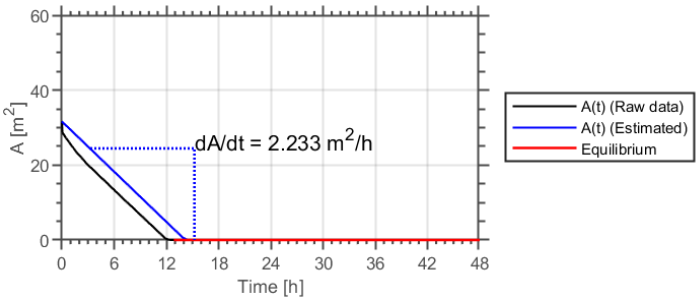

Figure F.42: A(t) of material C-3-2 (see Table B.1).

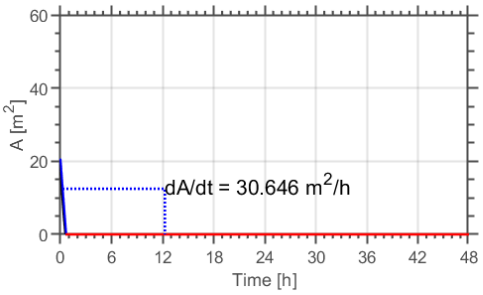

Figure F.43: A(t) of material C-3-3.

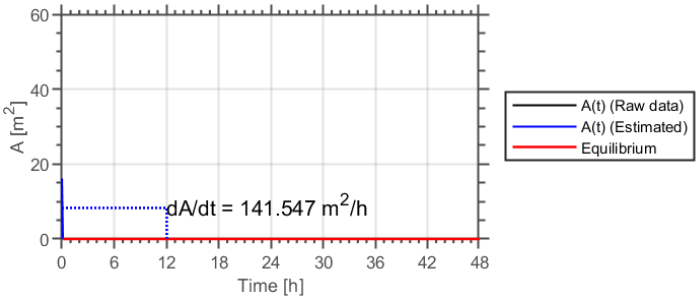

Figure F.44: A(t) of material C-3-4 (see Table B.1).

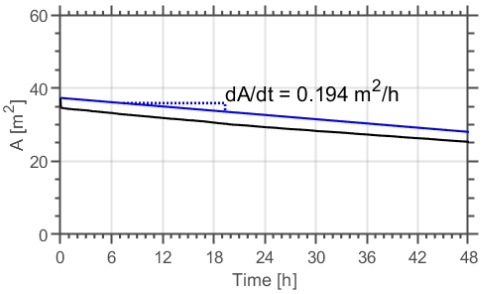

Figure F.45: A(t) of material C-4-1.

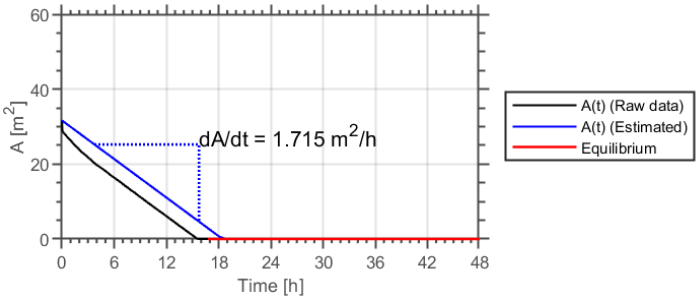

Figure F.46: A(t) of material C-4-2 (see Table B.1).

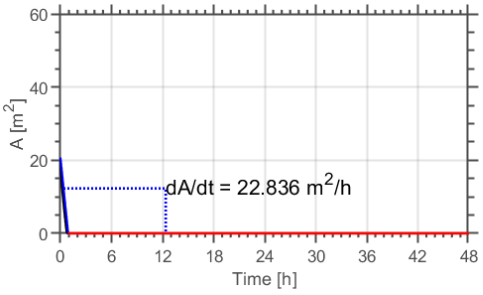

Figure F.47: A(t) of material C-4-3.

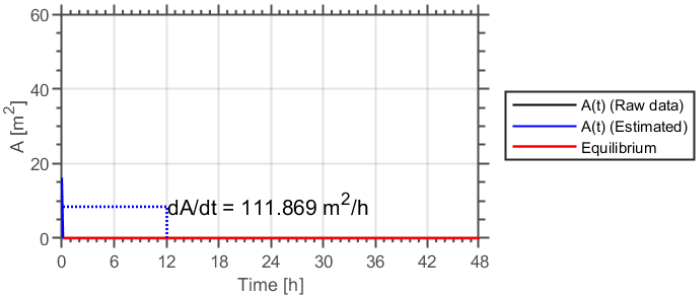

Figure F.48: A(t) of material C-4-4 (see Table B.1).

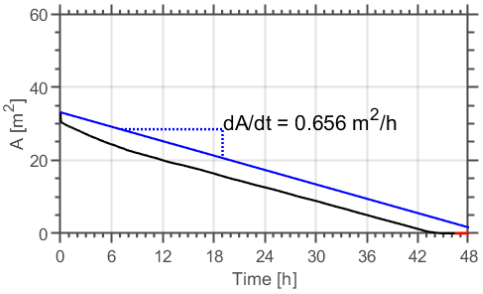

Figure F.49: A(t) of material D-1-1.

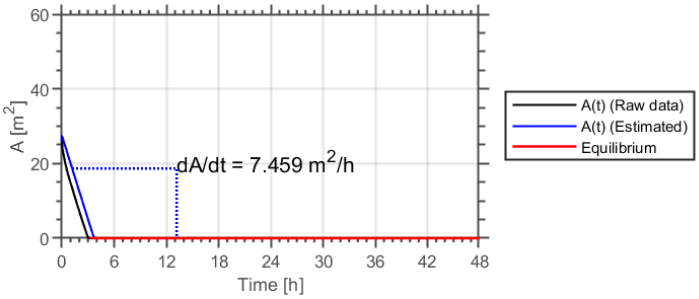

Figure F.50: A(t) of material D-1-2 (see Table B.1).

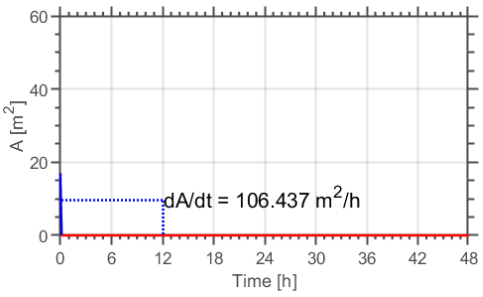

Figure F.51: A(t) of material D-1-3.

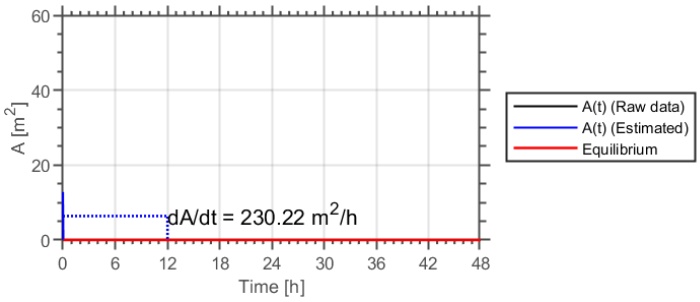

Figure F.52: A(t) of material D-1-4 (see Table B.1).

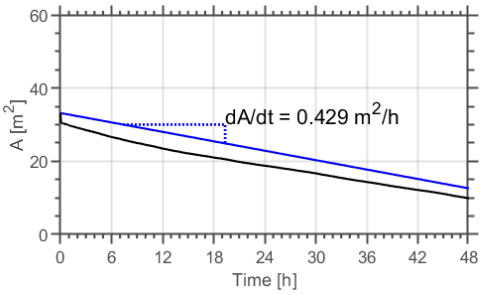

Figure F.53: A(t) of material D-2-1.

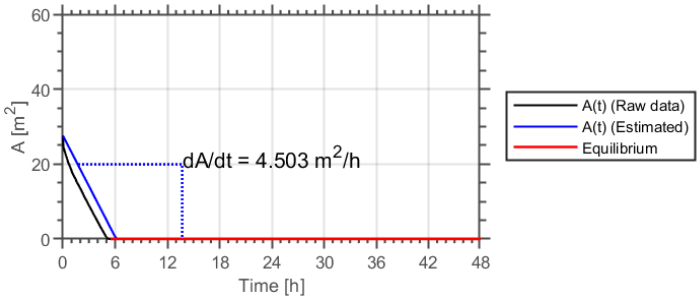

Figure F.54: A(t) of material D-2-2 (see Table B.1).

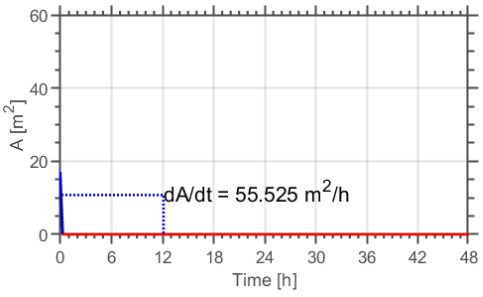

Figure F.55: A(t) of material D-2-3.

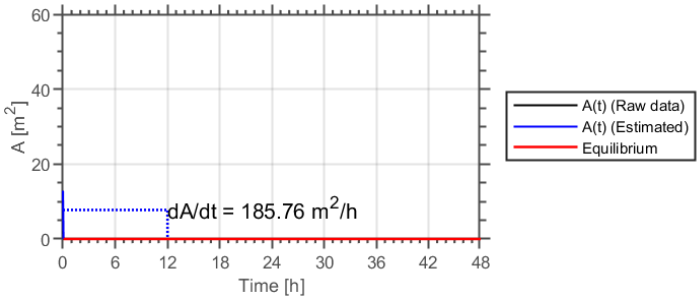

Figure F.56: A(t) of material D-2-4 (see Table B.1).

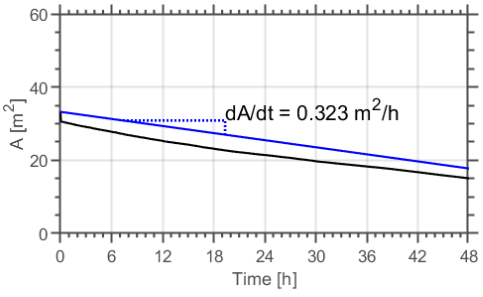

Figure F.57: A(t) of material D-3-1.

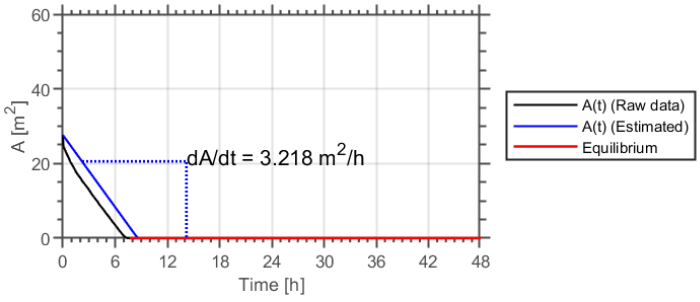

Figure F.58: A(t) of material D-3-2 (see Table B.1).

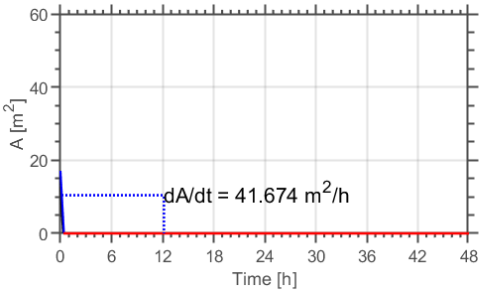

Figure F.59: A(t) of material D-3-3.

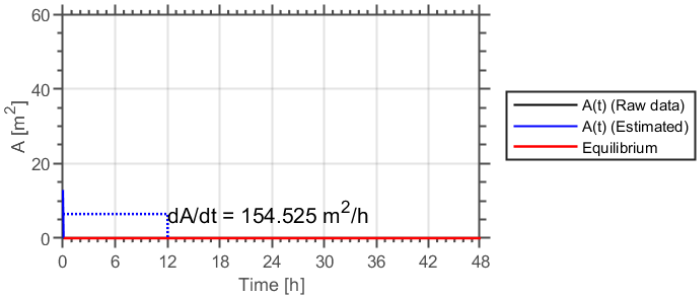

Figure F.60: A(t) of material D-3-4 (see Table B.1).

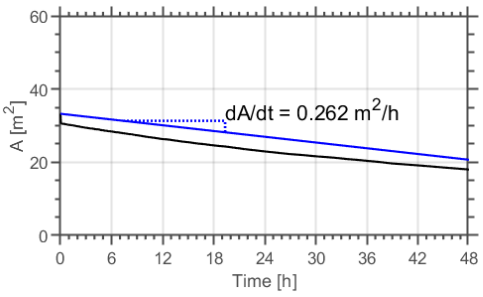

Figure F.61: A(t) of material D-4-1.

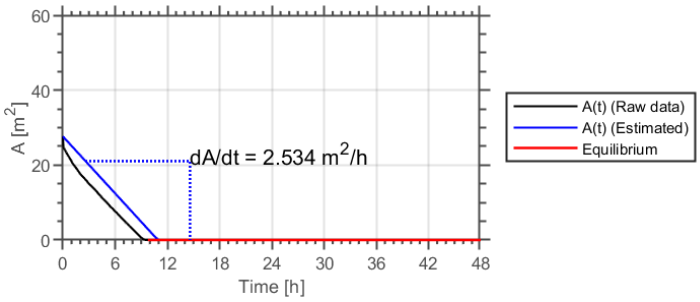

Figure F.62: A(t) of material D-4-2 (see Table B.1).

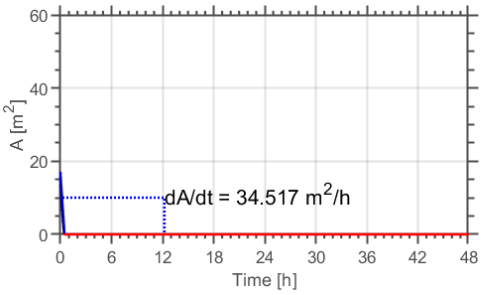

Figure F.63: A(t) of material D-4-3.

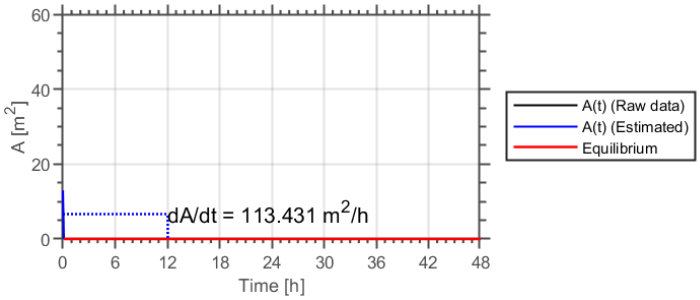

Figure F.64: A(t) of material D-4-4 (see Table B.1).

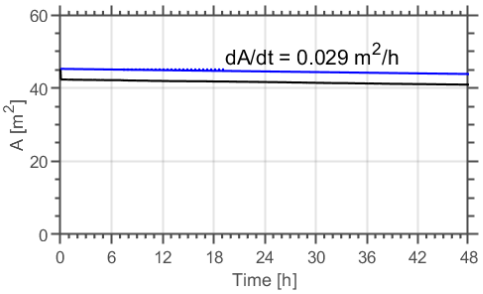

Figure F.65: A(t) of material E-1-1.

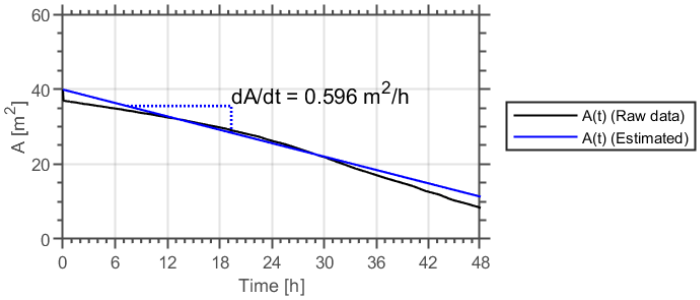

Figure F.66: A(t) of material E-1-2 (see Table B.1).

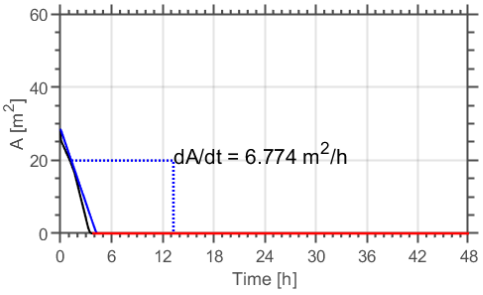

Figure F.67: A(t) of material E-1-3.

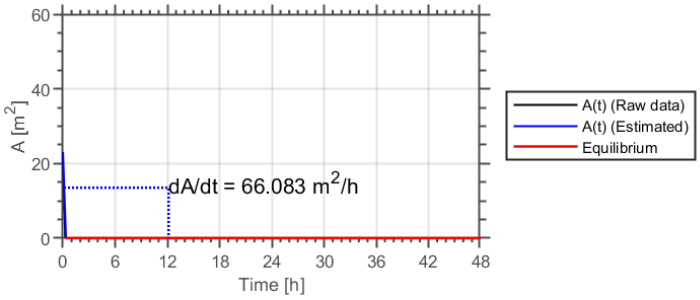

Figure F.68: A(t) of material E-1-4 (see Table B.1).

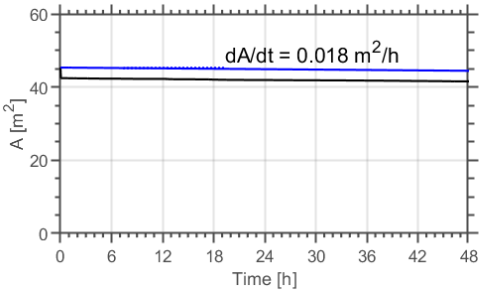

Figure F.69: A(t) of material E-2-1.

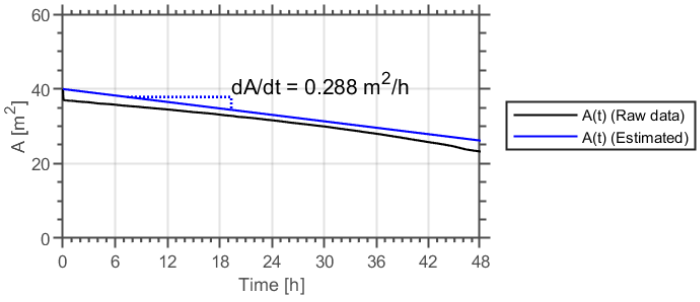

Figure F.70: A(t) of material E-2-2 (see Table B.1).

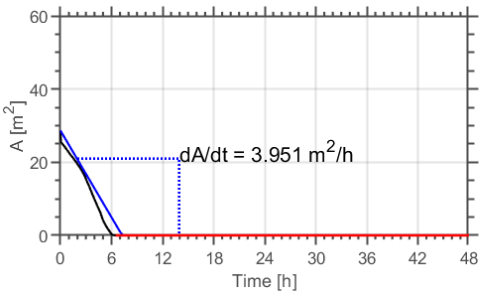

Figure F.71: A(t) of material E-2-3.

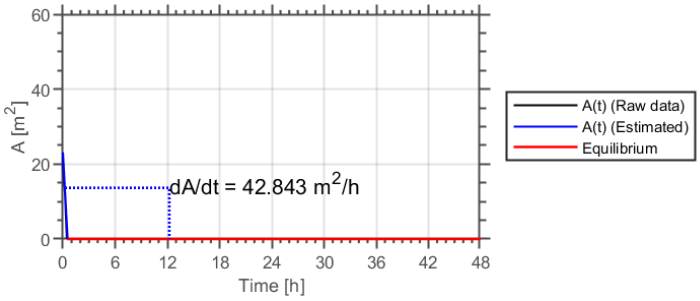

Figure F.72: A(t) of material E-2-4 (see Table B.1).

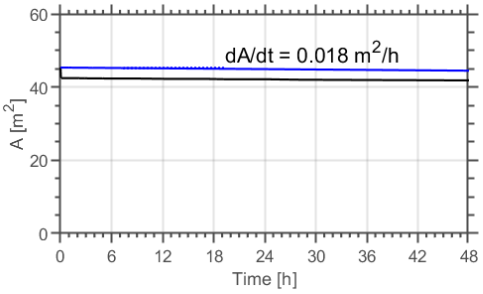

Figure F.73: A(t) of material E-3-1.

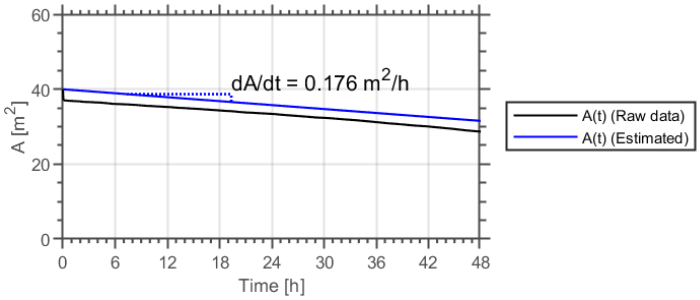

Figure F.74: A(t) of material E-3-2 (see Table B.1).

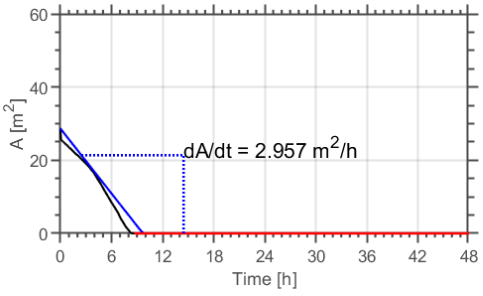

Figure F.75: A(t) of material E-3-3.

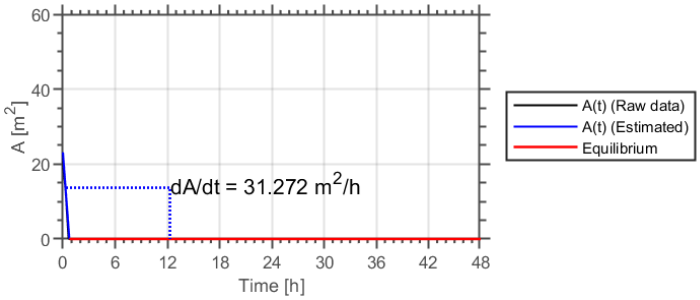

Figure F.76: A(t) of material E-3-4 (see Table B.1).

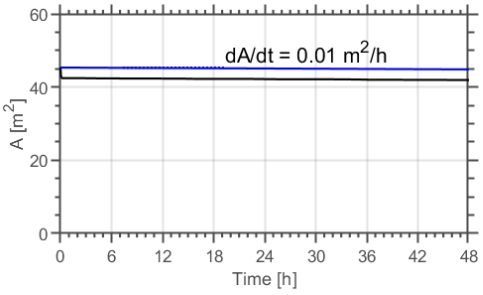

Figure F.77: A(t) of material E-4-1.

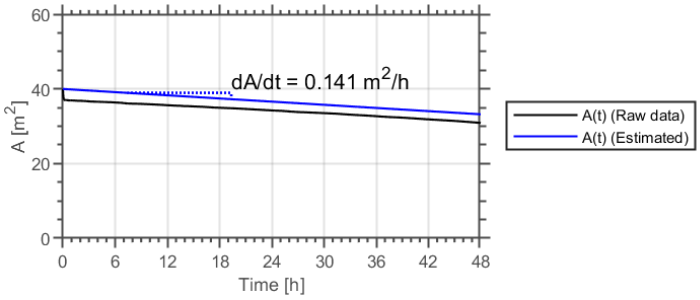

Figure F.78: A(t) of material E-4-2 (see Table B.1).

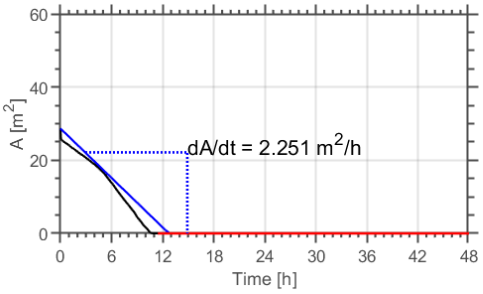

Figure F.79: A(t) of material E-4-3.

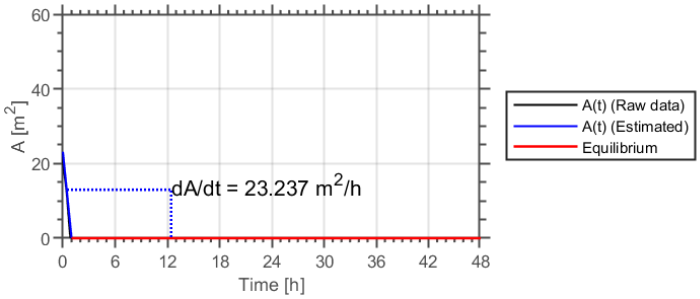

Figure F.80: A(t) of material E-4-4 (see Table B.1).

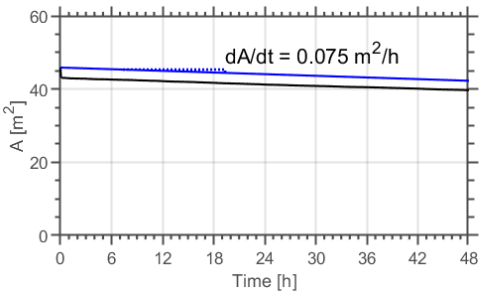

Figure F.81: A(t) of material F-1-1.

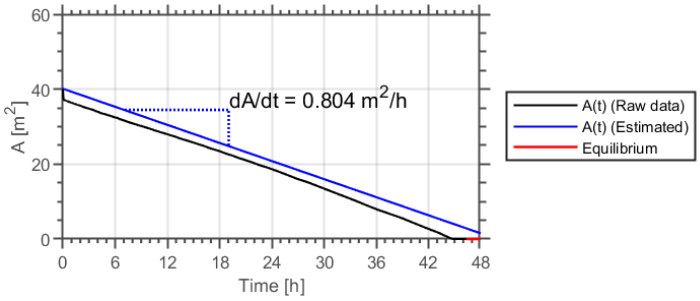

Figure F.82: A(t) of material F-1-2 (see Table B.1).

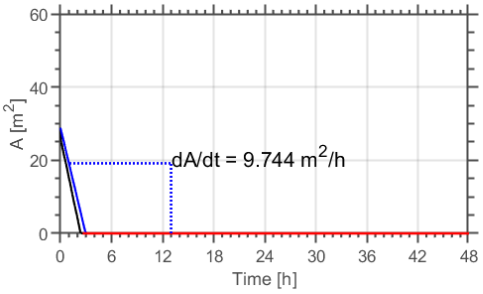

Figure F.83: A(t) of material F-1-3.

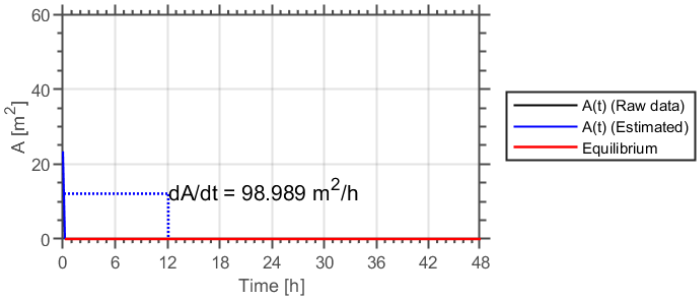

Figure F.84: A(t) of material F-1-4 (see Table B.1).

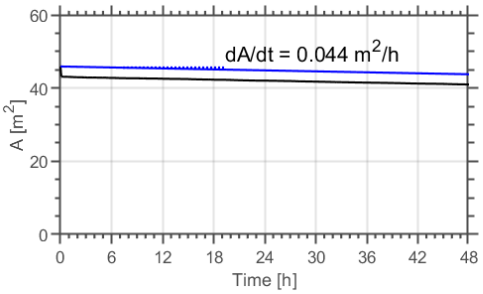

Figure F.85: A(t) of material F-2-1.

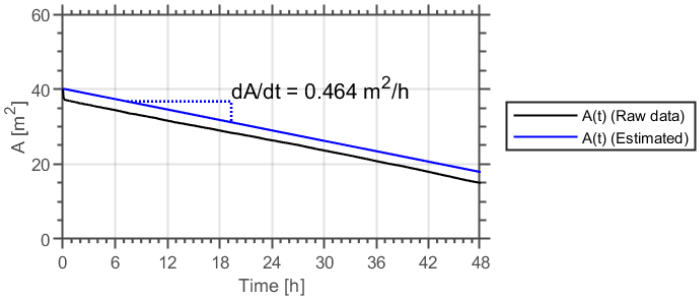

Figure F.86: A(t) of material F-2-2 (see Table B.1).

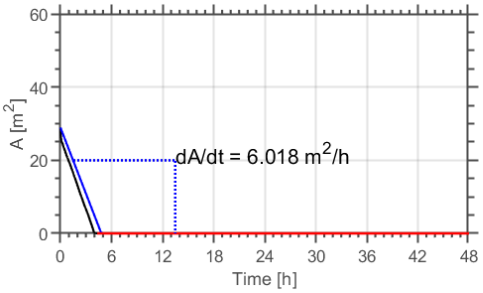

Figure F.87: A(t) of material F-2-3.

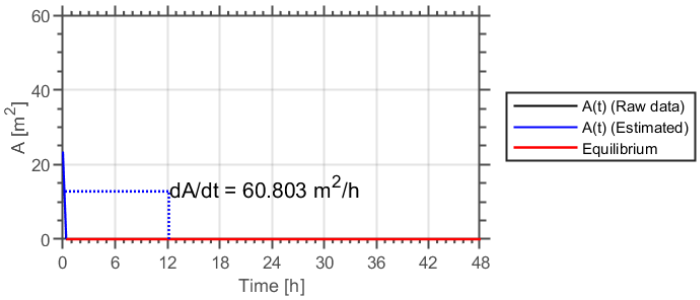

Figure F.88: A(t) of material F-2-4 (see Table B.1).

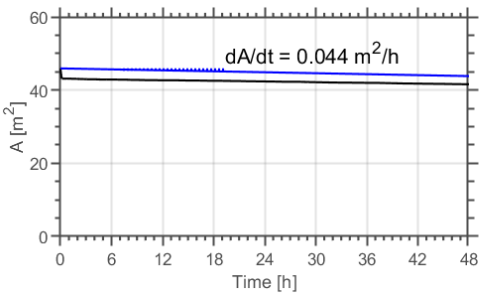

Figure F.89: A(t) of material F-3-1.

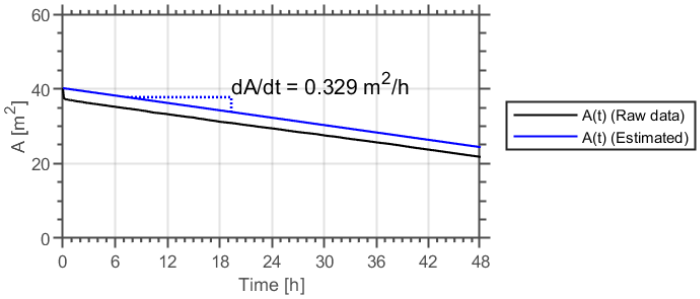

Figure F.90: A(t) of material F-3-2 (see Table B.1).

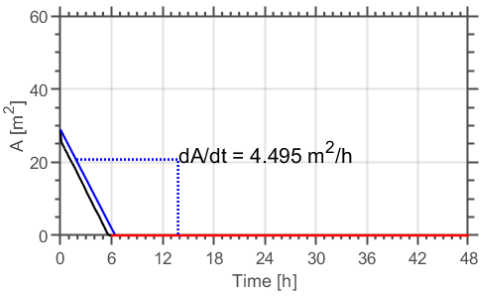

Figure F.91: A(t) of material F-3-3.

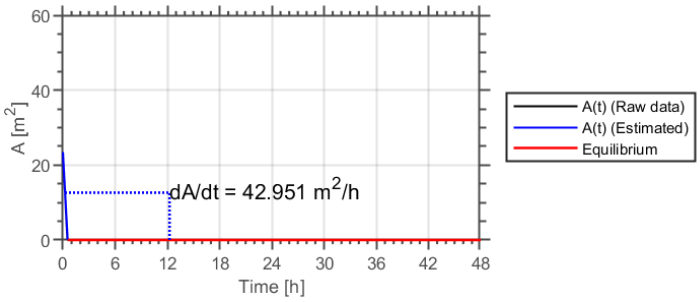

Figure F.92: A(t) of material F-3-4 (see Table B.1).

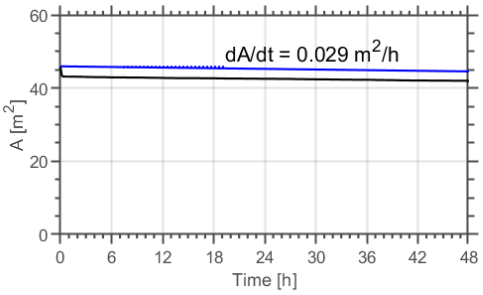

Figure F.93: A(t) of material F-4-1.

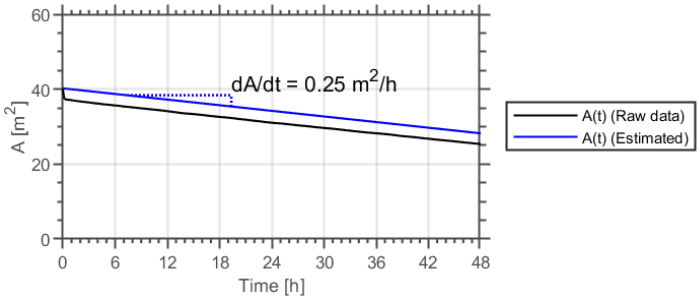

Figure F.94: A(t) of material F-4-2 (see Table B.1).

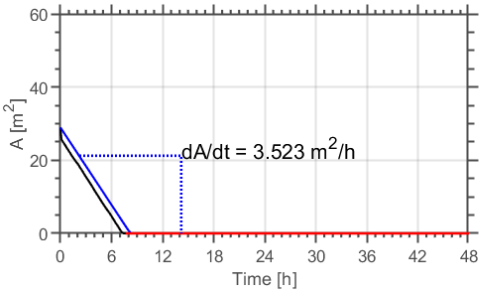

Figure F.95: A(t) of material F-4-3.

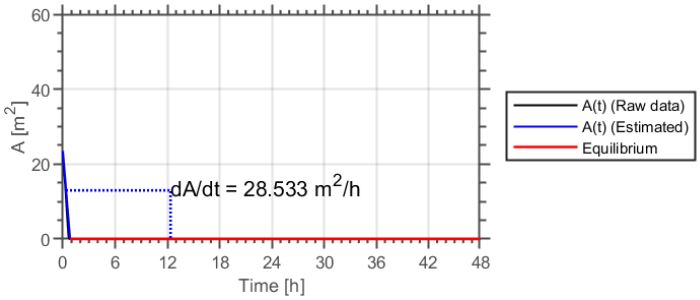

Figure F.96: A(t) of material F-4-4 (see Table B.1).

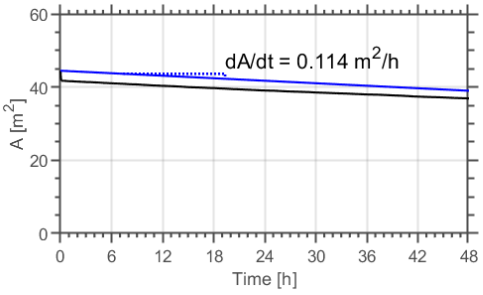

Figure F.97: A(t) of material G-1-1.

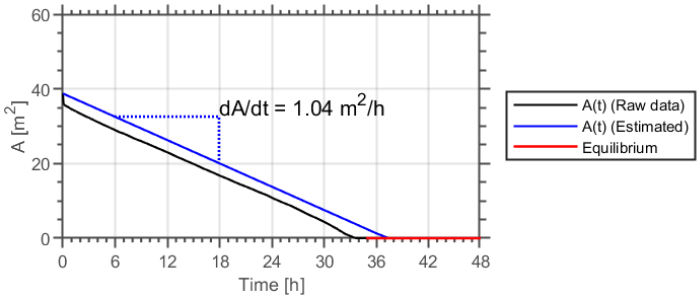

Figure F.98: A(t) of material G-1-2 (see Table B.1).

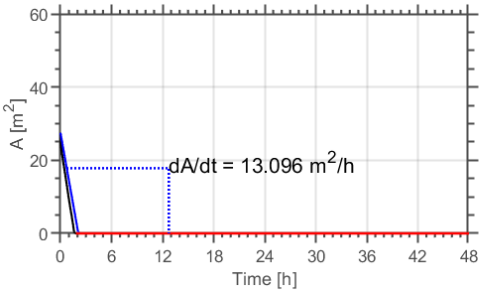

Figure F.99: A(t) of material G-1-3.

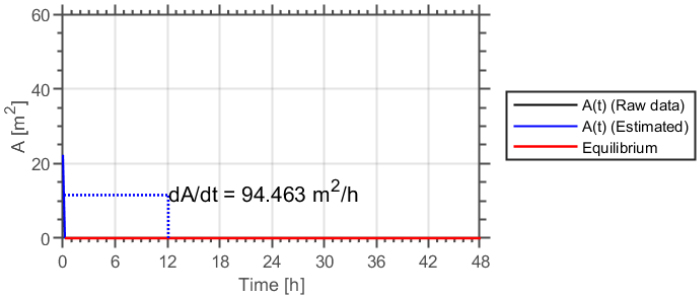

Figure F.100: A(t) of material G-1-4 (see Table B.1).

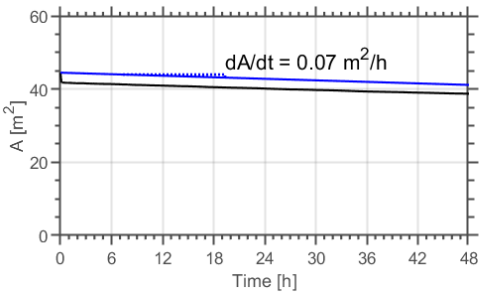

Figure F.101: A(t) of material G-2-1.

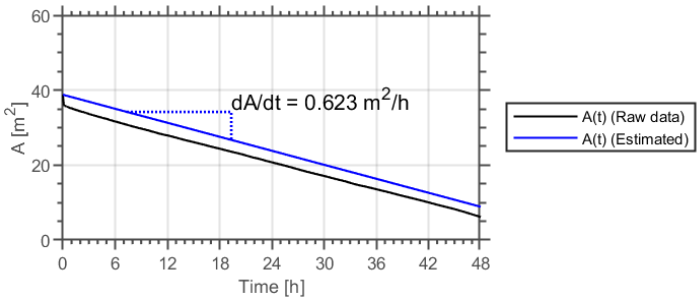

Figure F.102: A(t) of material G-2-2 (see Table B.1).

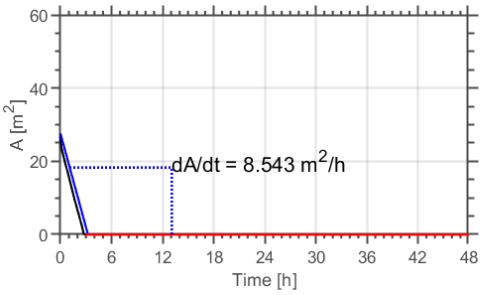

Figure F.103: A(t) of material G-2-3.

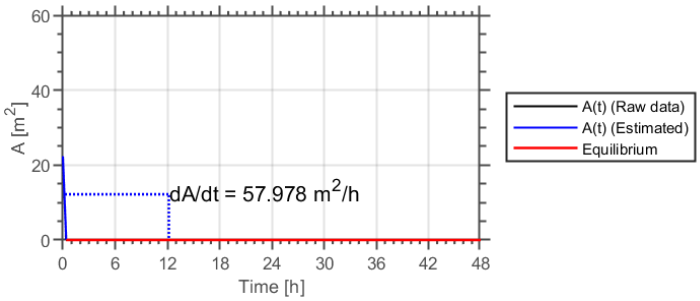

Figure F.104: A(t) of material G-2-4 (see Table B.1).

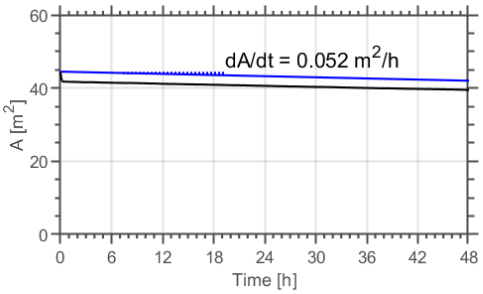

Figure F.105: A(t) of material G-3-1.

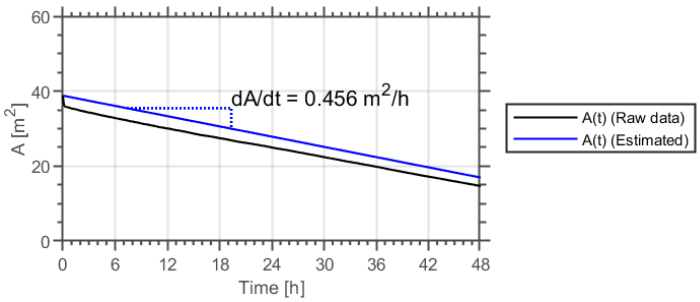

Figure F.106: A(t) of material G-3-2 (see Table B.1).

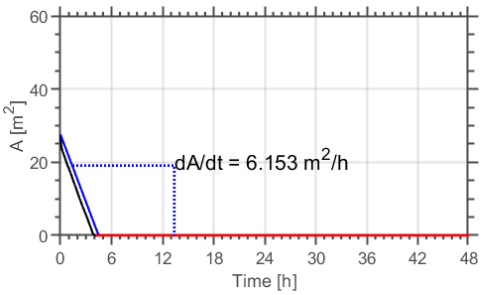

Figure F.107: A(t) of material G-3-3.

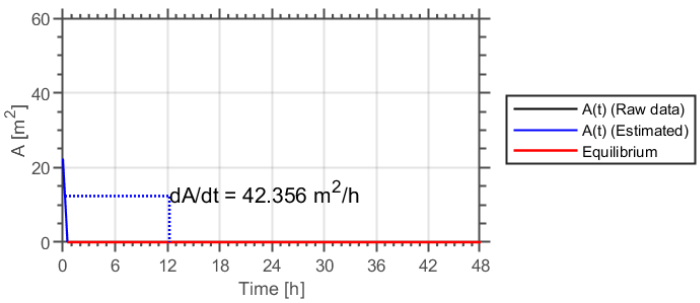

Figure F.108: A(t) of material G-3-4 (see Table B.1).

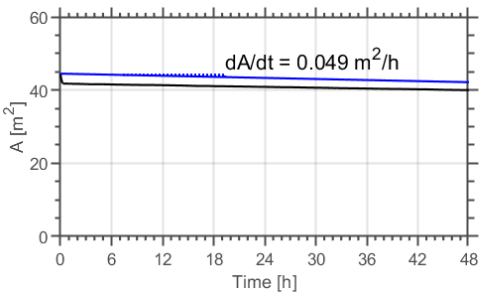

Figure F.109: A(t) of material G-4-1.

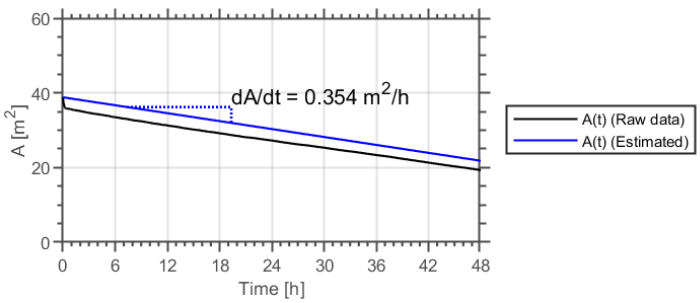

Figure F.110: A(t) of material G-4-2 (see Table B.1).

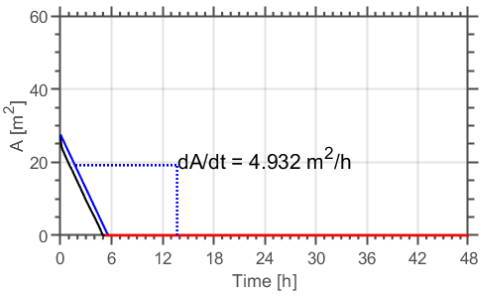

Figure F.111: A(t) of material G-4-3.

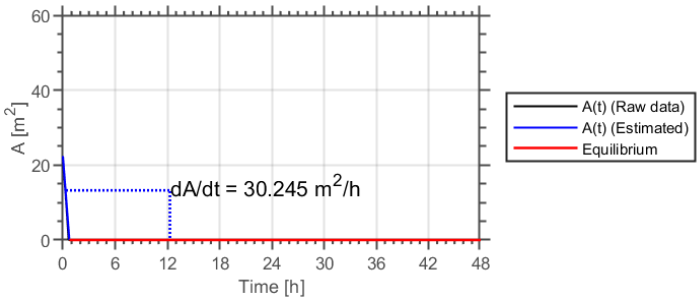

Figure F.112: A(t) of material G-4-4 (see Table B.1).

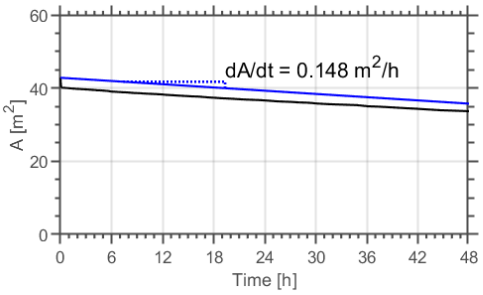

Figure F.113: A(t) of material H-1-1.

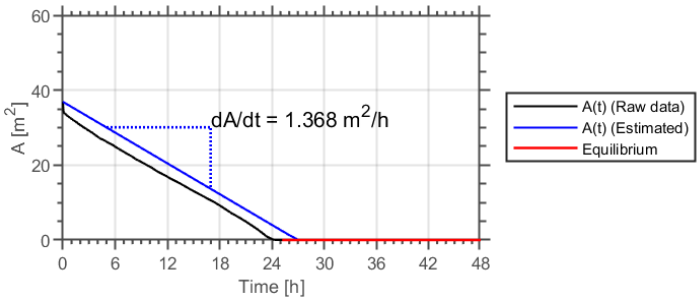

Figure F.114: A(t) of material H-1-2 (see Table B.1).

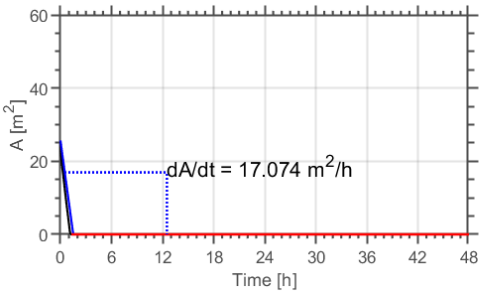

Figure F.115: A(t) of material H-1-3.

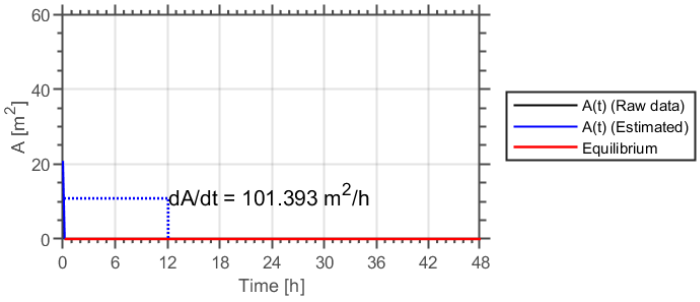

Figure F.116: A(t) of material H-1-4 (see Table B.1).

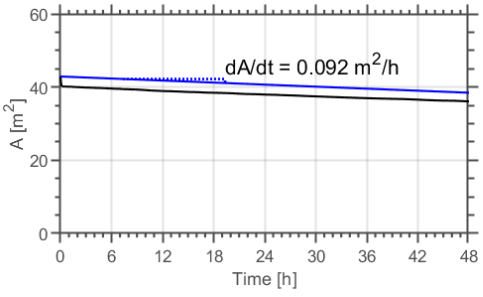

Figure F.117: A(t) of material H-2-1.

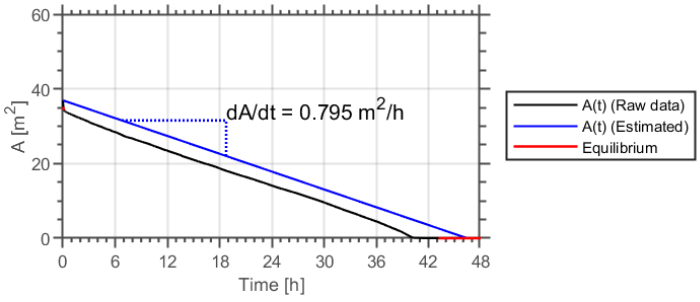

Figure F.118: A(t) of material H-2-2 (see Table B.1).

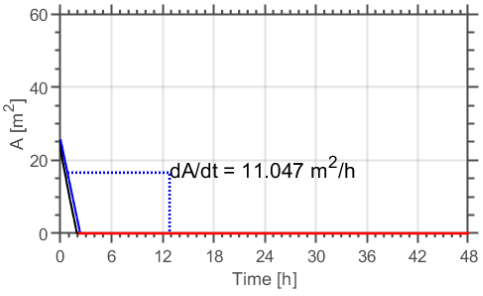

Figure F.119: A(t) of material H-2-3.

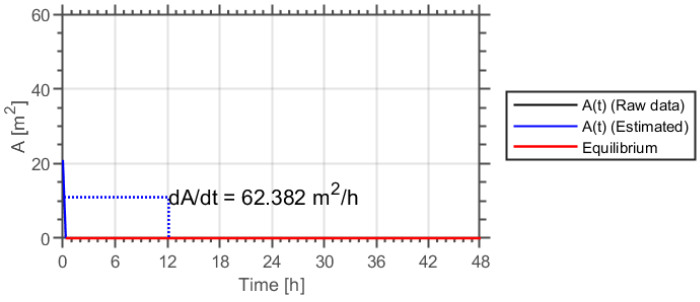

Figure F.120: A(t) of material H-2-4 (see Table B.1).

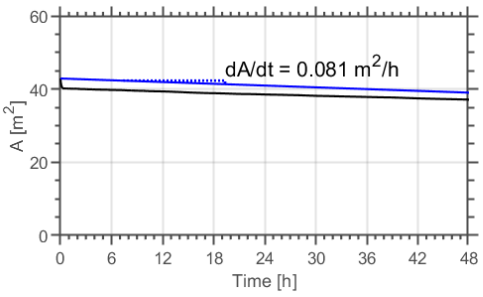

Figure F.121: A(t) of material H-3-1.

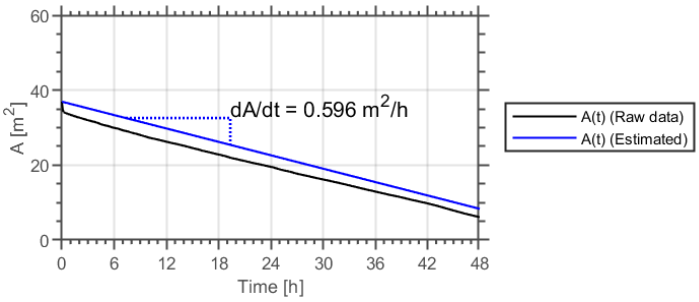

Figure F.122: A(t) of material H-3-2 (see Table B.1).

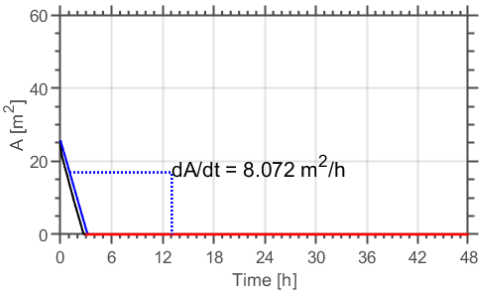

Figure F.123: A(t) of material H-3-3.

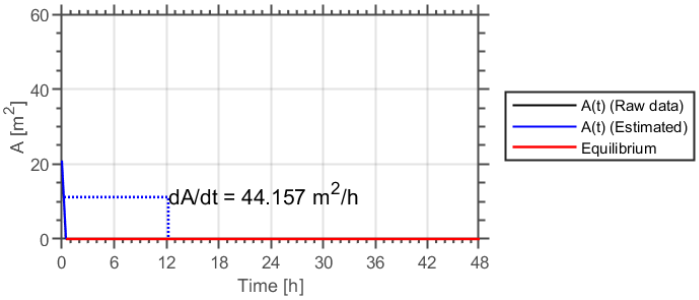

Figure F.124: A(t) of material H-3-4 (see Table B.1).

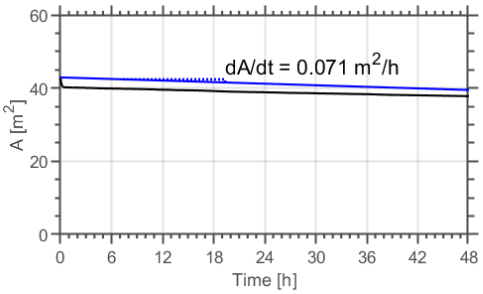

Figure F.125: A(t) of material H-4-1.

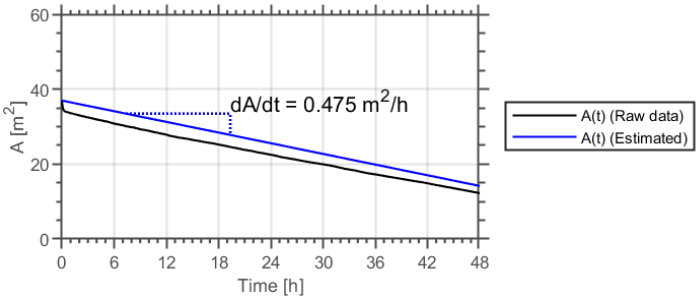

Figure F.126: A(t) of material H-4-2 (see Table B.1).

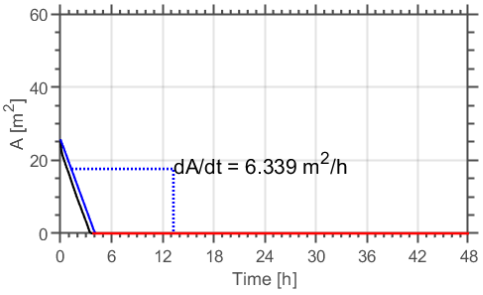

Figure F.127: A(t) of material H-4-3.

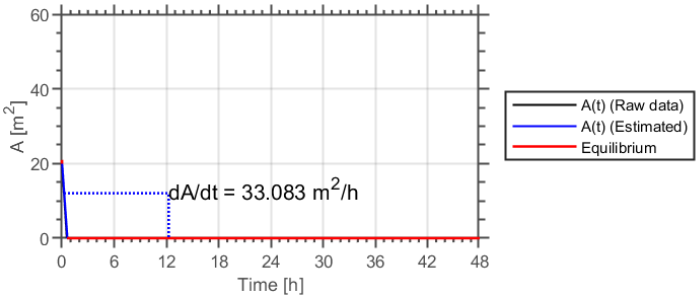

Figure F.128: A(t) of material H-4-4 (see Table B.1).

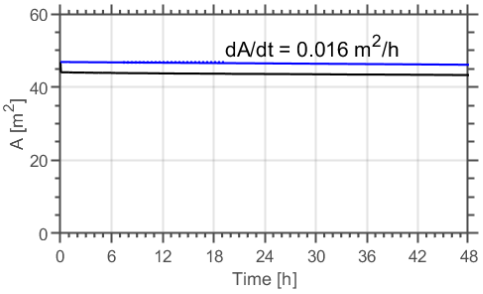

Figure F.129: A(t) of material I-1-1.

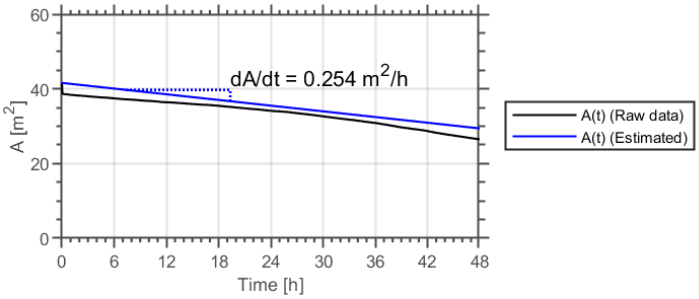

Figure F.130: A(t) of material I-1-2 (see Table B.1).

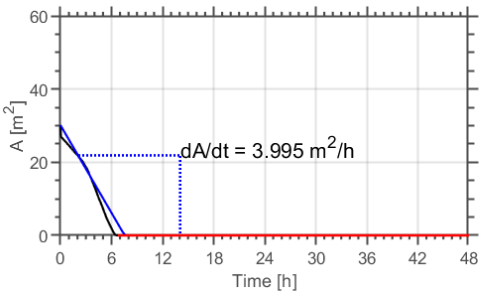

Figure F.131: A(t) of material I-1-3.

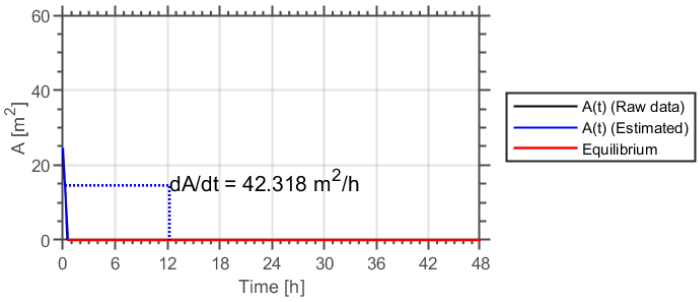

Figure F.132: A(t) of material I-1-4 (see Table B.1).

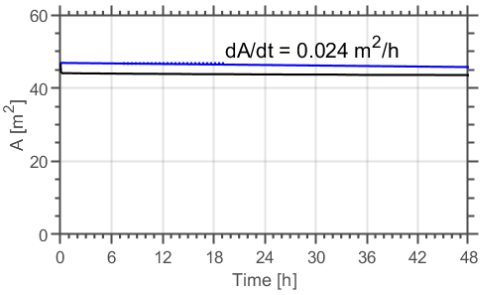

Figure F.133: A(t) of material I-2-1.

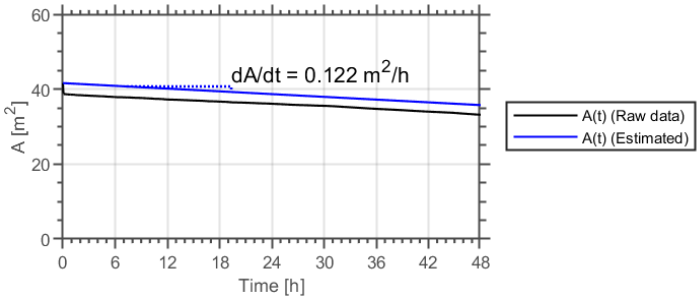

Figure F.134: A(t) of material I-2-2 (see Table B.1).

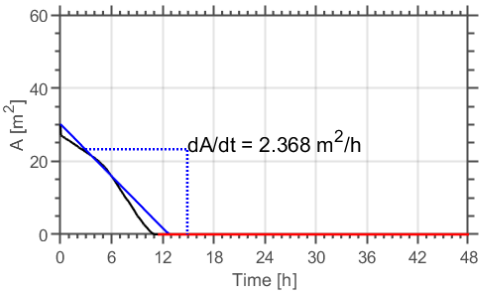

Figure F.135: A(t) of material I-2-3.

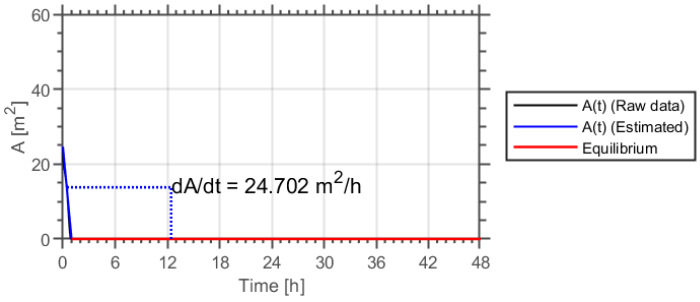

Figure F.136: A(t) of material I-2-4 (see Table B.1).

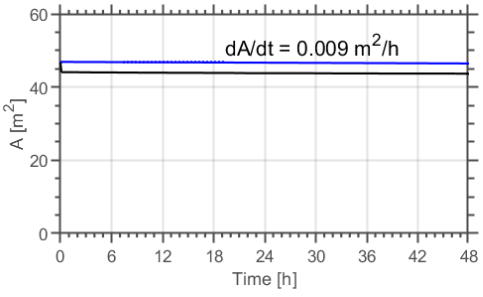

Figure F.137: A(t) of material I-3-1.

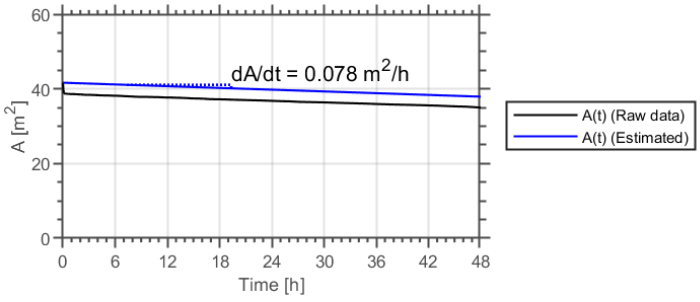

Figure F.138: A(t) of material I-3-2 (see Table B.1).

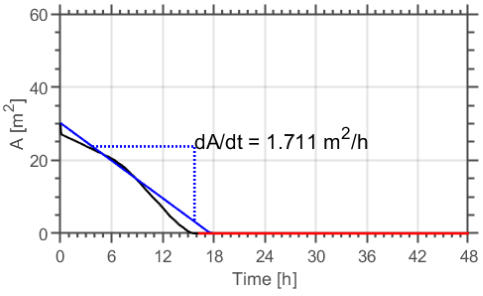

Figure F.139: A(t) of material I-3-3.

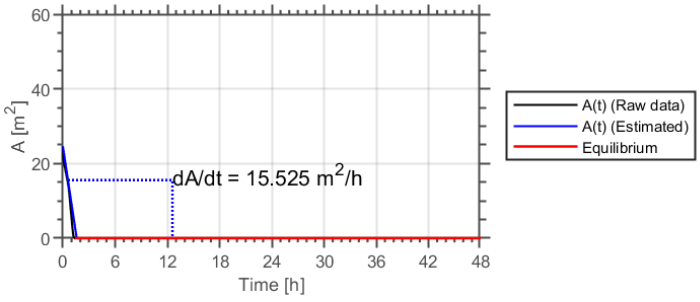

Figure F.140: A(t) of material I-3-4 (see Table B.1).

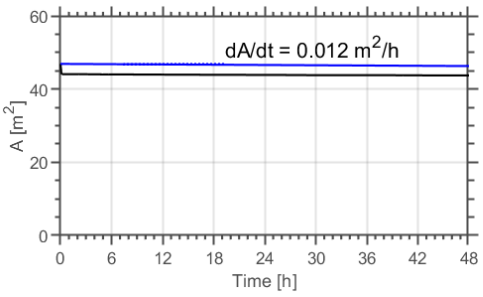

Figure F.141: A(t) of material I-4-1.

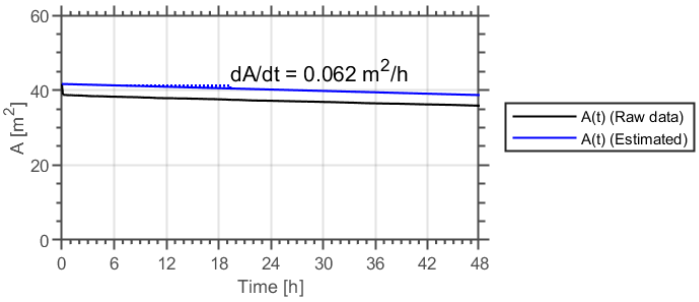

Figure F.142: A(t) of material I-4-2 (see Table B.1).

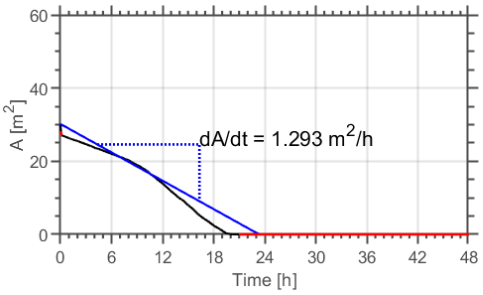

Figure F.143: A(t) of material I-4-3.

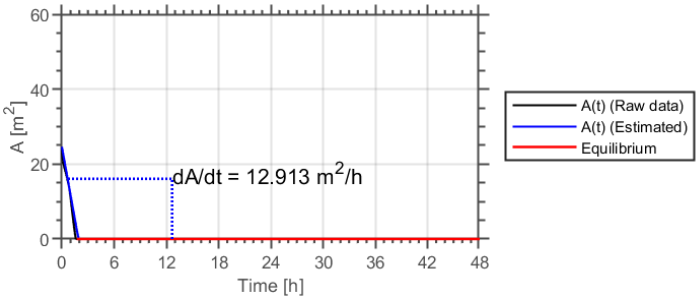

Figure F.144: A(t) of material I-4-4 (see Table B.1).

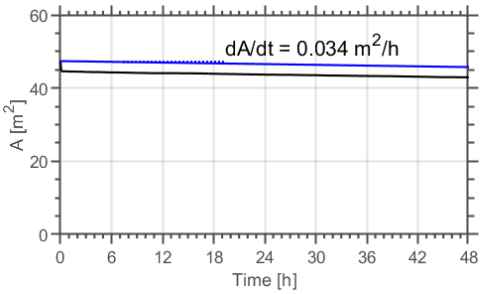

Figure F.145: A(t) of material J-1-1.

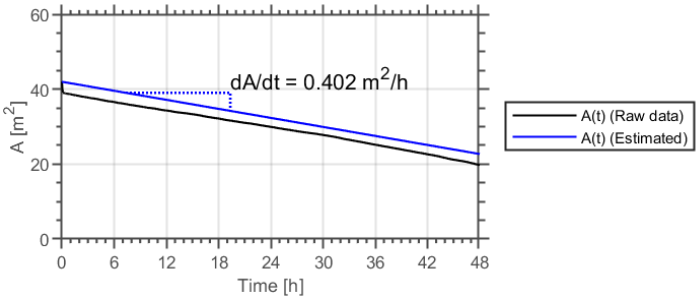

Figure F.146: A(t) of material J-1-2 (see Table B.1).

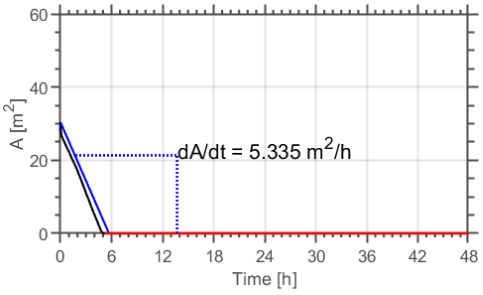

Figure F.147: A(t) of material J-1-3.

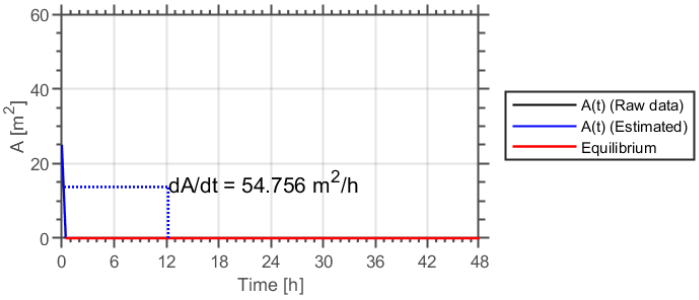

Figure F.148: A(t) of material J-1-4 (see Table B.1).

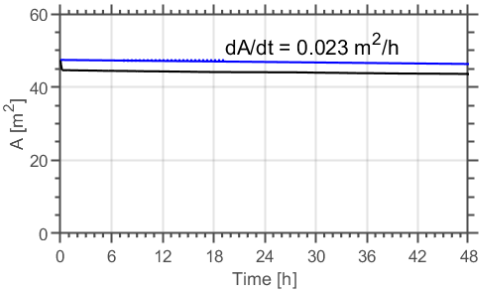

Figure F.149: A(t) of material J-2-1.

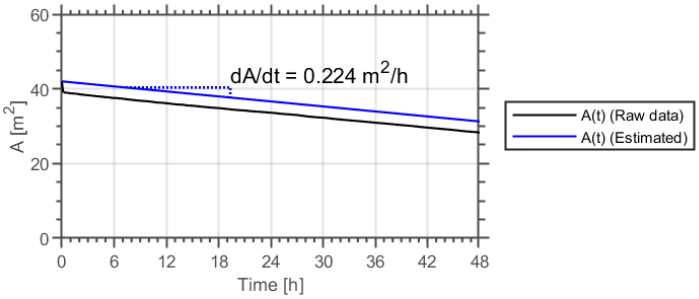

Figure F.150: A(t) of material J-2-2 (see Table B.1).

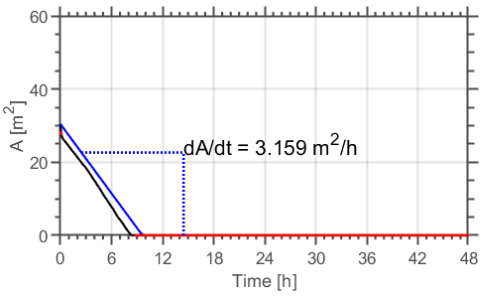

Figure F.151: A(t) of material J-2-3.

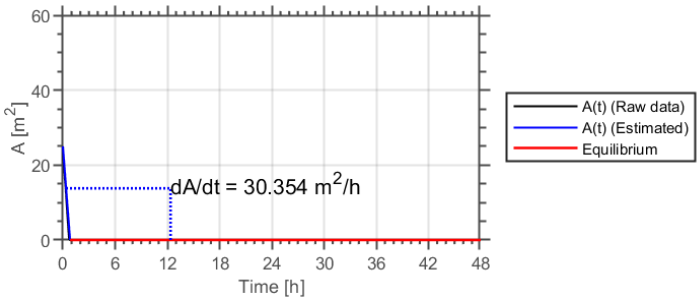

Figure F.152: A(t) of material J-2-4 (see Table B.1).

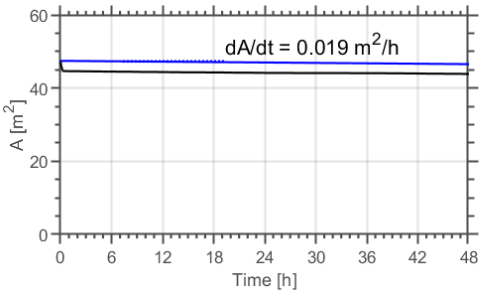

Figure F.153: A(t) of material J-3-1.

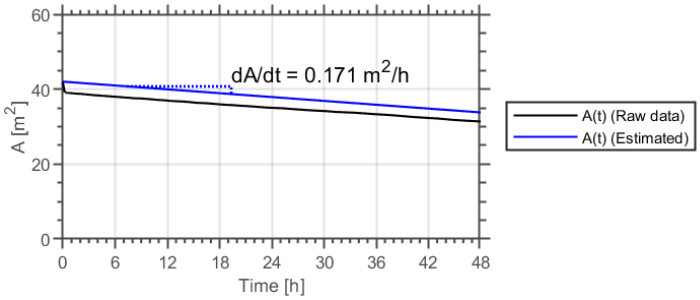

Figure F.154: A(t) of material J-3-2 (see Table B.1).

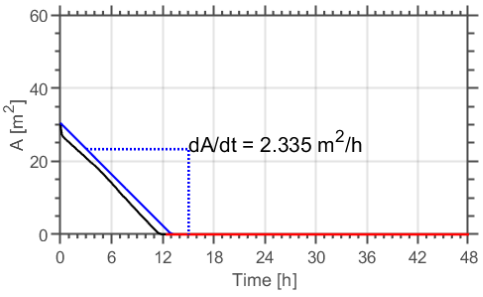

Figure F.155: A(t) of material J-3-3.

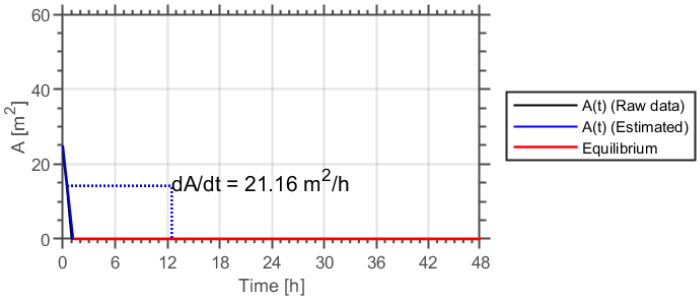

Figure F.156: A(t) of material J-3-4 (see Table B.1).

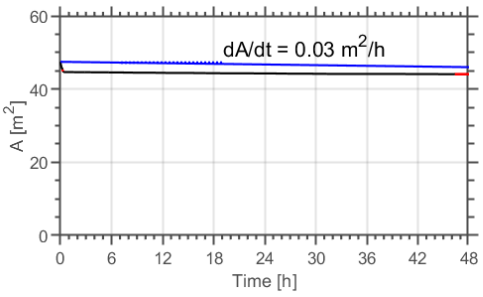

Figure F.157: A(t) of material J-4-1.

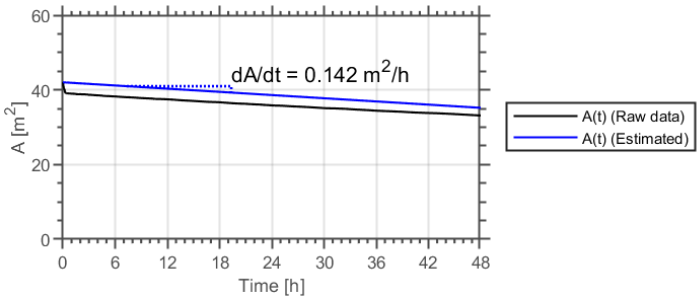

Figure F.158: A(t) of material J-4-2 (see Table B.1).

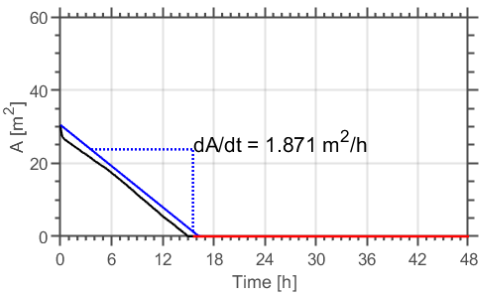

Figure F.159: A(t) of material J-4-3.

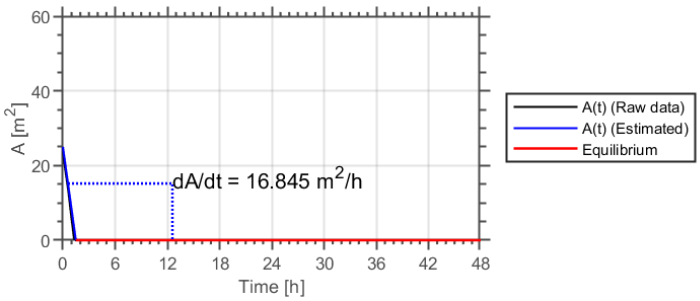

Figure F.160: A(t) of material J-4-4 (see Table B.1).

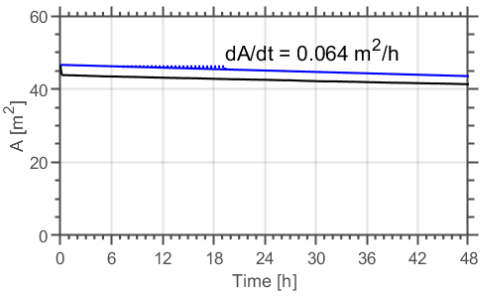

Figure F.161: A(t) of material K-1-1.

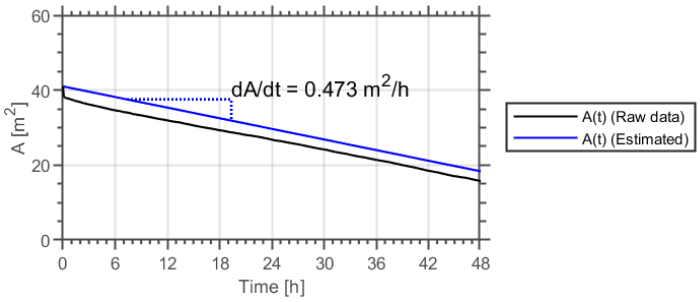

Figure F.162: A(t) of material K-1-2 (see Table B.1).

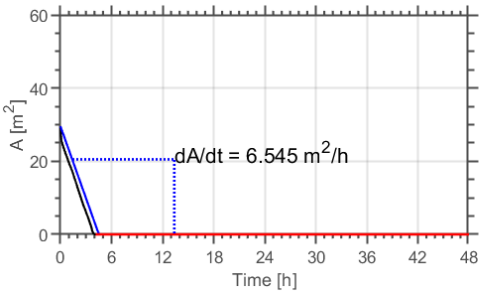

Figure F.163: A(t) of material K-1-3.

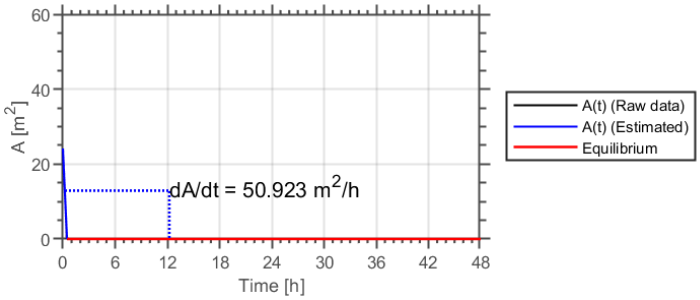

Figure F.164: A(t) of material K-1-4 (see Table B.1).

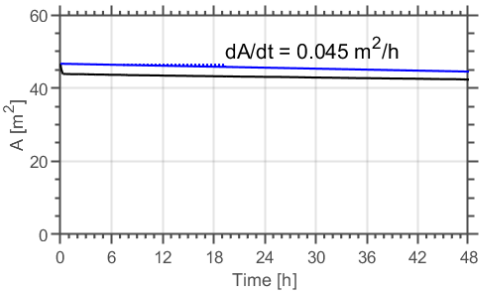

Figure F.165: A(t) of material K-2-1.

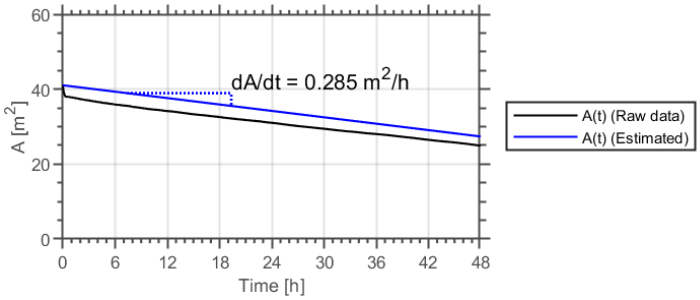

Figure F.166: A(t) of material K-2-2 (see Table B.1).

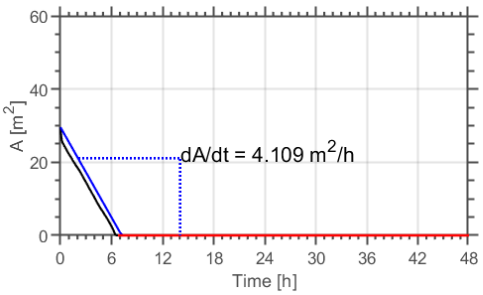

Figure F.167: A(t) of material K-2-3.

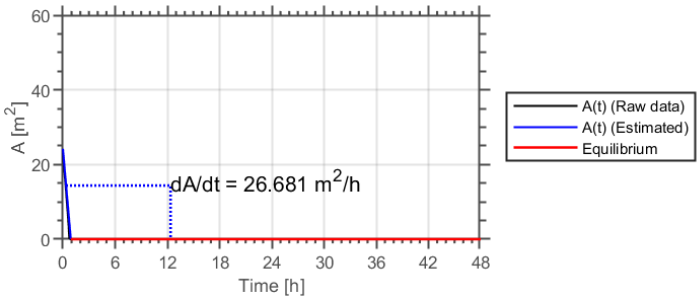

Figure F.168: A(t) of material K-2-4 (see Table B.1).

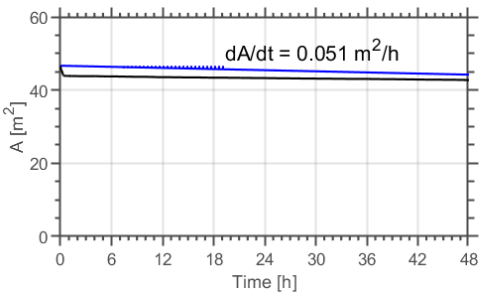

Figure F.169: A(t) of material K-3-1.

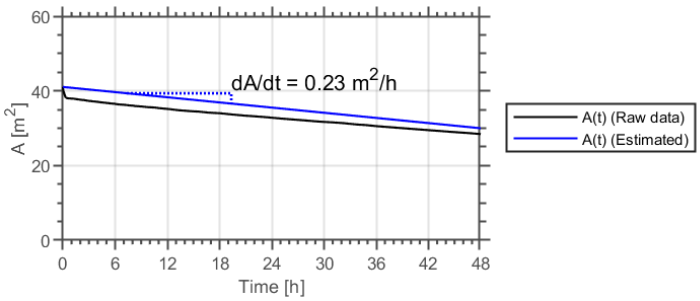

Figure F.170: A(t) of material K-3-2 (see Table B.1).

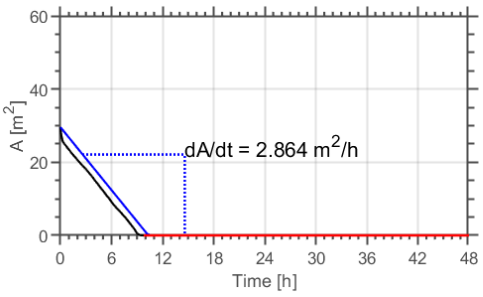

Figure F.171: A(t) of material K-3-3.

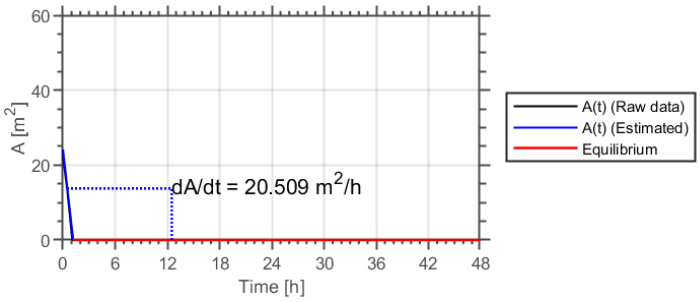

Figure F.172: A(t) of material K-3-4 (see Table B.1).

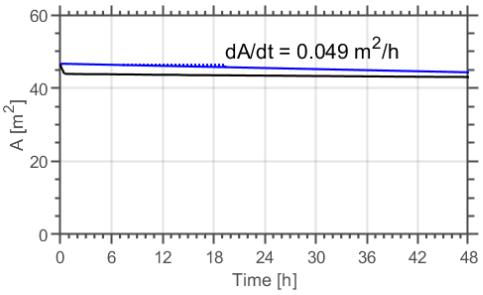

Figure F.173: A(t) of material K-4-1.

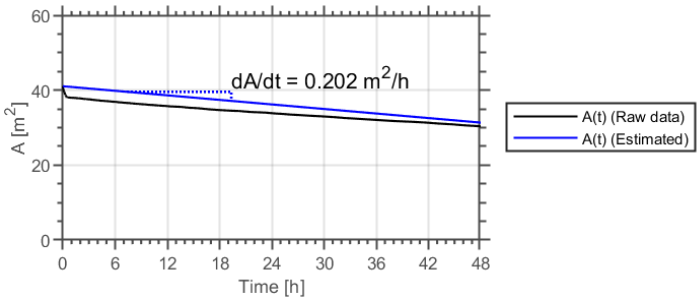

Figure F.174: A(t) of material K-4-2 (see Table B.1).

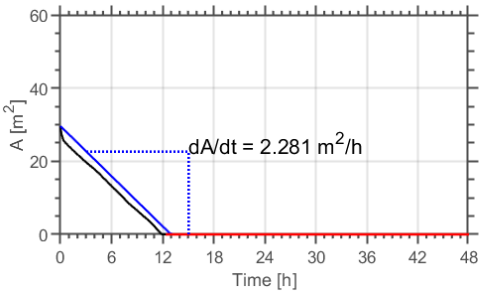

Figure F.175: A(t) of material K-4-3.

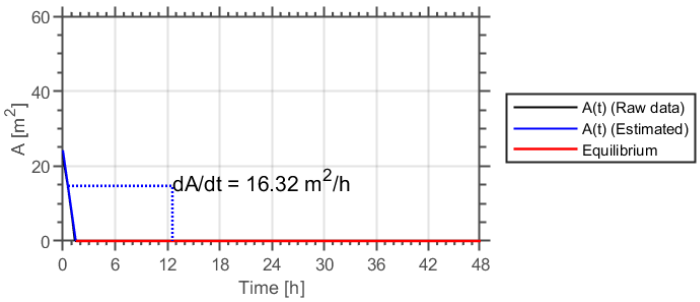

Figure F.176: A(t) of material K-4-4 (see Table B.1).

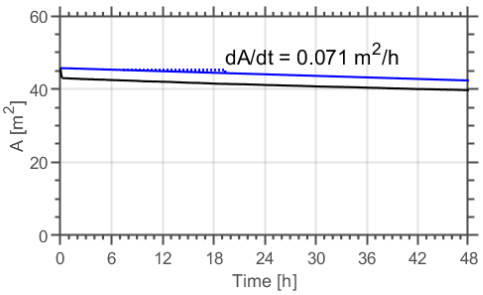

Figure F.177: A(t) of material L-1-1.

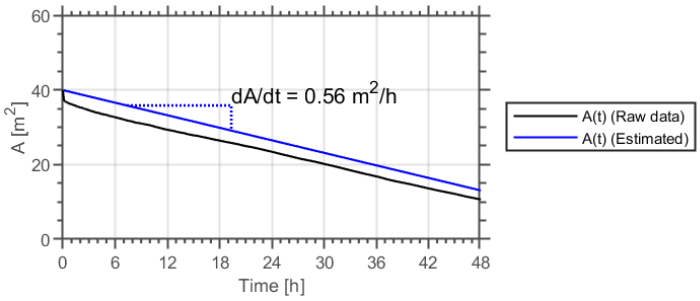

Figure F.178: A(t) of material L-1-2 (see Table B.1).

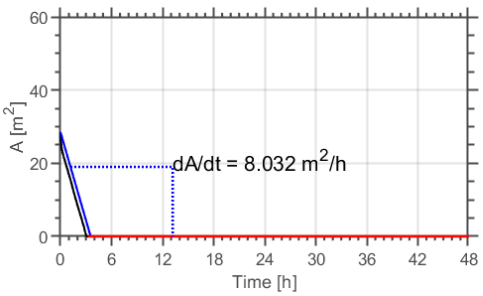

Figure F.179: A(t) of material L-1-3.

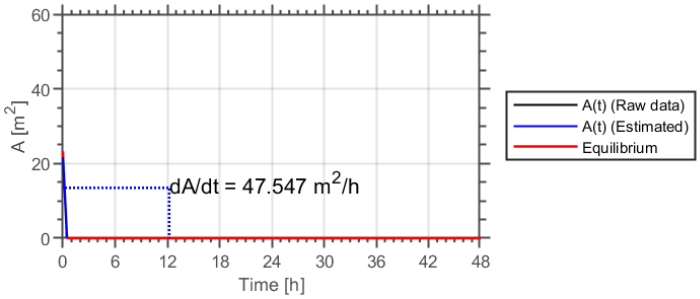

Figure F.180: A(t) of material L-1-4 (see Table B.1).

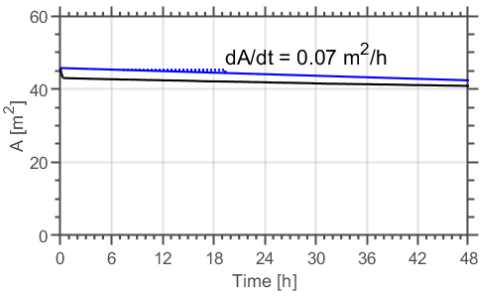

Figure F.181: A(t) of material L-2-1.

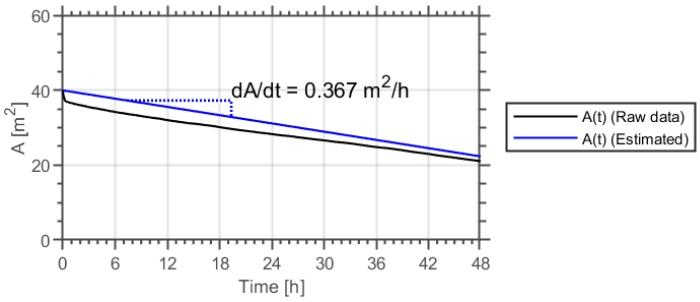

Figure F.182: A(t) of material L-2-2 (see Table B.1).

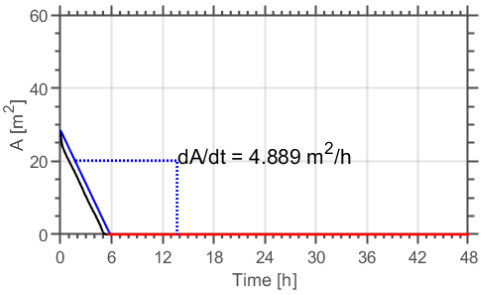

Figure F.183: A(t) of material L-2-3.

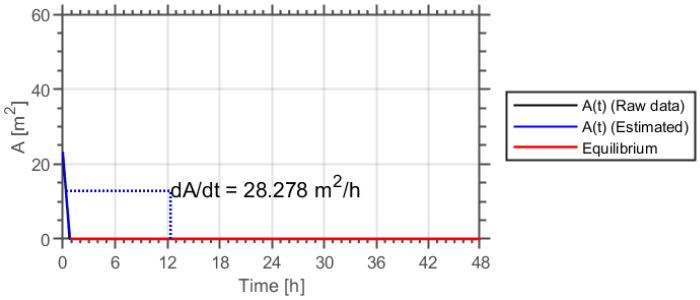

Figure F.184: A(t) of material L-2-4 (see Table B.1).

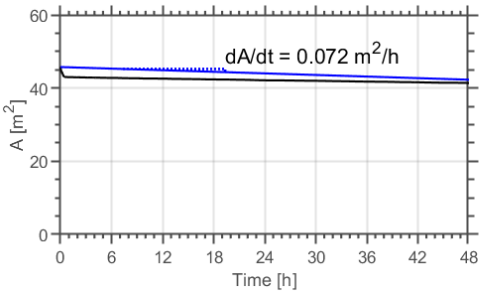

Figure F.185: A(t) of material L-3-1.

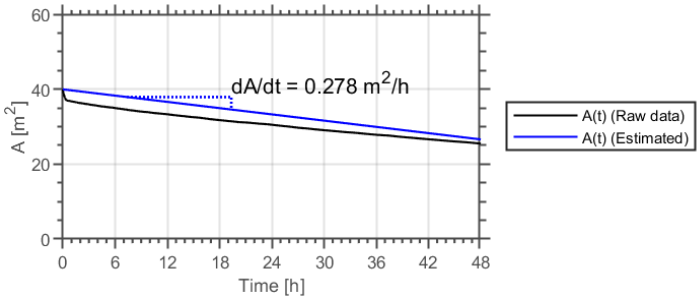

Figure F.186: A(t) of material L-3-2 (see Table B.1).

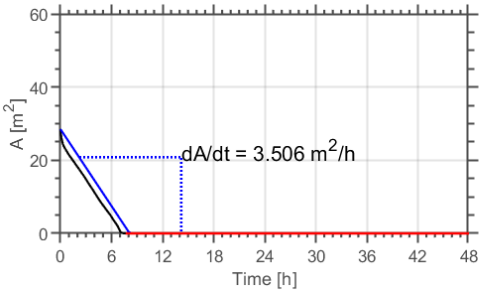

Figure F.187: A(t) of material L-3-3.

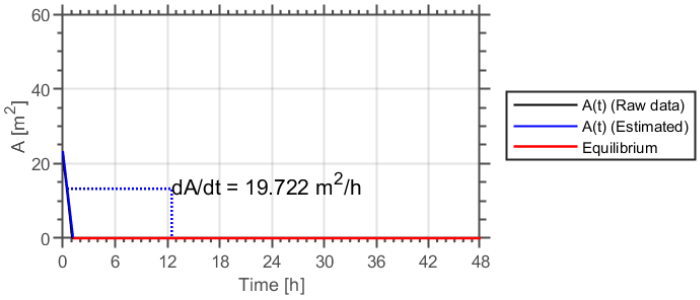

Figure F.188: A(t) of material L-3-4 (see Table B.1).

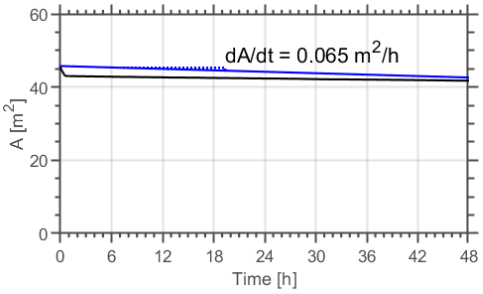

Figure F.189: A(t) of material L-4-1.

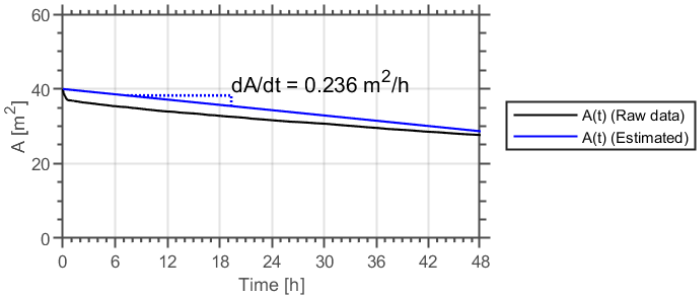

Figure F.190: A(t) of material L-4-2 (see Table B.1).

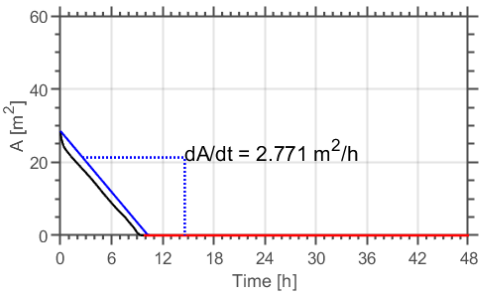

Figure F.191: A(t) of material L-4-3.

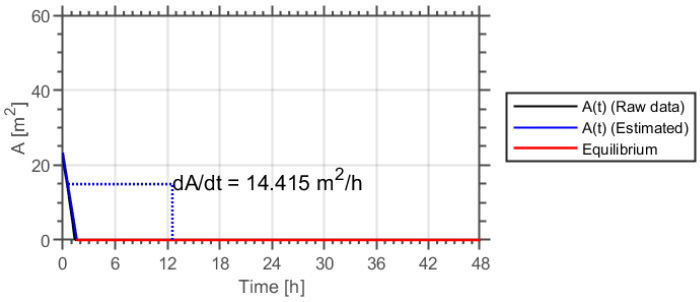

Figure F.192: A(t) of material L-4-4 (see Table B.1).

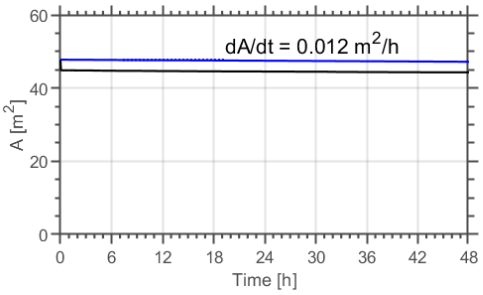

Figure F.193: A(t) of material M-1-1.

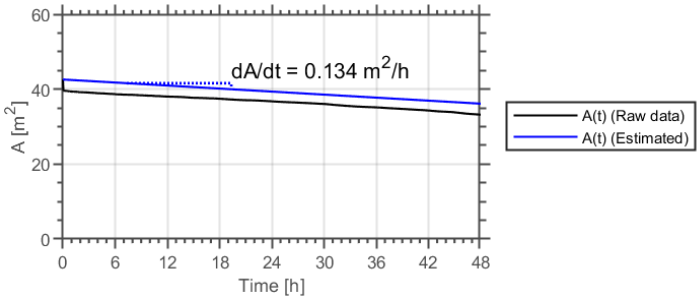

Figure F.194: A(t) of material M-1-2 (see Table B.1).

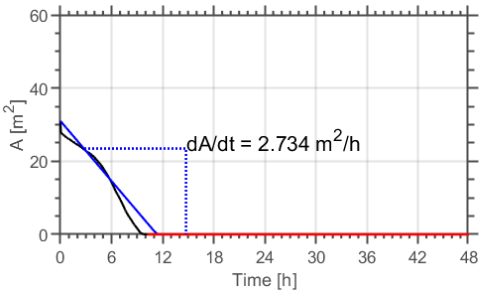

Figure F.195: A(t) of material M-1-3.

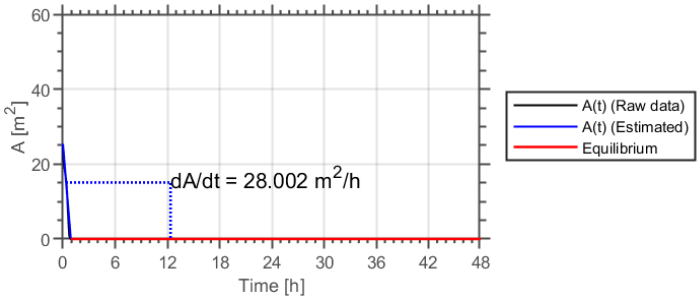

Figure F.196: A(t) of material M-1-4 (see Table B.1).

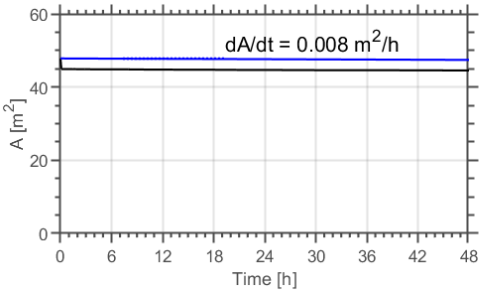

Figure F.197: A(t) of material M-2-1.

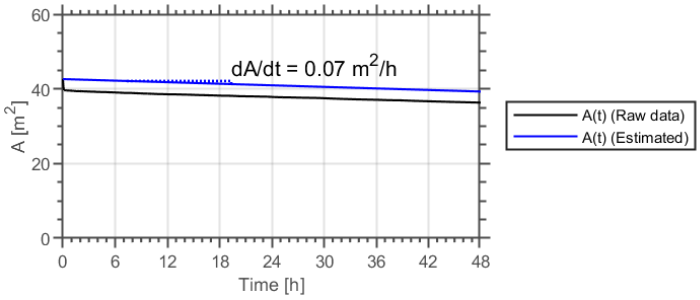

Figure F.198: A(t) of material M-2-2 (see Table B.1).

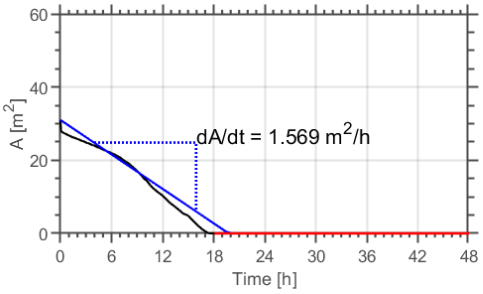

Figure F.199: A(t) of material M-2-3.

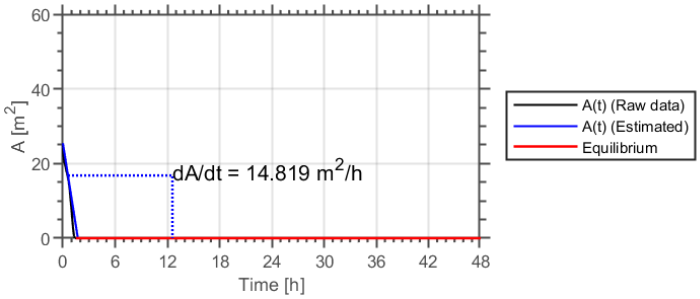

Figure F.200: A(t) of material M-2-4 (see Table B.1).

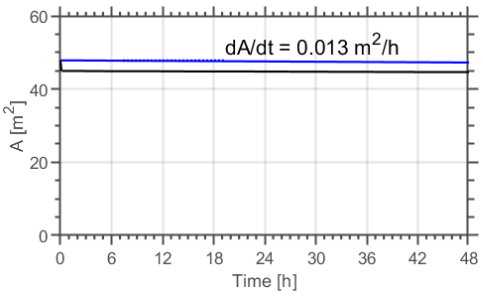

Figure F.201: A(t) of material M-3-1.

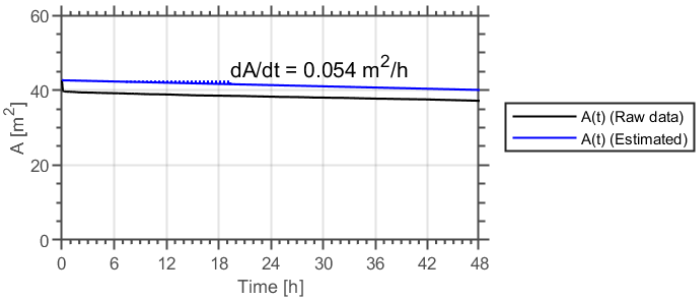

Figure F.202: A(t) of material M-3-2 (see Table B.1).

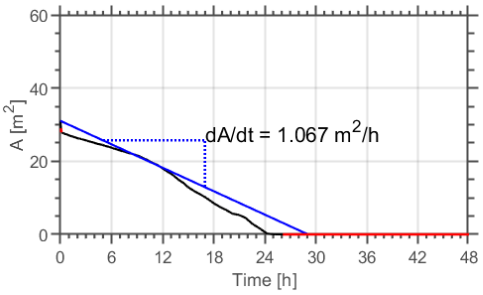

Figure F.203: A(t) of material M-3-3.

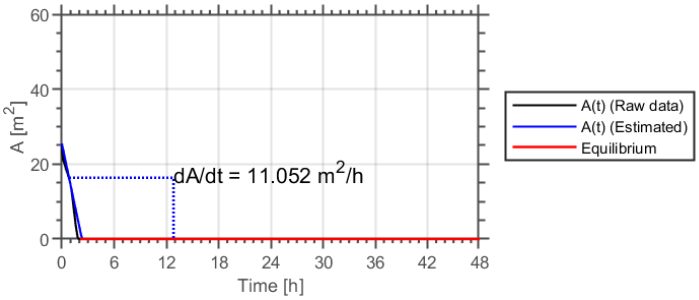

Figure F.204: A(t) of material M-3-4 (see Table B.1).

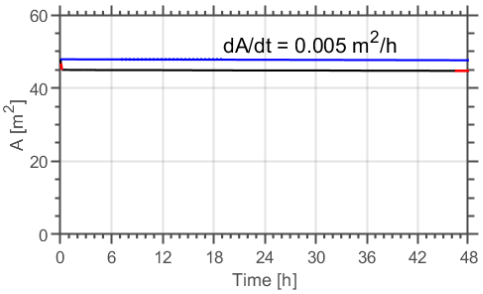

Figure F.205: A(t) of material M-4-1.

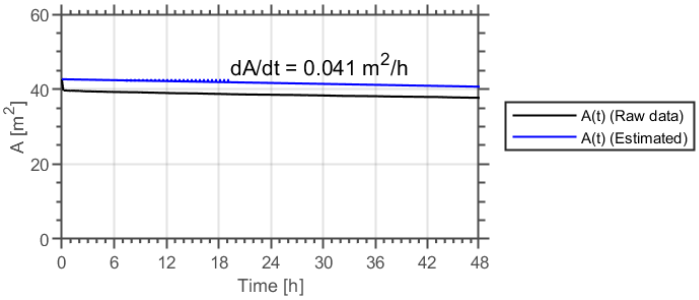

Figure F.206: A(t) of material M-4-2 (see Table B.1).

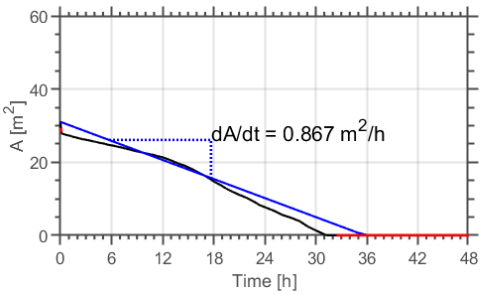

Figure F.207: A(t) of material M-4-3.

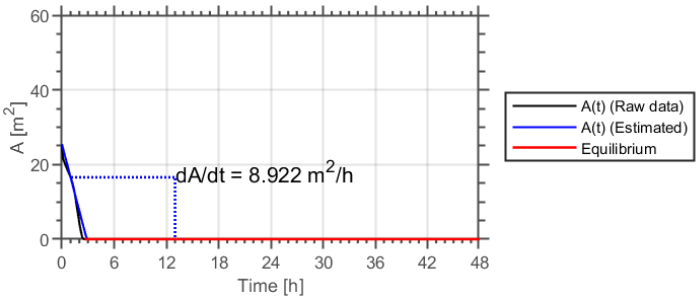

Figure F.208: A(t) of material M-4-4 (see Table B.1).

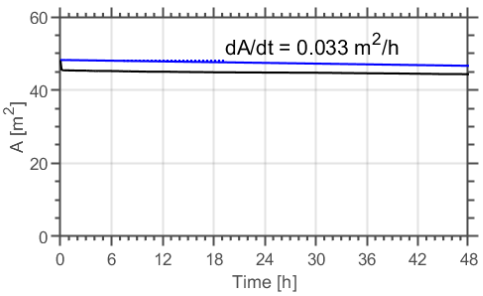

Figure F.209: A(t) of material N-1-1.

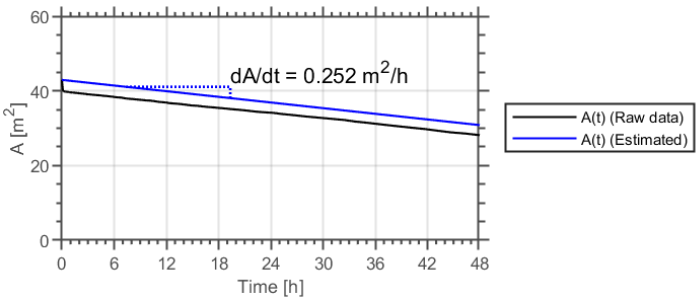

Figure F.210: A(t) of material N-1-2 (see Table B.1).

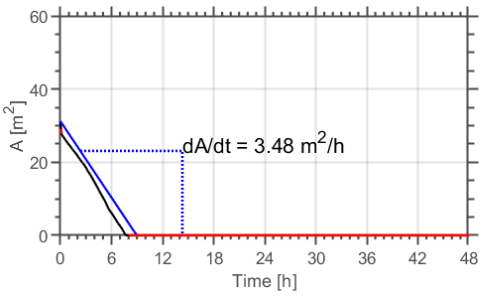

Figure F.211: A(t) of material N-1-3.

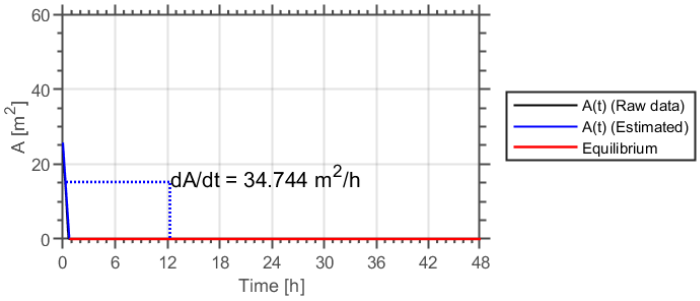

Figure F.212: A(t) of material N-1-4 (see Table B.1).

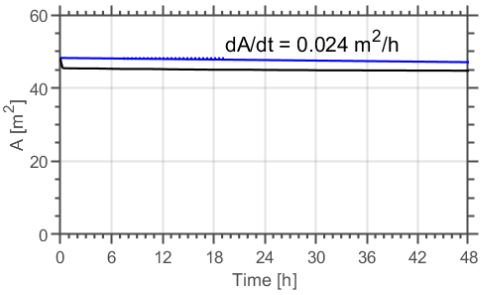

Figure F.213: A(t) of material N-2-1.

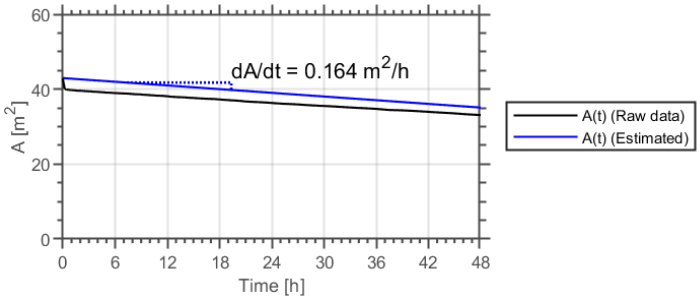

Figure F.214: A(t) of material N-2-2 (see Table B.1).

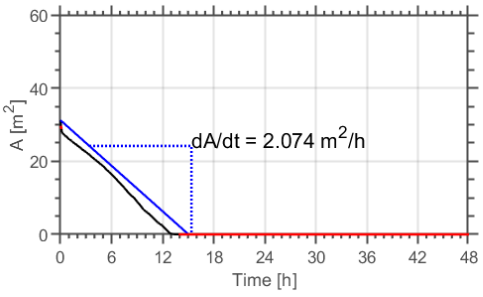

Figure F.215: A(t) of material N-2-3.

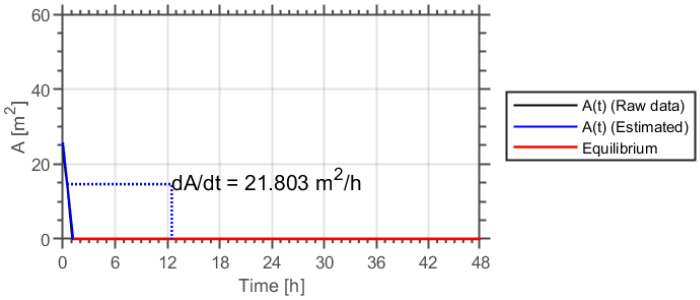

Figure F.216: A(t) of material N-2-4 (see Table B.1).

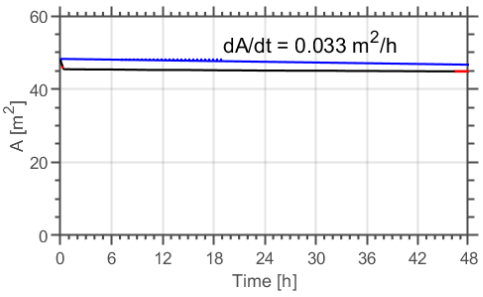

Figure F.217: A(t) of material N-3-1.

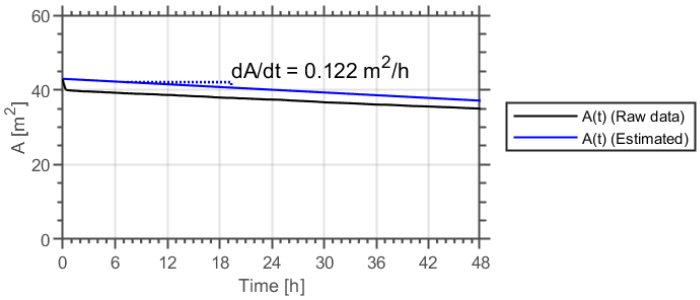

Figure F.218: A(t) of material N-3-2 (see Table B.1).

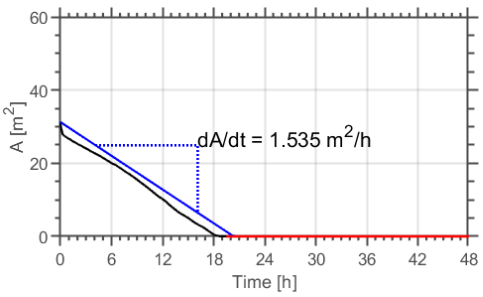

Figure F.219: A(t) of material N-3-3.

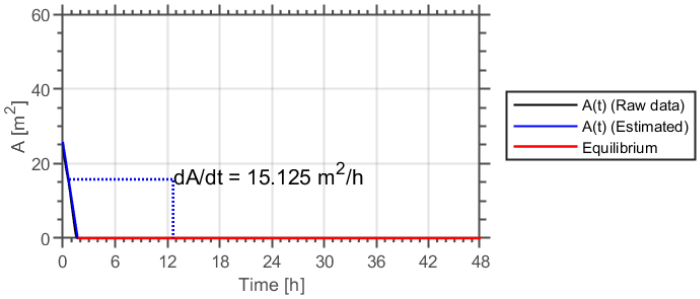

Figure F.220: A(t) of material N-3-4 (see Table B.1).

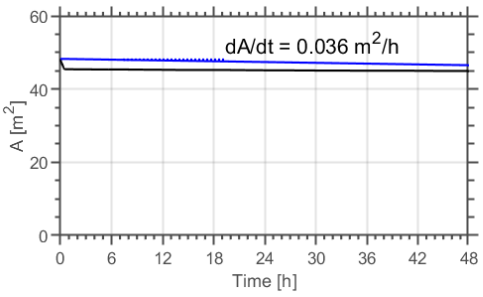

Figure F.221: A(t) of material N-4-1.

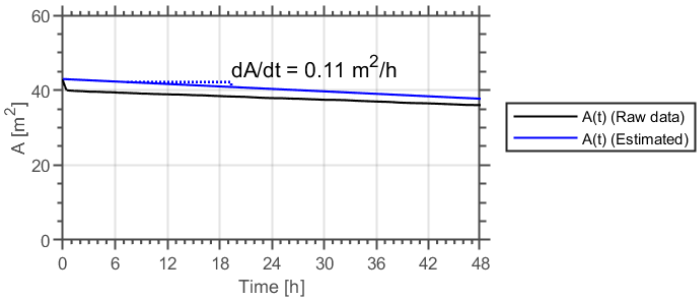

Figure F.222: A(t) of material N-4-2 (see Table B.1).

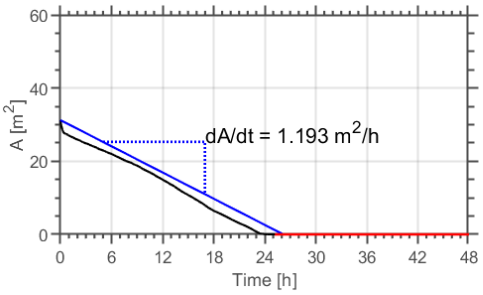

Figure F.223: A(t) of material N-4-3.

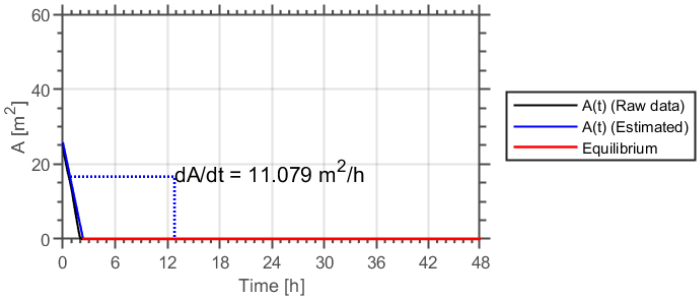

Figure F.224: A(t) of material N-4-4 (see Table B.1).

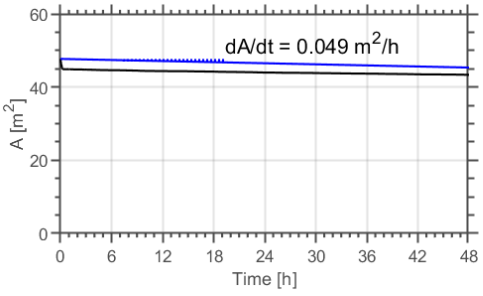

Figure F.225: A(t) of material O-1-1.

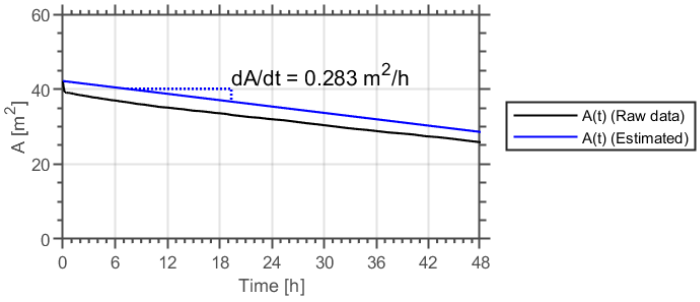

Figure F.226: A(t) of material O-1-2 (see Table B.1).

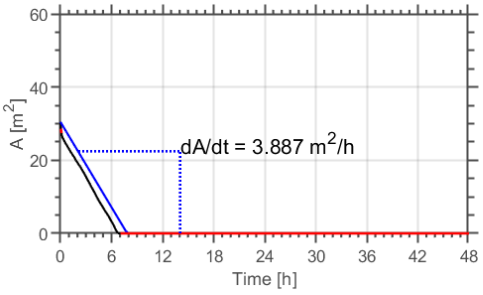

Figure F.227: A(t) of material O-1-3.

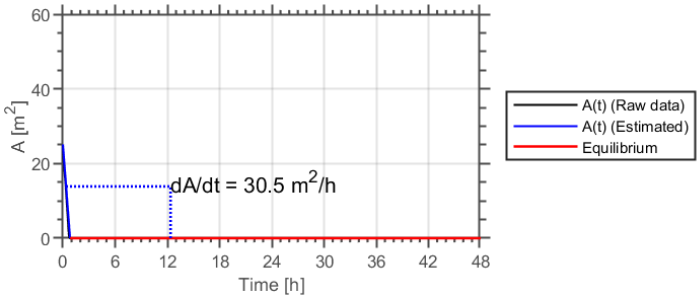

Figure F.228: A(t) of material O-1-4 (see Table B.1).

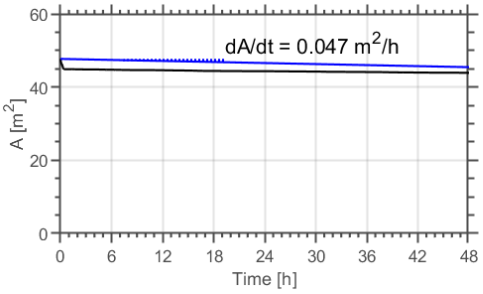

Figure F.229: A(t) of material O-2-1.

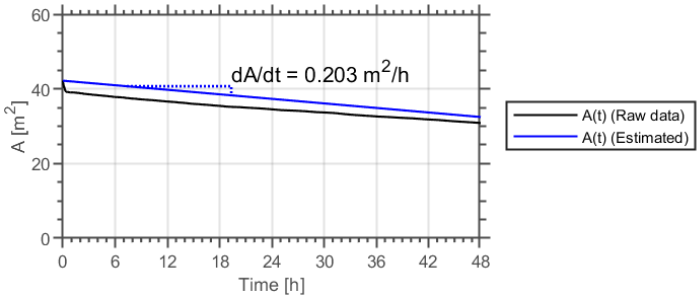

Figure F.230: A(t) of material O-2-2 (see Table B.1).

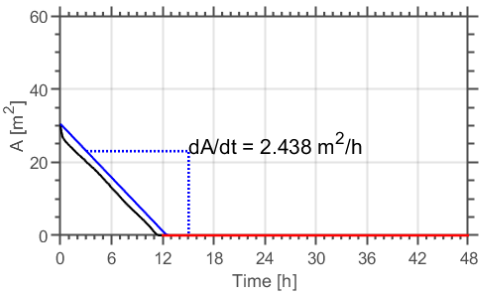

Figure F.231: A(t) of material O-2-3.

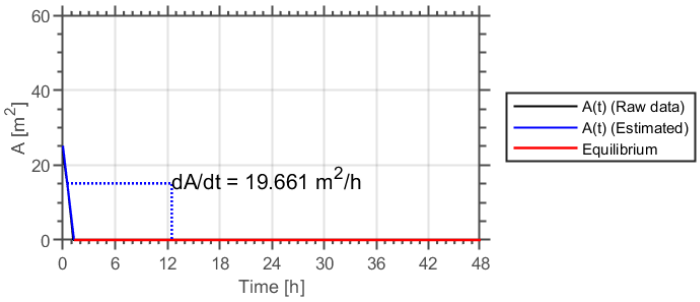

Figure F.232: A(t) of material O-2-4 (see Table B.1).

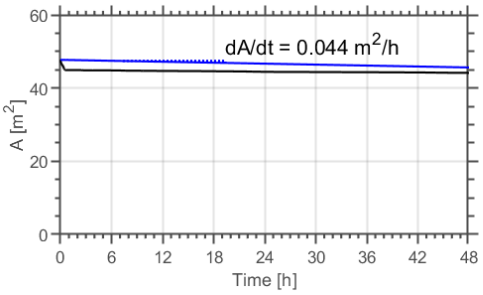

Figure F.233: A(t) of material O-3-1.

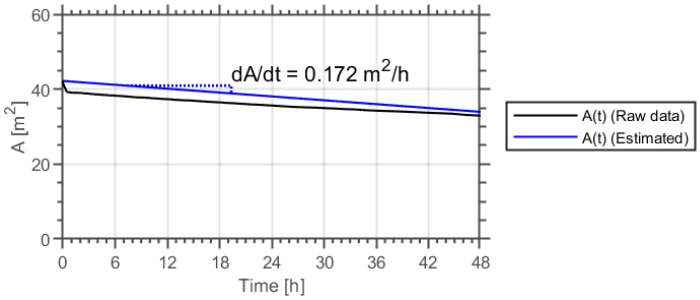

Figure F.234: A(t) of material O-3-2 (see Table B.1).

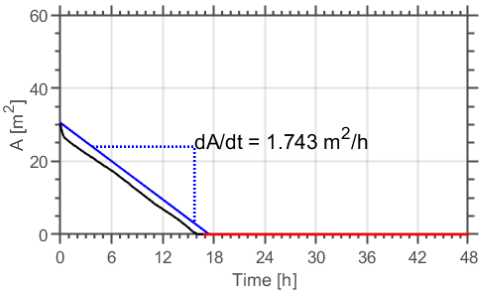

Figure F.235: A(t) of material O-3-3.

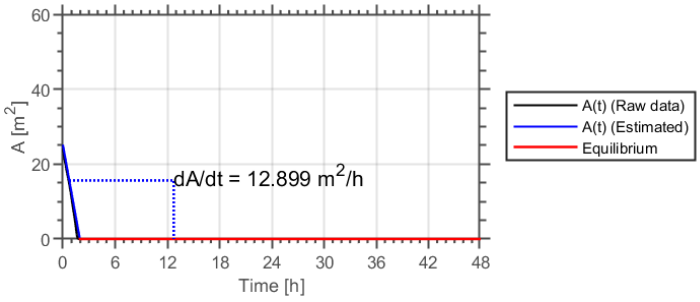

Figure F.236: A(t) of material O-3-4 (see Table B.1).

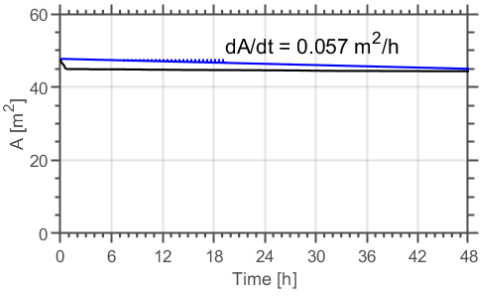

Figure F.237: A(t) of material O-4-1.

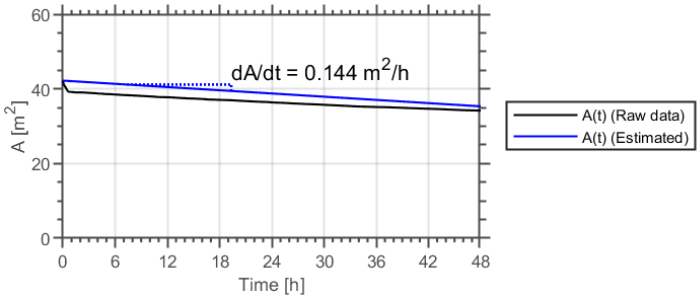

Figure F.238: A(t) of material O-4-2 (see Table B.1).

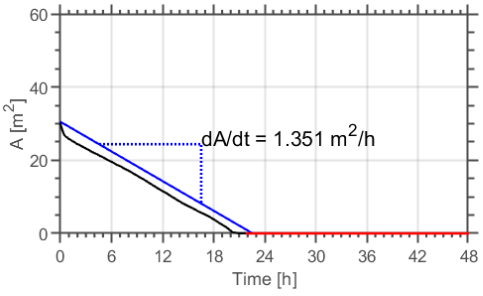

Figure F.239: A(t) of material O-4-3.

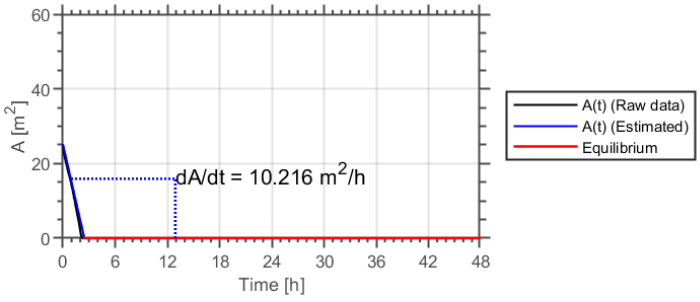

Figure F.240: A(t) of material O-4-4 (see Table B.1).

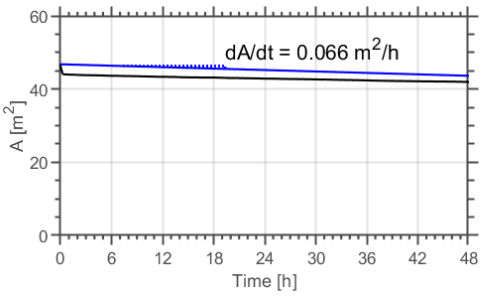

Figure F.241: A(t) of material P-1-1.

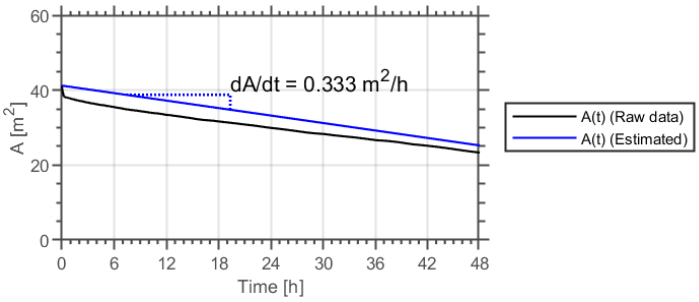

Figure F.242: A(t) of material P-1-2 (see Table B.1).

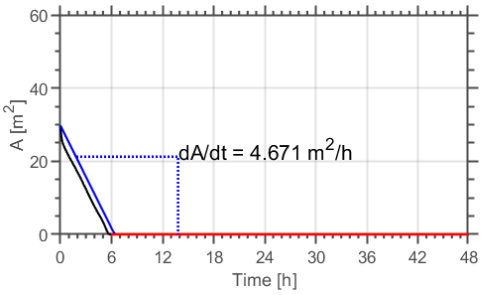

Figure F.243: A(t) of material P-1-3.

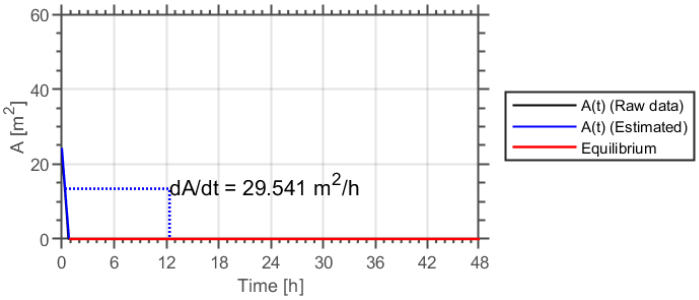

Figure F.244: A(t) of material P-1-4 (see Table B.1).

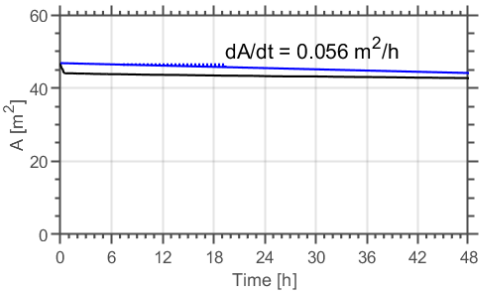

Figure F.245: A(t) of material P-2-1.

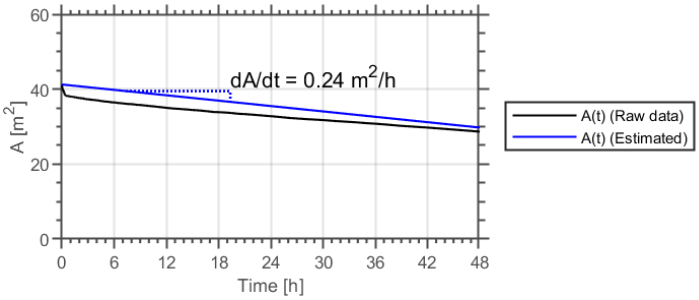

Figure F.246: A(t) of material P-2-2 (see Table B.1).

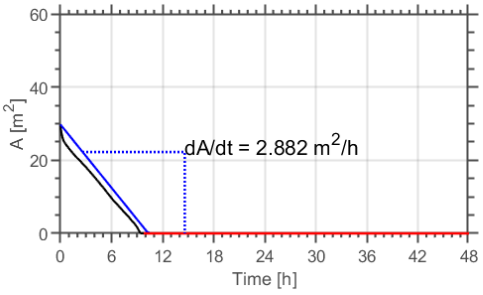

Figure F.247: A(t) of material P-2-3.

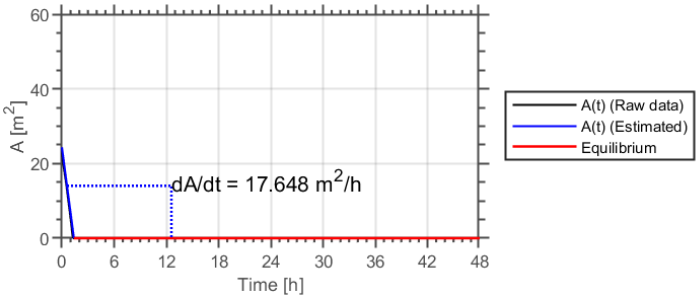

Figure F.248: A(t) of material P-2-4 (see Table B.1).

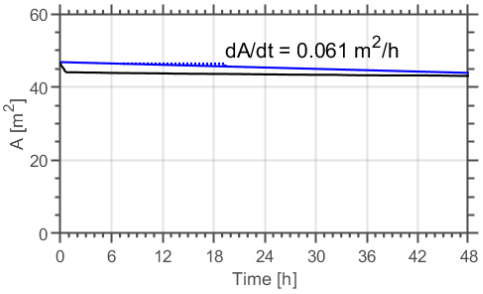

Figure F.249: A(t) of material P-3-1.

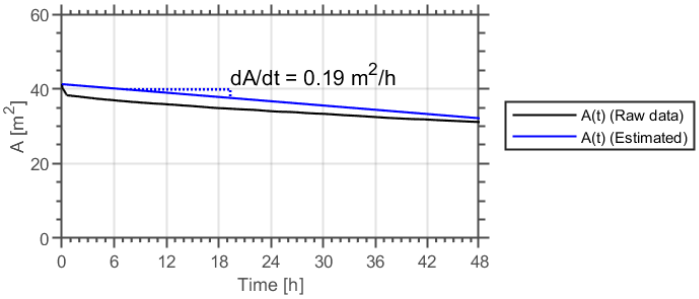

Figure F.250: A(t) of material P-3-2 (see Table B.1).

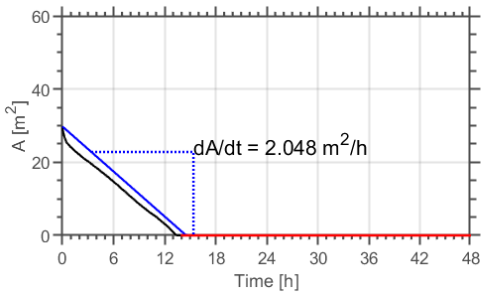

Figure F.251: A(t) of material P-3-3.

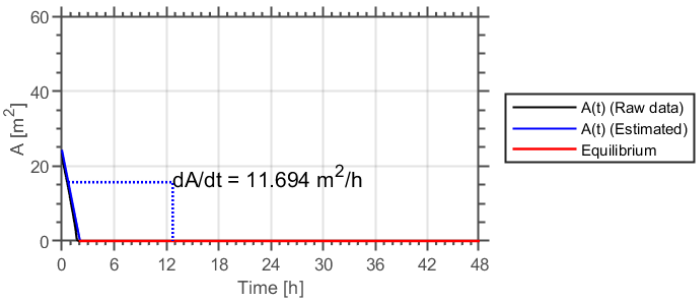

Figure F.252: A(t) of material P-3-4 (see Table B.1).

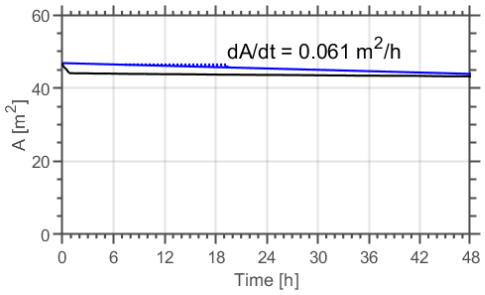

Figure F.253: A(t) of material P-4-1.

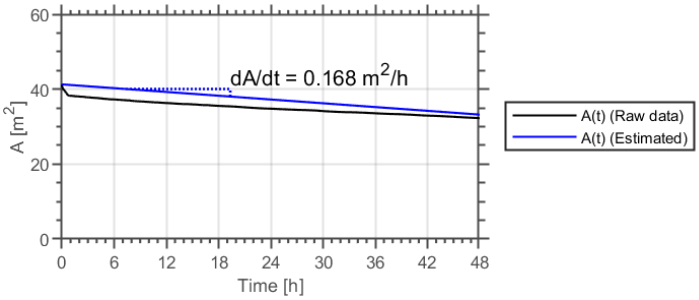

Figure F.254: A(t) of material P-4-2 (see Table B.1).

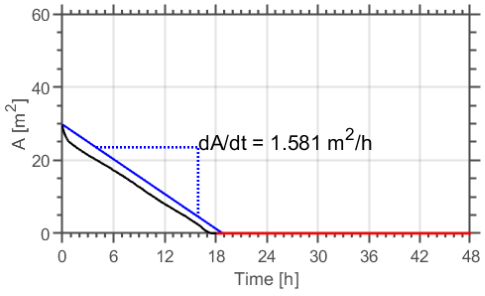

Figure F.255: A(t) of material P-4-3.

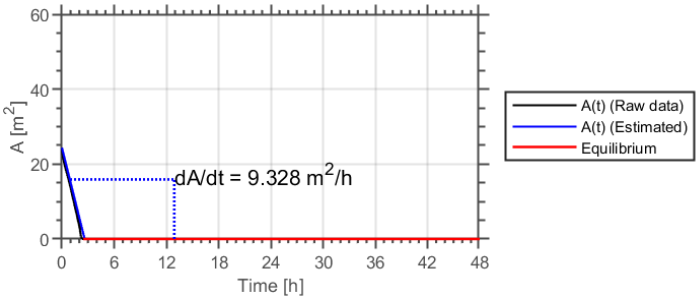

Figure F.256: A(t) of material P-4-4 (see Table B.1).

F.2 Simulation set 2

This section shows the area of the unsaturated zone over time for each of the simulations performed in set 1. The parameter values corresponding to each simulation are given in Table B.2.

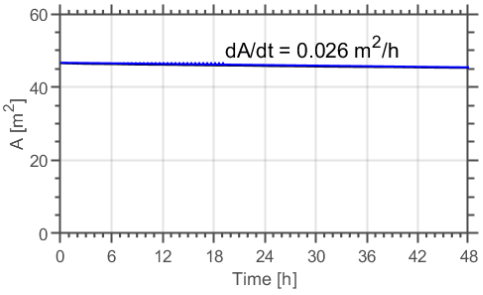

Figure F.257: A(t) of scenario 1 in set 2.

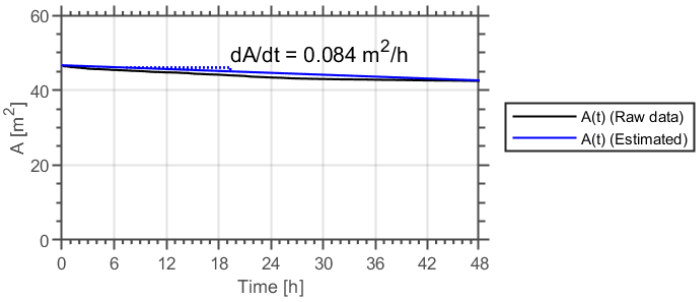

Figure F.258: A(t) of scenario 2 in set 2 (See Table B.2).

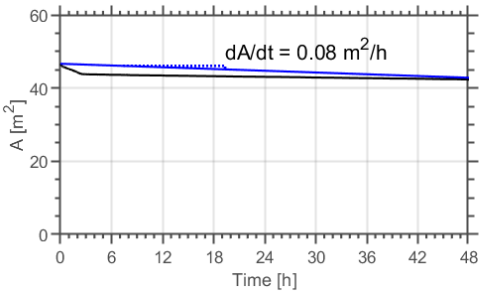

Figure F.259: A(t) of scenario 3 in set 2.

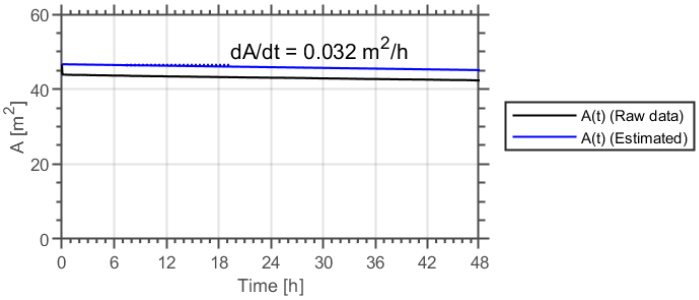

Figure F.260: A(t) of scenario 4 in set 2 (See Table B.2).

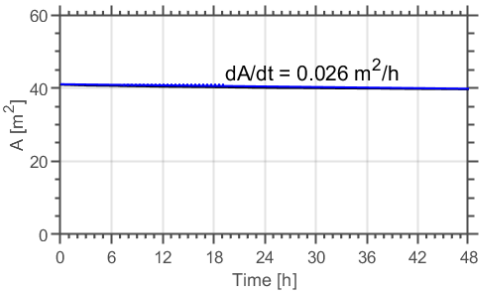

Figure F.261: A(t) of scenario 5 in set 2.

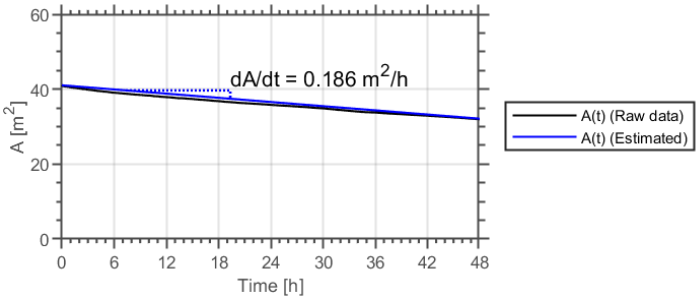

Figure F.262: A(t) of scenario 6 in set 2 (See Table B.2).

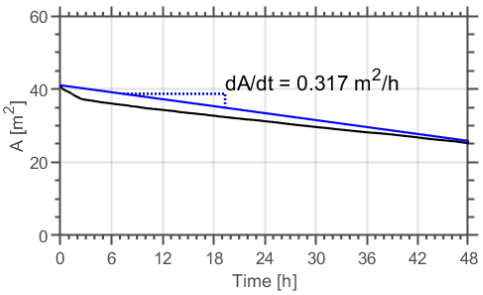

Figure F.263: A(t) of scenario 7 in set 2.

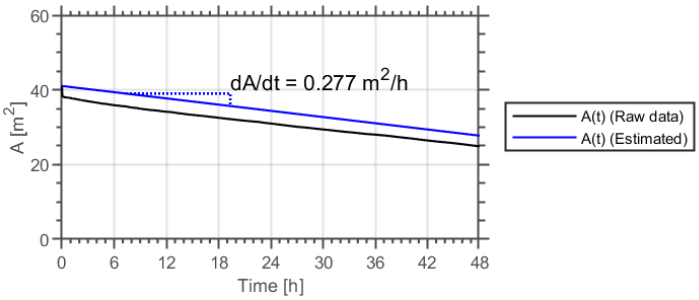

Figure F.264: A(t) of scenario 8 in set 2 (See Table B.2).

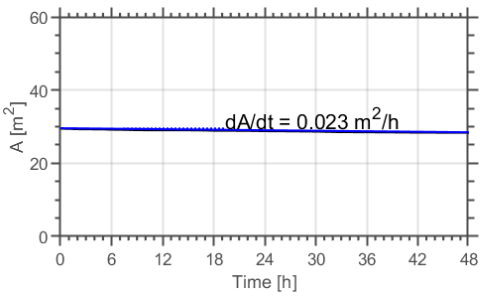

Figure F.265: A(t) of scenario 9 in set 2.

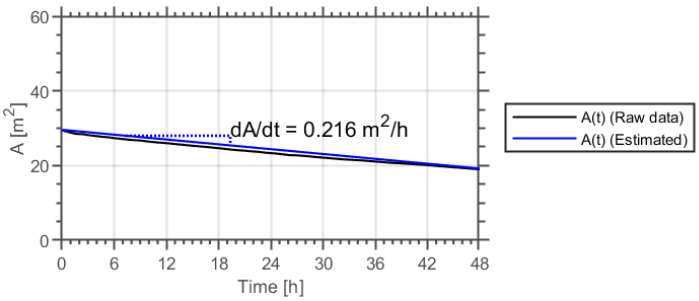

Figure F.266: A(t) of scenario 10 in set 2 (See Table B.2).

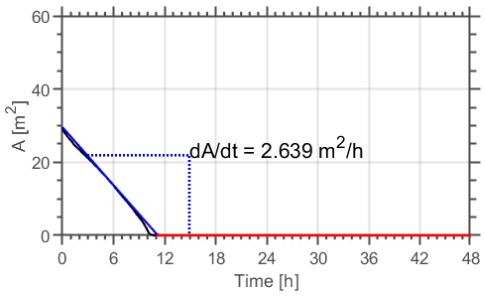

Figure F.267: A(t) of scenario 11 in set 2.

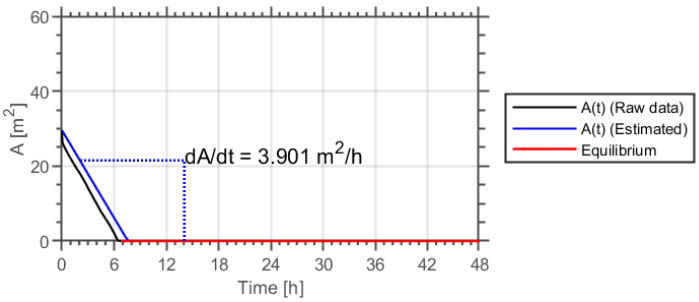

Figure F.268: A(t) of scenario 12 in set 2 (See Table B.2).

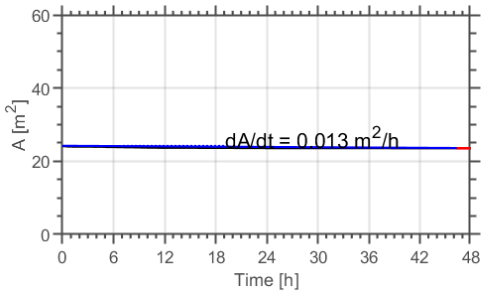

Figure F.269: A(t) of scenario 13 in set 2.

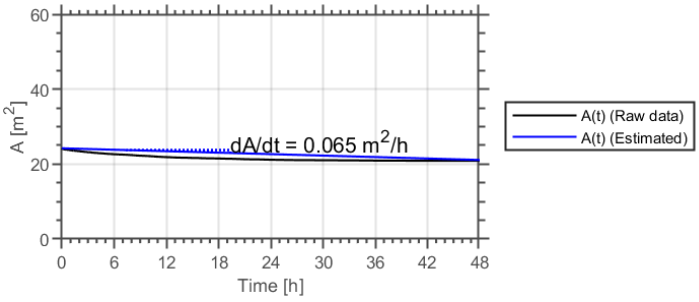

Figure F.270: A(t) of scenario 14 in set 2 (See Table B.2).

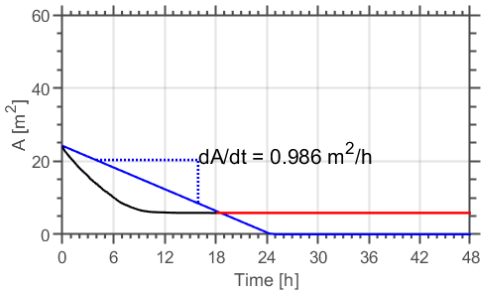

Figure F.271: A(t) of scenario 15 in set 2.

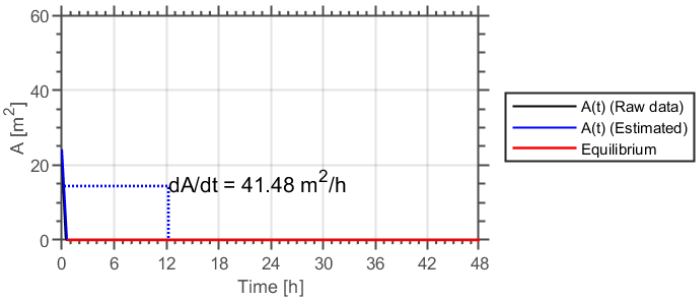

Figure F.272: A(t) of scenario 16 in set 2 (See Table B.2).

F.3 Simulation set 3

This section shows the area of the unsaturated zone over time for each of the simulations performed in set 1. The parameter values corresponding to each simulation are given in Table B.3.

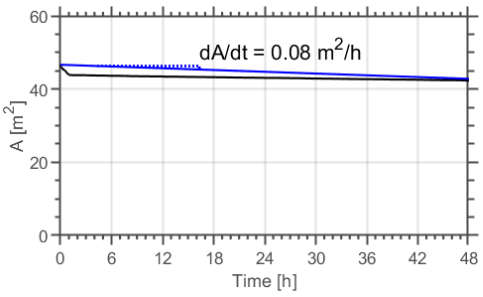

Figure F.273: A(t) of scenario 1 in set 3.

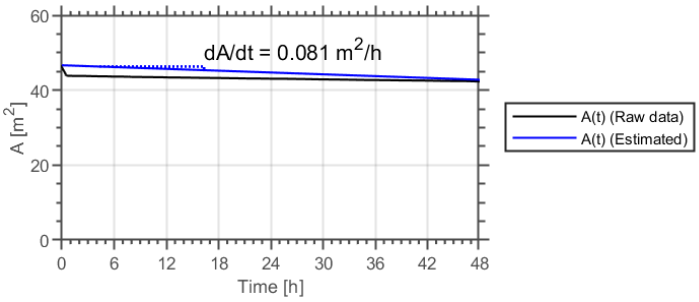

Figure F.274: A(t) of scenario 2 in set 3 (See Table B.3).

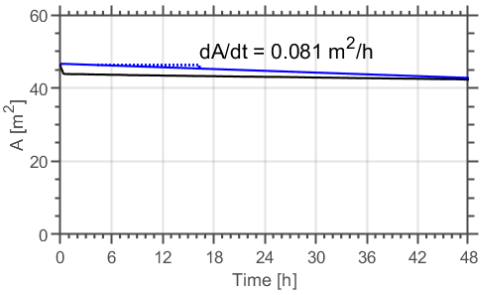

Figure F.275: A(t) of scenario 3 in set 3.

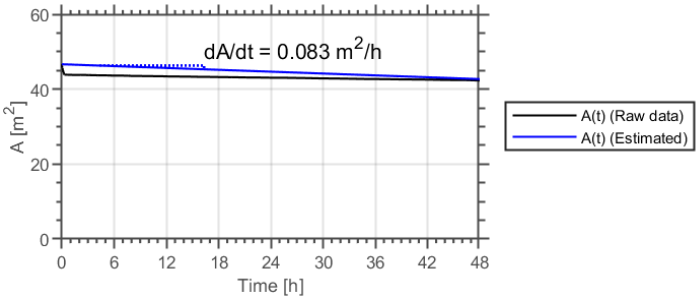

Figure F.276: A(t) of scenario 4 in set 3 (See Table B.3).

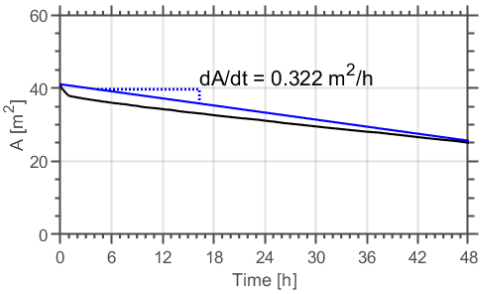

Figure F.277: A(t) of scenario 5 in set 3.

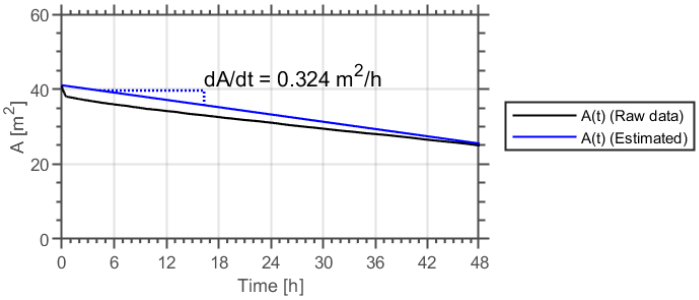

Figure F.278: A(t) of scenario 6 in set 3 (See Table B.3).

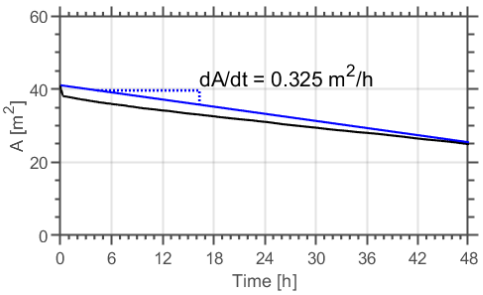

Figure F.279: A(t) of scenario 7 in set 3.

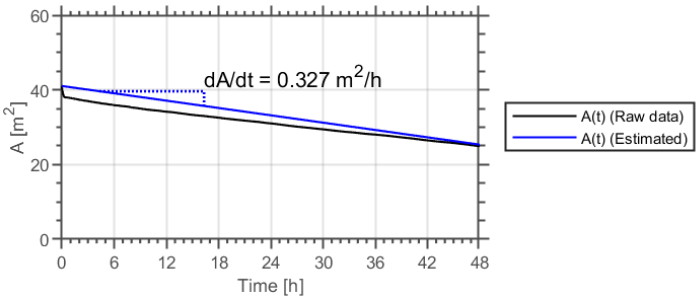

Figure F.280: A(t) of scenario 8 in set 3 (See Table B.3).

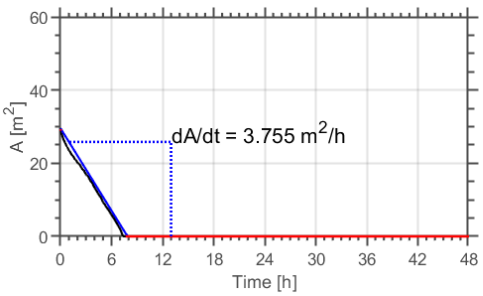

Figure F.281: A(t) of scenario 9 in set 3.

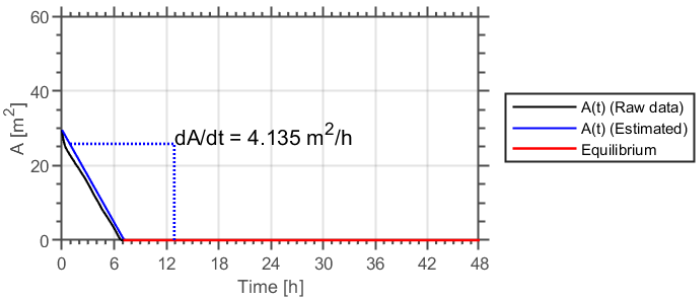

Figure F.282: A(t) of scenario 10 in set 3 (See Table B.3).

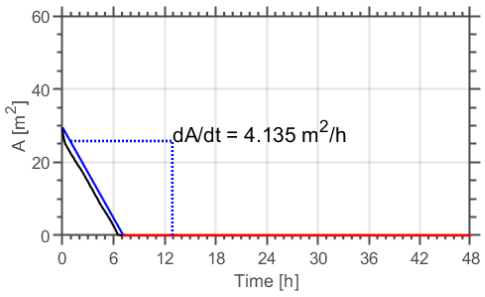

Figure F.283: A(t) of scenario 11 in set 3.

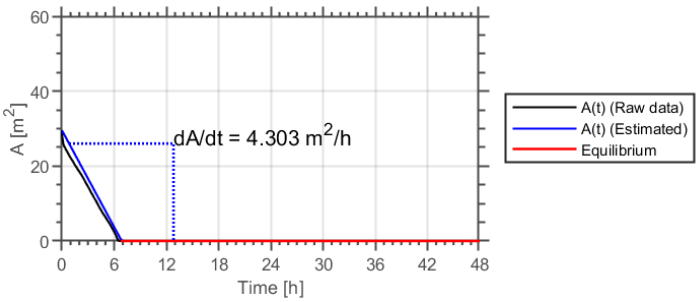

Figure F.284: A(t) of scenario 12 in set 3 (See Table B.3).

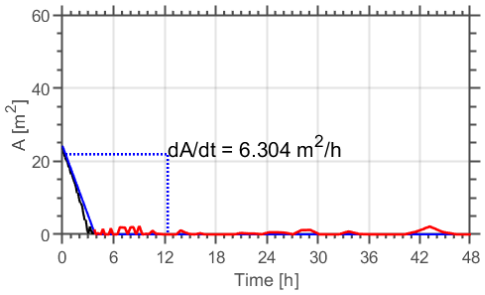

Figure F.285: A(t) of scenario 13 in set 3.

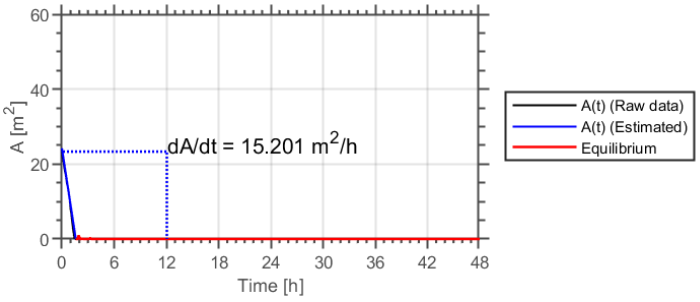

Figure F.286: A(t) of scenario 14 in set 3 (See Table B.3).

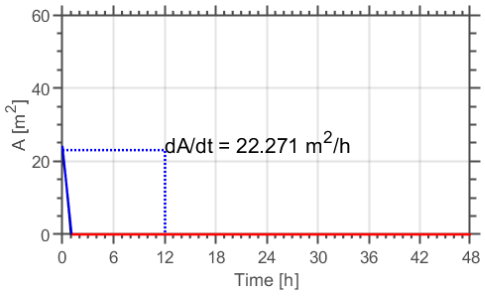

Figure F.287: A(t) of scenario 15 in set 3.

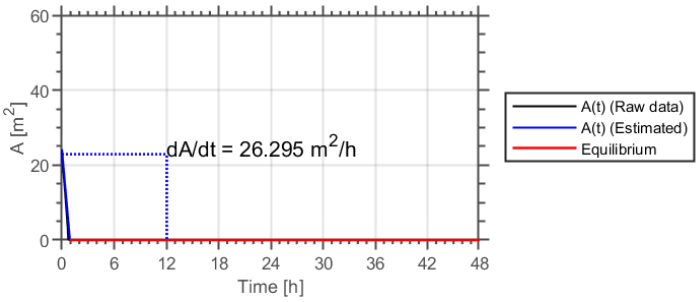

Figure F.288: A(t) of scenario 16 in set 3 (See Table B.3).

F.4 Simulation set 4

This section shows the area of the unsaturated zone over time for each of the simulations performed in set 1. The parameter values corresponding to each simulation are given in Table B.4.

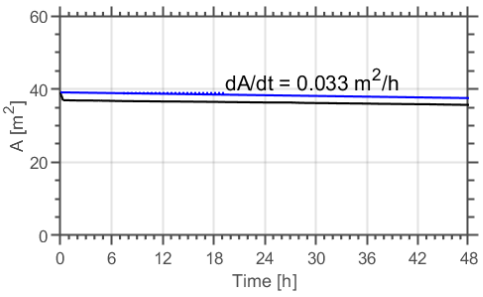

Figure F.289: A(t) of scenario 1 in set 4.

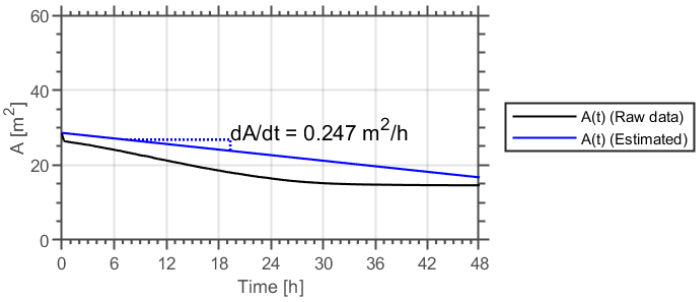

Figure F.290: A(t) of scenario 2 in set 4 (See Table B.4).

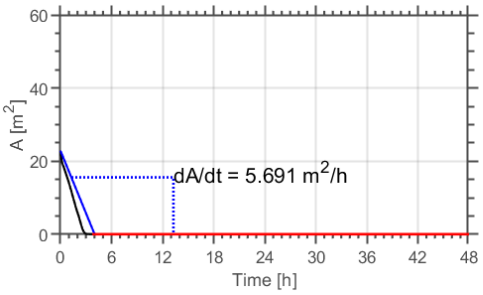

Figure F.291: A(t) of scenario 3 in set 4.

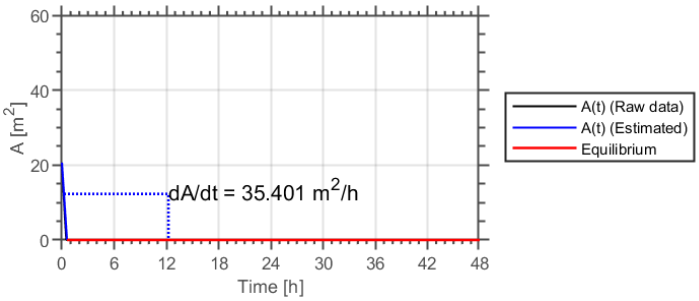

Figure F.292: A(t) of scenario 4 in set 4 (See Table B.4).

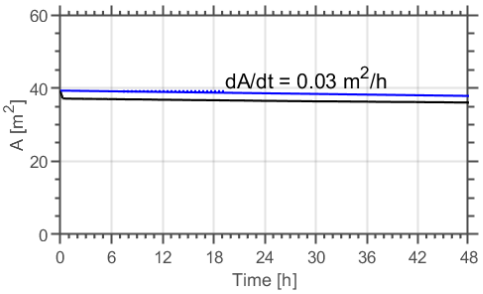

Figure F.293: A(t) of scenario 5 in set 4.

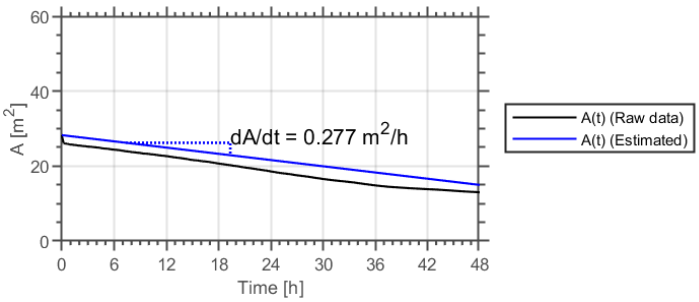

Figure F.294: A(t) of scenario 6 in set 4 (See Table B.4).

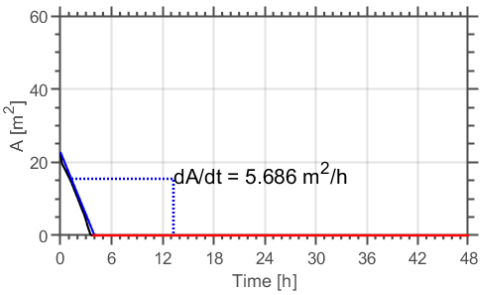

Figure F.295: A(t) of scenario 7 in set 4.

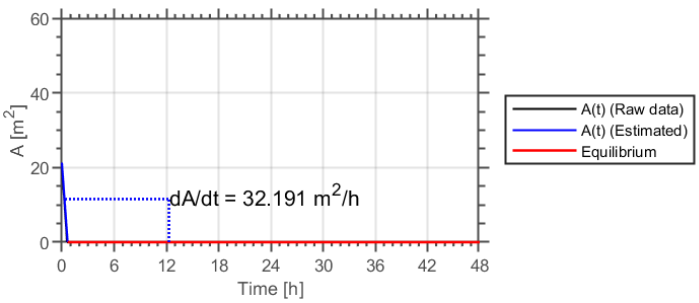

Figure F.296: A(t) of scenario 8 in set 4 (See Table B.4).

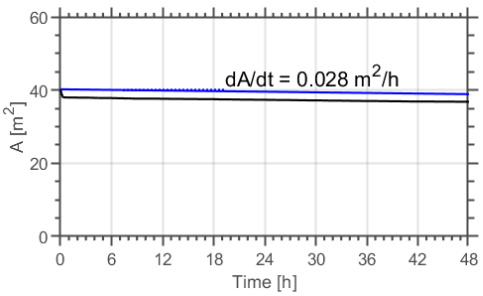

Figure F.297: A(t) of scenario 9 in set 4.

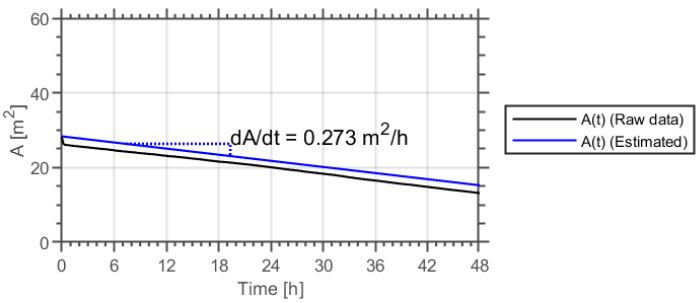

Figure F.298: A(t) of scenario 10 in set 4 (See Table B.4).

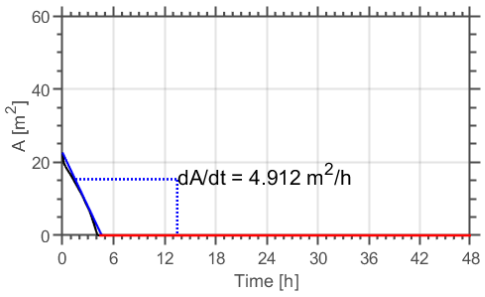

Figure F.299: A(t) of scenario 11 in set 4.

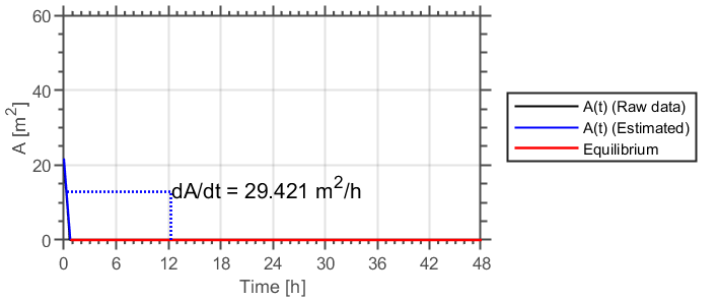

Figure F.300: A(t) of scenario 12 in set 4 (See Table B.4).

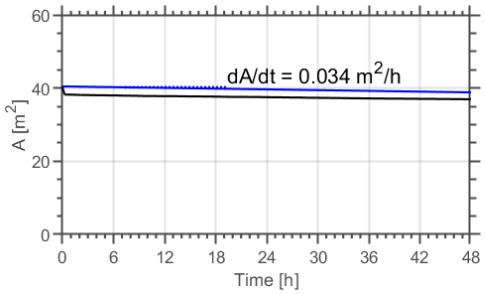

Figure F.301: A(t) of scenario 13 in set 4.

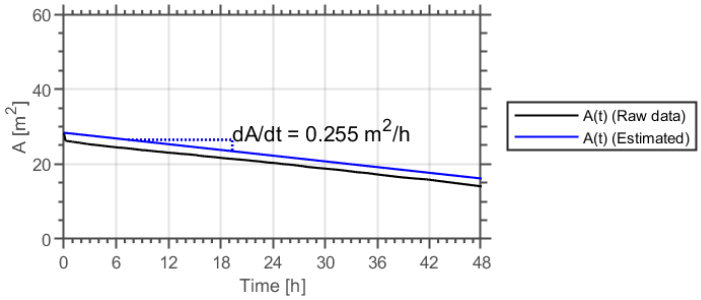

Figure F.302: A(t) of scenario 14 in set 4 (See Table B.4).

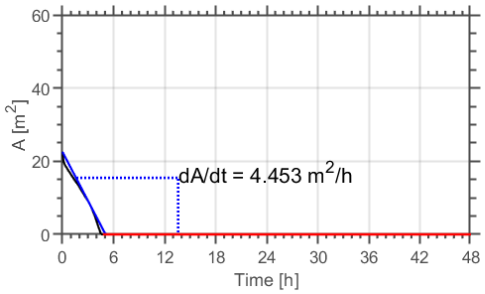

Figure F.303: A(t) of scenario 15 in set 4.

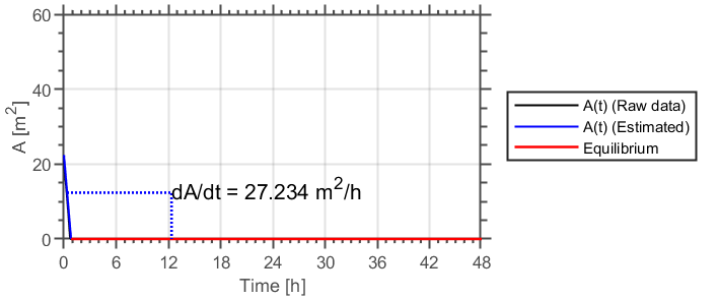

Figure F.304: A(t) of scenario 16 in set 4 (See Table B.4).

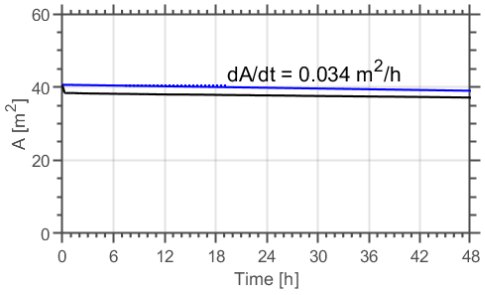

Figure F.305: A(t) of scenario 17 in set 4.

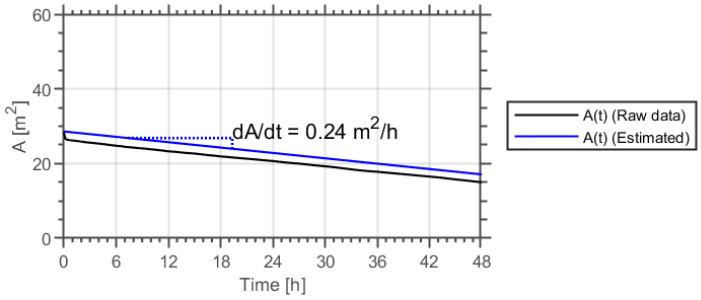

Figure F.306: A(t) of scenario 18 in set 4 (See Table B.4).

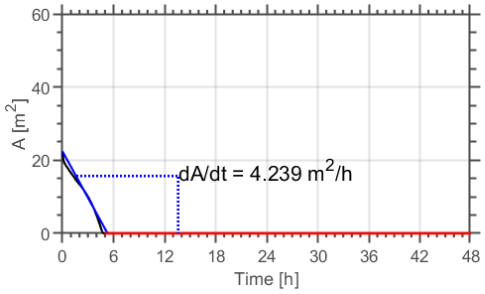

Figure F.307: A(t) of scenario 19 in set 4.

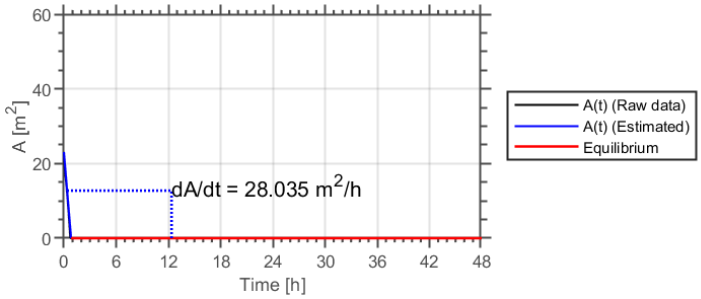

Figure F.308: A(t) of scenario 20 in set 4 (See Table B.4).